Herstellung, Charakterisierung und mikromechanische Modellierung von magneto-sensitiven Elastomeren

Von der Naturwissenschaftlichen Fakultät der

Gottfried Wilhelm Leibniz Universität Hannover zur Erlangung des Grades

Doktor der Naturwissenschaften

(Dr. rer. nat.)

genehmigte Dissertation

von

Dipl.-Phys. Sahbi Aloui

2018

Referent: Hon. Prof. Dr. rer. nat. habil. Manfred Klüppel

Korreferent: Prof. Dr. rer. nat. Jürgen Caro

Tag der Promotion: 16 Oktober 2018

Acknowledgement

Kurzfassung

Magneto-sensitive Elastomere (MSE) gehören zur Klasse der „Smart Materials". Sie zeigen ein sich selbst anpassendes und adaptives Verhalten in zufälligen Ereignissen und werden auch als intelligente Materialien bezeichnet. Sie zeichnen sich durch die Fähigkeit aus, in einem zielgerichteten Handeln auf Veränderungen der Betriebs- oder Umweltbedingungen ohne externe Regulierung zu reagieren.

MSE werden durch Mischen magnetischer Füllstoffe in der Kautschukmatrix hergestellt. Mechanische und magnetorheologische Messungen zeigen, dass Partikelgröße, Füllstoffgehalt und Haftvermittler die mechanische und die magnetische Eigenschaften von MSE erheblich beeinflussen. Die Leistung von MSE kann durch die Herstellung anisotroper Proben mit orientierten magnetischen Füllstoffpartikeln weiter verbessert werden. Das wird durch die Vulkanisation in einem externen Magnetfeld erreicht.

Dieser Prozess kann online durch magnetorheologische Messungen der unvernetzten Schmelzen untersucht werden. Die Orientierung der magnetischen Füllstoffpartikel in Strängen entlang der Magnetfeldlinien äußert sich in einer sukzessiven Erhöhung des Schubmoduls beim Einschalten des Magnetfeldes. Diese Schaltfähigkeit wird durch mikrofeine magnetische Füllstoffe gefördert und kann einen Wert von 600 % erreichen. Magnetische Füllstoffe im Nanogrößenbereich zeigen jedoch kaum einen Schalteffekt und tragen hauptsächlich zur mechanischen Verstärkung von MSE bei. Die Vernetzung gewährleistet die MSE höhere Modulwerte im Vergleich zu den Schmelzen, ein maximaler Schalteffekt von 36 % für anisotrope Proben wird aber gemessen.

MSE zeigen ein ähnliches mechanisches Ermüdungs- und Alterungsverhalten im Vergleich zu herkömmlichen Gummiproben.

Die Kopplung zwischen den magnetischen und mechanischen Eigenschaften von MSE wird weiter untersucht, indem die Messdaten mit dem mikromechanischen dynamischen Flokkulationsmodell modelliert werden. Es zeigt sich, dass die Fit-Parameter signifikant von der Verteilung der magnetischen Füllstoffpartikel innerhalb der MSE-Proben abhängen. Darüber hinaus werden einige Anpassungsparameter durch das angelegte Magnetfeld bestimmt, was bestätigt, dass die Änderung der magnetischen Eigenschaften der Umgebung die mechanischen Eigenschaften der Proben unvermeidlich beeinflusst.

Die Eigenschaftenoptimierung der MSE kann durch den Einsatz hybrider Füllstoffsysteme erreicht werden. Die Verbindung verschiedener Füllstoffe ergibt einen Synergieeffekt zwischen der Wirkung einzelner Füllstoffe und den Endeigenschaften von MSE. Ein zeitnaher Einsatz von MSE in technischen Anwendungen erscheint derzeit nur auf dieser Basis realistisch.

Schlüsselwörter: Smart materials, Magneto-sensitive Elastomere, Orientierung der magnetischen Füllstoffpartikel, Schalteffekt, magneto-mechanisches Verhalten, hybrid Füllsysteme.

Abstract

Magneto-sensitive elastomers (MSE) belong to the class of smart materials. They show a self-adjusting and adaptive behaviour in random occurrences and are also denoted as intelligent materials. They are characterised by the ability to react in a target-oriented acting to changes in operating or environmental conditions without external regulation.

MSE are prepared by mixing magnetic fillers within the rubber matrix. Mechanical and magnetorheological measurements show that particle size, filler loading and coupling agent considerably influence the mechanical and magnetic properties of MSE. The performance of MSE can be further improved by preparing anisotropic samples with oriented magnetic filler particles. This is achieved by curing in an external magnetic field.

This process can be examined online by magnetorheological measurements of the non-crosslinked melts. The orientation of the magnetic filler particles in strings along the magnetic field lines expresses itself in a successive increase of the shear modulus when the magnetic field is turned on. This switching ability is promoted by microsized magnetic fillers and can reach a value of 600 %. However, nanosized magnetic fillers show hardly any switching effect and mainly contribute to the mechanical reinforcement of MSE. The crosslinking ensures the MSE samples higher modulus values compared to the melts. But a maximal switching effect of 36 % for anisotropic samples is measured.

MSE show similar mechanical fatigue and ageing behaviour compared with conventional rubber samples.

The coupling between magnetic and mechanical properties of MSE is further investigated by modelling the measurement data using the micromechanical dynamical flocculation model. It is found that the fit parameters significantly depend on the distribution of magnetic filler particles within the MSE samples. Moreover, some fit parameters are governed by the applied magnetic field, thus confirming that changing the magnetic properties of the surroundings inevitably influences the mechanical properties of the samples.

The optimization of MSE properties can be achieved by applying hybrid filler systems. The association of different fillers provides a synergy effect between the action of single fillers and the MSE final properties. Indeed, a prompt use of MSE in technical applications only currently appears to be realistic on this basis.

Keywords: Smart materials, magneto-sensitive elastomers, orientation of magnetic filler particles, switching effect, magneto-mechanical behaviour, hybrid magnetic filler systems.

Table of content

Basic considerations

1 Introduction

Engineering constructions like buildings, bridges and offshore drilling rigs are exposed to dynamic loads. They arise naturally from strong earthquake excitations, extreme waves or strong winds and considerably affect the survivability of such structures [1, 2]. Undesirable vibrations occur also in a variety of technical and automotive systems as the consequence of a temporally periodic movement of a body about a rest position. These vibrations are disproportionately high in case of an unbalanced construction or special machines with high rotational speeds. If such systems are connected to the ground, the vibrations propagate further through mechanical waves affecting a reliable operation of machines placed nearby. Those generated technical disruptions are often accompanied by disturbing noise, showing that vibrations damping is not only survivability or reliable operation issue but also a comfort topic.

Mechanical vibrations are reduced by decoupling the main structure from the ground through elastic or viscoelastic elements. At each vibration, a part of the mechanical energy is transformed into heat due to friction. As a result, the oscillation amplitude decreases continuously until the vibrations are fully amortised. The attenuation of the structure movements by dissipating the energy generated is highly desired. The physical basics of mechanical vibrations were treated in-depth the last decades to become a better understanding of how unwanted resonances phenomena occur. The following small excursion into this field should give more insight in the subject by presenting the two major and easiest cases: the simple and damped harmonic oscillator in classical mechanics.

The simple harmonic oscillator in classical mechanics consists of a spherical body with a radius r and a mass m suspended on a spring with a spring constant D. For simplification purposes, the spherical body is assumed as a point mass. If the body is deflected from its rest position, a restoring force $\boldsymbol{F}$ occurs in the area of validity of Hooke's law where the total deformation $\boldsymbol{x}$ is sufficiently small and has the following form:

$$\boldsymbol{F} = -D\boldsymbol{x}\,. \tag{1}$$

The associated angular frequency is given by

$$\omega_0^2 = D/m. \tag{2}$$

If the body is immersed in liquid, the friction can no longer be neglected, and the Stokes friction force $\boldsymbol{F_d}$ shall be added:

$$\boldsymbol{F_d} = -6\pi\eta r\boldsymbol{v} \tag{3}$$

where η is the dynamic viscosity and $\boldsymbol{v}$ is the velocity of body. The damping constant γ of the damped harmonic oscillator depends on the ratio of resonance frequencies of the oscillating system to the damping element and it is given by

$$2\gamma := 6\pi\eta r/m. \tag{4}$$

The temporal behaviour of the body depends very decisively on the ratio of the average restoring force and the average friction force [3].

Nowadays, the modern damping systems are more complex than the individual elements discussed above but remain mostly a combination of both. For example, motor vehicles are equipped with suspension systems to attenuate vibrations. They consist mainly of a spring element and a shock absorber. The spring element catches the impacts and the shock absorber damps the vibrations by converting their energy into heat. Tuned mass dampers (TMD) are used in civil engineering structures following the same approach. They are composed of spring, damper and an additional payload or auxiliary mass. This damping system is installed in an upper floor of the building and starts to sway if unwanted oscillations take place. TMD applies inertial control forces to the structure and reduces the swinging in the desired manner. In some cases, combining several TMD is indispensable to reduce transverse and torsional motions [4, 5].

Those damping systems have the disadvantage of being able to fulfil their function in narrowly limited frequency bands. Therefore, significant concessions have to be made outside these frequency bands since, predominantly changing operating and oscillation conditions occur. For this reason, they are qualified as passive damping systems.

To overcome this limit, hybrid control systems were developed and have already been used successfully. The active horizontal displacement of whole structures is attenuated with a passive damping system combined with an active control actuator, mainly additional electrical or mechanical devices like servomotors or hydraulic pumps. The operating principle of hybrid control systems is to generate natural mechanical waves, which interfere destructively with incoming vibrations and cancel them out, thanks to targeted arrangements by means of active control actuator. To illustrate the functioning of such systems, hybrid mass damper (HMD) and hybrid base isolation (HBI) are discussed in the following. HMD consist of a passive TMD combined with an active control actuator. The TMD ensures with its natural motion a passive reduction of oscillations. The active control actuator improves the efficiency and reliability of HMD by a continuous determining of the TMD position. The control electronics compare the current position with the target position and regulate accordingly the desired damping value [5-11]. HBI combines a passive isolation system with an active control actuator. The passive isolation systems reduce the absolute acceleration of a building exposed to large displacements and inter-story drifts. The latter consist of the relative translational displacement between two consecutive floors [12, 13]. The active control actuator increases the efficiency of the displacement control process as described for HMD [14-21].

Nevertheless, serious challenges remain to be solved. Complex and well technically elaborated constructions lead to high capital costs and maintenance. No less important is the reliance on external power, which may fail during the vibrations. Based on these reflections, semi-active damping systems are developed. Compared with passive damping and hybrid

control systems, they offer a continuous control of the internal system features instead of introducing mechanical energy from a third source. They require less electrical power supply and earn more attention in the last years. Notable example is the variable orifice fluid damper. It consists of a passive fluid damper equipped with an electromechanically controlled variable orifice valve to regulate the fluid flow. The passive fluid damper, also referred to as hydraulic damper, consists of a piston attached to a piston rod and a cylinder filled with an incompressible fluid. The piston is permanently immersed in the cylinder. Together, they form a closed cavity, the workroom of the damper. If the piston moves due to occurring vibrations transmitted through the piston rod, the volume of the cavity varies forming a variable pressure level, which is known as hydraulic resistance. In order to better adjust the hydraulic resistance of the damping element, the fluid may be conducted in many balancing chambers and through different valve systems. The variable pressure level is based on a continuous transition between compression and decompression of the fluid. According to fluid dynamics, this state transition is accompanied by a temperature change. As discussed above, the operating principle of fluid damper remains also the same: the conversion of kinetic energy into thermal energy. In the case of variable orifice fluid damper, the hydraulic resistance is controlled solely by a valve having an orifice with variable opening degree [22-24].

Despite the efforts made to reduce the manufacturing costs and the complexity degree of the devices discussed above, the system reliability and especially the maintenance still remain a major problem. The reason lies in the need to be controlled by an external unity even if it is incorporated in the main structure.

It is highly recommended to consider systems, which can be controlled internally. They offer a large flexibility and high degree of freedom, while taking into account simple structures. Semi-active devices based on already developed controllable fluids represent a serious alternative.

Electrorheological fluid (ERF) was the first contender. It consists of an electrically insulating carrier liquid; such as water or mineral oil, in which electro-sensitive colloids; such as soft iron particles, are suspended. In the presence of an external electrical field, the viscosity of ERF changes significantly and hence the damping behaviour. These changes occur in the milliseconds range and are reversible. ERF was first used in clutch systems. A US-patent was registered in 1947 for ERF-based clutches by W. M. Winslow [25, 26]. The electrorheological clutches have the advantages over conventional clutches in the simple control of the transmitted torque, the fast response time and the low wear because the electromagnetic information is transmitted without any mechanical intermediate step. In 1948, J. Rabinow developed a clutch system based on magnetorheological fluid (MRF) [27]. MRF is the magnetic analogue of ERF. MRF have prevailed as controllable fluid than ERF because they are less sensitive to impurities and contaminants encountered during the production and the operating processes. Furthermore, the maximum yield stress of MRF compared with ERF is an order of magnitude larger, although their viscosities are similar [1].

The ability of ERF and MRF to vary in real time their dynamical and rheological properties in order to ensure adaptability to changing circumstances is considered as inbuilt intelligence of the system. This ability forms the basis for a new class in the area of material science, the so-called smart materials.

However, those controllable fluids are exposed to a sedimentation problem of the filler particles due to gravitation. A minor problem can occur, when the carrier liquid water comes in contact with the surroundings since it could be evaporated. These deficiencies can be reduced by adding antiwear and lubricity additives but are not completely eliminated. Those limitations opened the door to further developments of new types of smart materials.

In order to overcome the sedimentation deficiency of controllable fluids, rubber materials were considered. Compared to fluids, rubber materials have a higher molecular weight and exhibit therefore a considerably higher viscosity. Due to interaction with long strongly branched polymer chains, the mobility of filler particles is significantly restricted and the possibility to sediment is not given any more. Furthermore, rubber materials still remain the standard components of passive damping systems. Classical damping structures are made of laminated steel plates and elastomer layers [28].

An adaptive damping behaviour with a continuous control of the elasticity modulus and an ongoing adjustment of the resonance frequency is achieved by mixing magnetic fillers into the rubber matrix. This gives rise to magneto-sensitive elastomers (MSE), which are able to vary their mechanical properties and to adapt them to surroundings.

MSE are used in wide range of applications undergoing dynamic deformations as well as in the state of rest for actuator and sensor technologies.

In the area of disaster resistant constructions, adaptive vibration control systems have been successfully used in high-rise buildings [29-48]. Laminated MSE layers and steel plates are surrounded with electromagnetic coils generating a strong magnetic field. The latter regulates the vibration behaviour of the control systems, which react actively to strong vibrations by changing the lateral stiffness and damping force up to 45 % [33]. In the automotive industry, MSE are used in adaptive vehicle seat suspensions [49-51], in tuned engine mounts [52, 53], in active vehicle bumpers [54] and are introduced in new crash systems [55].

In the sensors segment, MSE are used in wireless and passive temperature indicators [56-58]. The temperature indicator is based on the Villari effect, i.e. the inverse magnetostrictive effect. This effect describes the change of magnetic susceptibility of a material when it is subjected to a mechanical stress. Its novelty is that it functions without electric current. A switch prepared from a magnetic shape memory alloy is placed between a permanent magnet and a resonator made of a soft magnetic ribbon. As soon as the temperature reaches a critical value, the switch undertakes a transition between the paramagnetic and ferromagnetic state. By exceeding a material-specifically temperature, the magnetic flux is changed and, therefore, the resonance frequency of the soft magnetic ribbon is shifted. This enables to determine temperature variations and to record them.

MSE are also used in strain sensors [59-63], in touch-screen panel [64] and in electromagnetic shielding systems [65, 66]. Electromagnetic radiations arise through different electromagnetic field sources in the environment. They are generated from diverse electrical devices on earth and they could come from the universe. The impact of some sunrays may even be perceptible on earth. Considering the ejected plasma (ionizing radiation) during sun eruptions, they may affect considerably the efficient work-flow of satellites and hence, our communication and navigation systems. On earth they can cause immense damage, like destroying current transformers. This was the case in North America in 1989. Millions of human being stayed for about ten hours without electric current and the economic repercussions were huge. In order to avoid such catastrophes, elastomer composites were used as an electromagnetic shielding system. They enable masking the devices and reflecting the electromagnetic radiations. MSE allow an effective absorbing of the electromagnetic radiations, due to the interaction with the magnetic particles, and converting them to harmless heat energy.

MSE are also used in actuators for valves [67] and in active noise barrier systems [68]. In microelectromechanical systems, MSE are used successfully in magnetometers [69], in microcantilevers [70], in tuned microvibration control systems [71] and in adaptive micropumps [72, 73]. There are aspirations in medical field to use MSE in adjustable prosthetic devices [74] and in artificial controllable lymphatic vessels [75].

Despite the successful use of the MSE in different technical structures, outstanding issues still remain and need to be studied. The deficiency of basic knowledge for conception, dimensioning and production impedes currently a global implementation of MSE in all industrial sectors. In particular, the relationship between structural parameters like rubber or filler type and technological properties is lacking in experience, guidelines and calculation tools.

In the framework of this thesis, these relevant issues are considered. At the beginning, a detailed overview on different aspects of the rubber technology and some relevant topics on magnetism are given. The experimental findings are then presented and discussed. The first part is devoted to characterisation and understanding of the key factors influencing mechanical and magnetic properties of the finished MSE. In a second part, a physical description of the coupling between magnetic and mechanical properties is discussed. This is based on the physical fundamentals of the rubber elasticity supplemented by the magnetism. In the last part, the optimization of dynamic-mechanical properties and magnetic sensitivity of the MSE are closely examined.

2   Elastomer composites

Elastomeric materials are widely used in nearly all industrial and technical applications. The carrier material is rubber. For application suitable products, supplementary components like fillers, plasticizers, vulcanisation systems and other necessary additives are added. Due to a large number of combinations of the different components, the properties of the finished elastomer composite can be adapted as needed for the individual application. In this chapter, the basics of rubber technology are highlighted. The different components used as well as the methods applied for the preparation of elastomer composites are described.

2.1   Rubbers

Rubbers are noncrosslinked polymers with a glass transition temperature T_g lower than the operating temperature. The term "polymer" goes back to the Greek words "poly" and "meros" which means many and parts respectively. Polymers are long molecular chains made from one or more types of repeating units known as monomers. Rubbers are macromolecular compounds usually composed of hydrocarbon polymer chains and can be natural or synthetic.

Natural rubber is obtained by conversion of natural products. Fully synthetic rubbers are crude oil-derived and are produced synthetically through condensation reactions, in which the atoms and molecules merge together to form the polymer chains. The polymerization processes of the different monomers occur under different and controlled conditions. They have been developed according to the diverse application fields and the expected properties of the finished product [76]. Monomers with the chemical structure $R - HC = CH_2$ form the so-called vinyl group and are the basic component of all conventional rubbers. The vinyl-group includes a carbon-carbon double bond and has a major role in the vulcanisation process of long polymer chains. This point is discussed in detail in a later section of this chapter.

The most outstanding feature of rubber compared to other materials is its high deformation rates when it is stretched. Rubber can show elongations up to 1000 % while solids cannot be strained more than 50 % even if both elastic and plastic deformations are considered [76]. This behaviour is based on the different mechanism of energy storage during the deformation. In the ideal solid state, the atoms occupy neighbouring lattice sites with predefined lattice spacing and atoms conformation. In the case of an external deformation, atomic distances as well as valence bond angles change, leading to a change in the internal energy of the ideal solid. The stress and strain of ideal elastic solid are linear interrelated according to the Hooke´s law. The wide-meshed polymer chains of rubber are organised in a rather flexible way and are randomly arranged. Above the glass transition area, the whole polymer chains or a part of it can undergo rotary and vibrational motions around chain segments. According to second law of thermodynamics, the most probable statistical state of the polymer chains corresponds to the state of maximum entropy The entropy is a quantity which measures the disorder in a closed system to calculate the internal energy degradation. The molecular statistical approach of the rubber elasticity is referred to the entropy elasticity. It is based on

the "random flight statistic" of the not deformed polymer chains, in which a Gaussian distribution function of the end-to-end distance of the individual chains can be derived. The deformation behaviour of rubber like materials is based on the change in entropy. If the polymer chains are stretched in one direction, the degree of disorder along the load direction decreases. Accordingly, the entropy decreases and the average end-to-end distance of the individual polymer chains is deviated from its most probable value. A restoring force of the deformed polymer network can then be determined. If the deformation is removed, the chain segments may take different random arrangements and the entropy increases consequently. When the polymer chains are completely unloaded, the system reaches the most statistically probable state; the state of biggest disorder. Rubber materials behave non-linearly. They are characterised by non-linear relationship between stress and deformation [76].

In the frame of this thesis, the following rubber types are considered.

2.1.1 Natural rubber

Natural rubber (NR) is a renewable raw material. It is produced by the coagulation of natural latex, the milky juice of Hevea brasiliensis - a variety of tropical plants, which is cultivated in large plantations in Africa, Asia and South America. The natural latex contains besides water and polymers, proteins, carbohydrates, sterols, fats and minerals. To increase its shelf life, ammonia NH_3 is usually added. In order to separate the polymer chains as a solid-like mass from the water, the coagulation is achieved with the acetic acid CH_3COOH or formic acid $HCOOH$. The coagulum is washed to remove undesired substances and dried in dry chambers for several days. NR has the chemical structure of polyisoprene und is available in the 1,4-cis or 1,4-trans-configuration as shown in Figure 1 [76].

Figure 1: Chemical structure of $\mathbf{1,4}$-cis (left) and $\mathbf{1,4}$-trans (right) NR monomer.

NR based materials are characterised by their outstanding elastic features under dynamic load. High tear strength, high elongation at break, low permanent deformation and low hysteresis make NR unique and irreplaceable for all dynamical applications. Besides, the self-reinforcing strain-induced crystallization sets NR apart and provides it high tear propagation resistance. It is a good electrical insulator, has a good cold behaviour but poor heat resistance. It has a bad weather, ultraviolet, ozone resistance and is not resistant against hydrocarbons, mineral oils and fats.

NR finds application mainly in the tire industry. It is also used to produce several technical goods like conveyor belts, toothed belts, rubber springs, rubber buffers, hoses as well as seals and surgical articles like medical gloves and medical tubes [76-78].

2.1.2 Acrylonitrile butadiene rubber

Acrylonitrile butadiene rubber (NBR) is a copolymer of butadiene with acrylonitrile. The chemical reaction is shown in Figure 2. The product entity on the right-hand side represents the NBR monomer. As the acrylonitrile content increases, the polarity of NBR increases as well. This affects the viscoelastic properties of final products and their chemicals resistance.
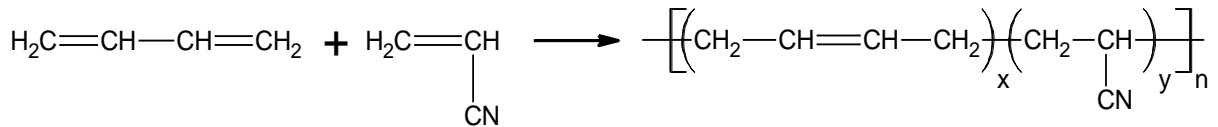
Figure 2: Chemical structure of NBR monomer.

NBR has a better ageing behaviour and lower abrasion than NR. NBR has an excellent resistance against fats, mineral oils, fuel, hydrocarbons, heat and abrasion. It is mainly used in manufacturing oil and fuel hoses. It is find application in other relevant areas like sealing gaskets, membranes, conveyor belts and roller covers due to its good mechanical properties [76-79].

2.1.1 Ethylene propylene diene terpolymer

Ethylene propylene diene terpolymer (EPDM) is prepared by coordinative anionic polymerization of ethylene $H_2C = CH_2$, propylene $H_2C = CH - CH_3$ and a diene component. EPDM belongs to M class rubbers having a fully saturated polymer backbone. Ethylidene norbornene (ENB) are by far the most commonly used tercomponent. ENB contains two double bonds and is compatible with sulphur crosslinking. The chemical structure of EPDM is illustrated in Figure 3.
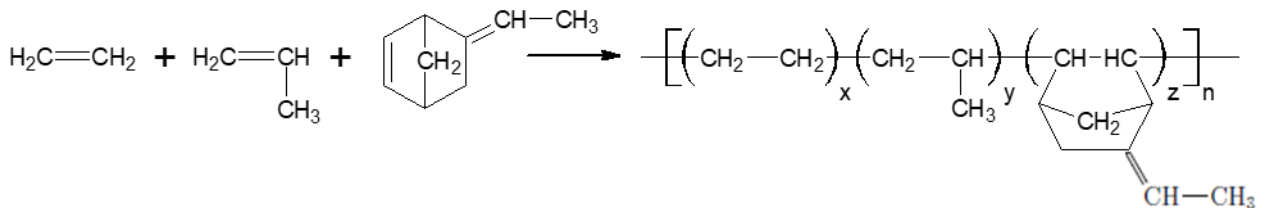
Figure 3: Chemical structure of EPDM monomer.

EPDM shows a very good resistance against weather, ultraviolet, ozone and heat. It has good electrical properties and is used in sealing purposes, cable sheathing and hoses production. Due to its soft rubber matrix, EPDM is not used for dynamical applications. By mixing EPDM with polyolefin such as polyethylene and polypropylene, thermoplastic elastomers can be produced combining various properties of rubber with those of thermoplastics [76-79].

2.1.2 Hydrogenated acrylonitrile butadiene rubber

Hydrogenated acrylonitrile butadiene Rubber (HNBR) is produced from the fully or partially hydrogenation of the double bonds in the NBR main chain. The production process is controlled in such a way that only the double bonds in the main chain are reduced. The triple bond of the acrylonitrile remains unchanged. The chemical structure of HNBR is shown in Figure 4.
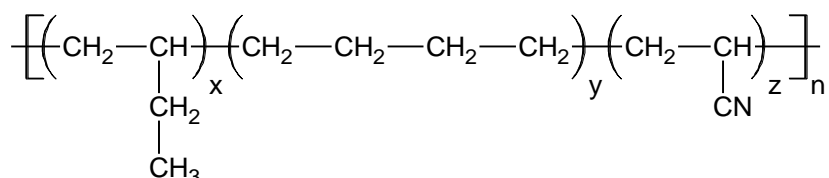
Figure 4: Chemical structure of a fully hydrogenated HNBR monomer.

HNBR is a high performance rubber, which has been developed for improving the mechanical properties and heat resistance of rubber materials. HNBR has besides the good mechanical properties a good oxidative, chemical resistance and ageing behaviour compared to NBR due to the saturated backbone of the main chains. HNBR based products are used mostly as seals and hoses in the crude oil production and as V-belts in the automotive industry when high oil, chemicals and heat resistance in addition to high level of mechanical strength and abrasion are required [76-79].

2.1.3 Carboxylated hydrogenated acrylonitrile butadiene rubber

Carboxylated hydrogenated acrylonitrile butadiene rubber (XHNBR) is prepared by terpolymerization of HNBR with acrylic acid ($H_2C = CH - COOH$). The chemical structure of XHNBR is shown in Figure 5.
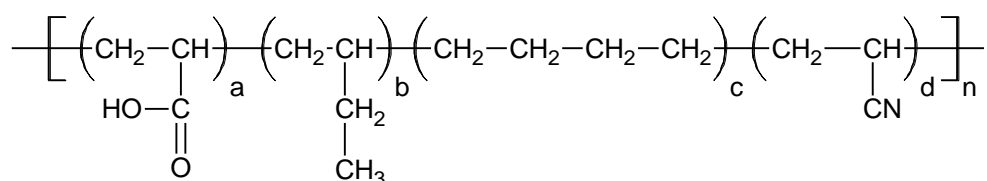
Figure 5: Chemical structure of XHNBR monomer

XHNBR stands out for its mechanical properties and ageing behaviour. It exhibits a high wear resistance at high temperatures compared to HNBR and has an excellent adhesion to metals. The application fields are restricted to special products which require extreme performance like oil well specialities, high performance belts, rubber rolls, seals and coatings [80, 81].

2.1.4 Styrene butadiene rubber

Styrene butadiene rubber (SBR) is a copolymer of butadiene with styrene at a weight ratio ranging between 0.765 to 0.235 and 0.60 to 0.40. SBR can be produced by free-radical

emulsion polymerization (E-SBR) or by ionic solution polymerization (S-SBR). The chemical structure of SBR is shown in Figure 6.
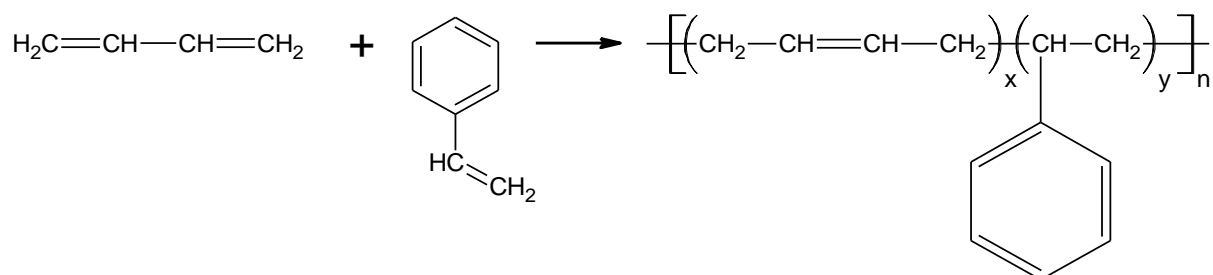
Figure 6: Chemical structure of SBR monomer

SBR represents the best synthetic rubber due to its performance-processing-cost profile. SBR is an excellent electrical insulating material. It has a lower elasticity but a better heat and ageing resistance than NR. SBR is used for producing technical rubber articles, sealing systems and conveyor belts [76-79]. Due to its high abrasion resistance, S-SBR enjoys a great interest in the tire industry, especially after the huge development made for the production of green tires [82, 83].

2.2   Vulcanisation

The vulcanisation refers to the production process of crosslinked high elastic elastomer composites through energy rich radiation or chemical crosslinking. The latter is currently the most used crosslinking method. The polymer chains are linked by covalent bonds, achieved mainly by use of sulphur, peroxide or metal oxides when supplied with heat [76].

Diene rubbers possess double bonds in the main or the side chain and are mostly crosslinked with sulphur. Sulphur is available as S_8-rings. It has a dissociation energy of 226 kJ/mol and it first has to be split off in order to contribute to vulcanisation process [84]. In addition, the crosslinking system can also involve different vulcanisation accelerators, activators and sulphur donors. Vulcanisation accelerators are organosulphur compounds or amine. Amines are organic compounds containing one nitrogen atom with a lone pair. Zinc oxide (ZnO) and stearic acid are used as activators. Together with the vulcanisation accelerators, the activators generate an active activator complex. The latter forms with sulphur a sulphur transfer complex. This reacts with the polymer chains and constitutes network sites in the form of monosulphide, disulphide or polysulphide bridges (see Figure 7) [76].

11
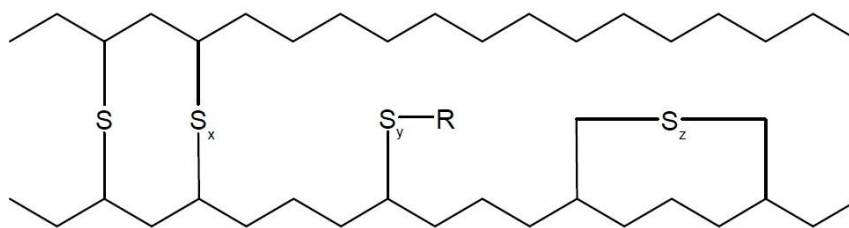
Figure 7: Sulphur bridges between polymer chains.

The chemical structure of sulphur bridges between two interconnected chains can be controlled by the ratio sulphur to vulcanisation accelerator and the temperature. The number of sulphur bridges, expressed by the crosslinking density, has an immense influence on the processing facilities, crosslinking time and properties of the final elastomer composites. Conventional sulphur-accelerator systems have a sulphur content of 2 to 3.5 parts per hundred rubber (phr), and a vulcanisation accelerator proportion of 0.5 to 1 phr. They are cost-effective, mainly form di- and polysulphide bridges and allow a wide variation in the vulcanisation kinetics. For semi-efficient systems, the vulcanisation accelerator content becomes 1 to 2.5 phr. This increase is associated with reducing the sulphur content in order to get a comparable crosslinking density with conventional systems. The exact quantity of sulphur is thus between 1 and 1.8 phr. Such systems lead to a good compromise between costs and final properties and generally form mono- and disulphide bridges. For efficient systems, a high vulcanisation accelerator content of 2 to 6 phr, and low sulphur amounts of 0.3 to 1 phr are used. These mainly form monosulphide bridges, which lead to a higher thermal resistance and lower elastic behaviour. In addition, these efficient systems are also the most expensive [76].

Within the scope of this thesis, only semi-efficient systems are used. Apart from sulphur, the accelerator N-cyclohexylbenzthiazol-2-sulfenamide (CBS) and 1,3-diphenylguanidine (DPG) are used. CBS is commonly used for diene rubber and is particularly suitable for the production of dynamically loaded composites due to its good resistance to fatigue cracking. DPG is a secondary accelerator and ensures the reduction of incubation time, which represents the time span before the beginning of crosslinking reactions.

The vulcanisation temperature range is limited at high temperature by the thermal decomposition of the polymer chains or crosslinking points and at low temperature by the glass transition temperature. Below the glass temperature, the polymer chains are frozen; the elastomer composite is in glassy state und behaves similarly to brittle materials. Both limits depend on the rubber used and the crosslinking system [76].

2.3 Functional fillers

At the beginning of industrial processing of rubber, fillers were used to reduce the price and tackiness of the natural rubber. This was achieved by addition of minerals like talcum or

kaolin. Later, mineral fillers were used as extenders with the aim of improving the processing and properties of final elastomer composites. Several investigations revealed that zinc oxide (ZnO) assign the crosslinked samples a mechanical reinforcement and improves their heat resistance. ZnO remained the most important reinforcing filler until the large-scale development of carbon black (CB). From the late 1920s with the rapid development of the automobile industry, CB became the main reinforcing filler in the rubber technology due to realised improvements of the wear resistance of the tyre tread compounds. Particularly important is the reinforcement potential of CB for amorphous synthetic rubbers like SBR [76].

CB is an organic filler which is principally made of carbon. The CB particles are spherical and may form chain-like aggregates. Regarding the morphology, it can be differentiated between primary particles (particle microstructure), aggregates (primary structure) and agglomerates (secondary structure). The primary particles used in the production of elastomers have medium particle diameter between $10\ nm$ and $300\ nm$ and a N_2-BET specific surface area between $9\ m^2/g$ and $138\ m^2/g$. The aggregates have an anisotropic structure and consist of several firmly connected primary particles. They represent the smallest stable unit and have a size between $100\ nm$ and $800\ nm$. CB aggregates can be bonded together via Van-der-Waals forces to form large agglomerates. The agglomerates can only be broken apart under the influence of mechanical forces.

Considering the interaction with the rubber matrix, CB is divided into reinforcing and not reinforcing fillers. The term reinforcement is understood as the sum of all rubber-filler interactions, which are expressed in physical properties for both non-crosslinked and crosslinked samples. Reinforcing, also called active, fillers are nanoparticles and have particle diameters between $10\ nm$ and $100\ nm$. They change by interaction with the polymer chains the viscoelastic properties of the rubber samples. They increase the viscosity of the rubbers and improve the fracture behaviour of the vulcanisates, such as tear strength, tear propagation resistance and abrasion. Not reinforcing or inactive fillers have particle diameters between $500\ nm$ and $1000\ nm$ and simply ensure that the rubber matrix become diluted. This causes a decrease of tearing energy, although the process ability or gas tightness can be positively influenced.

Due to its graphite-type crystalline structure, CB has an excellent electrical conductivity, which ranges between $10^{-1}\ S/cm$ and $10^2\ S/cm$. The electrical conductivity of CB depends on the degree of graphitization, the impurities and the chemical groups on the surface. By mixing CB in the rubber matrix, the dielectric conductivity of the prepared elastomer composites can be changed by 15 powers of ten. The increase of the dielectric conductivity mainly depends on the CB volume fraction when the percolation threshold is exceeded. The percolation process describes the formation of connected filler clusters to establish a filler network. It is the transition from isolated filler particles to linked filler clusters through chemical reactions, so that continuous paths along the filler network arise for charge carriers. The percolation threshold mainly depends on the properties of CB and their distribution in the

rubber matrix. The latter is strongly influenced by both the mixing and the curing process. The polymer chains have with $10^{-13}\,S$ a tiny contribution to the dielectric properties of elastomer composites. This is caused by molecular interactions.

Depending on the application field, the dielectric conductivity of elastomer composites is highly relevant when it comes to electrostatic charging by friction. For rotating car tyres, an electron transfer occurs between the tyre tread and the road because they have a different dielectric constant. The car becomes electrically charged. To prevent the passengers an electric shock, the electrostatic charge should continuously be discharged during the drive. This is only achieved by using conductive CB to fill the elastomer composites.

In order to increase the performance, safety and lifetime of modern tyres, bio-based alternatives to petrochemical materials and recycled raw materials are developed. No less interesting is the environmental impact of mobility nowadays. Different studies show that the mobility contributes to around 18 % of global CO_2-emissions, whereby 75 % of them is attributed to road transport. 24% of CO_2-emissions from passenger cars and 40% of CO_2-emissions from trucks are directly attributed to the tyres [82, 83]. More precisely, these CO_2-emissions results from the rolling behaviour of tyre and the corresponding fuel consumption. For sustainable mobility, new products are developed and intensively studied. Tyre labels were also introduced in order to increase not only the safety and the profitability, but also the ecological efficiency in the road traffic. This was successfully achieved by manufacturing the so-called "Green tyres". Green tyres are characterised by a low rolling resistance, outstanding brake properties and a long lifetime. This success is mainly attributed to the new filler Silica.

Silica is an inorganic filler and consists of amorphous silicon dioxide. It is finely dispersed colloids with N_2-BET specific surface areas ranging between $25\,m^2/g$ and $700\,m^2/g$. There are pyrogenic silica and precipitated silica. They differ by the structure of the aggregates and the chemical composition of the surface. Pyrogenic silica has a chain-like aggregate structure. The aggregates of the precipitated silica are substantially larger and consist of clusters with a porous structure which also leads to an inner surface. On the silica surface there are silanol groups ($R_3Si - O - H$) as well as siloxane groups ($R_2Si - [-O - SiR_2]_n - O - SiR_3$) [85]. Precipitated silica has 5 to 6 silanol groups per nm^2 on the surface. Pyrogenic silica has 2.5 to 3.5, mostly isolated silanol groups per nm^2 on the surface. The silanol groups are responsible for the acid and the strongly polar behaviour of silica. They are accessible for various chemical reactions. Of great practical importance is the reaction of the silanol groups with organic silanes. Reactive groups can be formed to initiate a covalent bonding between the polymer chains and the silica surface area. Silanisation reactions can only take place if silanol groups are present. Due to their polarity, the silica clusters tend to agglomerate via hydrogen bond than to be bonded with the polymer chains. This effect is more pronounced for silica than for CB filled elastomer composites.

Silica is used in the rubber industry as substitute or compliment to CB palette. A necessary prerequisite is the use of a bifunctional organosilane. In contrast to CB, silica is not

electrically conductive. For tyre application, a CB amount above the dielectric percolation threshold is always added [76]. Figure 8 depicts the two rubber fillers CB and silica.

Figure 8: Reinforcing rubber fillers: carbon black on the left and silica on the right.

In the scope of this thesis, two kinds of CB supplied by ORION Engineered Carbons GmbH and one silica type supplied by Evonik Industries are used. N 550 is a semi-active CB [86]. Printex XE2-B is a high reinforcing and a super conductive CB [87]. Ultrasil 7000 GR (U 7000) is a precipitated amorphous silicon dioxide [88]. U 7000 is one of the most used silica in the rubber industry. Some of the physical properties of the two CB and silica are summarized in Table 1.

Table 1: Physical properties of fillers

		N 550	Printex XE2-B	U 7000
Average particle size	**[nm]**	56	30	14
N_2-BET specific surface area	**[m²/g]**	40	1000	175
Density (20 °C)	**[g/cm³]**	1.8	1.7– 1.9	2

Besides the mechanical reinforcement potential, rubber fillers can also be classified according to their behaviour in an applied magnetic field. The conventional rubber fillers discussed above, CB and silica, are non-magnetic materials and do not interact with an external magnetic field. The magnetic field can flow such as in a vacuum or air. Regarding magnetism, they can be considered as irrelevant. Other filler materials may be affected in various degrees by magnetic fields. They can cause a considerable strengthening and bundling of magnetic field lines. They may even magnetise themselves. It can be distinguished between magnetically soft and magnetically hard materials. This distinction is particularly important in terms of applications. Soft magnetic materials are mainly iron, nickel, cobalt and low alloy steels. The magnetic field flows more easily through them und the magnetic flux density becomes higher. By removing the magnetic field, a large part of the magnetisation gets lost. A small material-dependent residual magnetism may remain. Hard magnetic materials possess a permanent magnetic behaviour. After being magnetised, they retain their magnetic properties and are marked by a high energy density. Such materials are characterised by a high

remanence and high coercivity. A general overview of different magnetic fillers is depicted in Figure 9, adapted from [89].
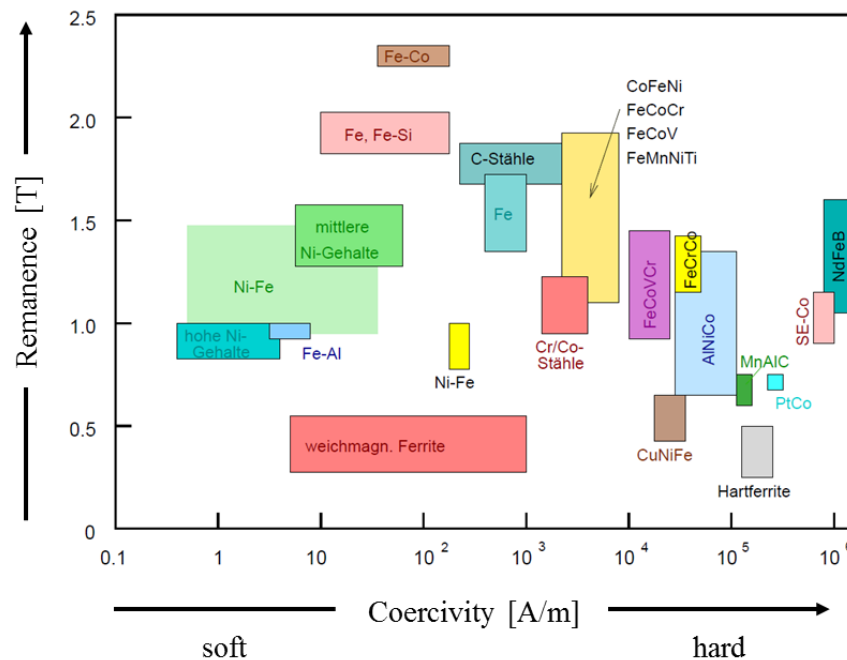
Figure 9: Magnetic materials.

The origin of the different magnetisation behaviours is discussed in detail in the next chapter.

2.4 Rubber additives

Rubber additives are auxiliary materials that are added to rubber compounds in order to facilitate the processing and to set better features of fully operational elastomer composites. They are used for the designing of end products from mixing steps through control of chemical reactions like curing process or salinization to achieving desired properties during the service life, even if these properties are mainly supported by rubber type, fillers and crosslinking systems.

In the processing of rubber compounds, plasticizers play an important role and have a large influence on the properties of the finished products. Plasticizers are low viscous fluids and should comply with different requirements. Basically, they should be readily soluble in the rubber, oxidation resistant, have good ageing behaviour and do not disturb the crosslinking systems. They increase the chain mobility and lower the viscosity as well as the glass transition temperature. They are classified in two groups: mineral oil and synthetic plasticizers. The ester plasticizers build the largest synthetic plasticizer group. The mineral oil plasticizers comprise three categories: paraffinic, naphthenic and aromatic plasticizers. Paraffinic plasticizers are more compatible with nonpolar rubber like EPDM. Weakly polar rubber like NR and SBR interact well with naphthenic plasticizers. Aromatic and synthetic plasticizers are suited for polar rubber. In the framework of this thesis, dioctyl phthalate

(DOP), a phthalic acid ester is used for polar rubbers. Treated distillate aromatic extract (TDAE) is used for nonpolar rubber. The addition of plasticizers leads to a dilution of the rubber matrix. The mixing ratios affect the viscoelastic plateau of finished elastomer composites by shifting the range of glass transition towards higher or lower temperatures. The desired thermal properties can then be set very precisely. Mechanical characteristics like modulus of elasticity, stress value or hardness also change accordingly. They decrease with increasing the plasticizer content.

Processing aids are used to promote principally the mixing process of components. However, they influence in a similar manner the properties of the finished products as the plasticizers.

In order to attain application relevant properties, rubber compounds should be first vulcanised. In the framework of this thesis, this is achieved by sulphur crosslinking during the curing process. In addition to elementary sulphur, vulcanisation accelerators and activators are added. Almost all vulcanisation accelerators are highly reactive only in the presence of metal oxides. As seen in section 2.3, zinc oxide (ZnO) is used. Furthermore, the stearic acid is used as activator. It forms with ZnO zinc stearates, a necessary preliminary stage for sulphur crosslinking. Zinc stearates increase the solubility of the crosslinking system in the rubber by forming soluble complexes. ZnO and stearic acid are present in the finished compounds at very low levels.

Furthermore, antioxidants are used to inhibit the oxidation of the polymer chains by ozone or oxygen. The oxidation reactions may have adverse changes of the properties and the life time of the elastomer composites. Diene rubbers are particularly vulnerable to ageing processes due to their double bonds. N-(1,3-dimethylbutyl)-N'-phenyl-p-phenylenediamine (6PPD) and N-isopropyl-N'-phenyl-p-phenylenediamine (IPPD), supplied by Lanxess, are used.

Besides, coupling agents can be useful to enhance the adhesion of polymer chains to surface area of filler particles. These are strictly necessary if the surface areas of both polymer chains and filler particles have different polarities. In this case, the coupling agent silane bis-(triethoxysilylpropyl)-tetrasulfide (TESPT), also known under the trade name Si69, is added. It is used to functionalize the surface area of magnetic filler particles making them more compatible with the polymer chains [76].

3 Magnetism and magnetic filler particles

This chapter is devoted to the theory of magnetism and magnetic fillers used in the rubber technologies. The most important concepts of magnetism are presented. The different types of magnetism are introduced and the reasons of their occurrence are discussed. The magnetic dipole-dipole interaction is explained in more detail. Afterwards, different magnetic materials are presented. This is followed by the magnetic fillers for rubber compounds.

3.1 Magnetism

Magnetism is one of the fundamental phenomena of solid-state physics. The Greeks discovered that certain iron ores found in a city called Magnesia, now in Turkey, could attract other pieces of iron. The ancient Chinese discovered that certain types of natural iron ore, when suspended freely always points in a north-south direction. The Chinese use this property to make a simple form of compass for navigational purposes. During a lecture demonstration in 1819, the Danish scientist Hans Oersted found that compass needle has been deflected via an electric current in a wire. This discovery brought for the first time the magnetic field and the electrical current together. This milestone was the beginning of our understanding of the origin of magnetism. James Clerk Maxwell was the first who describes that magnetism is a property of a charged particle in motion. Otto Stern and Walther Gerlach succeeded in explaining this phenomenon, which was not comprehensible within the framework of classical physics. In the Stern-Gerlach experiment, named after the two researchers as recognition of their findings, an electron gun shoots out a beam of electrically neutral silver atoms across an evacuated tube. If a bar magnet is held at the side of the tube, the beam is deflected up or down [90-92]. The experimental setup is shown in Figure 10.
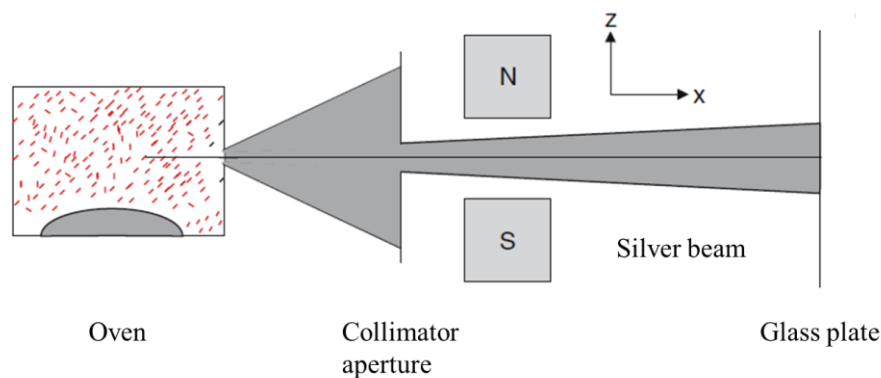

Figure 10: Stern-Gerlach experiment [**90**].

From the intensity distribution of the silver beam with and without magnetic field, depicted in Figure 11, Stern and Gerlach concluded that the silver atoms must possess an additional intrinsic feature which was unknown until then and is able to explain this deflexion behaviour. This was the spin of electrons.
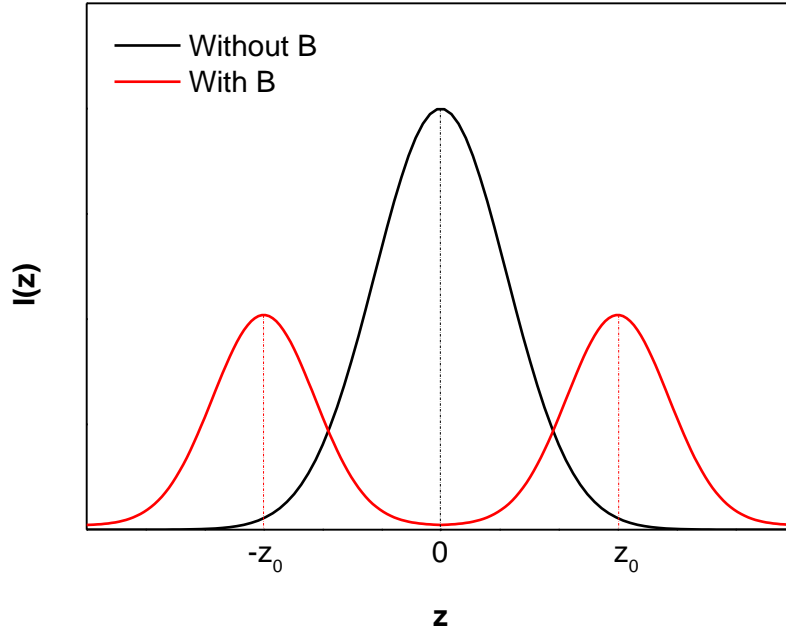
Figure 11: Intensity distribution of silver beam with and without magnetic field.

This concept implies that all magnetic phenomena are attributed to the spin state within the atoms. The silver atoms occupied only two states when the magnetic field was switched on. This means that the magnetic moments in atoms just occur in two spatial quantized states. According to quantum theory, the spin of electron is $\frac{1}{2}$. The corresponding magnetic moment μ is defined as

$$\mu = g_s \frac{q}{2m} \, \boldsymbol{S} \tag{5}$$

where g_s is the g-factor, q is the charge of the particle, m is its mass and $\boldsymbol{S}$ is its spin angular momentum.

When the electrons take different spin states, different form of magnetism can be observed. Inside materials, the atoms are considered as tiny magnets and are arranged in groups called domains. The size of these domains and their orientation affect strongly the magnetic properties of magnetic materials. The magnetic materials can be classified in diamagnetic, paramagnetic, ferromagnetic, antiferromagnetic and ferrimagnetic materials.

For diamagnetic materials like hydrogen (H), copper (Cu) and silver (Ag), the individual atoms do not possess any net magnetic moment. In the absence of external magnetic field, the net magnetic dipole moment over each atom or molecule is zero due to the pairing of electrons. When diamagnetic materials are brought in an external magnetic field, they get feebly magnetised in the opposite direction of the magnetic field and experience a repelling force.

For paramagnetic materials like aluminium (Al), calcium (Ca), platinum (Pt) and dioxygen (O_2), each individual atom has a net non-zero magnetic moment. They possess a permanent dipole moment due to some unpaired electrons. When they are placed in an external magnetic field, they get weakly magnetised in the same direction as the magnetic field and experience a feeble attractive force.

Ferromagnetism, antiferromagnetism and ferrimagnetism are macroscopic phenomena associated with the so-called collective magnetism. Collective magnetism is a phenomenon in which the magnetic moments mutually align themselves due to interaction of the electron spins. This behaviour is based on the coupling of the magnetic moments. Depending on the strength of the coupling and the ordering temperature (Curie or Néel temperature); below which the interaction energy of the magnetic moments is greater than the thermal energy, a spontaneous magnetic order occurs without the action of external magnetic fields.

For ferromagnetic materials like manganese (Mn), iron (Fe), cobalt (Co) and nickel (Ni), spontaneous magnetisation occurs below the Curie temperature T_C. At the temperature absolute zero, all atomic magnetic moments are aligned in the same direction so that the spontaneous magnetisation takes its maximum value. When the temperature increases, the ferromagnetic ordering is gradually disturbed and disappears at the Curie point T_C. The ferromagnetic materials experience a very strong attractive force when they get magnetised in the presence of an external field. The magnetic domains, randomly oriented in the unmagnetised material, become aligned in the same direction as the external field.

In the case of antiferromagnetism, there is no spontaneous magnetisation. The magnetic moments are arranged in sublattices, which have opposite magnetisation. The negative exchange energy between adjacent magnetic moments additionally leads to a vanishing of the total magnetisation. At the temperature absolute zero, the spin chain within the material consists of an alternating antiparallel position of the spins. If the temperature increases, the thermal excitation turns over the individual spins, so that the spatial arrangement of magnetic moments is disturbed. The antiferromagnetic ordering disappears above the antiferromagnetic Néel temperature T_N and becomes a paramagnetic ordering.

Ferrimagnetic materials have a spontaneous magnetisation below the Curie temperature T_C similar to the ferromagnetism. For ferrimagnetic materials like nickel (Ni) and ferrite, any two magnetic dipoles are aligned anti-parallel. Since the magnitudes of magnetic dipoles are not equal, a net magnetisation remains. In some ferrimagnetics, the total magnetisation can be reversed at a compensation temperature T_k. If the magnetisations of the sublattices are equal, antiferromagnetism is observed [90-95].

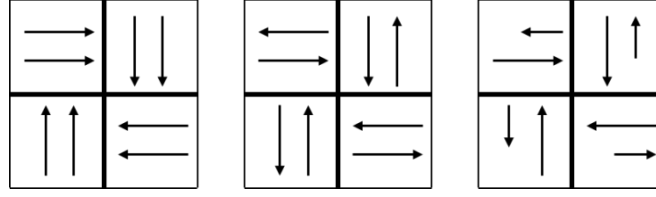The different forms of collective magnetism are displayed in Figure 12.

Figure 12: Form of magnetism in solids: ferromagnetic, antiferromagnetic and ferrimagnetic domains. The thick lines represent the Bloch walls between the single domains.

In the case of ferrimagnetic particles, if the particle size falls below a critical value, no magnetic domain can be built. The thermal energy is greater than the magnetocrystalline anisotropy energy and the magnetisation direction follows the thermal fluctuation. Such particles are one-domain particles and have no remanence. This phenomenon is called superparamagnetism [93,95].

The magnetic field is a zero divergence field as already stated by James Clerk Maxwell. The Gauss´s law for magnetism has the following form:

$$\mathrm{div}\, \boldsymbol{B} = 0 \tag{6}$$

This means that the source of magnetism is not the magnetic load carriers. In contrast to electron in electricity, the source of magnetism is the moving electric charges or time varying electric fields. The magnetic field is described by two different physical quantities: the magnetic flux density or magnetic induction $\boldsymbol{B}$ and the magnetic field strength $\boldsymbol{H}$. $\boldsymbol{B}$ describes the spatial density of the magnetic flux Φ and has the unit Tesla (T). $\boldsymbol{H}$ describes the strength of the magnetic field generated by free currents and has the unit Ampere per meter (A/m). $\boldsymbol{B}$ and $\boldsymbol{H}$ are related in vacuum as follows:

$$\boldsymbol{B} = \mu_0 \boldsymbol{H} \tag{7}$$

where $\mu_0 = 4\pi.10^{-7}\,\frac{\mathrm{V\,s}}{\mathrm{A\,m}}$ is the vacuum permeability.

If a material is placed in a magnetic field, the existing magnetic dipoles interact with it. The material becomes magnetised and the magnetic flux density **B** changes to

$$\boldsymbol{B} = \mu_0 m_r \boldsymbol{H} \tag{8}$$

where m_r is the relative permeability of the material. The magnetic flux density can be also expressed by

$$\boldsymbol{B} = \mu_0 (\boldsymbol{H} + \boldsymbol{M}) \tag{9}$$

where **M** is the magnetisation. The magnetisation **M** indicates the magnetic field caused by bound surface currents. Those microscopic ring currents are present in each molecule and are the origin of the magnetism [94-97]. In general, the magnetisation **M** is location-dependent. For homogeneous external magnetic field and isotropic samples, **M** is given by the spatial means over all magnetic dipoles and takes the following form:

$$\boldsymbol{M} = \frac{\sum_i m_i}{V} := \frac{m_r}{V} \tag{10}$$

22

The magnetisation **M** is defined as the density of the existing magnetic dipoles within the material. For infinitesimal small volume, the sum operator can be changed to an integral and the relative permeability of the sample becomes as follows:

$$\boldsymbol{m}_r = \int_V \boldsymbol{M} dV \tag{11}$$

From equation (8) and equation (9), a relation between **H** and **M** can be derived.

$$\boldsymbol{M} = (\mu_r - 1)\boldsymbol{H} \tag{12}$$

$$\boldsymbol{M} := \chi \boldsymbol{H} \tag{13}$$

where the proportionality factor χ is the magnetic susceptibility [90-95]. It is a material specific property and it is considered as the material response function to external magnetic field. It represents with the relative permeability μ_r the key features of magnetic materials. Indeed χ and μ_r take different values for different materials. The value ranges for diamagnetic, paramagnetic and ferromagnetic materials are listed below

- diamagnetic materials $\qquad \chi < 0 \qquad m_r < 1$
- paramagnetic materials $\qquad \chi > 0 \qquad m_r > 1$
- ferromagnetic materials $\qquad \chi \gg 0 \qquad m_r > 1$

3.2 Magnetic dipole interaction

In this section the stationary phenomena of the magnetic field are more closely treated. According to quantum theory, every atom can have a non-zero magnetic moment and the existing magnetic dipoles can occupy different quantum states. In the presence of an external magnetic field, the coupling between individual magnetic moments induces a magnetically ordered state, as described in the last section [90-95].

The magnetic energy of a magnetic dipole **m** in an external magnetic field **B** looks as follows:

$$E = -\boldsymbol{m} \cdot \boldsymbol{B} = -m B \cos\theta \tag{14}$$

where θ represents the angle between magnetic dipole and magnetic field direction as pictured on Figure 13.
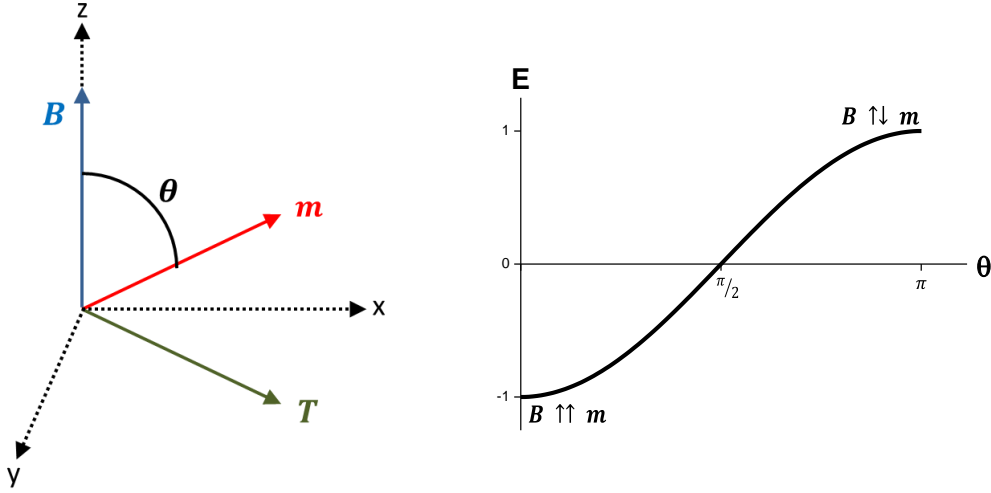
Figure 13: Orientation of the magnetic dipole in magnetic field displayed on the left. Torque $\boldsymbol{T}$ acts on the magnetic dipole to bring it in the energetically most favorable position. The curve on the right side illustrates the angle dependence of the energy E of magnetic dipole in magnetic field.

If the magnetic dipole $\boldsymbol{m}$ is parallel to the magnetic field $\boldsymbol{B}$, the magnetic energy E is minimal. It becomes maximal if $\boldsymbol{m}$ and $\boldsymbol{B}$ are arranged antiparallel. Between the two extreme values, the magnetic energy E varies with the cosine of the angle between the two vectorial quantities. A torque $\boldsymbol{T}$ is applied und is attempting to turn the magnetic dipole to the energetically most favourable position, parallel to $\boldsymbol{B}$. The torque $\boldsymbol{T}$ has the following form:

$$\boldsymbol{T} = \boldsymbol{m} \times \boldsymbol{B} = m\,B\,sin\theta \tag{15}$$

A magnetic dipole $\boldsymbol{m}_1$ creates at the origin of the coordinate system a magnetic field $\boldsymbol{B}(\boldsymbol{r})$ of the form:

$$\boldsymbol{B}(\boldsymbol{r}) = \frac{\mu_0}{4\pi}\frac{3(\boldsymbol{m}_1\cdot\boldsymbol{r})\boldsymbol{r}-(\boldsymbol{r}.\boldsymbol{r})\boldsymbol{m}_1}{r^5} \tag{16}$$

A second magnetic dipole $\boldsymbol{m}_2$ located at the position $\boldsymbol{r}_{12}$ couples to this magnetic field and interacts with $\boldsymbol{m}_1$ as shown in Figure 14. The magnetic dipoles $\boldsymbol{m}_1$ and $\boldsymbol{m}_2$ can then be described by the interaction energy E_{12}

$$E_{12} = -\,\boldsymbol{m}_2 \cdot \boldsymbol{B}(\boldsymbol{r}_{12}) \tag{17}$$

$$= -\frac{\mu_0}{4\pi}\frac{3(\boldsymbol{m}_1\cdot\boldsymbol{r}_{12})(\boldsymbol{m}_2\cdot\boldsymbol{r}_{12})-(\boldsymbol{r}_{12}.\boldsymbol{r}_{12})\boldsymbol{m}_1\boldsymbol{m}_2}{{r_{12}}^5} \tag{18}$$

If the two magnetic dipoles are aligned along the magnetic field lines, the interaction energy can be simplified to

$$E_{12} = -\frac{\mu_0}{4\pi}\frac{m_1 m_2(1-3\cos^2\theta)}{{r_{12}}^3} \tag{19}$$

The inner product $\boldsymbol{m}_i \cdot \boldsymbol{r}_{12}$ with $i = \{1,2\}$ is equal to $m_i r_{12}\cos\theta$. The angle θ denotes the deviation of the connection vector $\boldsymbol{r}_{12}$ from the direction of the magnetic field. The interaction energy E_{12} depends on the relative orientation of the two magnetic dipoles. It is

proportional to the product of the two magnetic moments and is inversely proportional to the cube of their distance.
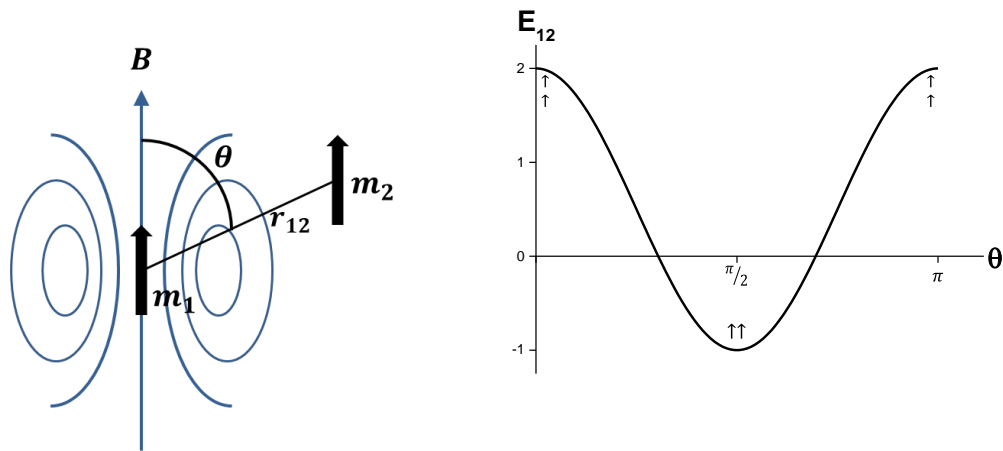

Figure 14: Dipole-dipole coupling in magnetic field is illustrated on the left. The angle dependence of the dipole-dipole interaction energy E_{12} in magnetic field is displayed on the right.

The interaction energy E_{12} is at its largest when r_{12} is parallel to the direction of the magnetic field [90-95].

3.3   Magnetic materials

The magnetic permeability μ_r reveals the magnetic sensitivity of the examined material. Different materials affect in various ways the pattern of the magnetic field lines. As long as no external magnetic field is applied, even ferromagnetic materials seem to be not magnetic from a certain temperature because the magnetic domains are spontaneously arranged. Due to the disorder of elementary magnets, the material does not show outwards any magnetic phenomena.

Applying an external magnetic field moves first the Bloch walls separating the single magnetic domains (see Figure 12). Increasing the magnetic field change the size of the magnetic domains and their orientation. If all magnetic domains are aligned, the magnetisation attains its maximum and has the same direction as the magnetic field. Once this state is reached, a further increase of the magnetisation is no longer possible even if the magnitude of the external magnetic field increases. In other words, if all dipole moments are parallel to the external magnetic field, the material is magnetically saturated. These processes are reversible. When the external magnetic field is switched off, the magnetisation does not disappear completely. It remains a residual magnetisation B_r, which disappears with an opposite field at the level of the coercivity H_C. The magnetic flux density B becomes zero.

The entire process of magnetisation can be determined by considering the evolution of the magnetic flux density B and the magnetic field strength H. The obtained relationship between B and H represents a characteristic curve for each material and is called the hysteresis loop. Figure 15 displays the hysteresis loop of a ferromagnetic material [90].

If a ferromagnetic material is exposed to a magnetic field for the first time, both B and H are equal zero because the material is completely unmagnetised. With increasing the magnetic field strength H, the magnetic flux density B increases also. From a certain magnetic field strength H, B increases slightly to reach a saturation state. This phenomenon corresponds to the sub curve (a) in Figure 15 and is called initial magnetisation curve. By reducing the magnetic field, the magnetic field strength H decreases. The magnetic flux density B decreases also, however, not according to the initial magnetisation curve but rather an upper sub curve (b). Even at a zero magnetic field strength H, a non-zero magnetic flux density B remains. This material dependent value is referred to as magnetic remanence or residual magnetisation B_r. If the direction of the magnetic field is reversed, the magnetic flux density B returns zero at a non-zero magnetic field strength H. This particular value corresponds to the coercivity H_C. A further increasing of the magnetic field strength towards negative values leads the material to reach again the saturation state. When this process is turned over, same steps in reverse order are obtained according to sub curve (c).
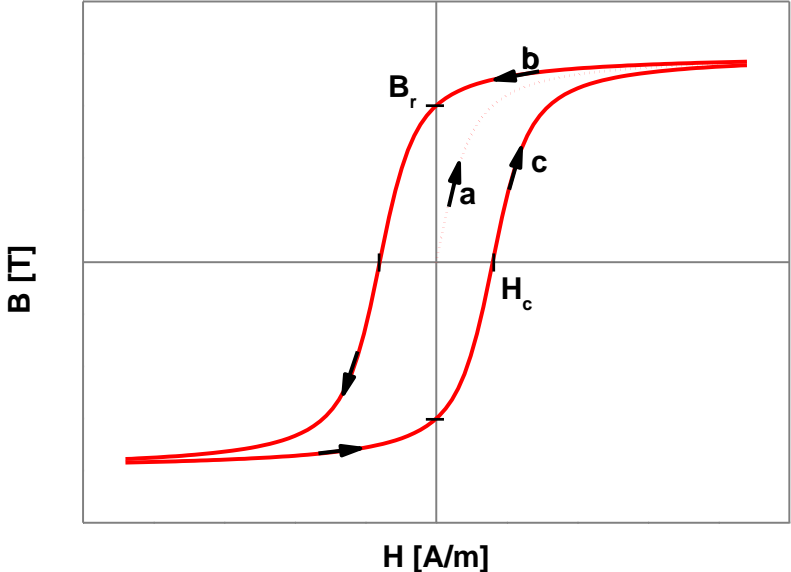

Figure 15: Hysteresis loop of a ferromagnetic material.

Ferromagnetic materials are divided into two groups, differing in the shape of the hysteresis loop and the magnetisation energy. Hard magnetic materials need a strong external magnetic field to become magnetised. But once magnetised, they do not readily lose their magnetisation. They are characterised by a strong reluctance, which means that a high magnetic energy is stored. The hysteresis loop has a rectangular shape with high coercivity and remanence values. Hard magnetic materials are mainly used as a magnetic field source, generating a continuous magnetic flux. Soft magnetic materials have a hysteresis loop with small area and very small magnetic energies can be stored. The low coercivity and remanence

values are a hint for a low energy requirement for the magnetisation process. Their magnetism is temporary and get lost as soon as the exciter field current stops. Soft magnetic materials are characterised by a high permeability and are used in general for guiding the magnetic flux [90-92].

In the following subsections, different magnetic materials will be examined more closely. On this basis, the magnetic fillers used in this thesis are presented.

3.3.1   Iron

In the periodic table of elements, iron is the chemical element with the atomic number 26. It is a part of transition metals and has the symbol Fe, coming from Latin for ferrum. It is the fourth most common element in the earth's crust with a total amount of 6.2 %. Iron represents the final stage of nuclear fusion in the stars, which is hurled into the environment by supernova explosions. Already in antiquity, iron objects from meteorites were known. Due to its origin, this type of iron is called meteoric iron and consists of an iron nickel alloy. Historically, iron production was first carried out by the Hittites. Nowadays, the iron is mainly obtained in the blast furnace by means of chemical reduction of the iron oxide of the iron ores with carbon [85]. Pure iron can also be obtained in the laboratory by reduction of iron oxides with hydrogen at temperature ranging from 400 to $700\,°C$ or by pyrolysis of iron pentacarbonyl $Fe(CO)_5$ at $250\,°C$. Pure iron has the highest saturation magnetisation, the highest magnetic permeability and the lowest remanence of all elements. A summary of the properties of iron is presented in Table 2 [90].

Table 2: Physical properties of iron.

	Fe
Atomic number	26
Standard atomic weight (A$_r$)	55,847(3)
Electron configuration	[Ar] 3d^6 4s^2
Density (at room temperature)	8.874 kg/m^3
Electronegativity (Allred-Rochow scale)	1.6
Most common isotope (natural abundance $> 91\%$)	^{56}Fe
Melting point	1539 $°C$
Curie point	768 $°C$

The crystal structure and magnetic ordering of iron are temperature dependent. They are listed in

Table 3.

Table 3: Crystal structure and magnetic ordering of iron

Temperature [°C]	Occurrence	Crystal structure Bravais lattice	Magnetic ordering
906	α-Fe	body-centred cubic (bcc)	ferromagnetic
1401	γ-Fe	face-centred cubic (fcc)	paramagnetic
1539	δ-Fe	body-centred cubic (bcc)	paramagnetic

α-Fe is ferromagnetic up to the Curie point of $768\,°C$. After that, it loses its spontaneous magnetisation and remains ferromagnetic only in the presence of an external field [85].

3.3.2 Iron oxides

Naturally occurring iron oxides are wüstite (FeO), hematite (α-Fe_2O_3), maghemite (δ -Fe_2O_3) and magnetite (Fe_3O_4). Figure 16 shows the iron-oxygen phase diagram [85].
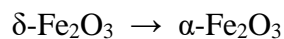
Wüstite (FeO) is an iron monoxide known also as iron (II)-oxide or ferrous oxide. It has a sodium chloride structure with an iron deficiency. It has a cations blanks/voids ranging between 0.12 and 0.05, and hence a typical composition from $Fe_{0.88}O$ to $Fe_{0.95}O$. The iron deficiency is compensated by Fe^{3+} ions. Wüstite is stable as a non-stoichiometric compound $Fe_{1-x}O$ only above $560\,°C$. Below $560\,°C$, FeO is metastable and contains a disproportionate amount of α-Fe and Fe_3O_4. At room temperature, wüstite is paramagnetic. It becomes antiferromagnetic at a temperature range of $-70\,°C$ to $-62\,°C$. The Néel temperature T_N is not constant anymore and is within a certain range because it depends on the concentration of defects in the structure [96-97].

Hematite and maghemite represent the two natural modifications of iron (III)-oxide. Hematite (α-Fe_2O_3) crystallizes in corundum structure. It is weakly ferromagnetic at room temperature and has a Currie temperature T_C of $683\,°C$. Below $-13\,°C$, hematite undergoes a spin-flop transition and becomes antiferromagnetic. This temperature limit marks the so-called Morin transition where the spin orientation is turned 90 degrees. Hematite can be superparamagnetic at room temperature when the particles are smaller than $8\,nm$ [96-97].

Maghemite (δ-Fe_2O_3) crystallizes in spinel structure with blanks/voids and is ferrimagnetic at room temperature. The Curie temperature T_C of maghemite ranges between $547\,°C$ and $713\,°C$. T_C is not well-defined because maghemite transforms to hematite at temperature between $-267\,°C$ and $527\,°C$ [96-97]. The following chemical reactions can illustrate this transition. Maghemite can be obtained by oxidation of magnetite at a temperature between 250 and $300\,°C$.

$$2Fe_3O_4 + ½\,O_2 \rightarrow 3\,δ\text{-}Fe_2O_3$$
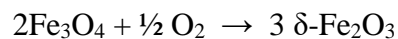
Above $300\,°C$, δ-Fe_2O_3 changes to α-Fe_2O_3.

$$δ\text{-}Fe_2O_3 \rightarrow α\text{-}Fe_2O_3$$

Maghemite can be superparamagnetic at room temperature when the particles are smaller than $10\,nm$.

Magnetite (Fe_3O_4) is iron (II,III)-oxide and is considered as natural magnet. Fe_3O_4 crystallizes in the inverse spinel structure Fe^{+3} [$Fe^{+2}Fe^{+3}$]O_4. The tetrahedral sites are occupied by Fe^{3+}. The octahedral sites are occupied by Fe^{+3} and Fe^{+2}. Magnetite is ferrimagnetic. Its Curie temperature is $577\,°C$ and its magnetic moment has a theoretical value of 4 $μ_B$. The experimental magnetic moment of magnetite ranges between 4.0 and 4.2 due to contribution

28

of the angular momentum. Magnetite can be superparamagnetic at room temperature when the particles are smaller than $6\ nm$. Moreover, Fe_3O_4 is a good electrical conductor because on the octahedron sites occurs a rapid electron exchange between the Fe^{2+}- and Fe^{3+}- ions [85, 96-97].
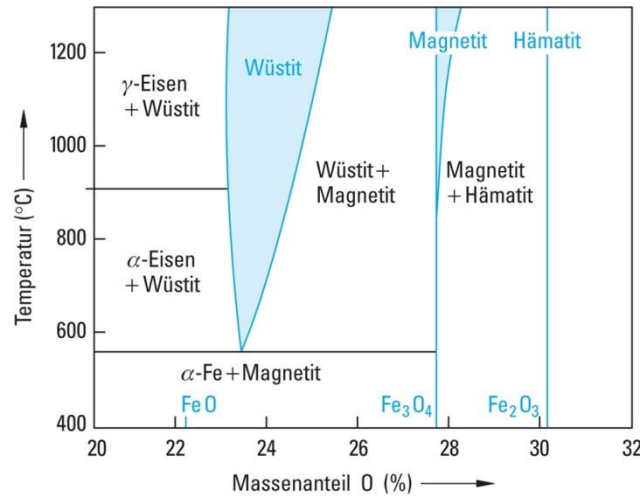

Figure 16: Iron-oxygen phase diagram [**85**].

There are also two different artificial iron (III)-oxides: Beta phase (β-Fe_2O_3) and epsilon phase (ε-Fe_2O_3), which do not play a major role in the framework of this thesis.

3.3.3   Ferrite

Ferrites are ferrimagnetic materials and are mostly composed of three components. Most ferrites are a mixture of iron, manganese and zinc. Iron is the most important metal in the ferrite with a share of 70 %. The manganese part is about 25 %. The remaining amount of 5 % is zinc. Every single iron atom generates its own small magnetic field just like any other manganese atom. In an external magnetic field, the magnetisation fields are oriented in different directions and partially cancel out one another. Therefore a ferrite is a weaker magnet than pure iron [85].

The ferrites are produced from various oxides and occur in various structures. One illustration can be the formula unit Me-Fe_2O_4, where Me represents a divalent metal. It crystallizes in the spinel structure. The metal ions are located on the places of two sublattices A and B with a tetrahedral or octahedral dioxygen (O_2) environment. The A-lattice is occupied exclusively by Fe^{3+} ions, while the sublattice B is occupied by Me^{2+} and the remaining Fe^{3+}-ions

In the normal spinel structure, the sublattices are occupied by only one ion type, whereas in the case of inverse spinel ferrites, the A lattice is occupied exclusively by Fe^{3+} and the B lattice is statistically occupied by Fe^{3+} and Me^{2+}. The metals and the oxygen form crystals with differently sized crystallites. Since each crystallite is electrically isolated from its neighbouring one, electric current can flow only within a crystallite. The ferrite shows almost no electrical conductivity. In contrast to pure iron, a high-frequency magnetic field induces a very small current in the ferrite. The AC losses are consequently low.

Ferrites can have different and mixed structures. The arrangement of the atoms in the crystals, the oxygen content and the crystallite size determine the direction of the magnetic field in the iron and manganese atoms. If some iron atoms are replace by manganese atoms, nickel is used instead of zinc or the oxygen content is increased, the magnetic and the electrical properties of the ferrite considerably change.

The ferrites are used in switching power supplies. They supply notebooks with electrical energy. They transmit high-frequency signals from satellites and mobile phones and work as an antenna in radio-controlled clocks [85].

3.3.4 Magnetic fillers used in this study

In order to prepare magneto-sensitive elastomers, soft magnetic filler were mixed into rubber matrix. Earlier works have revealed that only MSE filled with magnetic fillers based on iron or iron oxides show a sufficiently good sensitivity to external magnetic field [98-107].

In the framework of this thesis, pure iron based filler is used. It consists of carbonyl iron particles SW-S (CIP) and is supplied by BASF SE. The second magnetic filler used is MAGSILICA. It is based on iron oxides embedded in a silica matrix and is supplied by Evonik Industries.

Iron carbonyl is a fine iron powder prepared from thermal decomposition of iron pentacarbonyl $Fe(CO)_5$. Iron (Fe) and carbon monoxide (CO) are arranged in a trigonal bipyramidal structure, in which five carbon monoxide ligands are coordinated to an iron atom. The electrical charge carries are homogeneously distributed throughout the atoms so that iron pentacarbonyl does not possess any molecular dipole.

Iron pentacarbonyl is prepared by direct reaction of iron with carbon monoxide. Finely dispersed iron reacts at temperatures between $150\,°C$ and $200\,°C$ under a carbon monoxide pressure of 50 to 200 bar according to the following chemical formula:

$$Fe \quad + \quad 5\,CO \quad \longrightarrow \quad Fe(CO)_5$$
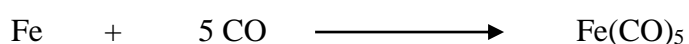
The prepared iron pentacarbonyl is available as yellow-red solution and contains impurities such as nickel (Ni), molybdenum (Mo) and chromium (Cr). The impurities are removed by distillation. In a second step, the reverse reaction takes place at higher temperature according to the following chemical formula:

$$Fe(CO)_5 \quad \longrightarrow \quad Fe \quad + \quad 5\,CO$$

Iron (Fe) is transported chemically through the gas phase of carbon monoxide (CO). This process is known as chemical transport reaction and leads to separate pure iron Fe from gaseous carbon monoxide (CO) [108-113].

The grey-coloured iron carbonyl prepared represents the hard grade. It is the product from the primary decomposition without further chemical processing. It has an onion skin structure as pictured on the left of Figure 17. It contains up to $97,8\,\%$ iron Fe, a maximum of $1\,\%$ carbon C, a maximum of $0.9\,\%$ nitrogen N and a maximum of $0.5\,\%$ oxygen O. Soft grade

CIP is produced by annealing of hard grades under hydrogen H. In this process, the onion skin structure becomes a polycrystalline structure as depicted on Figure 17. The iron Fe content increases at least to 99.8 %. C, N and O are strongly reduced [114-115].

Figure 17: Structure of carbonyl iron particles. Onion skin structure of hard grade CIP is depicted on the left. The right picture illustrates the polycrystalline structure of soft grade CIP [**114**].

The CIP used in this thesis contain more than 99 % pure iron and less than 0.4 % carbon. The relative permeability μ_r of CIP is larger than 29. Additionally, the CIP particles are coated with a thin layer of polyol containing multiple hydroxyl functional groups. The average diameter of CIP lies in a range between 3 μm to 4.5 μm [114-115].

MAGSILICA is a rust-red nanoscaled magnetic filler. It consists of a mixture of different iron oxides coated with a 3 nm thick silica layer. The iron oxide content is 85 ± 5 % According to the supplier, MAGSILICA contains 55 ± 5 % magnetite (Fe_3O_4), 35 ± 5 % maghemite (γ-Fe_2O_3) and less than 15 % hematite (α-Fe_2O_3). The average diameter of MAGSILICA particles ranges between 5 nm to 30 nm. The special saturation magnetisation is more than 45 Am^2/kg. The coercivity is between 8 kA/m and 11 kA/m [106, 116]. Below certain size ranges, hematite, maghemite and magnetite show a superparamagnetic behaviour and possess a higher magnetic moment than paramagnetic materials. At room temperature, magnetite (Fe_3O_4) is ferrimagnetic. The magnetic moments have different magnitudes and are arranged antiparallel within the Weiss domains. Maghemite (γ-Fe_2O_3) is a ferrimagnetic material. The magnetic moments are parallel within the Weiss domains, so that the total magnetisation is larger compared to magnetite [117-118]. Hematite (α-Fe_2O_3) is antiferromagnetic below the temperature of Morin transition, otherwise weakly ferromagnetic. The magnetic moments have the same magnitude and are arranged antiparallel within the Weiss domains [119-121]. The size distribution of MAGSILICA particles and the structure of MAGSILICA aggregates are shown in Figure 18.
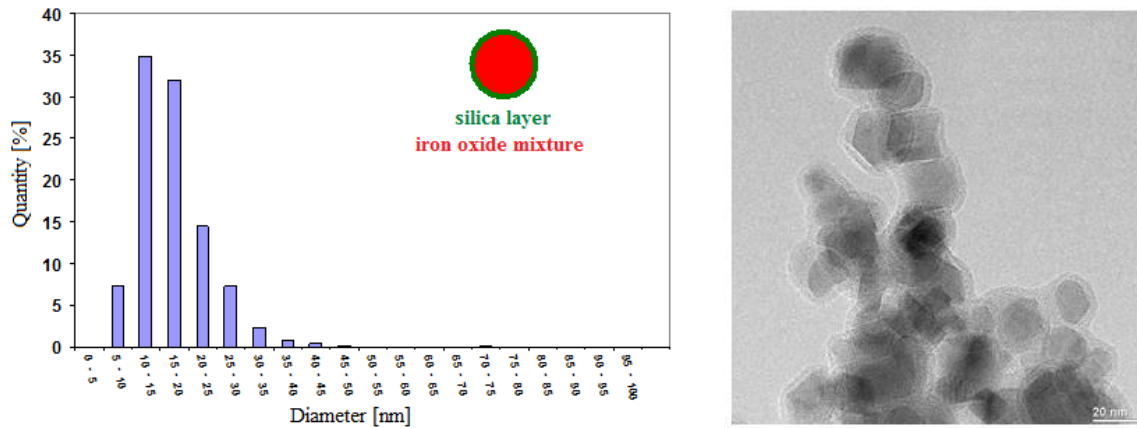
Figure 18: Size distribution of MAGSILICA particles is shown on the left. The inset illustrates the core-shell structure. On the right, the structure of MAGSILICA aggregates is shown by means of transmission electron micrograph (TEM) [116].

CIP mainly differs from MAGSILICA in the composition and size. Figure 19 shows a view of MAGSILICA and CIP [114, 115].

Figure 19: Magnetic fillers used. MAGSILICA is on the left. CIP is on the right [114].

The coating layers of MAGSILICA and CIP are magnetically dead layers. They do not contribute to the magnetisation weather of the magnetic filler particle itself or subsequently to MSE. The coating is highly relevant in order to protect the surrounding rubber matrix and to provide electrical insulation for electrically conductive substances, which avoids eddy currents. In addition, the coating enables a better chemical bonding of the filler particles to the polymer chains with a silane [106, 107].

4 Modelling and data treatment

This chapter presents the main analysis methods and evaluation tools used to characterise the viscoelastic materials. The dynamic-mechanical thermal analysis (DMTA) gained an important standing in the rubber technology since it enables an accurate description of the macroscopic viscoelastic behaviour of elastomer composites. DMTA provides information about the properties of a viscoelastic material as a function of frequency, temperature and force or deformation amplitude. The collected measurement data can be used to expend the measurement range of the DMTA to overcome some technical restrictions concerning the application temperature or frequency, which can be extremely interesting for several applications like high frequency spectroscopy. The viscoelastic properties can be also used as input for diverse theoretical models to gain more knowledge about the reinforcement mechanism of filled elastomer composites as well as the internal dynamic and relaxation processes of the different components within the sample.

4.1 Dynamic-mechanical thermal Analysis

In a dynamic-mechanical measurement, the sample is subjected to a static and dynamic load, generally a sinusoidal pulse with pre-set frequency, temperature and force amplitude. As a result, the sample deforms. Between the exerting force and the dynamic-mechanical response, a phase shift can occur. On this basis all materials can be assigned to one of the following categories. For purely elastic materials like steel springs, the deformation occurs almost simultaneously with the sample excitation. The phase shift between excitation and response is zero. For purely viscous materials like oil, a time delay between excitation and response is observed. The phase shift is $\pi/2$. However, elastomer composites possess both elastic and viscous properties. This behaviour is typical for viscoelastic materials. Force and deformation are phase shifted by an angle ranging between 0° and 90°.

If the test specimen is subjected to a dynamic force $F(t)$ with constant amplitude F_0, angular frequency ω and phase shift δ, $F(t)$ can be expressed as follows

$$F(t) = F_0.\sin(\omega t + \delta) \tag{20}$$

The deformation $x(t)$ with the deformation amplitude x_0 takes the following form

$$x(t) = x_0.\sin(\omega t) \tag{21}$$

In order to compare different test samples and make reliable statements about them, it is appropriate to derive geometrically independent relative values. In the case of shear deformation, the mechanical stress $\tau(t)$ is defined as force $F(t)$ per cross section area A and has the following form:

$$\tau(t) = \frac{F(t)}{A} = \tau_0.\sin(\omega t + \delta) \tag{22}$$

where τ_0 is the stress amplitude with the unit Pascal. The strain $\gamma(t)$ is determined as the ratio between the initial length x_0 and the extension of the sample $\Delta x = x(t) - x_0$, calculated by

subtracting the initial length x_0 from the current distance $x(t)$. It is dimensionless and can be expressed as

$$\gamma(t) = \frac{x(t) - x_0}{x_0} = \frac{\Delta x}{x_0} = \gamma_0 . \sin(\omega t) \tag{23}$$

where γ_0 is the strain amplitude. Figure 20 illustrates the time-dependent curve progression of both mechanical stress $\tau(t)$ and strain $\gamma(t)$ of viscoelastic materials.
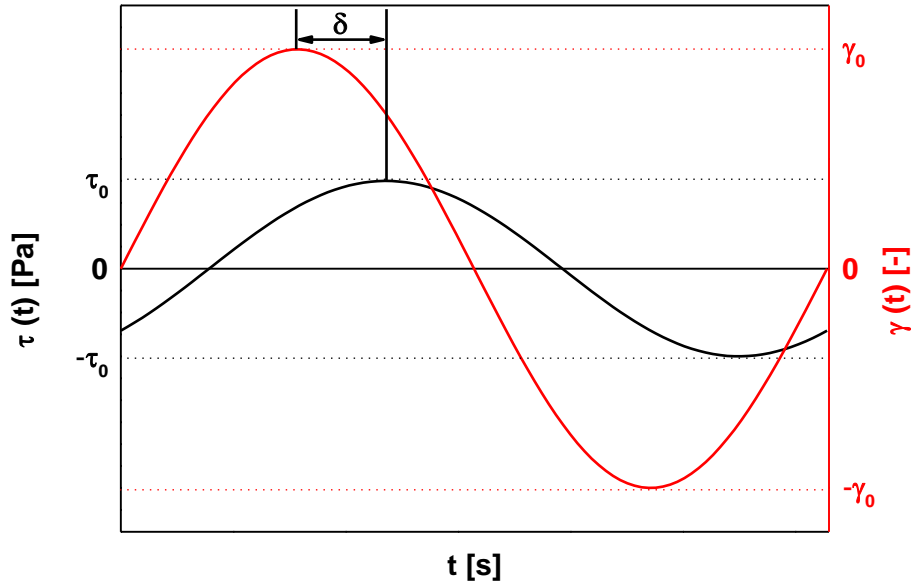

Figure 20: Time evolution of mechanical stress $\tau(t)$ and strain $\gamma(t)$ of viscoelastic materials. The phase shift δ between them is also displayed.

The relationship between exerting force and deformation can be further expressed by a complex quantity to associate the mechanical stress with the strain. This is the shear modulus $G^*(t)$ in case of a shear or torsion deformation. The shear modulus $G^*(t)$ is calculated by dividing the mechanical stress by the strain as follows:

$$G^*(t) = \frac{\tau(t)}{\gamma(t)} \tag{24}$$

By inserting the previous equations (22) and (23) and developing the sum formula of the sine function, $G^*(t)$ becomes

$$G^*(t) = \frac{\tau_0 . \sin(\omega t + \delta)}{\gamma_0 . \sin(\omega t)} \tag{25}$$

$$G^*(t) = \frac{\tau_0 . \cos(\delta) \sin(\omega t) + \tau_0 . \sin(\delta) \cos(\omega t)}{\gamma_0 . \sin(\omega t)} \tag{26}$$

Using the identity $\cos(\omega t) = \sin(\omega t + \pi/2)$, $G^*(t)$ becomes

$$G^*(t) = \frac{\tau_0 . \cos(\delta) \, \sin(\omega t) + \tau_0 . \sin(\delta) \, \sin(\omega t + \pi/2)}{\gamma_0 . \sin(\omega t)} \tag{27}$$

$$G^*(t) = \frac{\tau_0 . \cos(\delta) \, \sin(\omega t)}{\gamma_0 . \sin(\omega t)} + \frac{\tau_0 . \sin(\delta) \, \sin(\omega t + \pi/2)}{\gamma_0 . \sin(\omega t)} \tag{28}$$

$$:= G' + i . G'' \tag{29}$$

where

$$G' = \frac{\tau_0}{\gamma_0} \cos(\delta) \tag{30}$$

$$G'' = \frac{\tau_0}{\gamma_0} \sin(\delta) \tag{31}$$

The complex shear modulus $G^*(t)$ is splitted into two parts. The real part at which stress and strain are in phase is referred to as the storage modulus, denoted by G'. It describes the elastic properties of the sample and it is a measure of the mechanical stored energy W_{el}. The imaginary part at which the stress and the strain are shifted by $\pi/2$ is referred to as the loss modulus, denoted by G''. It refers to the viscous properties of the sample and it is a measure of the mechanical dissipated energy W_{dis}.

The quotient of loss and storage modulus describes geometrically the tangent of the phase shift δ between sample excitation and response and it looks as follows

$$\tan(\delta) = \frac{G''}{G'} = \frac{1}{2\pi} \frac{W_{dis}}{W_{el}} \tag{32}$$

The phase shift δ indicates the fraction of energy irreversibly dissipated. This is only a part of the energy introduced during a deformation cycle and is transformed into heat. The larger the phase shift between exciting force and resulting deformation, the larger the sample damping [122, 123].

4.1.1 Generation of master curve

DMTA is designed to determine the rheological behaviour of test samples under a wide range of practical conditions by varying frequency, temperature and load or strain amplitude. Due to technical limitations, the material properties at high frequency are often not possible to be characterised, although it is extremely interesting to better understand e.g. the behaviour of tyre tread due to friction or during braking processes. To overcome these technical restrictions, the collected measurement data can be evaluated according to the time-temperature superposition principle [124].

This principle states that there is a time-temperature equivalence of the properties of viscoelastic materials. The reason lays in the molecular processes and global molecular rearrangements, which determine the relaxation behaviour of the material. These molecular processes are thermally activated and will be much faster when the temperature increases. However, the number of molecular processes or their type remains unchanged. The curve shape of the relaxation spectrum and therefore the viscoelastic properties remain also constant. Only the time or frequency position of the viscoelastic properties changes with the temperature.

For elastomer composites, the time-temperature superposition principle has acquired a great significance to predict long-term behaviour. If the curve progression of storage modulus $G'(t)$ is known at different temperatures, a master curve can be determined by horizontal shifting the individual curves at a reference temperature T_{ref} according to the Williams-Landel-Ferry law, known as WLF law after M. L. Williams, R. F. Landel and J. D. Ferry [125]. The master curve covers therefore a time or frequency interval which is not accessible by any experimental measurements. This procedure can be applied for rheological simple systems. Figure 21 shows a generated master curve of the storage modulus according to WLF at 20 °C.

The shift factor $\log a_T$ is temperature- dependent and it has the following form:

$$\log a_T = -\frac{C_1(T-T_{ref})}{C_2+(T-T_{ref})} \tag{33}$$

where T is the measurement temperature and T_{ref} is the reference temperature. C_1 and C_2 are intrinsic material coefficients. The WLF law can be also described on the basis of Arrhenius equation

$$\log a_T = -\frac{E_a}{2.303R}\left(\frac{1}{T}-\frac{1}{T_{ref}}\right) \tag{34}$$

where E_a is the activation energy and R is the gas constant.
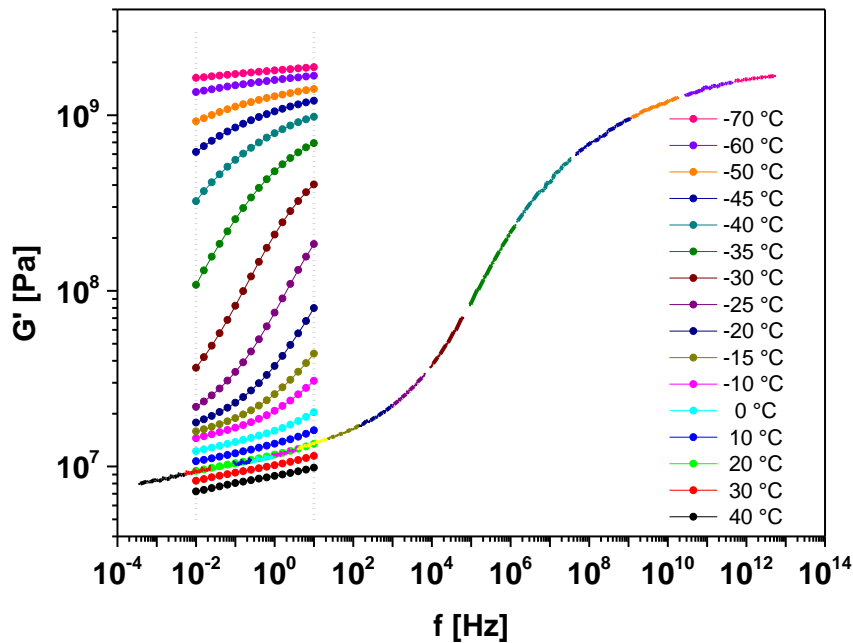
Figure 21: Single frequency sweeps at different temperatures are illustrated between the two lines. The generated master curve according to WLF at 20 °C is the nearly continuous curve.

In order to shift the single frequency sweeps properly, the Kramers-Kronig relations are taken in account [124]. The Kramers-Kronig relations, according to H. A. Kramers and R. Kronig,

relate the real and imaginary part of complex functions in the form of an integral equation. The relationship between the real and imaginary part is not a material property, but an expression of the principle of causality, which states that the system response happens first when the system is excited.

If an excitation force produces within a system the response $h(t)$, the Fourier transform of $h(t)$ provides its frequency response $H(\omega)$, which takes the general form:

$$H(\omega) = \frac{1}{\sqrt{2\pi}} \int dt \, h(t) e^{-i\omega t} \tag{35}$$

$H(\omega)$ can be splitted into real and imaginary part describing a Hilbert transformation, in which the real part depends on the imaginary part.

$$Re \, H(\omega) = \quad \frac{2}{\pi} \int_{-\infty}^{\infty} d\omega' \frac{Im \, H(\omega')}{\omega' - \omega} \tag{36}$$

$$Im \, H(\omega) = -\frac{2}{\pi} \int_{-\infty}^{\infty} d\omega' \frac{Re \, H(\omega')}{\omega - \omega'} \tag{37}$$

According to the Kramers-Kronig relations, the shift factors $\log a_T$ needed to shift the storage modulus $G'(\omega)$- the real part of the shear modulus $G^*(\omega)$- are the same factors to shift the loss modulus $G''(\omega)$- the imaginary part of the shear modulus $G^*(\omega)$. Since the real part and the imaginary part of the shear modulus are interdependent, they can be expressed as follows

$$G'(\omega) = \quad \frac{2}{\pi} \int_0^{\infty} d\omega \frac{\omega'}{\omega^2 - \omega'^2} G''(\omega') \tag{38}$$

$$G''(\omega) = -\frac{2}{\pi} \int_0^{\infty} d\omega \frac{\omega}{\omega^2 - \omega'^2} G'(\omega') \tag{39}$$

Using equations (38) and (39), it can be proven that the shift of storage modulus G' and loss modulus G'' can be also determined by the shift of their quotient G''/G'. This means that the horizontally shifting of loss angle $\tan \delta$ is sufficient to generate master curves with the same shift factors [124].

4.1.2   Evaluation of relaxation time spectra

DMTA is used to characterise the rheological properties of materials. By varying temperature or frequency, according to the time-temperature superposition principle, the time dependence of the material behaviour can also be identified. This allows a better understanding of the molecular dynamics within the sample since the different internal relaxation processes are related to macroscopic viscoelastic behaviour. Besides, the evaluation of relaxation time spectra can also be important for the investigation of the fatigue behaviour and crack growth mechanism within elastomer composites since some material-specific coefficients from both approaches are interrelated [124].

The relaxation time spectrum maps all the properties of the viscoelastic material behaviour in terms of relaxation times. It is the interface between macroscopically measurable material properties and the microscopic structure. It is more a question of the dynamic of polymer chains than crosslinking points and filler. Polymer chains can undertake a variety of conformations by slipping, bending or rotating around the chemical bonds. These

conformations are constantly changing due to the Brownian motion and external deformation of the material. The relaxation times spectra describe the transition rates at which this conformational change takes place. Since different microscopic processes are associated with different conformational changes, their characteristic relaxation times generally vary in a wide range: from local changes, which sometimes take place very quickly, until changes in larger chain segments associated with longer periods. As a result, the individual microscopic processes can be identified in different areas of the relaxation spectrum [126-130].

To introduce the approach of relaxation spectrum, viscoelastic materials are assumed as phenomenological Maxwell model. This rheological model maps well the complex behaviour of viscoelastic materials only if the relationship between mechanical stress and deformation is linear. The viscoelastic material is modelled by a series of Maxwell elements, which are arranged parallel as shown in Figure 22. The Maxwell element consists of a Hook spring with the modulus G_i, which is arranged in series with an ideal viscous damping element with the Newtonian viscosity η_i .
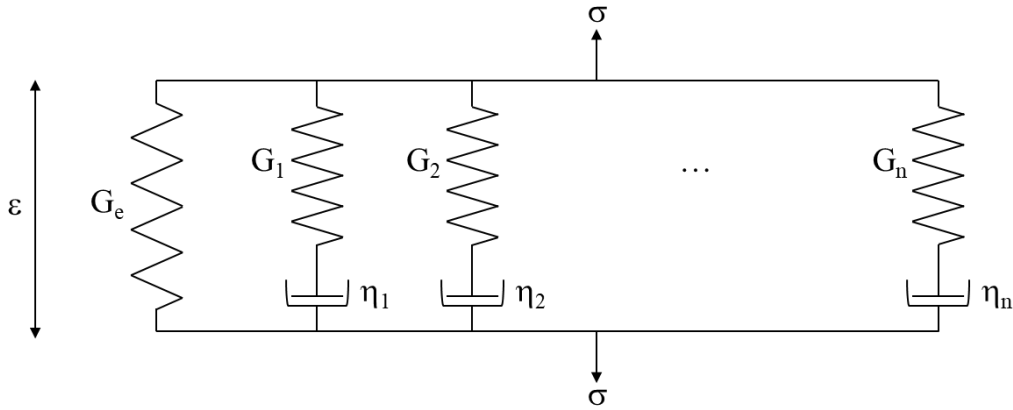
Figure 22: Maxwell model of viscoelastic materials.

The mechanical stress $\sigma(t)$ is a time dependent variable. It is a sum of the contribution of each individual Maxwell element and has the following form:

$$\sigma(t) = \sigma_e + \sum_{i=1}^{n} \sigma_i(t) \tag{40}$$

The relaxation modulus $G(t)$ is calculated by dividing the mechanical stress in equation (40) by the elongation $\varepsilon(t)$. $G(t)$ takes the following discrete form

$$G(t) = G_e + \sum_{i=1}^{n} G_i(t) \tag{41}$$

$$:= G_e + \sum_{i=1}^{n} G_i e^{-\frac{t}{\tau_i}} \tag{42}$$

where $G_i(t)$ is the ith relaxation module of the ith Maxwell element. Furthermore, the relaxation moduli $G_i(t)$ can be expressed as a function of the relaxation times τ_i. G_i represents the amplitude of the relaxation modulus $G_i(t)$.

Since these relaxation times are very close together, it is appropriate to derive continuous relaxation time spectra $H(\tau)$. The relaxation modulus $G_i(t)$ becomes

38

$$G(t) = G_e + \int_{-\infty}^{+\infty} dln(\tau) \, e^{-\frac{t}{\tau}} H(\tau) \tag{43}$$

The Fourier transformation of the relaxation modulus yields to the following relationship between the relaxation time spectrum and the experimentally available dynamic moduli:

$$G'(\omega) = G_e + \int_{-\infty}^{+\infty} dln(\tau) \, H(\tau) \frac{\omega^2\tau^2}{1+\omega^2\tau^2} \tag{44}$$

$$G''(\omega) = \int_{-\infty}^{+\infty} dln(\tau) \, H(\tau) \frac{\omega\tau}{1+\omega^2\tau^2} \tag{45}$$

The relaxation time spectra $H(\tau)$ are determined by an iterative approximation according to Williams and Ferry [113-115]. $H(\tau)$ has the following form:

$$H(\tau) = AG'(\omega) \frac{d \, G'(\omega)}{d \, log\omega} \tag{46}$$

with

$$A = \frac{2-p}{2\Gamma\left(2-\frac{p}{2}\right)\Gamma\left(1+\frac{p}{2}\right)} \tag{47}$$

where p is the local slope of $H(\tau)$ at $\frac{1}{\omega} = \tau$. Γ is the gamma function.

In the frame of multiscale approach, $G(t)$ can be expressed as the superposition of high frequency part of the glass transition zone, Rouse-like regime at the intermediate frequencies and reptation regime at low frequencies [128-130]. For unfilled rubbers, the relaxation modulus due to bending rigidity of chains follows a power-law asymptotic behaviour with the exponent $-3/4$ according to

$$G_{glass}(t) \propto \left(\frac{t}{\tau_0}\right)^{-3/4} \tag{48}$$

The relaxation behaviour at the high frequency glass transition regime is caused by the bending rigidity of the polymer chains and is similar to relaxation time of a Kuhn segment. The Rouse-like regime describes the low frequency part of the glass transition zone. The relaxation modulus decreases more slowly than in the glassy regime and it can be written as follows

$$G_{Rouse}(t) \propto \left(\frac{t}{\tau_0}\right)^{-1/2} \tag{49}$$

$G_{Rouse}(t)$ follows a power-law asymptotic behaviour with the exponent $-1/2$. The reptation regime describes the sliding motion of entangled network strands and it depends on the crosslink density. The last relaxation mechanism occurs at very high frequencies. It describes small vibrations of chain fragments comparable with the size of monomers. The exponent of the power law can be derived from the right flank of the loss modulus curve. For the further consideration within the framework of this thesis, only the glass transition is significant. The focus will be put on the glassy and Rouse-like regime.

The generated master curve for unfilled NR sample is presented in Figure 23. The storage modulus $G'(\omega)$ and loss modulus $G''(\omega)$ are plotted against the frequency ω. The different

slopes correspond to four relaxation mechanisms according to the four different microscopic dynamics discussed above. The different slopes are drawn up in the graph.
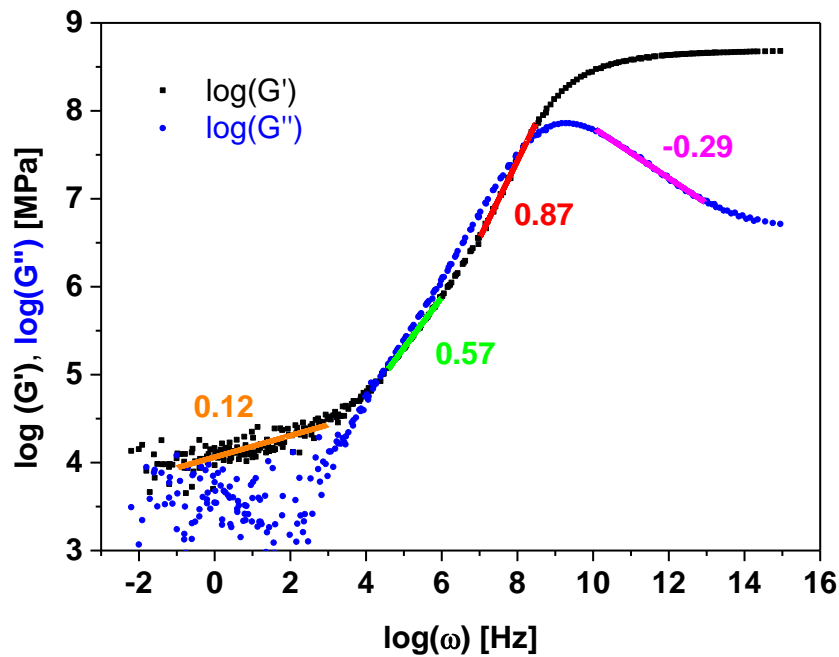

Figure 23: Viscoelastic master curves of an unfilled NR sample at reference temperature of **20 °C**. The different scaling ranges are indicated.

The different relaxation times do not exactly match with the theoretical values but remain in the valid range. The corresponding relaxation time spectrum for unfilled NR sample can be derived from the master curves according to equation (44) and (45). It is depicted in Figure 24.

The different relaxation behaviours still remain valid for filled samples. One precondition must be fulfilled: no additional network exists besides the polymer chains network. It is to note that the glassy and Rouse-like regime can no longer be distinguished. The relaxation time spectrum for filled NR sample is depicted in Figure 25.
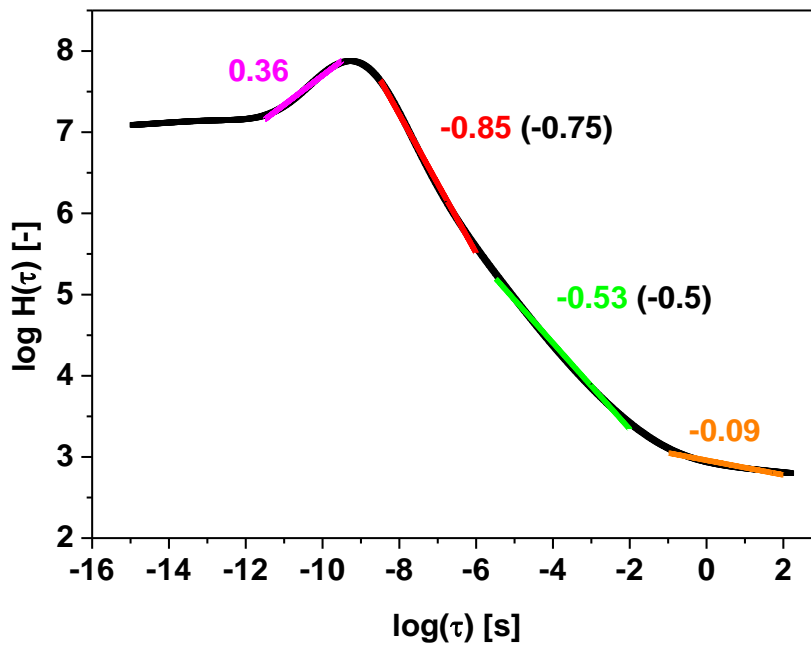
Figure 24: Relaxation time spectrum for the unfilled NR sample. The different scaling ranges are indicated. The theoretical values are shown between parentheses.
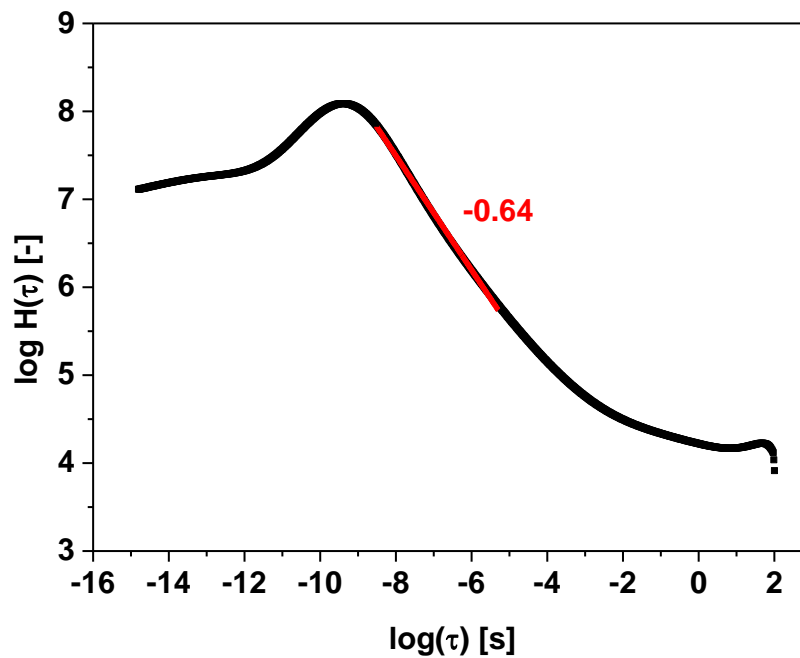
Figure 25: Relaxation time spectrum for anisotropic NR sample filled with 20 vol.% CIP.

4.2 Dynamical Flocculation Model

The dynamical flocculation model (DFM) is a physical motivated micromechanical model for the description of isotherm change in state of elastomers by a given deformation. DFM provides an excellent agreement with the experimental stress-strain behaviour of elastomer composites. It represents an extension of the non-affine tube model. A non-Gaussian length distribution of the polymer chains is assumed. This means that the polymer chains have a finite length; also qualified as finite chain extensibility. The extended tube model assumes that polymer networks with high entanglement density are strongly hindered in their fluctuation. This hindrance is described by fluctuation-limiting virtual tubes around the network chains. Under deformation of the polymer network, these tubes do not deform affine [131-146]. Figure 26 illustrates a schematic representation of a network chain in a virtual tube. Graph is adapted from [132].
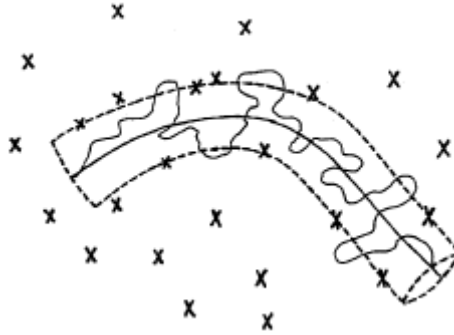
Figure 26: Schematic representation of a network chain in a virtual tube. The tube diameter is given by the mean spacing of the topological constraint centre, i.e. crosslinks and entanglements, indicated as crosses.

For an isothermal reversible deformation, the mechanical energy inducing a state change of an unfilled elastomer is equal to the free energy function $W(\varepsilon_\mu)$. According to Klüppel et al. [132], the entropy-elastic rubber contribution W_R has the constitutive form:

$$W_R = \frac{G_c}{2}\left\{\frac{\left(1-\frac{1}{n}\right)\left(\sum_{\mu=1}^{3}\lambda_\mu^2-3\right)}{1-\frac{1}{n}\left(\sum_{\mu=1}^{3}\lambda_\mu^2-3\right)} + ln\left(1 - \frac{1}{n}\left(\sum_{\mu=1}^{3}\lambda_\mu^2 - 3\right)\right)\right\} + 2G_e\left(\sum_{\mu=1}^{3}\lambda_\mu^{-1} - 3\right) \quad (50)$$

where G_c is the crosslink modulus, G_e is the entanglement modulus, λ_μ is the stretch ratio and n is the finite extensibility parameter. $n := n_e/T_e$ where n_e is a polymer specific quantity representing the number of chain segments between two entanglements and T_e is a crosslink-dependent trapping factor indicating the proportion of elastically active entanglements. DFM has the peculiarity that all free parameters are linked with molecular structure of the rubber samples. The crosslink modulus $G_c := \nu_c k_B T$ depends on the number density of mechanically active network strands between the junctions ν_c and the absolute temperature T. k_B is the Boltzmann constant. The entanglement modulus $G_e := \nu_e k_B T/\sqrt{6}$ depends on the number density of chain fragments between entanglements ν_e. The finite extensibility parameter

$n_e/T_e := v_s k_B T/(\sqrt{6}\, G_e T_e)$ gives the number of segments between two adjacent entanglements. Here $v_s := n_e v_e$ is the segment number density.

The polymer contribution to the total stress is defined as the first derivative of the free energy function W_R with respect to the stretch ratio λ_μ in the spatial direction $\mu := 1, 2$ and 3. λ_μ is defined as

$$\lambda_\mu := 1 + \varepsilon_\mu \tag{51}$$

where ε_μ is the strain in the direction μ. The total stress takes the following form:

$$\sigma_{R,\mu} := \frac{dW_R}{d\lambda_\mu} \tag{52}$$

The elastomer composites are assumed as incompressible materials. This means that the volume of the sample remains constant independently of the load conditions. The following applies:

$$\frac{\Delta V}{\Delta V_0} = \lambda_1 \lambda_2 \lambda_3 \equiv 1 \tag{53}$$

In other words, if the sample is sheared in direction 1, it will be compressed in direction 3 and remains unaffected in direction 2. The principle stress axes η and ξ of the deformation ellipsoid rotate with increasing amplitude in the direction of the shearing surfaces as shown in Figure 27.
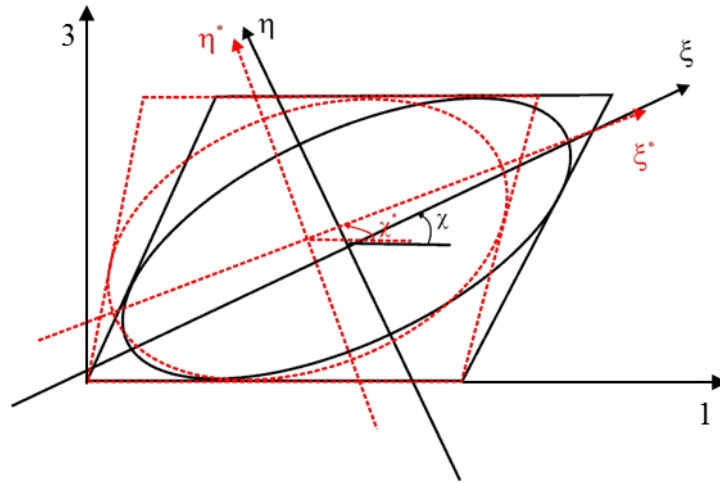
Figure 27: Variation of the angle χ between the principle stress axes η and ξ. Sample is sheared in direction **1**. Direction **2** is perpendicular to plane $(1, 3)$.

The principal stretch ratios in the main axes η and ξ take the following form:

$$\lambda_1 = \sqrt{1 + \frac{\chi^2}{4}} + \frac{\chi}{2} \tag{54}$$

$$\lambda_2 = 1 \tag{55}$$

$$\lambda_3 = \sqrt{1 + \frac{\chi^2}{4}} - \frac{\chi}{2} \tag{56}$$

χ is the angle between the two principal axes η and ξ. Taking into consideration the volume constancy of the sample and redefining the stretch ratio in direction 1 as:

$$\lambda_1 \equiv \lambda \tag{57}$$

the following applies:

$$\lambda_2 \equiv 1 \tag{58}$$

$$\lambda_3 \equiv \frac{1}{\lambda} \tag{59}$$

The simple shear stress takes the following form:

$$\sigma_R = G_c(\lambda - \lambda^{-3})\left\{\frac{1-\frac{1}{n}}{\left(1-\frac{1}{n}\left(\lambda^2-2+\frac{2}{\lambda^2}\right)\right)^2} - \frac{\frac{1}{n}}{1-\frac{1}{n}\left(\lambda^2-2+\frac{2}{\lambda^2}\right)}\right\} + 2G_e(1 - \lambda^{-2}) \tag{60}$$

For filled elastomers, the free energy function $W(\varepsilon_\mu)$ is the sum of the rubber and filler energy functions, weighted by the effective filler volume fraction:

$$W(\varepsilon_\mu) = \left(1 - \Phi_{eff}\right)W_R(\varepsilon_\mu) + \Phi_{eff}W_A(\varepsilon_\mu) \tag{61}$$

where $W_A(\varepsilon_\mu)$ is the energy-elastic contribution of filler and Φ_{eff} is the mechanical effective filler volume fraction. If an unfilled sample is stretched, the polymer deformation in a small local area corresponds to the global external deformation. In filled samples, the free polymeric phase is subject to a greater mechanical stress than the overall filler clusters once a load is applied. The reason is that the rigid filler clusters enclose parts of the polymers, which are no longer accessible for the stress. The additional loads must be then intercepted by the free polymer phase which implies that the local strain is greater than the global one. The consideration of this effect is carried out through the hydrodynamic amplification factor X_μ. The local deformation described in terms of the internal stretch ratio κ_μ is then related to the external strain ε_μ of the sample through:

$$\kappa_\mu := 1 + X_\mu \varepsilon_\mu \tag{62}$$

The hydrodynamic amplification factor X_μ depends on the principal strain history of the sample and more precisely on the maximum load ε_{max}. X_μ gives rise to stress softening effect of filler-reinforced rubber, well known as Mullins effect [135]. For fractal filler clusters, X_μ is formulated as follows:

$$X\left(\varepsilon_{\mu,max}\right) := 1 + c.\Phi_{eff}^{2/(3-d_f)}\sum_{\mu=1}^{3}\frac{1}{d}\left(d + \int_0^{\xi_{\mu,min}} d\xi\left(\frac{\xi_\mu}{d} - 1\right)^{d_w-d_f}\phi(\xi)\right) \tag{63}$$

where $c \approx 2.5$ represents the Einstein coefficient for spherical inclusions [147]. d_f is the fractal dimension of the filler clusters, d is the primary particle size, d_w is the anomalous diffusion exponent, $x_\mu = \xi_\mu/d$ is the related filler cluster size and $\phi(\xi)$ is the filler cluster size distribution.

According to the kinetics model of cluster-cluster aggregation (CCA), a Smoluchowski size distribution of the filler cluster is taken into consideration:

$$\phi(x_\mu) = \frac{4x}{\langle x_\mu \rangle^2} e^{-2x/\langle x_\mu \rangle} \tag{64}$$

where $\langle x_\mu \rangle$ is the mean filler cluster size. In the further handling, the size distribution of the filler clusters is assumed to be isotropic. This means that

$$\langle x_1 \rangle = \langle x_2 \rangle = \langle x_3 \rangle \equiv x_0 \tag{65}$$

Within this model and according to Meakin, the exponents take the following values [148].

$$d_f = 1.8 \tag{66}$$
$$d_w = 3.1 \tag{67}$$

Besides, the minimal filler cluster size is expressed as follows

$$x_{\mu,min} = \frac{\xi_{\mu,min}}{d} = \frac{Q_v \varepsilon_{v,b}}{d^3 \hat\sigma_{R,\mu}(\varepsilon_{\mu,min}; \varepsilon_{\mu,max})} \equiv \frac{s_v}{\hat\sigma_{R,\mu}(\varepsilon_{\mu,min}; \varepsilon_{\mu,max})} \tag{68}$$

where Q_v is the elastic constant due to deformation of virgin filler-filler bonds and $\varepsilon_{v,b}$ is the final strain of the bonds under loading. $\hat\sigma_{R,\mu}(\varepsilon_j; \varepsilon_k)$ is the relative rubber stress according to two given states of strain ε_j and ε_k and is defined as follows:

$$\hat\sigma_{R,\mu}(\varepsilon_j; \varepsilon_k) := \sigma_{R,\mu}(\varepsilon_j) - \sigma_{R,\mu}(\varepsilon_k) \tag{69}$$

Furthermore, s_v represents the strength of the virgin filler-filler bonds.

The stress-strain relationship of the rubber matrix $\sigma_{R,\mu}$ is defined as the first derivative of the free energy function W_R with respect to the stretch ratio κ_μ, which takes into account the hydrodynamic amplification factor X_μ:

$$\sigma_{R,\mu} := \frac{dW_R}{d\kappa_\mu} \tag{70}$$

Locally, large filler clusters carry more local stress than small clusters and break first. Two different types of clusters arise. Increasing the deformation breaks the next largest clusters. This process is continuous so that the boundary between unbroken hard filler clusters and reaggregated soft clusters shifts to smaller values with increasing maximum deformation. Figure 28 shows the distribution of filler cluster sizes within a test specimen. The filler cluster size x_{min} represents the borders between unbroken and broken filler clusters.
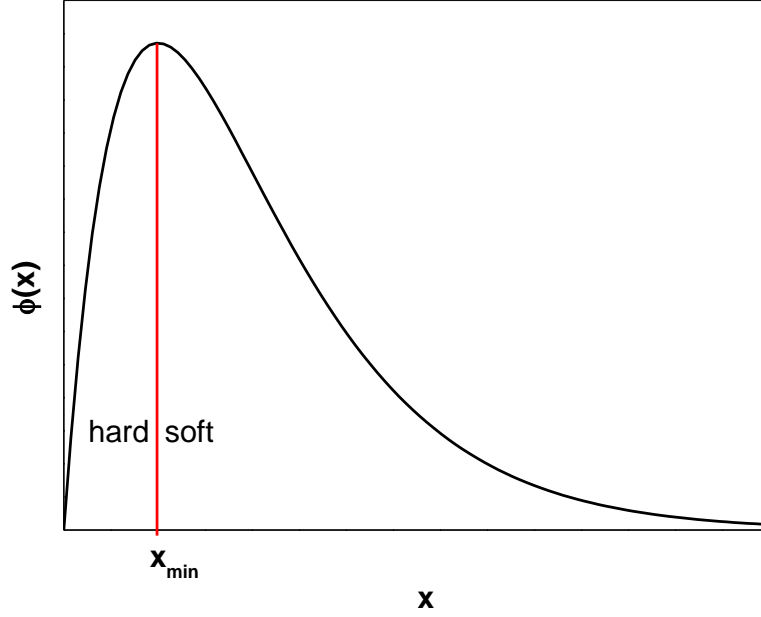
Figure 28: Distribution $\Phi(x)$ of filler cluster sizes x within a test specimen.

The hard filler clusters are virgin clusters which have never experience any mechanical loading while the soft filler clusters have already been exposed to prior damage. The filler contribution W_A to the free energy density takes place through the softer reaggregated clusters and has the following form

$$W_A(\varepsilon_\mu) = \sum_\mu^{\partial \varepsilon_\mu / \partial t > 0} \frac{1}{2d} \int_{\xi_{\mu,min}}^{\xi_\mu(\varepsilon_\mu)} d\xi_\mu \, G_A(\xi_\mu) \varepsilon_{A,\mu}^2(\xi_\mu, \varepsilon_\mu) \, \phi_\mu(\xi_\mu) \tag{71}$$

where ξ_μ is the filler cluster size, $G_A(\xi_\mu)$ is the elastic modulus of a filler cluster in the direction μ and $\varepsilon_{A,\mu}$ is the strain of filler clusters; determined by a stress equilibrium between the rubber matrix and the filler clusters. This stress equilibrium keeps the microscopic cluster stress in every spatial direction constant. It can be expressed as follows:

$$G_A(\xi_\mu) \varepsilon_{A,\mu}(\xi_\mu, x_\mu) = \hat{\sigma}_{R,\mu}(\varepsilon_\mu; \varepsilon_{\mu,min}) \tag{72}$$

The critical size of currently breaking soft clusters is:

$$x_\mu = \frac{\xi_\mu}{d} = \frac{Q_d \varepsilon_{d,b}}{d^3 \hat{\sigma}_{R,\mu}(\varepsilon_j; \varepsilon_k)} \equiv \frac{s_d}{\hat{\sigma}_{R,\mu}(\varepsilon_j; \varepsilon_k)} \tag{73}$$

Here Q_d/d^3 is the elastic modulus, $\varepsilon_{d,b}$ is the failure strain and s_d is the tensile strength of damaged bonds. The fitting parameters of DFM are summarized in Table 4.

Table 4: DFM fitting parameters

Parameter	Unit	Designation
G_c	MPa	Crosslink modulus
G_e	MPa	Entanglement modulus
n	-	Finite extensibility parameter
s_v	MPa	Tensile strength of virgin bonds
s_d	MPa	Tensile strength of damaged bonds
x_0	-	Mean filler cluster size
Φ_{eff}	-	Effective filler volume fraction

4.3 Fatigue crack growth

Technical elastomers suffer damages and some of them with disastrous consequences. This happens despite the careful examinations and rigorous calculations to determine the material lifetime and resistance to environmental crack formation. The most failures occur due to mechanical fatigue. That is why elastomer composites have to fulfil increasingly high requirements regarding loading and fatigue life. The damage is mainly caused by crystal defects and micro-voids in the components, formed already during the manufacturing process. Small imperfections are always present. But they must not lead to failure at any operating time. In order to determine the conditions under which an elastomer fails in consequence of long operating time, it seems to be necessary to focus on how fatigue cracks grow within the sample. According to fracture mechanics, the conditions at the crack tip are essential for the fatigue crack propagation process. A fatigue crack grows and propagates means exerting a mechanical force. If the crack length reaches a critical value, the fatigue crack propagation becomes unstable and happens with a high speed. The critical crack length and critical load are therefore the principal characteristics governing the fatigue and damage behaviour of elastomer composites [149].

Within the scope of this thesis, the principal emphasis is placed on describing how fatigue cracks propagate within the rubber matrix. If the elastomer composite contains a crack of a size c, the fatigue crack can propagate when the sample is subjected to mechanical stress. By a tensile load, the crack propagates perpendicular to the crack plane. Such crack opening mode corresponds to mode I of the fracture mechanics. A. A. Griffith developed a thermodynamical approach for deformable bodies to describe how cracks propagate under the effect of cyclic mechanical loading. He studied the energy balance in a cracked body during crack propagation. He assumed that the plastic zone at the crack is small enough compared to the crack length and the sample dimensions [150,151].

According to Griffith, the energetic break criterion states that in order to initiate and maintain quasistatic crack propagation in a conservative system, the energy release rate provided must be greater than the dissipated fracture energy per crack area. If a material under mechanical stress starts deforming, it stores elastic energy. As a result, the breaking resistance can be locally exceeded and thus a crack is initiated from crystal defects and micro-voids. A transition from a stationary to a moving crack takes place. If the crack propagates further, it

further relieves the material under stress and releases energy to move forward the opening edge. Beyond a certain limit, the energy released is sufficient to open more and more the crack. The crack propagation continues until the material, in a catastrophic case scenario, tears. The energy balance established by Griffith results from a balance between the elastic strain energy relieved and the interfacial energy of the crack; the energy required to open it [150,151].

The energy balance for the case of crack propagation in an infinitely extended plate of finite thickness was first discussed by Griffith [150]. According to Griffith, the crack propagation occurs when the elastic strain energy W_e, released by elongation of the crack, is equal to or greater than the surface energy W_0 required in order to create the fracture surfaces. This can be expressed as follows:

$$W_e \geq W_0 \tag{74}$$

The criterion of unstable crack propagation is

$$\frac{dW_e}{dc} \geq \frac{dW_0}{dc} \tag{75}$$

The elastic strain energy W_e is defined as

$$W_e := \frac{\pi c^2}{E} \sigma^2 \tag{76}$$

where c is the crack size, σ is the mechanical stress and E is the modulus of elasticity. The surface energy W_0 is

$$W_0 = 4c\gamma_0 \tag{77}$$

where γ_0 is the surface tension [149, 152]. The crack grows if the elastic strain energy W_e is at least two times larger than the surface tension γ_0 [153]. The Griffith criterion of crack propagation leads to the following relationship:

$$2\frac{\pi c}{E} \sigma^2 \geq 4\gamma_0 \tag{78}$$

An existing fatigue crack can propagate without any external energy supply. According to the equations (74), (76) and (77), the critical tension required for the crack propagation is

$$\sigma_c := \sqrt{\frac{2E\gamma_0}{\pi c}} \tag{79}$$

The associated critical crack length is

$$c_0 := \frac{2E\gamma_0}{\pi\sigma^2} \tag{80}$$

Fatigue crack growth curves and life prediction can be obtained from a cyclic fracture mechanics tests. Test specimens can be examined under real conditions using a tear fatigue analyser [154]. Figure 29 illustrates the experimental results. Paris et al. found that the crack growth rate in elastomers was related to the magnitude of the tearing energy [155]. The crack growth rate corresponds to the change in the crack length as a function of load change. It is

given in differential form dc/dn, where dc is the crack propagation and n is the number of loading cycle. The Paris-Erdogan law is expressed as follows

$$\frac{dc}{dn} = B.T^{\beta} \tag{81}$$

B and β are material-dependent constants. T is the tearing energy and is calculated as follows

$$T = \frac{2\pi}{\sqrt{\lambda}} c\, W_e \tag{82}$$

where λ is the stretching ration, c is the crack length and W_e is the elastic strain energy available for the crack to propagate. A double logarithmic plot of a crack propagation curve is shown in Figure 29. The crack growth rate is plotted against the tearing energy T.
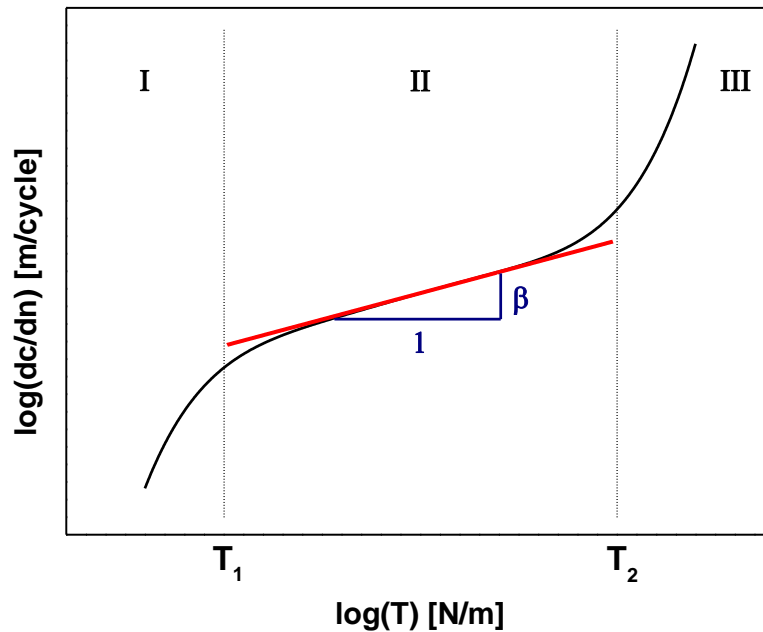
Figure 29: Illustration of the Paris-Erdogan law. Fatigue crack growth in elastomer composites

Three regions in the crack propagation curve can be discerned. The lower limit of the curve is determined by the threshold value of the tearing energy T_1. If the tearing energy is smaller than T_1, the fatigue crack cannot propagate. T_1 represents the lower limit of the crack propagation curve until which the sample is fatigue endurable. In the subsequent region II, the influence of the mechanical stress dominates. In this area a linear progression of the crack growth curve can be observed [156, 157]. It can be approximated by the Paris-Erdogan law presented in equation (81). Region III marks the transition to brittle violent cracking. The upper limit T_2 indicates the stress at which the crack propagation becomes unstable.

5   Experimental methods

This chapter is devoted to the different experimental methods used for the preparation and characterisation of MSE. In a pre-investigation phase the reinforcement potential of the different magnetic fillers used have been determined using the static volumetric gas adsorption. The sample preparation begins with mixing the different components and ends after the curing process. The preparation of isotropic or anisotropic MSE additionally requires the presence of an external magnetic field generated by a coil system during the vulcanisation. Different testing methods are then conducted to characterise the viscoelastic properties of MSE.

5.1   Static volumetric gas adsorption measurements

The method of static volumetric gas adsorption serves to characterise the surface of fine particles and dispersed solids. This technique makes use of the fact that reference gas molecules can be adsorbed onto the surfaces of the sample to be tested. At a constant temperature, a pressure drop can then be measured. From the pressure difference, the adsorbed gas volume can be determined. If more and more gas is gradually led to the measurement cell, the pressure increases in turn. The dependence of the adsorbed gas volume $V(p, T)$ on the partial gas pressure p at a given temperature T can be used to create adsorption isotherms. For this purposes the gas adsorption measuring unit BELSORP-max from BEL Japan Inc is used. Before starting a measurement, the magnetic filler was first pre-treated. It was annealed in a controlled vacuum atmosphere at $100\,°C$ for three hours in order to remove any possible deposits like water and other impurities. During the gas adsorption measurement, the classic BET gas nitrogen with a boiling point at $77\,K$ was used [106].

5.2   Sample preparation

5.2.1   Mixing

The mixing process aims to ensure the finished product homogenous properties despite the use of multiple components. The mixing process was carried out using the laboratory internal mixer Haake PolyLab OS from Thermo Scientific. It consists of a motor unit connected to a mixing chamber with a mixing volume of $60\,ml$ and a filling level of $70\,\%$. The chamber is electrically heated and the internal temperature can be partially regulated by means of air cooling. The mixing geometry is two Banbury rotors that work tangentially. During the mixing process, torque, rotational speed, mixing chamber temperature and the temperature of the mixture are recorded.

The mixing process was performed on different steps. Rubber, magnetic filler and silane were first mixed together to obtain a chemical bonding between polymer chains and filler particles. The so-called silanisation process was carried out at a constant temperature ranging between $130\,°C$ and $135\,°C$ for 10 minutes by adapting the rotor speed. The other additives except the curing system were than added. The crosslinker was mixed at the end on a roller mill by room

temperature to ensure that curing reactions only starts in the heat press and not during the mixing process.

5.2.2 Vulcanisation in a magnetic field

Rubber became a valuable technical product only after the hot vulcanisation process, introduced by the American Goodyear in 1839. It still remains the most important vulcanisation process for standard and conventional rubbers [76].

The vulcanisation process is the thermally induced setting up of the filler network and chemical crosslinking of the polymer chains. It was characterised by the vulcameter MDR 2000 from Alpha Technologies. The required torque is measured at a deflection angle of $0.5\,°$, which corresponds approximately to a deformation of $6\,\%$, and a frequency of $1.67\,Hz$. The curing temperature for all prepared samples was $150\,°C$. The real part of the torque S' is evaluated and the so-called t_{90}-time is determined. It is the time at which S' reached $90\,\%$ of its maximum value. This time serves as basis for determining the vulcanisation time of the samples to avoid any reversion, thermal ageing and/or over-crosslinking. The effective vulcanisation time is the t_{90}-time plus one minute for each one millimetre sample thickness.

The samples were cured in an electrical heating press from Wickert & Söhne at 300 bar pressure and a vulcanisation temperature of $150\,°C$. The vulcanisation was achieved in the presence of an external magnetic field delivering anisotropic MSE composites with filler particles oriented in the direction of the magnetic field. Isotropic MSE composites having homogenous filler dispersion were obtained when no magnetic field was applied. The magnetic field was generated by two square-shaped magnetic coils enclosed by an iron core as shown in Figure 30. A nearly uniform magnetic field of about $0.3\,T$ was measured with an unfilled vulcanisation mould at $23\,°C$. The MSE melts were filled in a vulcanisation mould made of aluminium plates $300\,mm$ x $300\,mm$ x $2\,mm$ with a central quadratic cavity of $100\,mm$ x $100\,mm$ x $2\,mm$. The field strength is set by the magnitude of the electrical current flowing through the solenoids and is probably slightly modified during the vulcanisation process taking place at $150\,°C$. The magnetic field strength will be reduced at this high temperature. However, an increasing magnetic field strength is expected due to the bundling of magnetic field lines going through the magnetic rubber sample more readily than the surrounding mould made of aluminium with low magnetic susceptibility $\chi = 2.4 \times 10^{-5}$. Due to this geometrical construction, the exact value of the magnetic field strength in the rubber sample remains unknown [106-107].
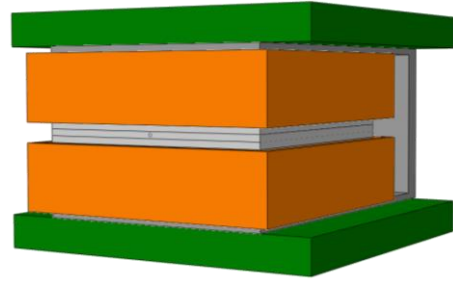
Figure 30: Schematic of the curing setup for the preparation of anisotropic MSE during vulcanisation in an electrical heating pres. Horizontal iron plates, **10 mm** thick, and a vertical iron block, **30 mm** thick, form a closed magnetic core are coloured in grey. The magnetic coils are shown in orange. The heating press is displayed in green. The vulcanisation mould is labelled with a circle, its thickness is **2 mm** and it is not true to scale.

The natural rubber used was a high-grade pale crepe rubber. The different synthetic rubbers used were supplied by Lanxess AG Germany. Keltan 4450 is an amorphous EPDM containing 52 wt.% ethylene and 4.3 wt.% ENB [158]. Perbunan 3945 is a medium-viscous NBR with 39 wt.% acrylonitrile [159]. Therban 3467 is a partially saturated HNBR with 34 wt.% acrylonitrile. It has a residual double bonds content of 5.5 wt.%, which makes it suitable for sulphur crosslinking [160]. Therban XT is a carboxylated HNBR (XHNBR). It contains 33 wt.% acrylonitrile and 3.5 wt.% residual double bonds [161]. A medium-viscous solution SBR containing 25 wt.% styrene and 25 wt.% vinyl is used [162]. For sample identification, the rubber designations are abbreviated as described in Table 5.

Table 5: Rubber abbreviation

Type	Abbreviation
EPDM	E
HNBR	H
NBR	N
NR	NR
SBR	S
XHNBR	X

Further, the MSE samples are labelled "XaYbZ". X designates the rubber type as presented in Table 5. Y and Z label the filler used in hybrid filler systems. "a" and "b" are natural numbers representing the filler fraction in vol.% respectively. If just one filler is used, the additional designation Yb is omitted. One sample is prepared without silane and received at its end the additional term \Si. Depending on the orientation of the magnetic filler particles, the letters A or I is added for anisotropic or isotropic samples respectively. A general overview of the different compositions of the sample prepared is given in Table 6.

Table 6: Composition of the samples in vol.%

Sample	Rubber	TDAE	Sunpar	DOP	CIP	MAGSILICA	CB	Silica	Si69	6PPD	IPPD	St.acid	ZnO	S	CBS	DPG
E20C	51	-	23	-	20	-	-	-	3.6	1.3	-	0.5	0.4	0.3	0.7	-
H20C	49	-	-	24	20	-	-	-	3.8	1.4	-	0.5	0.4	0.2	0.7	-
N0	63	-	-	33	0	-	-	-	0	1.9	-	0.7	0.6	0.3	1.0	-
N06C	58	-	-	30	6	-	-	-	1.6	1.7	-	0.6	0.5	0.3	0.9	-
N13C	53	-	-	28	13	-	-	-	2.9	1.6	-	0.6	0.5	0.3	0.8	-
N20C	48	-	-	25	20	-	-	-	3.9	1.4	-	0.5	0.4	0.2	0.7	-
N28C	43	-	-	22	28	-	-	-	4.6	1.3	-	0.4	0.4	0.2	0.6	-
N36C	37	-	-	19	36	-	-	-	5	1.1	-	0.4	0.3	0.2	0.4	-
NR20C	49	-	24	-	20	-	-	-	3.7	1.4	-	0.5	0.4	0.2	0.7	-
NR20C03P	51	-	25	-	20	-	0.8	-	0.4	1.4	-	0.5	0.4	0.2	0.7	
NR20C05P	50	-	25	-	20	-	1.3	-	0.4	1.4	-	0.5	0.4	0.2	0.7	
NR20C07P	50	-	24	-	20	-	1.8	-	0.4	1.4	-	0.5	0.4	0.2	0.7	
S0	72	22	-	-	0	-	-	-	0	-	1.2	1.4	0.4	0.6	1	0.6
S05C	67	20	-	-	5	-	-	-	3.5	-	1.2	1.3	0.3	0.5	1	0.5
S10C	63	19	-	-	10	-	-	-	3.3	-	1.1	1.3	0.3	0.5	0.9	0.5
S10C	60	18	-	-	15	-	-	-	3.1	-	1	1.2	0.3	0.5	0.9	0.5
S20C	56	17	-	-	20	-	-	-	2.9	-	1	1.1	0.3	0.4	0.8	0.4
S20C\Si	58	18	-	-	20	-	-	-	0	-	1	1	0.3	0.4	0.8	0.5
S20M	56	17	-	-	-	20	-	-	3	-	1	1	0.3	0.4	0.8	0.5
S05C15M	56	17	-	-	5	15	-	-	3	-	1	1	0.3	0.4	0.8	0.5
S10C10M	56	17	-	-	10	10	-	-	3	-	1	1	0.3	0.4	0.8	0.5
S15C05M	56	17	-	-	15	5	-	-	3	-	1	1	0.3	0.4	0.8	0.5
S05C15S	56	17	-	-	5	-	-	15	3	-	1	1	0.3	0.4	0.8	0.5
S10C10S	56	17	-	-	10	-	-	10	3	-	1	1	0.3	0.4	0.8	0.5
S15C05S	56	17	-	-	15	-	-	5	3	-	1	1	0.3	0.4	0.8	0.5
X20C	48	-	-	25	20	-	-	-	3.8	1.4	-	0.5	0.4	0.2	0.7	-

5.3 Physicals

The term Physicals is a collective term for different methods of material testing. It includes the destructive stress-strain testing as well as non-destructive hardness, rebound and abrasion tests.

5.3.1 Stress-strain curves

To measure the stress response as a function of strain, the universal tensile tester Zwick Z 010 from Zwick Roell materials testing systems was used. Tensile tests were carried out on S3A-specimens according to DIN 53504. S3A-specimens were prepared from $2\ mm$ thick plates of cured material, placed on sample holder and uniaxial elongated until they break. The measurements were carried out at room temperature with a preload of $0.5\ N$ and a cross-head speed of $200\ mm/min$. Due to sample fluctuations five samples per MSE were measured.

5.3.2 Multihysteresis measurements for fitting with the DFM

Multihysteresis measurements were carried out to complete the quasi-static tensile test. The measurements were performed in a simple shear mode as shown in Figure 32. The sample was measured uniaxial and quasi-static using a universal testing machine from MTS Systems Corporation at a crosshead speed of $1\ mm/min$ [163]. Five deformation cycles per deformation step were performed with increasing deformation maxima. The force was measured as a function of the deformation. This preconditioning leads to stress equilibrium of the elastomer composite. These data can then be fitted and evaluated using the DFM. The multihysteresis measurements were carried out in the presence of an external magnetic field. The intrinsic mechanical properties can then be associated to magnetic properties of the test specimens. Synergy effects were expected.

Figure 31: Multihysteresis measurements for fitting with the DFM. The dynamic mechanical analyser MTS is shown on the left. The measurement setup is depicted on the right.

5.3.3 Shore A hardness

The measurements were carried out with the testing apparatus Frank 38230 from Karl Frank GmbH according to the specifications in DIN 53505. The Shore A hardness represents a characteristic value used for elastomer composites and rubbery materials. It is related to penetration depth of an intender. A spring-loaded pin made of hardened steel is used as an indenter and it has the shape of a truncated cone. It is pressed 3 seconds with a spring force of $12.5 \pm 0.5\,N$ into the specimen. The specimen is a 6 mm thick disc. Each sample is measured at 5 different locations to reduce the sample fluctuations due to possible orientation effects and several dispersion degrees.

5.3.4 Rebound

The rebound elasticity was carried out according to the specifications in DIN 53512 using the Zwick 5109 rebound resilience tester. It is a measure of the elasticity of rubber samples. A pendulum hammer fell free onto the specimen. When it came into contact with the sample, it was deflected. The rebound is the relationship between the fall energy and the recovered energy, derived from the quotient of rebound height to height of fall of the pendulum. Similar to Shore A hardness measurements, the specimen is a 6 mm thick disc.

5.3.5 Abrasion

The abrasion tester from Karl Frank GmbH is used to determine the resistance of elastomers regarding the friction loss according to the specifications in DIN 53516. Test sample moves along a $40\,m$ long path under a defined pressure with a constant speed. An abrasive sheet with defined attack strength is used. The volume loss of the MSE samples determines the abrasion resistance. The sample is a $6\,mm$ thick disc and has a diameter of $16\,mm$.

5.4 DMTA testing instruments

The DMTA testing instruments used are based on off-resonance forced oscillation method. The sample is subjected to a static and dynamic load, generally a sinusoidal pulse. On the basis of the measured force and deformation amplitudes, the phase angle and the complex module can be determined. The measuring modes used for DMTA measurements are shown in Figure 32. The tensile and/or compression mode is presented at the left. The picture at centre shows the double shear mode. The torsion mode is depicted on the right.
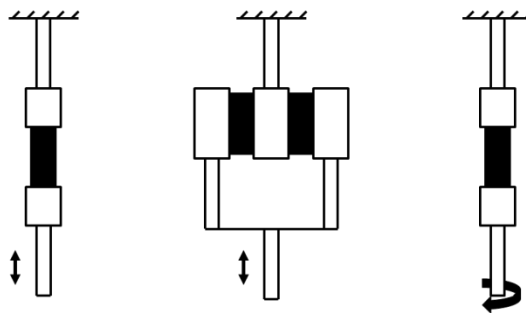
Figure 32: Measuring modes used for dynamic-mechanical thermal analysis

Temperature-frequency sweeps were performed with the advanced rheometric expansion system (ARES) from Rheometric Scientific TM on $30\ mm$ long, $10\ mm$ wide and $2\ mm$ thick strip samples. ARES is pictured in Figure 33. The samples were measured in torsion under constant normal force of $1\ N$. The deformation is controlled by a motor unit located at the lower part of the device and the shear stress is recorded via a transducer located at the upper part of the device [164]. The complex shear modulus G^* and the loss factor $\tan\delta$ are determined as a function of the temperature and frequency. The deformation amplitude is kept constant at $0.1\ \%$. The temperature ramp was driven from low to high temperatures, from $-80\ °C$ to $60\ °C$ with temperature increment of $5\ °C$ in the area of glass transition and $10\ °C$ otherwise. Low temperatures were controlled by means of liquid nitrogen while high temperatures are achieved by using heating elements. For each temperature step, a frequency sweep from $0.01\ Hz$ to $10\ Hz$ was performed. For every test temperature, a soak time of $10\ °C$ is maintained to attain thermal equilibrium of the sample with the ambient temperature.

Figure 33: The rotational rheometer ARES.

Strain sweeps were carried out with Eplexor® $500\ N$ from Gabo Qualimeter Testanlagen GmbH. The strain-sweeps were performed in a shear mode using a double sandwich sample holder as shown in Figure 34. No static preload is needed and previous damage of the sample is avoided. Dynamic deformation is generated by a separate electrodynamic oscillator [165]. The dynamic amplitude ranged between $0.01\ \%$ and $100\ \%$ at constant frequency of $1\ Hz$ and room temperature. The specimens consist of two discs, $2\ mm$ thick with a diameter of $20\ mm$, glued to the sample holders.

Figure 34: The dynamic mechanical analyser Eplexor® 500 N is shown on the left. The measurement cell is shown on the right.

5.5 Crack propagation behaviour: Tear fatigue analyser

The fracture mechanics properties of MSE samples were investigated by analysing the dynamic crack growth rate under cyclic loading. The measurements were performed with a tear fatigue analyser (TFA) from Bayer/Coesfeld. The samples were analysed in tensile mode. Strain amplitude of 15 % and frequency of 10 Hz were kept unchanged over the entire measuring time. The investigations were carried out under pulsed loading with a pulse length of 50 milliseconds. The TFA allows the simultaneous testing of up to 10 samples. Each loading and unloading cycle is recorded separately for each sample. The detection of crack length occurs automatically and is achieved over the entire period of the test by determining the crack contour length c with a CCD camera. For each individual measuring station, the force F, the deformation x, the elastic strain energy W_e and the crack contour length c are recorded separately [166]. The sample geometry used for fatigue tests is the 65 mm long, 15 mm wide and almost 1.7 mm thick single notched tension sample (SENT). It is shown in Figure 35.
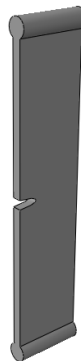
Figure 35: Schematic representation of the single notched tension sample SENT used to characterise the crack propagation behaviour of elastomers

5.6 Magnetorheological measurements

Magnetorheological investigations were carried out with the plate-plate rheometer Physica MCR 501 from Anton Paar GmbH. The rheometer is equipped with a magnetic measuring cell. Physica MCR 501 is able to simultaneously record the dynamic-mechanical and magnetic properties of the samples. Figure 36 shows the setup for combined rheological and magnetic testing as well as the measuring principle [167]. On the left, the picture shows the device for rheological measurements. Magnetic investigations occur in general in closed space in order to bundle the magnetic field lines through the test sample and prevent magnetic losses. This is shown in the middle picture. The schematic picture on the right illustrates the measuring principle.

The measurements were carried out in a shear mode using $2\ mm$ thick discs with a diameter of $20\ mm$. Both melts and vulcanised samples can be characterised in the presence of a magnetic field. While the melts measurements were strain-controlled, i.e. the gap distance was kept constant, the measurements on vulcanised samples were controlled by a constant normal force F_N of $25\ N$. The measurements were performed at a constant shear strain of $0.1\ \%$ and a frequency of $10\ Hz$.

Figure 36: Setup for combined rheological and magnetic testing of elastomer composites. On the left, the device for rheological measurements is shown. Magnetic investigations occur in closed space shown in the middle picture in order to prevent magnetic losses [**167**]. On the right, the measuring principle is schematically drawn.

The direction of shearing was perpendicular to direction of the magnetic field. To examine the magnetorheological relaxation behaviour of the MSE, an on-and-off switching mode of the magnetic field was applied. Measurements on melts were realised at a constant magnetic field of about $0.74\ T$. The magnetic field was switched on and off alternatingly for several times. It was switched on for $150\ s$ and then switched off for $30\ s$. Measurements on vulcanisates were achieved by a stepwise increase of the magnetic field from $0.2\ T$ to $0.74\ T$. The magnetic field was alternatingly switched on for $100\ s$ and then switched off for $20\ s$ during the total measurement period. During the measurement procedure, a moderate heating of the magnetic cell was observed due to high electrical current controlling the magnetic field. A temperature increase of about $10\ °C$ for the melts and about $2\ °C$ for the vulcanisates was seen.

5.7 Combined rheological and dielectric measurements

The plate-plate rheometer Physica MCR 501 from Anton Paar GmbH can also be equipped with a dielectric measuring cell. The mechanical settings were the same as discussed in the previous section. The additional dielectric spectroscopy allows a frequency and temperature-dependent characterisation of the polarization and conductivity behaviour of MSE samples in the alternating electric field in order to describe their molecular kinetics. Dielectric measurements were performed with a broadband dielectric spectrometer BDS 40 supplied by Novocontrol GmbH. Figure 37 shows the setup for combined rheological and dielectric testing of elastomer composites [168]. Unlike magnetorheological measurements, covering the measurement cell is necessary just for temperature-dependent electrorheological analysis.

Figure 37: Setup for combined rheological and dielectric testing of elastomer composites [**168**]. The four thin cables connect the lower and upper plates of the measurement cell to dielectric spectrometer in order to create a dielectric closed loop.

The structure of the dielectric analyzer is based on the measuring principle of the capacitive electric field. The sample to be examined is located between two electrodes. This forms a sample capacitor. The electrical field was a set parameter while the frequency and temperature were free variables. The measured quantities were the amount of electrical impedance and the phase between the alternating current and the AC voltage. A complex conductivity and a complex permittivity can be derived for the sample in the plate capacitor.

In the impedance spectroscopy of materials, the AC voltage $u(t)$ with a frequency f has the following form:

$$u(t) = Re\left(U^* \, e^{i\omega t}\right) = U_1 \cos(\omega t) \tag{83}$$

A phase-shifted current $i(t)$ with the same frequency f and a phase angle φ is generated. It looks as follows:

$$i(t) = Re\left(I^* \, e^{i\omega t}\right) = I_1 \cos(\omega t + \varphi) \tag{84}$$

At low voltage amplitude of $U_0 = 1\,V$, the sample polarization remains linear and there is no need to consider high harmonics since the response signal is a pure sine wave. The impedance takes the following form:

$$Z^* := \frac{U^*}{I^*} \qquad (85)$$

The complex capacity C^* can be then expressed as

$$C^*(\omega) = - \frac{i}{\omega Z^*(\omega)} \qquad (86)$$

The dielectric response of the sample is evaluated from the sample cell impedance and the sample geometry. It can be expressed through the sample dielectric function

$$\varepsilon^*(\omega) = \varepsilon' - i\varepsilon'' \qquad (87)$$

or its specific conductivity

$$\sigma^*(\omega) = \sigma' - i\sigma'' \qquad (88)$$

The complex dielectric function is related to complex capacity C_p^* by

$$\varepsilon^*(\omega) = \varepsilon' - i\varepsilon'' = \frac{C^*(\omega)}{C_0} = - \frac{i}{\omega Z^*(\omega)} \frac{1}{C_0} \qquad (89)$$

where C_0 is the empty cell capacity. The specific conductivity is defined as

$$\sigma^*(\omega) = \sigma' - i\sigma'' = i\omega\varepsilon_0(\varepsilon^*(\omega) - 1) \qquad (90)$$

where ε_0 is the vacuum permittivity [169].

Results and discussion

6 Characterisation of filler particles by static volumetric gas adsorption technique

In order to identify the mechanical reinforcing potential of the filler in the final elastomer composite, the polymer-filler interaction should be characterised. The static volumetric gas adsorption technique enables the determination of interaction between filler particles and a test gas. If a high surface activity of the filler particles is observed with the test gas, a high interaction between polymer chains and filler particles in crosslinked samples is expected.

Static volumetric gas adsorption measurements have been carried out using the instrument BELsorp max from BEL Japan Inc to characterise the morphological structure and surface activity of filler particles. The standard test gas used here is nitrogen N_2. The amount of gas adsorbed on the surface of the magnetic filler particles is determined as a function of pressure. Before starting a measurement, the test sample has been pretreated at $100\ °C$ in a vacuum for three hours. A pressure range between $p/p_0 = 10^{-6}$ and $p/p_0 = 1$ was considered by recording the adsorption isotherms. The surface activity of the filler was determined by evaluating the adsorption isotherms at low pressure $p/p_0 = 10^{-6}$. The low pressure area is important in the analysis of heterogeneities on the surface of filler particles. Due to the small number of gas molecules, the first molecules will attach to the sites of the surface that have the highest interaction energies. The specific surface area is an additional parameter for the characterisation of fillers and it is determined using the BET theory. The specific surface area is mainly determined by the size of the primary particles at a pressure range between $p/p_0 = 0.1$ and $p/p_0 = 0.3$. The surface activity and the specific surface area are needed and mostly sufficient to determine the mechanical reinforcing potential of the filler. In some cases, the filler particles have a high specific surface area. But, they show a very low reinforcing potential. This is then explained with a very low surface activity.

Figure 38 shows the N_2-adsorption isotherms for the fillers MAGSILICA, CIP, N 550 (carbon black) and U 7000 (silica). The relative pressure-dependency of surface coverage is shown in a double logarithmic plot. The surface coverage is defined as adsorbed N_2-amount V divided by the monolayer amount V_m and is a measure of the surface wetting. The monolayer volume V_m is the volume which occupies exactly one monolayer on the filler surface and it is obtained according to the Brunauer, Emmett and Teller model.

For a relative pressure of $p/p_0 = 10^{-4}$, the surface coverage is around 6.7 % for CIP, 16.5 % for MAGSILICA, 23 % for N 550 and 27.3 % for U 7000. Compared to the other fillers, CIP shows the lowest amount of adsorbed nitrogen. This behaviour is also retained for the entire measurement. This proves that CIP has the lowest surface activity in this filler pool.

This outcome is related to the surface finish of the different filler. The surface area of CIP is covered by polyhydric alcohols. The surface area of MAGSILICA consists of a silicon dioxide layer with the molecular formula SiO_2. The surface area of N 550 consists mainly of

graphitic nano-crystallites. The surface area of U 7000 consists of siloxane $(Si - O - Si)$ and a high amount of silanol groups $(Si - OH)$ [106, 107].
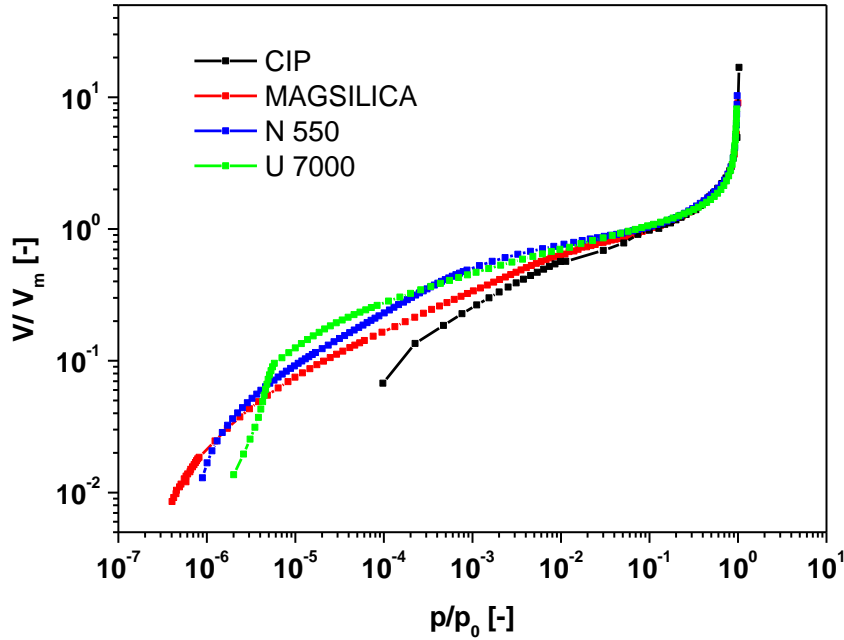
Figure 38: N_2-adsorption isotherms of different fillers, as indicated. The surface coverage V/V_m is plotted as function of the relative pressure p/p_0. The monolayer volume V_m is obtained according to BET theory.

The specific surface area of the different fillers is obtained using the BET model. It maps out the ability of the filler particles to agglomerate, an important prerequisite to determine the mechanical reinforcement of the samples. The specific surface area of CIP is $0.4\ m^2/g$. It is two orders of magnitude smaller than the specific surface area of MAGSILICA, which is by almost $54\ m^2/g$. Therefore, MAGSILICA particles have a larger tendency to agglomerate than CIP particles. It may be expected at this point that the mechanical reinforcement potential is high for MAGSILICA compared with CIP. The specific surface area of N 550 is $39\ m^2/g$. The specific surface area of U 7000 is $162.5\ m^2/g$ [106, 107].

7 Mechanical properties and ageing behaviour

7.1 Physicals

The mechanical properties of elastomer composites can be characterised by different mechanical tests. This kind of testing is a punctual measurement and is used to measure and observe material behaviour over a short period of time. The measuring parameters are fixed and remain unchanged over the entire measuring time. Such measurements are often used for first orientation to quickly get an idea of the sample reaction to an applied force or deformation.

Figure 39 summarises the results obtained for anisotropic SBR samples filled with the magnetic filler CIP. The CIP content varies from 5 vol. % to 20 vol.%. The amount of the other components was kept constant. Hardness Shore A, Rebound and DIN abrasion are considered.
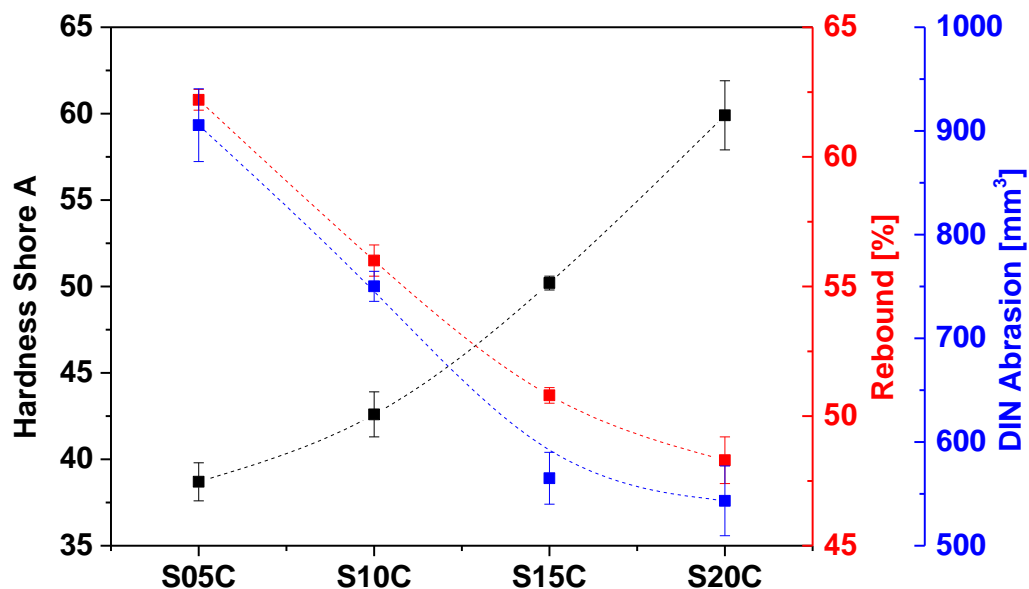
Figure 39: Mechanical testing for anisotropic SBR samples with different magnetic filler content at room temperature.

The measure of the hardness Shore A is the penetration depth of an intender, a truncated cone, by applying a constant force. The sample S05C with 5 vol.% CIP shows a hardness of about 38 Shore A. Increasing the magnetic filler content increases the hardness of the sample. It reaches 60 Shore A for the anisotropic sample S20C with 20 vol.% CIP. This behaviour is explained by the different hardness values of rubber and magnetic filler. The magnetic filler is a solid body. The polymer chains of rubber are much softer by far. The more magnetic filler in the sample is, the harder the MSE sample is.

This findings can also be connected to the elasticity of the samples. The more rubber in the sample compared to filler is, the more elastic is the sample. This behaviour can be confirmed by rebound measurements. The energy balance before and after the impact can be determined using a rebound resilience tester. The potential energy of the pendulum hammer in the starting position can be derivated from its height. After the impact, the pendulum hammer reaches a lower height level. This process describes an inelastic collision, in which some kinetic energy is dissipated. The rebound resilience is determined from the difference in the height. This constitutes a qualitative measure of the elasticity of the material investigated. Figure 39 shows that the anisotropic sample S20C reaches a rebound value of about 62 %. Decreasing the magnetic filler content leads to more elastic samples. These findings are consistent with the results obtained from previous hardness measurements

The analysis of wear behaviour of elastomer components is of high interest to manufacturers in rubber industry. Several mechanisms are usually involved in the wear process at the same time, but with different proportions. Elastomers show first the mechanisms of abrasion and fatigue wear, followed by crack initiation and crack growth. The wear behaviour of elastomers depends not only on the material properties and sample composition, but also on the interactions that occur with another friction partner and the level of mechanical stress. Wear is therefore a system property and not an intrinsic material property. The DIN abrasion test is preferably used due to the simplicity of the sample preparation and the experimental procedure. Abrasion is generally associated with fatigue, crack resistance and crack growth. It has the advantage that the time required for testing is low compared to other methods. Figure 39 shows that the increasing of the magnetic filler content reduces the abrasion behaviour of the MSE. Indeed, the DIN abrasion goes from $900\ mm^3$ for the anisotropic SBR sample S05C with 05 vol.% CIP to $540\ mm^3$ for the SBR sample 20C with 20 vol.% CIP. This behaviour is very similar to the rebound experiment. The magnetic filler stabilises the rubber matrix and reduces the internal friction. The formation of stable bonds is attributed to multiple contact points between the surface area of the magnetic filler particles and the polymer chains. The elastomer composites become wear resistant.

7.2   Stress-strain curves

Tensile tests are among the most frequently performed static methods in mechanical material testing. They are used to characterise the stiffness and deformation behaviour of a test sample in uniaxial elongation. The material behaviour is examined with increasing load. The load is usually applied slowly and steadily increasing until the specimen is broken. These formal conditions are known as quasi-static tensile testing.

During a tensile test, the force F and the sample deformation x are registered simultaneously. Plotting the measured force against the resulting deformation creates a force-elongation diagram of the investigated material. If the geometric parameters of the specimen like initial length and initial cross section are considered, a stress-strain curve can be derived.

Different factors can affect the stress-strain behaviour of MSE samples. Besides the internal microstructure of the samples, the choice of magnetic filler itself, the filler-polymer and the filler-filler interactions are of crucial importance. The filler content can additionally be very decisive. The following subsections are dedicated to the examination of those factors and which influence they may have on the stress-strain behaviour of the MSE.

7.2.1   Influence of particle size

MSE samples were prepared on the basis of SBR with 17 vol.% DOP as plasticiser. The crosslinking system consisted of sulphur and the two vulcanisation accelerators CBS and DPG. The microscaled CIP and the nanoscaled MAGSILICA were used. The magnetic filler fraction was kept constant at 20 vol.%. The silanisation was taken into account. The samples were vulcanised with and without external magnetic field to prepare anisotropic and isotropic MSE respectively. Uniaxial tensile tests have been performed with the cured S3A-specimens to evaluate the mechanical reinforcement potential of the different magnetic filler systems. Figure 40 shows the stress-strain behaviour of the different samples at room temperature.
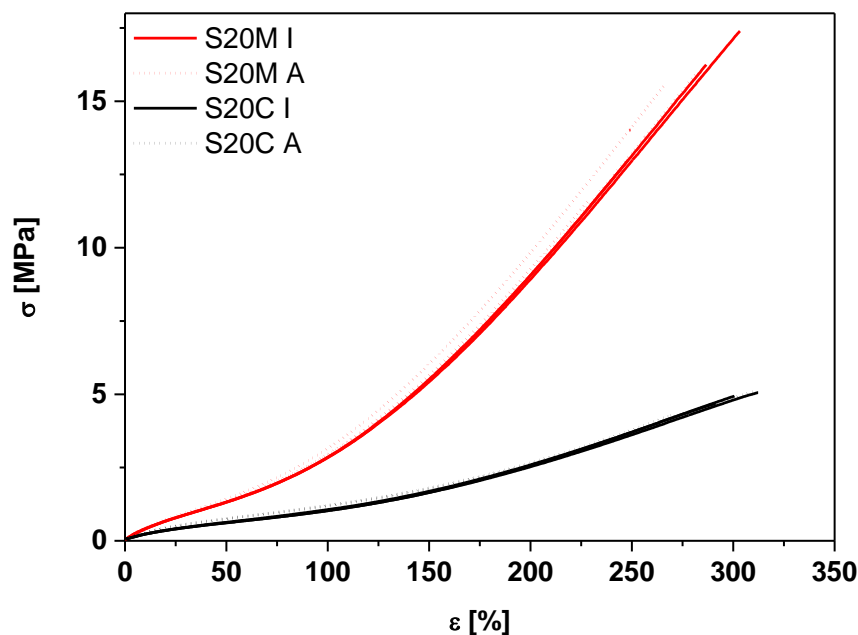
Figure 40: Stress-strain curves at room temperature for isotropic (full lines) and anisotropic (dashed lines) SBR-samples with **20** vol.% magnetic fillers.

The MAGSILICA filled SBR samples show high stress values than the CIP filled samples. The isotropic sample S20M I with 20 vol.% MAGSILICA shows stress-strain behaviour similar to conventional reinforcing fillers like silica or carbon black. The stress-strain curves start with a low slope and a typical upturn to higher stress values. The stress-strain curves of the isotropic sample S20C I with 20 vol.% CIP is more flat and the stress values become smaller at the same deformation. At a strain of 300 %, the MSE composites filled with 20

vol.% MAGSILICA show a stress value of about 17 MPa while the samples filled with 20 vol.% CIP show a significantly smaller stress value of just 5 MPa. These stress values are typical for nanoscaled and microscaled filler particles.

This difference is explained by a better filler networking of the nanoscaled MAGSILICA particles compared to microscaled CIP particles. The mechanical reinforcement potential is attributed to the formation of a physically bonded filler network and to strong polymer-filler couplings. MAGSILICA with a specific surface area of $54 \, m^2/g$ provides the polymer chains a larger surface area to adhere compared to CIP with a specific surface area of $0.4 \, m^2/g$. Additionally, the coupling reactions of the silane with the magnetic filler during mixing and with the polymer chains during the vulcanisation establish a strong chemical bonding at the polymer-filler interface. Due to the surface finish, the polymer-filler interface is larger with MAGSILICA than with CIP. For these reasons, MAGSILICA provides better networking features necessary for mechanical reinforcement than CIP [106, 107]. This behaviour confirms the findings that the filler networking is promoted by the particle size as discussed by Vilgis et al. [170].

No effect of the orientation of the magnetic filler particles is found on the stress and strain values of the SBR samples because the loading direction was perpendicular to the magnetic filler strings.

7.2.2   Variation of filler loading

MSE composites were prepared on the basis of NBR and the magnetic filler CIP. The silanisation was taken into account. The silane content has been adjusted to magnetic filler volume fraction. The plasticiser TDAE was used. The crosslinking system consists of sulphur and the vulcanisation accelerator CBS. The samples were vulcanised with and without external magnetic field in order to prepare anisotropic and isotropic MSE respectively. Uniaxial tensile tests have been performed with the cured S3A-specimens to evaluate the mechanical reinforcement potential of the different magnetic filler systems. The stress-strain curves for the isotropic and anisotropic NBR samples with different filler volume fractions at room temperature are depicted in Figure 41.
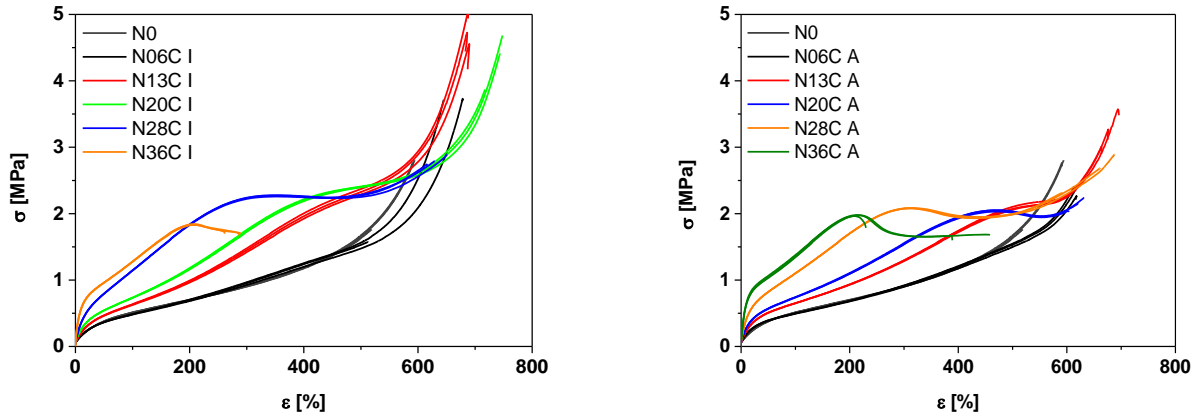
Figure 41: Stress-strain curves at room temperature for isotropic (right) and anisotropic (left) NBR samples with different filler volume fractions.

Considering first the filler concentration, a systematic increase of stress values as well as tensile strength with increasing CIP content for the isotropic MSE is observed until a critical filler amount of about 20 vol.% is reached. A maximum stress value of about 5 MPa and a maximum extensibility of 750 % were attained for the isotropic N20C. The anisotropic MSE do not follow this tendency. They show the highest stress and extensibility values for the sample N13C with 13 vol.% CIP.

Concerning the entire domain of the stress-strain curves for both isotropic and anisotropic MSE, two different behaviours can be observed depending on the magnetic filler amount of the samples. While the stress-strain curves for the unfilled MSE look quite usual, the stress-strain curves for the filled MSE are rather uncommon for elastomer composites showing at about 2 MPa a yield-like behaviour. Obviously, the filler morphology is not affecting this significantly. Accordingly, the yielding behaviour is probably related to the formation of voids due to a detachment of the polymer chains from the filler surfaces. The voids grow as the strain increases and a more or less pronounced plateau with a constant stress arises [171].

Previous work has shown rather common stress-strain curves without yielding if non-polar rubber were used [106, 107]. The present behaviour may thus be associated with the polarity of the rubber matrix. Indeed, the polar acrylonitrile groups of polymer chains interact with the polar hydroxyl group of the magnetic filler particles due to the available permanent dipoles. A physical bonding between the polymer chains and the filler particles based on dipole-dipole forces can be built. This is relatively weak in comparison to the chemical bonding between the polymer chains and the filler particles due to the use of silane. Accordingly, it appears that the silanisation reaction was not sufficient for getting a reasonable chemical bonding. One reason could be the large number of the acrylonitrile groups (39 %) that cannot react with the silane. Nevertheless the physical bonds may contribute to the established network and improve the mechanical properties of the MSE. The yield point could, thus, indicate that the interaction between the polar groups of polymer chains and the magnetic filler fails if a critical stress of the samples is reached.

To investigate the influence of the polarity of rubber on stress-stress behaviour of MSE, additional four different samples were prepared with a constant CIP concentration of 20 vol.%. The different rubbers show different polarities. A non-polar EPDM (E), a weakly polar NR, a polar HNBR (H) and a very polar XHNBR (X) were used. The stress-strain curves for the isotropic and anisotropic samples at room temperature are illustrated in Figure 42.
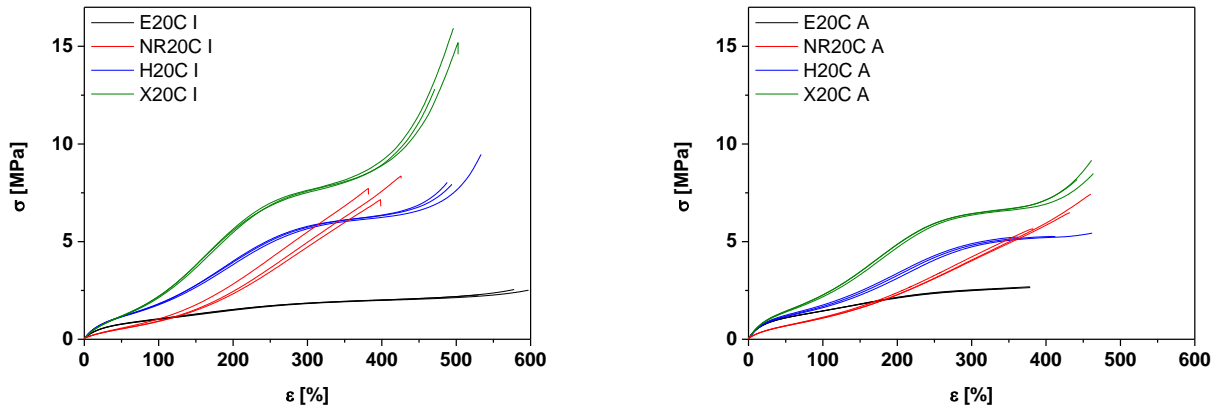
Figure 42: Stress-strain curves at room temperature for isotropic (right) and anisotropic (left) samples on the basis of different rubbers with different polarities. The CIP volume fraction is kept constant at **20** vol.% for all samples.

Figure 42 confirms the measurement findings for the polar NBR samples. It seems that the polarity of rubber plays a crucial role in the stress-strain behaviour of the MSE composites.

7.2.3   Influence of coupling agent

MSE composites were prepared with an without silane on the basis of SBR and 20 vol.% CIP. The plasticiser DOP was used. The crosslinking system consists of sulphur and the two vulcanisation accelerators CBS and DPG. The samples were vulcanised with and without external magnetic field in order to prepare anisotropic and isotropic MSE respectively. Uniaxial tensile tests have been performed with the cured S3A-specimens to evaluate the reinforcement potential of the different magnetic filler systems. The stress-strain curves for the isotropic and anisotropic samples with and without silane at room temperature are illustrated in Figure 43.
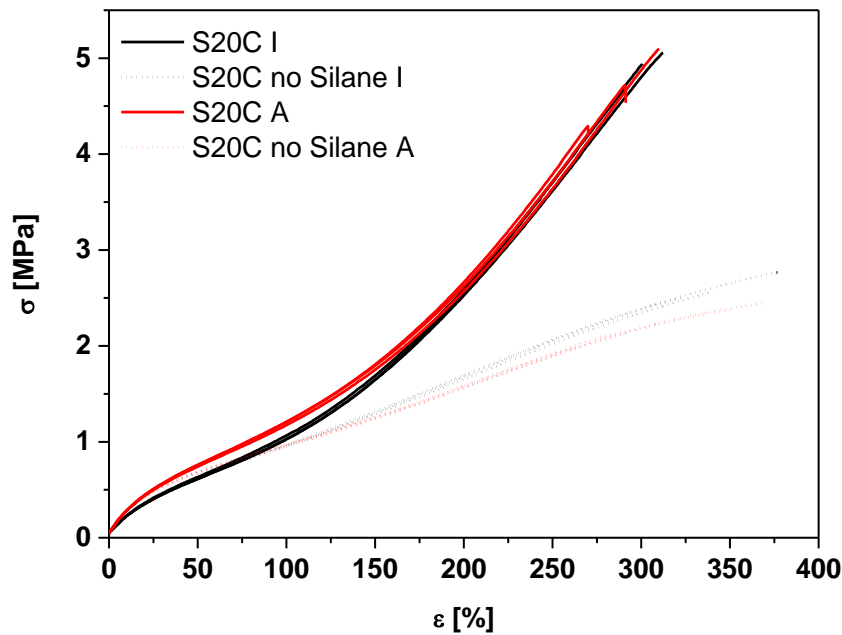
Figure 43: Effect of silane on stress-strain curves at room temperature for silanized (full line) and non-silanized (dashed line) SBR samples including the effect of particles orientation.

The silanized samples show higher stress values compared to non-silanized ones. This indicates that a larger chemical polymer-filler coupling is realized with silane. The interaction between the polymer chains and the polyol-coated CIP particles is enhanced. This leads to a better distribution of magnetic filler particles in the sample and thus to a high mechanical reinforcement.

The orientation of magnetic filler particles does not play a major role under uniaxial loading because the columnar CIP strings are perpendicular to the tensile direction [106, 107].

7.3 Dynamic-mechanical thermal analysis

Dynamic-mechanical thermal analysis is used to characterise the rheological behaviour of elastomer composites. Similar to the stress-strain behaviour of MSE, the dynamic-mechanical behaviour of MSE is affected by several factors. In addition to the choice of magnetic filler, the magnetic filler content and the filler-polymer interaction, the internal microstructure of MSE plays for the dynamic-mechanical analysis a key role compared to quasistatic stress-strain curves. All these aspects are evaluated in the following subsections.

7.3.1 Vulcanisation in a magnetic field

Elastomer composites are produced by curing the rubber component with a crosslinking system in a heating press. The crosslinking is a chemical reaction in which the polymer chains are linked by means of sulphur into a three-dimensional network. The vulcanisation process substantially improves the stiffness values and it is aimed to meet the required mechanical

properties of elastomer composites. If the curing process takes place in the presence of an external magnetic field, the internal distribution of the magnetic filler particles within the rubber matrix can be strongly influenced. This depends on the strength of the magnetic field. Anisotropic samples with oriented magnetic filler strings are then realised.

The analysis of the amplitude dependence of the storage modulus G' at room temperature is sufficient to provide insights in how the internal microstructure of elastomer composites looks like. MSE composites were prepared on the basis of SBR and the magnetic filler CIP. The samples were vulcanised with and without external magnetic field in order to prepare anisotropic and isotropic MSE respectively. For the preparation of anisotropic samples, 3 different magnetic field strengths were applied: $0.08\,T$, $0.11\,T$ and $0.2\,T$. Strain sweeps in shear mode for SBR samples cured with different magnetic field strengths at room temperature and a frequency of $1\,Hz$ are shown in Figure 44. The orientation of the magnetic filler particles was perpendicular to the shearing direction.
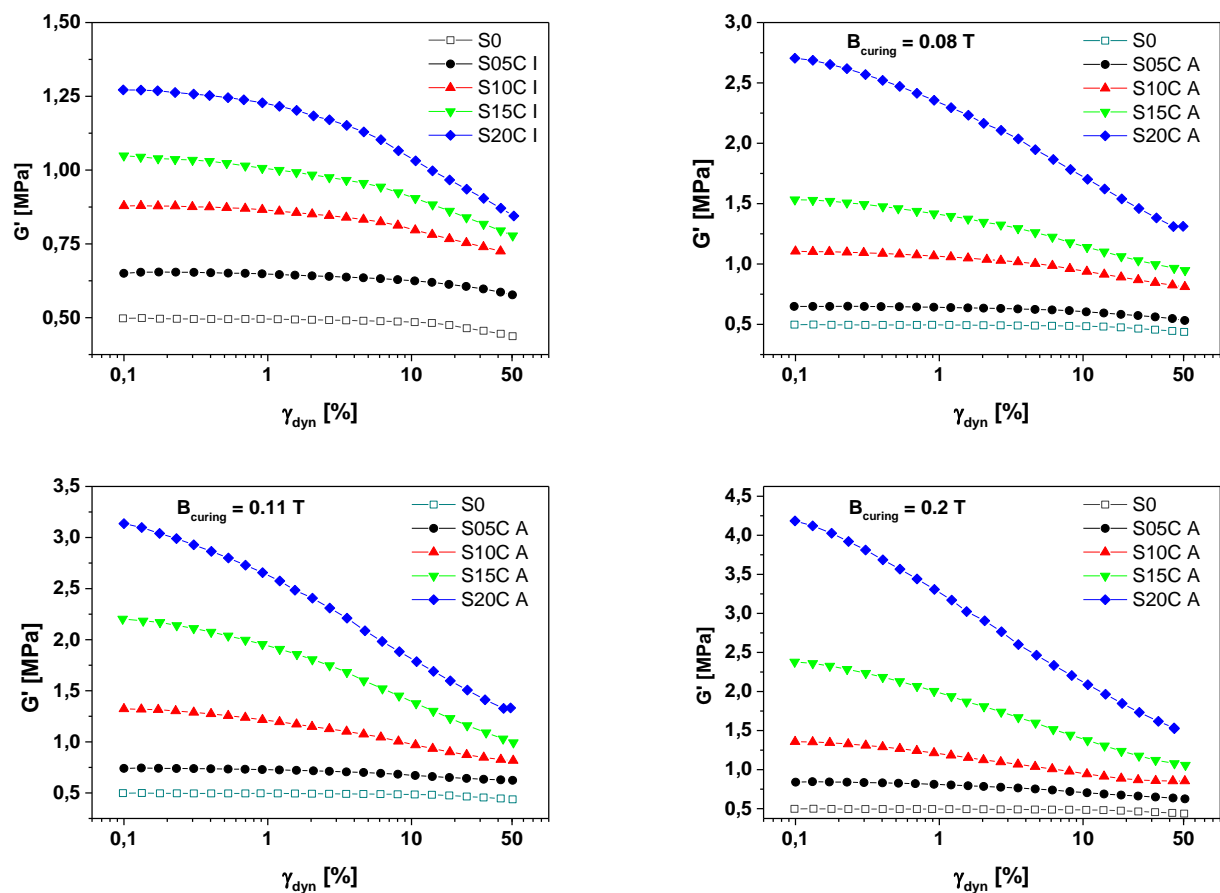
Figure 44: Amplitude dependence of the storage modulus at $\mathbf{23\,°C}$ and a frequency of $\mathbf{1\,Hz}$. Measurement results for isotropic SBR-samples in the top left corner. Measurement results for anisotropic SBR-samples cured with a magnetic field of $\mathbf{0.08\,T}$, $\mathbf{0.11\,T}$ and $\mathbf{0.2\,T}$ are shown in the top right, bottom left and bottom right corner respectively.

Obviously, all MSE samples show a Payne effect [172]. The strain storage modulus continuously decreases with increasing the strain amplitude. This indicates a continuous

breakdown of the magnetic filler network. The storage modulus G' increases systematically with increasing the CIP content. The magnetic filler particles build together larger filler clusters and create a stiffer magnetic filler network. This stabilises the polymer matrix and delivers improved mechanical properties.

In order to examine the effect of orientation of the magnetic filler particles, the samples containing the same filler concentration are compared. The isotropic MSE samples were cured without magnetic field. A maximal storage modulus G' of 1.3 MPa at a strain amplitude of 0.1 % is measured for the sample S20C I with 20 vol.% CIP. The storage modulus G' increases significantly for anisotropic samples. It is quite obvious that the higher the magnetic field during curing is, the higher is the storage modulus. The anisotropic sample S20C A with 20 vol. % CIP has a storage modulus G' of 4.2 MPa at a strain amplitude of 0.1 %, when it is cured at $0.2\ T$.

The increase of the storage modulus of the MSE samples can be associated with the interaction strength between the magnetic filler particles and the applied magnetic field during curing. According to equation (19), increasing the strength of the magnetic field increases the magnetic energy available. This leads to a better alignment of the magnetic filler particles along the magnetic field lines. The magnetic filler particles within a string come closer to each other. This increases the anisotropic shape of the filler network and promotes the mechanical reinforcement of MSE samples. A columnar structure is created. The particle distribution Φ of the magnetic filler depending on the strength of the magnetic field during curing is depicted in Figure 45. The magnetic filler strings become narrower and longer when the magnetic field during the vulcanisation B_z increases.
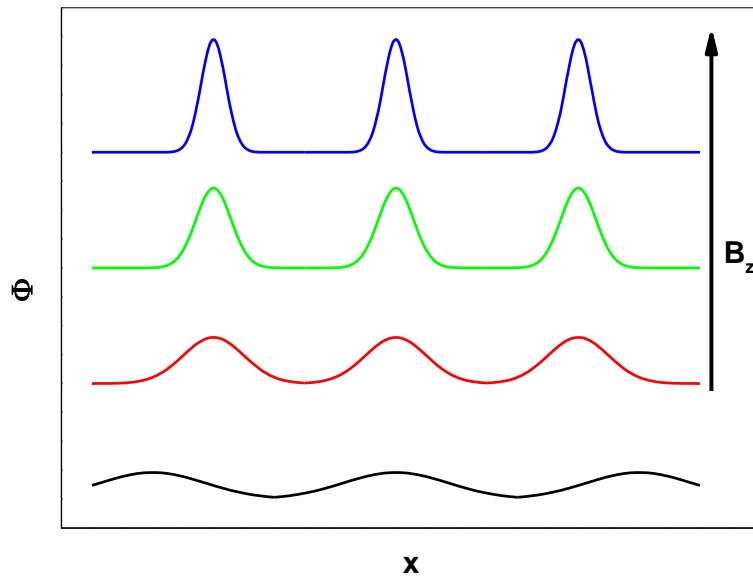
Figure 45: The particle distribution of the magnetic filler depending on the strength of the magnetic field during curing.

7.3.2   Influence of particle size

In order to evaluate the influence of the size of the magnetic filler particles on the dynamic-mechanical properties of MSE, SBR based MSE samples with a constant magnetic filler fraction of 20 vol.% were prepared on the same way as discussed in section (7.2.1). The microscaled CIP and the nanoscaled MAGSILICA were used again. The samples were vulcanised with and without external magnetic field to prepare anisotropic and isotropic MSE respectively. Strain sweeps in shear mode have been performed. The orientation of the magnetic filler particles was perpendicular to the shearing direction. Figure 46 shows the amplitude dependence of the storage modulus of the different MSE samples at room temperature and a frequency of $1 \; Hz$.
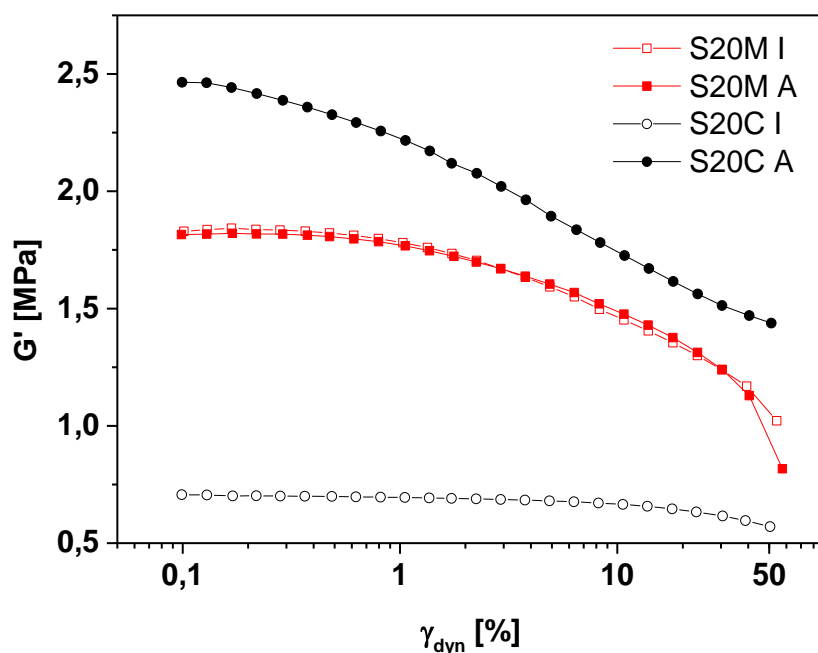
Figure 46: Amplitude dependence of the storage modulus at room temperature for isotropic and anisotropic SBR samples with **20** vol.% magnetic fillers, indicated with empty and full symbols respectively.

Both MSE composites show more or less pronounced the Payne effect. For the samples filled with MAGSILICA, the strain storage modulus G' of the isotropic SBR samples decreases faster with increasing the strain amplitude than G' of the isotropic CIP filled samples. This behaviour shows that the mechanical reinforcing potential for the nanosized magnetic filler is much higher compared to that of the microsized magnetic filler. As discussed earlier, the magnetic filler network becomes stiffer when the size of the magnetic filler particles gets smaller.

Considering the orientation of the magnetic filler particles, the strain storage modulus G' increases substantially for the anisotropic sample S20C with 20 vol.% CIP due to anisotropy. G' increases nearly threefold at a shear strain value of 0.1 %. G' is less affected for the anisotropic sample S20M with 20 vol.% MAGSILICA. The orientation effect in a magnetic field appears to be more significant for the microscaled CIP particles than for the nanoscaled MAGSILICA. This is related to the alignment ability of magnetic filler particles along the magnetic field lines during the curing process. These spatial orientation skills are promoted by the particle size. In fact, the microsized particles deliver sufficient attraction in an external magnetic field and get slowly saturated than the nanosized ones. Earlier works confirmed this behaviour [102, 103]. Magnetic microscaled particles contribute more strongly to mechanical stiffness of the MSE samples than the magnetic nanoscaled ones.

7.3.3 Variation of filler loading

Dynamic-mechanical measurements were performed in order to analyse the influence of the magnetic filler volume fraction on the viscoelastic properties of the MSE. NBR based MSE samples with different magnetic filler content were prepared on the same way as discussed in section (7.2.2). The samples were vulcanised with and without external magnetic field in order to prepare anisotropic and isotropic MSE respectively. Strain sweeps in shear mode have been performed to evaluate the mechanical reinforcement potential of the different magnetic filler systems. The orientation of the magnetic filler particles was perpendicular to the shearing direction. The strain-dependent storage moduli of the isotropic and anisotropic MSE at room temperature and a frequency of 1 Hz are illustrated in Figure 47.
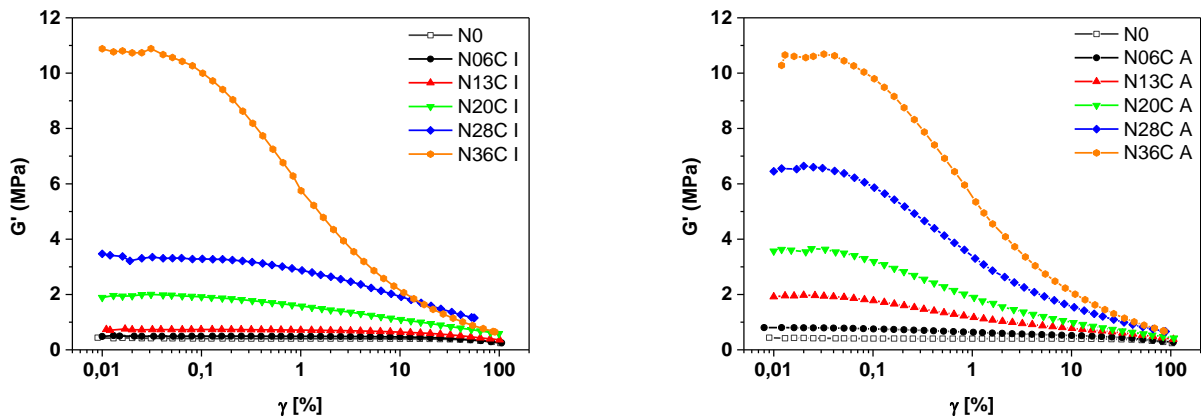
Figure 47: Amplitude dependence of the storage modulus of isotropic (right) and anisotropic (left) NBR samples at room temperature for different filler volume fractions.

The storage modulus of all MSE decreases with increasing the strain amplitude. This indicates a breakdown of the magnetic filler network. Accordingly, all samples show a more or less pronounced Payne effect. The storage modulus G' increases systematically with increasing the CIP content. During the vulcanisation process, the magnetic filler particles create a stiffer filler network. This stabilises the polymer matrix and delivers improved mechanical properties. Considering the effect of orientation of the magnetic filler particles, all anisotropic MSE except the samples N36C, show higher storage moduli at the same concentration. The relative increase of G' due to the orientation of the magnetic filler particles at a dynamic shear strain of 0.02 % is listed in Table 7. This can be associated with the arrangement of the magnetic filler particles during the curing process in anisotropic strings, which delivers a pronounced contribution to the stiffness of the MSE samples. Obviously the spatial distribution of the filler particles does not affect the dynamical behaviour of the MSE samples N36C with 36 vol.% CIP because the volume fraction of rubber and the magnetic filler are almost equal in this case. This implies that the mobility of the polymer chains is strongly restricted. This shows that the filling of the MSE cannot increase indefinitely. Otherwise, the curing with an external magnetic field does not really affect the dynamic-mechanical responses of the samples [171].

Table 7: Characteristic values of the storage modulus of the MSE samples due to orientation of magnetic filler particles at a dynamic strain of **0.02** %. The indices '*I*' and '*A*' stand for isotropic and anisotropic samples, respectively.

	G'_I [MPa]	G'_A [MPa]	$\Delta G'$ [MPa]
N0	0.42	0.42	0.00
N06C	0.49	0.80	0.31
N13C	0.75	1.95	1.20
N20C	1.94	3.60	1.66
N28C	3.37	6.53	3.16
N36C	10.70	10.70	0.00

Next, the response of the MSE samples regarding dynamic deformation at higher frequencies is taken into consideration. Temperature-frequency sweeps at small deformation and different temperatures within a limited frequency range were measured. These series of isothermal branches of the frequency-dependent shear modulus were horizontally shifted along the logarithmic frequency axis to generate master curves. The time-temperature superposition principle according to the Williams, Landel and Ferry approach relating the frequency and temperature dependency of viscoelastic materials above the glass transition temperature T_g is used.

The master curves of storage and loss moduli G' and G'' as well as loss factor $\tan \delta$ for both isotropic and anisotropic MSE samples are presented in Figure 48. The reference temperature T_{ref} was 20 °C. The WLF parameters derived from the horizontal shifting have the following values $C_1 = 4.64$ and $C_2 = 88.89$ °C. The associated shift factors and the corresponding WLF-fit are depicted in Figure 49, demonstrating that the WLF equation (33) fits well the data for temperature T higher than the glassy transition temperature $T_g \approx -35$ °C.

Considering the frequency dependency of the storage moduli shown in Figure 48, the elastic plateau, also known as the rubbery plateau, covers the low frequency or high temperature part of the master curves. It reaches out over 5 frequency decades, which range between $3.6 \ 10^{-4} \ Hz$ and $10^2 \ Hz$. The rubbery plateau is followed by the glass transition domain. This covers the frequency range between $10^2 \ Hz$ and $10^8 \ Hz$. The slope of the master curves below the glassy plateau increases with increasing frequency or decreasing temperature. At lower temperature, the MSE samples become stiffer and begin to lose gradually their elasticity. An important characteristic of the polymer dynamic within this frequency range is the glass transition temperature. It stands at almost -35 °C and represents the lowest conceivable operating temperature for the NBR based MSE [171].
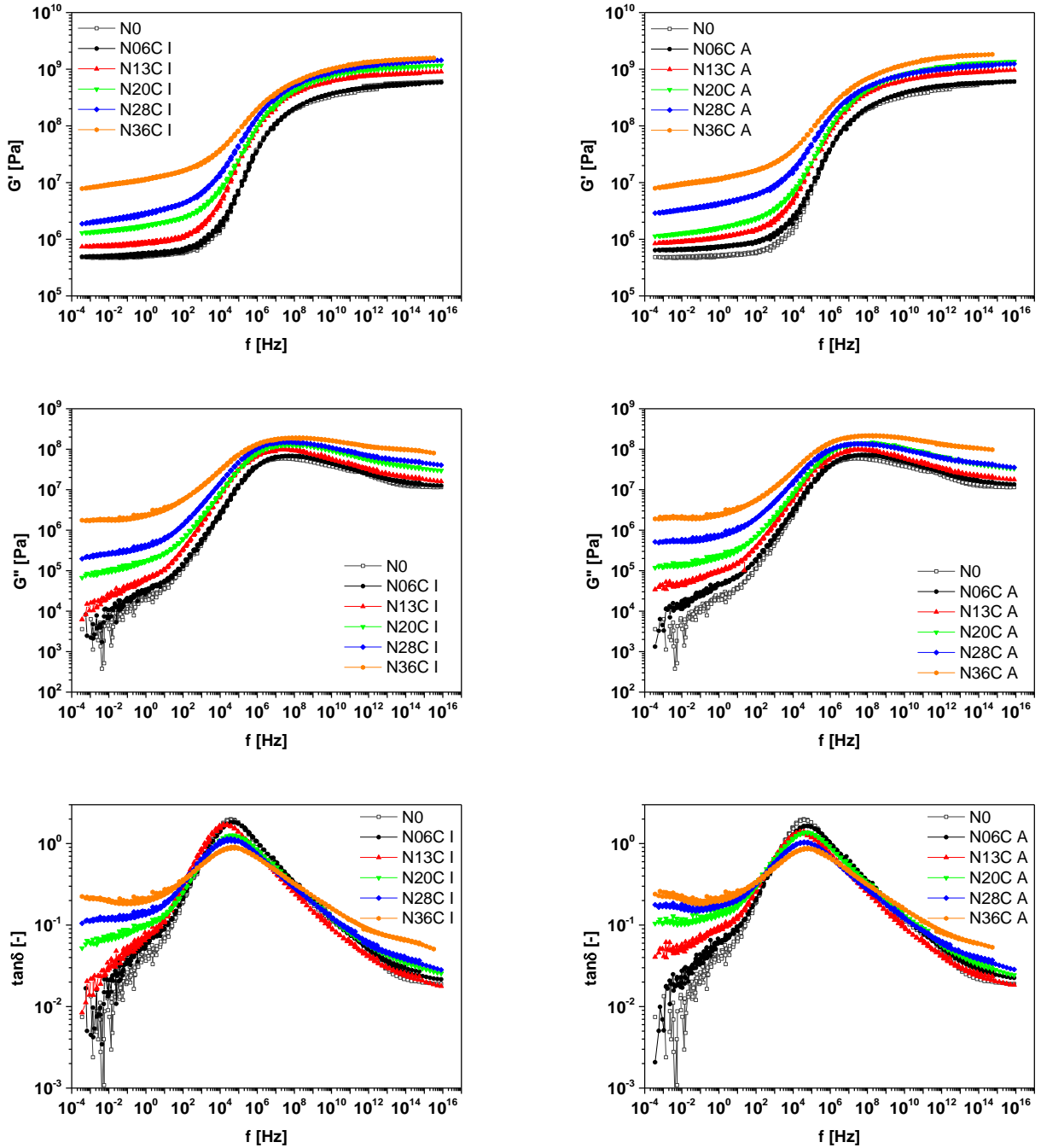
Figure 48: Viscoelastic master curves of the MSE at a reference temperature $T_{ref} = 20\,°C$. Isotropic samples are shown on the left and anisotropic samples on the right. Storage moduli are shown at the top, loss moduli at the centre and loss factor at the bottom.

The master curves for both isotropic and anisotropic MSE samples show a similar behaviour as conventional carbon black- or silica-filled samples. In the rubbery plateau, the slope of the master curves of storage moduli G' increases with increasing the filler loading. This is characteristic for the networking potential of the filler particles. Regarding the effect of orientation of the magnetic filler particles, slightly larger storage and loss moduli for the

anisotropic MSE samples are observed. This is related to the columnar structure of CIP, which delivers an additional contribution to the stiffness and hysteresis of the samples.

The glass transition frequency at $20\,°C$ is located at about $10^5\,Hz$ as deduced from the maximum of the loss factor $\tan\delta = G''/G'$. It is important to note that the magnetic filler content and the effect of orientation do not affect T_g. This behavior remains similar for the maximum of $\tan\delta$, since it is not shifted. The loss factor $\tan\delta$ shows a pronounced increase of energy dissipation with the filler loading in the rubbery plateau and less pronounced increase in the glassy state while the maximum decreases. This behaviour is similar to conventional carbon black- or silica-filled samples [171].
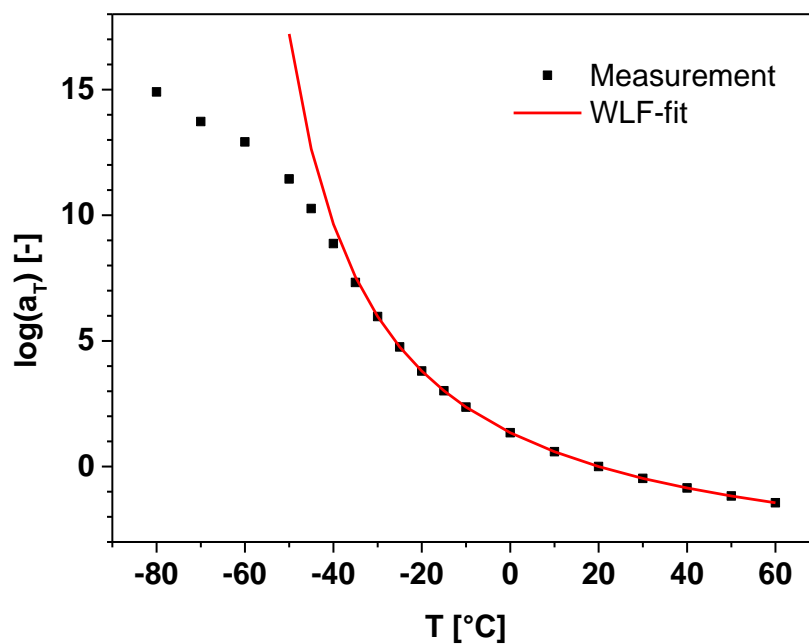
Figure 49: Shift factors of the NBR samples obtained by horizontal shifting of the isothermal branches of the frequency-dependent loss factor $\tan\delta$ (symbols) and the corresponding WLF-fit (line) according to equation (33)

7.3.4 Influence of coupling agent

In order to examine more closely the influence of silane on the magnetically induced flocculation during the curing process, dynamic-mechanical investigations were performed. The orientation of magnetic filler particles was perpendicular to the shearing direction. The strain-dependent storage moduli of MSE composites with and without silane are presented in Figure 50.
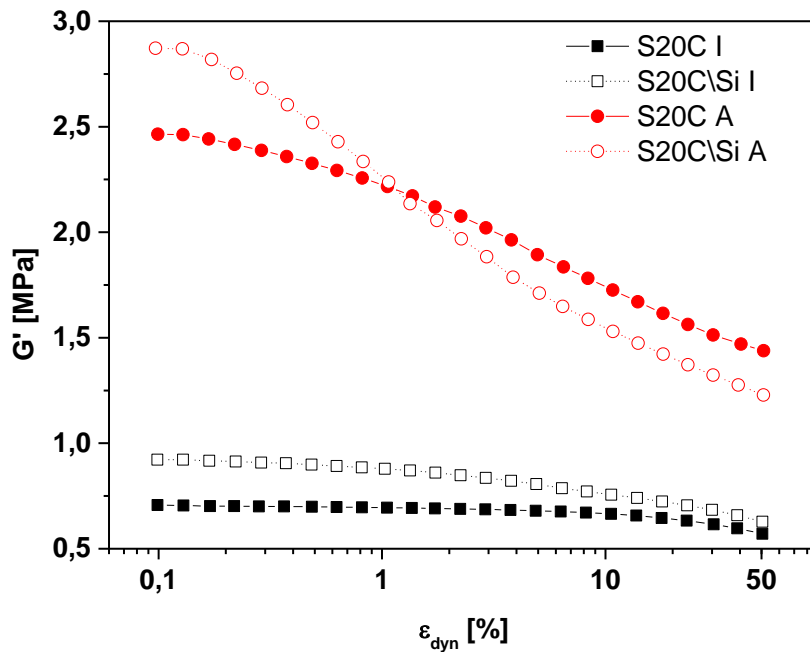
Figure 50: Effect of silane on the amplitude dependence of the storage modulus (Payne effect) at room temperature for silanized (closed symbols) and non-silanized (open symbols) SBR samples including the effect of particles orientation.

All MSE samples show a more or less pronounced Payne effect. The storage modulus G' decreases with increasing the shear strain due to continuous breakdown of the filler network. Figure 50 shows that the storage moduli G' are smaller for silanized MSE composites compared with the non-silanized samples. These results are independent of the orientation of the magnetic filler particles. In addition, G' decreases slower for the silanized samples compared with the non-silanized ones due to increasing strain amplitude. For the anisotropic samples, this even leads to an intersection of the two curves at a dynamical strain of about 1 %.

The observed mechanical performance is explained by the fact that the silane layer at the filler surface acts as a kind of space-holder. This prevents the filler particles to come in close contact and delivers more flexible filler-filler bonds [170]. This is the main reason why the samples with silane are less stiff than the non silanized samples, independently from their orientations. Furthermore, the sulphur units of the silane react during the vulcanisation with the polymer chains leading to a strong chemical coupling between the polymer matrix and the magnetic filler particles. This improves the phase bonding and stabilises the filler network The covalent chemical bonds make the magnetic filler network more stable. [106, 107].

7.4 Fatigue crack propagation and ageing behaviour

Ageing is the totality of chemical and physical changes over time that lead to a change in mechanical properties of the elastomer composites so that their usefulness is reduced in time [173, 174]. These changes can lead to sample failure and the finished product can no longer fulfil its function [175]. The thermal ageing occurs at any time during the manufacturing and operation processes. The fatigue happens when the samples are temporarily or constantly exposed to diverse mechanical loads [176].

At a molecular level, irreversible physical and chemical processes caused by fatigue and ageing occur. These processes include polymer chain scissions, post-crosslinking and reformation of covalent bonds (re-combination). While the polymer chain scission causes a decrease in the viscosity, a post-crosslinking of the material leads to an increase in the stiffness. A combination of both mechanisms can eventually lead to the formation of microcracks that limit the lifetime of the elastomer composites. Materials in which the chain scission process occurs tend to form cracks on the surface. The degree of ageing-related changes depends strongly on the material structure and the ageing conditions such as temperature, time and mechanical stress. The ageing can be divided into an internal and an external ageing. The internal ageing represents the degradation of residual stresses, recrystallisation, phase separation in multicomponent systems (plasticizer migration e.g.). It is caused by thermodynamically unstable states of the rubber material. External ageing phenomena are stress cracking, fatigue cracking, thermo-oxidative degradation or swelling and are caused by complex physical or chemical environmental effects. The fatigue and ageing resistance can be characterised in the context of durability tests. Here, the elastomer composites are subjected to artificial ageing under realistic conditions in order to evaluate the effect of fatigue and ageing on the structure and properties [177].

7.4.1 Mechanical fatigue of magneto-sensitive elastomers

The fatigue crack growth is related to the microstructural inhomogeneity of the test samples and the mechanical load applied. Each material contains microcracks due to manufacturing tolerances. Applying mechanical stresses leads to a local exceeding of the breaking strength and thus to crack initiation. The crack initiation is in principle the transition from an inactive to a moving fracture. Depending on the available elastic energy, the fracture propagates or stops.

As discussed earlier (see section 4.3), the crack propagation is labelled with the crack growth rate. Stable crack propagation is characterised by a relatively low crack growth rate. The cracks keep growing when more and more energy is externally supplied. At higher crack growth rates, the cracks grow faster and can quickly turn into catastrophic regime. The crack propagation becomes unstable.

In order to examine the fatigue crack growth of MSE, experimental measurements were conducted using single notched tension sample SENT and were performed with the TFA. In the fracture mechanical testing of rubber samples, initial cracks are manually introduced with

a razor blade. The initial crack has a length c_0 of about $1 \pm 0.2\ mm$. The aim is to go beyond the least interesting region I in the crack propagation process (see Figure 29). The fatigue crack behaviour of anisotropic EPDM, HNBR and NR based MSE is examined. The magnetic filler content is kept constant at 20 vol.% CIP. For each MSE, three samples are tested to minimize the scattering measurement values. The fatigue crack behaviour of EPDM-based MSE is depicted in Figure 51.
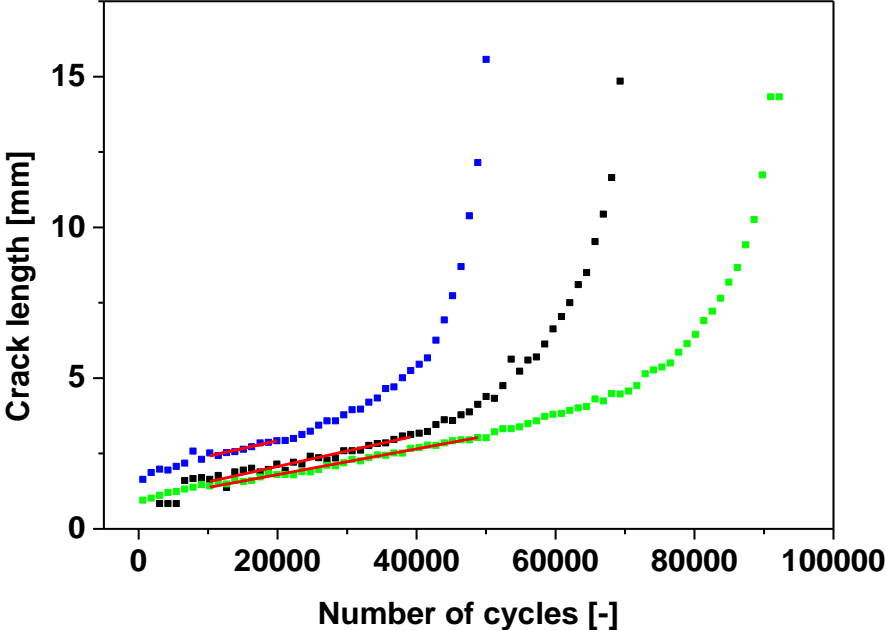
Figure 51: Fatigue crack growth on three anisotropic EPDM based MSE samples at dynamic strain of **15** % and frequency **10 Hz**.

After the crack initiation, fatigue cracks propagate only when the material dependent and critical energy release rate is exceeded. As described above, fatigue cracks grow first linearly. This region is marked by stable crack propagation. This part of the curve can be fitted by a linear straight. The slopes of the curves describe the fatigue crack growth rate dc/dn and are listed in Table 8.

Table 8: Fatigue crack growth rate for three EPDM based MSE filled with **20** vol.% CIP.

Sample	1	2	3
$\frac{dc}{dn}$ [mm/cycle]	$5.11\ 10^{-5}$	$4.27\ 10^{-5}$	$5.14\ 10^{-5}$

The value $5.11\ 10^{-5}\ mm/cycle$ for the first sample means that the fatigue crack grows $51.1\ nm$ per loading cycle. Although the scattering of the measurement data may appear to be too large, it remains acceptable due to inevitable measurement conditions. For technical reasons, the image of the crack opening cannot be completely synchronized with the mechanical loading when the crack reaches a critical size. Indeed, the image recording of the

crack opening takes place although the desired deformation has not yet been reached. This leads to a discrepancy between the optical and mechanical measurement data but only in the critical regime of the fatigue crack propagation.

For further calculations, a mean crack length c for each MSE is taken from the linear range of the fatigue crack growth measurement. The related elastic energy W_{el} is taken from the measurement data and is inserted into the Paris-Erdogan law. This deterministic law relates the crack growth rate with the magnitude of the tearing energy. Double logarithmic plot of the fatigue crack growth rate dc/dn (see equation (81)) in function of the tearing energy T (see equation (82)) is depicted in Figure 52.
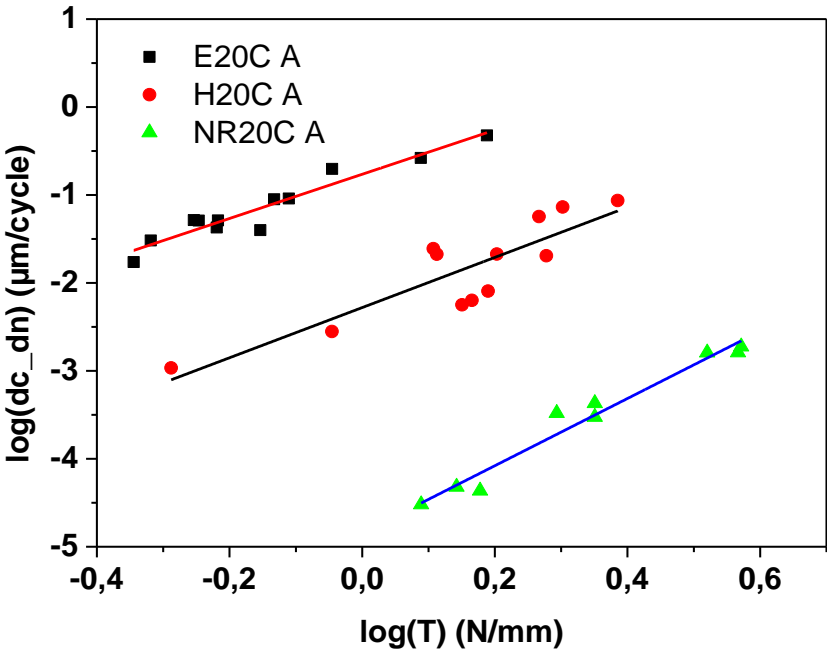
Figure 52: The relationship between the fatigue crack growth rate and the tearing energy for three different anisotropic MSE samples according to Paris-Erdogan law.

The corresponding coefficients B and β of the Paris-Erdogan law for three different MSE samples are summarised in Table 9.

Table 9: The corresponding coefficients B and β of the Paris-Erdogan law for three different MSE

Sample	E20C A	H20C A	NR20C A
$log(B)$	-0.76	-2.28	-4.84
B	0.17	$5.24 \ 10^{-3}$	$1.43 \ 10^{-5}$
β	2.51	2.85	3.82

Obviously, the EPDM-based MSE show the highest fatigue crack growth, followed by HNBR- and NR-based MSE. Figure 52 shows that at a tearing energy of $1.54 \ N/mm$, the fatigue crack propagates with a rate of about $0.48 \ \mu m/cycle$ for the EPDM samples. It is

around $8.06 \, 10^{-3} \, \mu m/cycle$ for the HNBR-based MSE and $4.34 \, 10^{-5} \, \mu m/cycle$ for NR samples. Accordingly, the EPDM samples display the worst values of the fatigue crack propagation compared to HNBR and NR ones. The large crack growth rate for EPDM rubber is the main reason why is not suitable for any dynamic applications. NR confirms with its small fatigue crack growth rate its standing as the most appropriate rubber for dynamic applications. NR owes its outstanding resistance to crack growth to the strain-induced crystallisation (SIC). SIC depends on the loading direction. When the amorphous NR gets stretched at room temperature, the polymer chains become strongly oriented and many of them remains partially immobilized. A lamellar structure emerges within the rubber matrix. This forms additionally separate networks, which are perpendicular to the loading direction. These crystallite networks reduce locally the crack formation and can inhibit the crack propagation in the rubber matrix. SIC increases the stiffness and improves the resistance to crack growth of the NR samples. The values of HNBR samples come somewhere in between. Fatigue cracks in HNBR samples propagate 2 decades slower than in EPDM-based MSE and 2 decades quicker than in NR-based MSE. Nevertheless, HNBR is often used for dynamic applications like NR. It is mainly used in high temperature applications where a good mechanical stiffness is also required. This is the case for timing belts of automotive engines or in the sealing technology.

According to Persson et al [178], the coefficient m from the relaxation time spectra as well as the coefficient β from the Paris-Erdogan law are interrelated as follows:

$$b = \frac{1-m}{2-m} := \frac{1}{\beta} \tag{91}$$

Klüppel showed that the last relationship (equation (91)) is also valid for viscoelastic materials [179]. The coefficient m from the relaxation time spectra as well as the coefficient β from the Paris-Erdogan law are summarised in Table 10. The different models used to describe the mechanical response of rubber and, consequently, to determine these coefficients are mentioned again between the brackets.

Table 10: Summary of the coefficient $\boldsymbol{m}$ from the relaxation time spectra as well as the coefficient $\boldsymbol{\beta}$ from the Paris-Erdogan law. The different models used are mentioned between the brackets.

Sample	E20C A	H20C A	NR20C A
$\boldsymbol{m}$ $(\boldsymbol{H(\tau)})$	0.37	0.56	0.64
$\boldsymbol{b}$	$\boldsymbol{0.38}$	$\boldsymbol{0.30}$	$\boldsymbol{0.25}$
$\boldsymbol{\beta}$ **(Paris-Erdogan)**	2.51	2.85	3.82
$\boldsymbol{1/\beta}$	$\boldsymbol{0.39}$	$\boldsymbol{0.35}$	$\boldsymbol{0.26}$
Relative error [%]	3.16	14.84	0.80

Table 10 shows that the b-values of the different MSE samples, derived from the coefficient m from the relaxation time spectra according to equation (91), are in good agreement with the coefficient β from the Paris-Erdogan law.

For the anisotropic NR and EPDM samples, the evaluation of the relaxation time spectra lead to predict with almost good accuracy the coefficient β. This represents the principal factor to determine the fatigue crack growth rate of the MSE samples. With a relative error of 0.81 % and 3.17 %, the results for NR and EPDM samples are very good. However, the result for HNBR samples show a lager discrepancy with a relative error of 14.84 %.

These relative errors still remain acceptable although the incorrect evaluation of lifetime or crack propagation rate can lead to disastrous consequences for the MSE performance. Errors during the TFA measurements are unavoidable due to the technical design. Errors can also occur by generating the master curves and/or evaluating the relaxation time spectra.

7.4.2   Thermal Ageing of magneto-sensitive elastomers

Diene rubbers are irreplaceable for technical elastomer products exposed to high dynamic loads. The reason lies in the typical molecular inner structure of rubber. Long chain molecules with a very regular structure provide outstanding elastic properties. However, the unsaturated chemical bonds in the polymer backbone make it susceptible to decomposition by ozone and oxygen or a gradual post-crosslinking by radicals, ultraviolet radiation and heat. This leads in the long term to crack formation and ultimately tearing of elastomer composites [76, 173].

Rubber materials degrade by heat treatment. This process may get worse when oxidative reactions take place simultaneously. Rubber components and elastomer composites generally undergo disadvantageous changes during prolonged storage under unfavourable air and temperature conditions due to initiated post-crosslinking and oxidation reactions.

For the experimental analysis of the thermal ageing of MSE composites, SBR samples were prepared with different magnetic filler content. The magnetic filler was the microscaled CIP. Since atmospheric oxygen is a relatively aggressive environment for rubber materials, IPPD was added to make MSE temporary ozone-resistant. Additives slow down the ageing process but they cannot be a permanent solution. IPPD is one of the indispensable additives in the rubber technology. It is used as an antioxidant and antiozonant for statically and dynamically highly stressed elastomer composites like in the tyre sector and in technical rubber articles such as hoses, vehicle moulded parts, cable sheaths and conveyor belts. IPPD continuously accumulates on the rubber surface to prevent the oxidative degradation and crack formation.

The MSE samples were put under normal atmospheric conditions in an oven at a temperature of $100\,°C$ for a maximum term of 28 days. Ageing repercussions and changes in the internal structure of the MSE samples can be reliably evaluated by considering the changes in the elongation at break and tensile strength at break. The measurement results are depicted in Figure 53 and Figure 54 respectively.
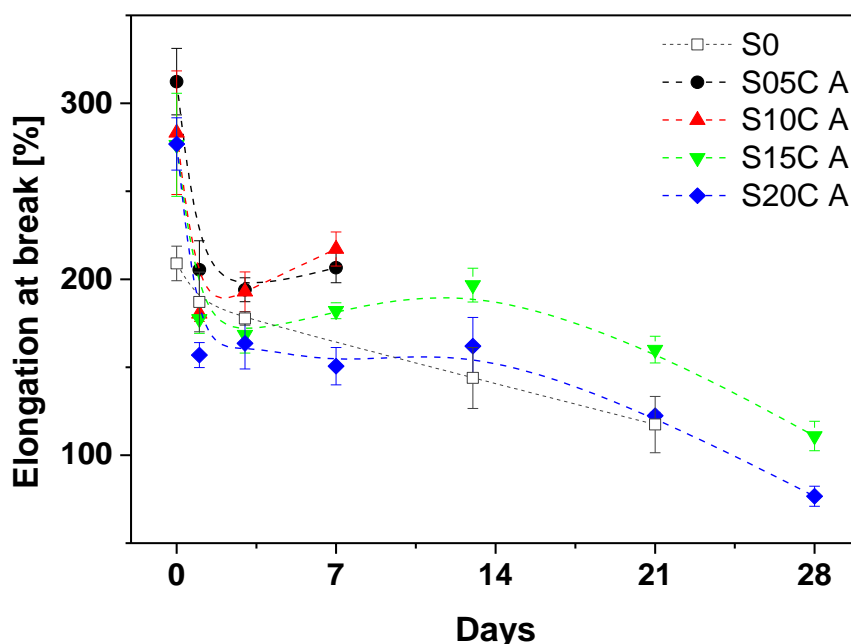
Figure 53: Elongation at break for thermally aged MSE samples with the anti-ageing agent IPPD under air at atmospheric pressure.

The dynamic-mechanical behaviour of MSE can be explained by a shortening of the long polymer chains and continuous post-crosslinking reactions during the ageing process. The drop of the elongation at break for all MSE samples shows that the existing polymer network is constantly destroyed. The reason is that the chemical and molecular bonds are thermally activated. At high temperature, the polymer chains decompose. The MSE samples lose a large part of their restoring force. The crosslinking is also a thermally activated process. If the sulphur is not completely used during the vulcanisation or do not lead to a fully crosslinked structure (see the chemical bond $S_y - R$ and S_z in Figure 7), the sulphur residues may react with the polymer chains and form new crosslinking points. These post-crosslinking reactions make the MSE samples stiffer. However, this often leads the samples to break at relatively low strains [76, 173].

Figure 54 shows that the tensile strength at break increases for all samples. The anisotropic samples S05C A and S10C A with 5 vol.% and 10 vol.% CIP respectively are broken after 7 days. For the sample S15C A and S20C A with 15 vol.% and 20 vol.% CIP respectively, the tensile strength at break increases until the 21st day and then decreases again. This results from the polymer chain scissions and the subsequent softening of the MSE samples.
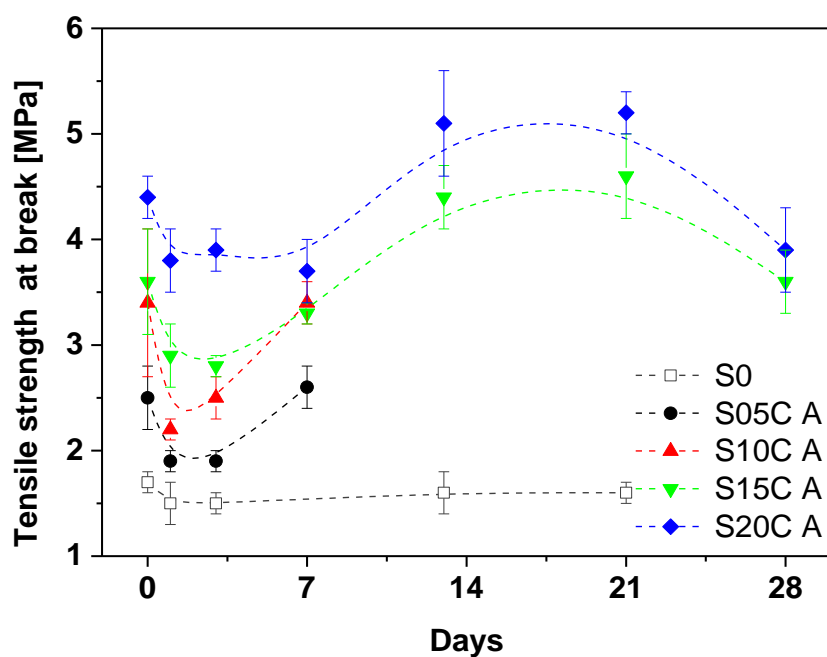
Figure 54: Tensile strength at break for thermally aged MSE samples with the anti-ageing agent IPPD under air at atmospheric pressure.

The changes of the tensile strength σ_{50} at an elongation of 50 % give more insight into the network structure due to post-crosslinking. This is shown in Figure 55. The tensile strength of the anisotropic MSE samples increases with increasing the ageing time period. This indicates that the network density has significantly increased. σ_{50} of the sample S20C A with 20 vol.% CIP tripled from 0.8 MPa to 2.5 MPa after 28 days of thermal ageing.
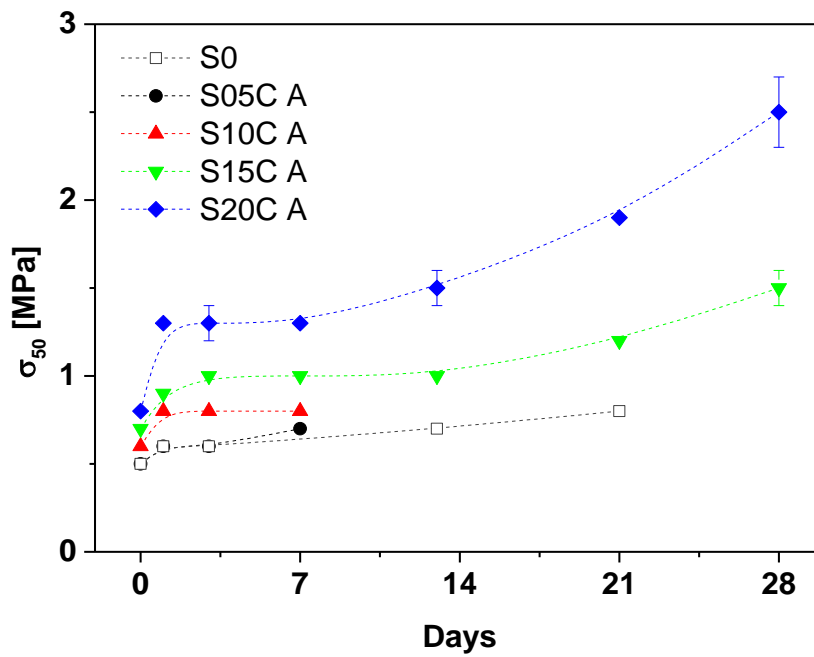
Figure 55: Tensile strength at an elongation of **50** % for thermally aged MSE samples with the anti-ageing agent IPPD under air at atmospheric pressure.

8 Magnetorheology of melts

The effect of particle orientation during the curing process can be observed online by magnetorheological measurements in the non-crosslinked melts. The orientation of the magnetic filler particles in strings along the magnetic field lines expresses itself in a successive increase of the shear modulus, which is measured at small strain amplitudes to avoid disturbance of the system. The storage modulus G' monitors the magnetically induced flocculation of the magnetic filler particles due to their interaction with the magnetic field. To analyse the intensity of the interaction between the magnetic filler particles and an external magnetic field, an on-off switching mode of the magnetic field with alternating polarity is considered. The shearing direction in this experiment is perpendicular to the direction of the magnetic field [106, 107].

The storage modulus G' of a non-crosslinked melt is caused by the physical entanglements of the polymer chains. The crosslinking introduces chemical crosslinking points into the system. In filled systems, the magnetic filler particles provide additional large surface areas in the raw mixture. More stable bonds are formed because more contact points between the surface area of the magnetic filler and the polymer chains are available. An increase in the magnetic filler content thus represents an increase in the surface area offered and an increases of the number of bound polymer chains in the system. In addition, the distances between the several magnetic filler particles are significantly reduced and progressively loose chain ends are built [106, 107].

8.1 Flocculation

The flocculation is a chemical process by which colloids come together to form a compact and uniform mass. In the rubber technology, the flocculation can be understood as the process by which a stable network is created [138, 146]. This is the result of the curing process. The polymer chains, magnetic fillers and additives are linked together through crosslinking systems and organofunctional silanes.

In order to examine the flocculation process, MSE samples were prepared with a constant magnetic filler fraction of 20 vol.% on the same way as discussed in section (7.2.1). The microscaled CIP and the nanoscaled MAGSILICA were used. The silanisation was taken into account. Strain sweeps in shear mode were performed to evaluate the magnetorheological response of the different samples. The magnetic flux density $\boldsymbol{B}$ is $0.74\,T$. Figure 56 shows the magnetically induced flocculation during switching on and switching off the magnetic field at a shear strain amplitude of 0.5 % and an initial temperature of $50\,°C$.
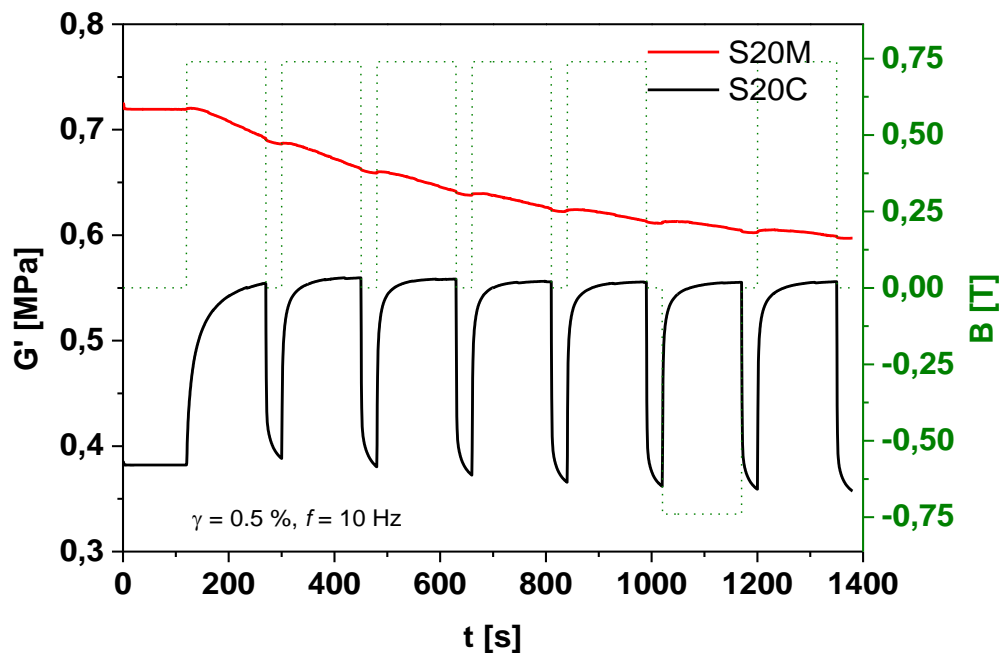
Figure 56: Variation of the storage modulus at shear strain γ of 0.5 % and initial temperature of $50\,°C$ during the switching on and switching off the magnetic field for the SBR-melts with 20 vol.% magnetic fillers.

The MSE sample S20C with 20 vol.% CIP shows a pronounced switching effect compared to the sample S20M with 20 vol.% MAGSILICA. The storage modulus G' increases by more than 40 % once the magnetic field is turned on. The MAGSILICA-filled sample S20M shows hardly any switching effect. Furthermore, S20M shows a continuous decrease of the storage modulus with increasing flocculation time. This is the consequence of the unwanted heating of the magnetic cell during the measurement by about $10\,°C$ after 1400 seconds. This is the general case for filled elastomer composites with nanoscaled fillers, the stiffness decreases considerably with increasing temperature due to thermal activation of the filler-filler bonds. The CIP-filled sample seems little affected by the increase in temperature because there exist two effects, which influence each other. The increase in temperature reduces on the one hand the sample viscosity and, correspondingly, its stiffness. On the other hand, it promotes the orientation of the magnetic dipoles of the magnetic filler particles along the magnetic field lines. Strings of magnetic filler particles are then formed. These structure contribute to an additional mechanical reinforcement of the MSE sample and accordingly, high stiffness values are obtained.

The large switching effect observed for the CIP-filled sample confirms the good interaction of the microscaled magnetic filler particles with the external magnetic field. Obviously, the magnetic moments of nanoscaled MAGSILICA are too small to sufficiently interact with the external magnetic field. Additionally, switching on and off the magnetic field does not affect the maximum of the storage modulus G' of the CIP-filled MSE sample. Not even the polarity

90

change of the magnetic field leads to any improvement. It seems that the induced magnetic dipole are fully saturated.

The MAGSILICA-filled sample shows a larger storage modulus G' than the CIP-filled sample during the entire measurement. This confirms the capacity of nanoscaled MAGSILICA to build a stronger filler network than the microscaled CIP [106, 107].

The relative magnetorheological effect (MRE) represents a relative measure of the switching effect of MSE samples. The MRE is defined as the difference between the initially storage modulus G'_0 when the magnetic field is turned off and the maximum of the storage modulus G'_{inf} once the magnetic field is turned on, divided by G'_0. Mathematically, the MRE can then be expressed as follows:

$$MRE = \frac{G'_{inf} - G'_0}{G'_0} \tag{92}$$

Figure 57 shows schematically how the MRE can be determined.
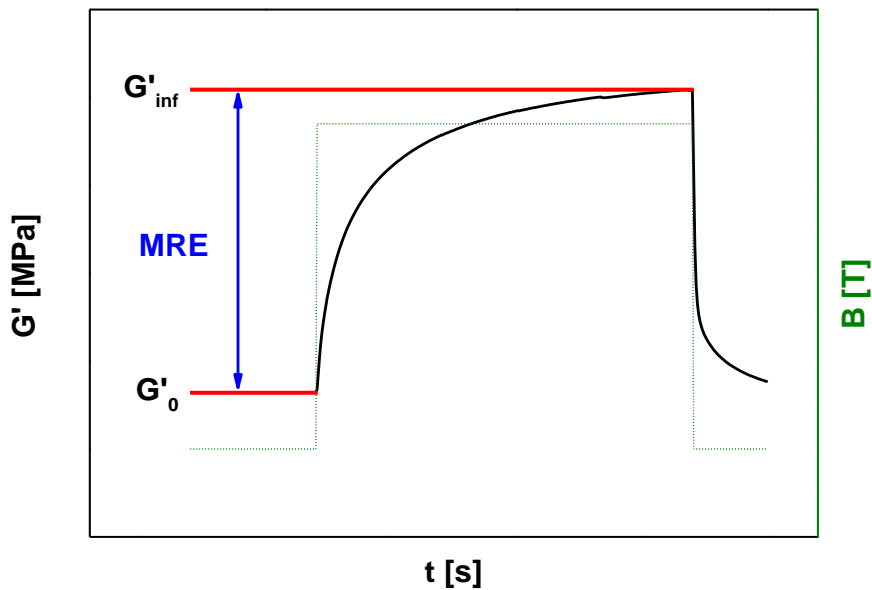
Figure 57: Schematic diagram to determine the magnetorheological effect MRE as a measure of the switching ability of the MSE samples.

8.2 Influence of coupling agent on the relative magnetorheological effect

In order to examine the influence of silane on MSE, two different SBR samples were prepared at a constant magnetic filler volume fraction of 20 vol.% with and without silane on the same way as discussed in section (7.2.1). The effect of silane on the variation of the storage modulus at a shear strain amplitude of $0.5\,\%$ and a start temperature of $50\,°C$ is shown in Figure 58.
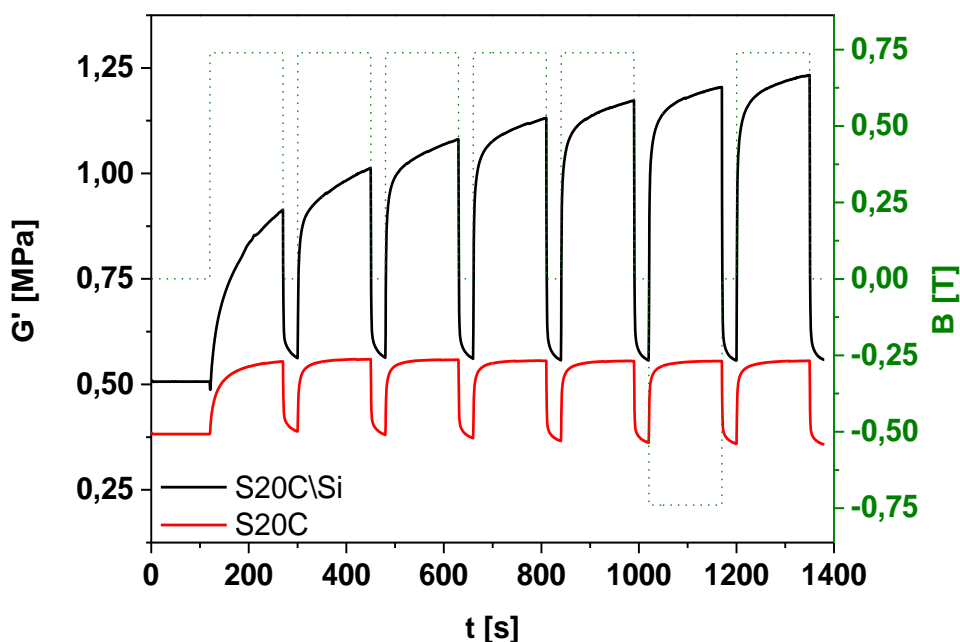
Figure 58: Effect of silane on the variation of the storage modulus at shear strain of **0.5** % and initial temperature of **50 °C** during switching on and switching off the magnetic field for the SBR melts with **20** vol.% CIP.

The storage modulus G' for both samples increases with time by switching on a magnetic field with a flux density of about $0.75\,T$. The effect on silanized sample is significantly weaker. Temporarily turning off the external magnetic field relaxes the shear modulus to lower values because the magnetically induced dipole-dipole attraction between neighbouring magnetic filler particles gets lost. G' increases for the silanized sample from $0.38\,\text{MPa}$ to $0.53\,\text{MPa}$ after around 2 minutes. This corresponds to a MRE of nearly $40\,\%$. After turning off the magnetic field G' drops approximately to its initial value. This behaviour is observed to be roughly the same in the following sequences. For the sample without silane, G' increases gradually from its initial value of $0.51\,\text{MPa}$ once the magnetic field is turned on, until it reached a maximum of approximately $1.23\,\text{MPa}$ after 1320 seconds. This corresponds to a MRE of more than $140\,\%$. This behaviour is related to the combined effect of a higher mobility of the magnetic filler particles without a shielding silane layer and the ability of the magnetic filler particles to come in close contact when they arrange in strings along the magnetic field lines. In the presence of a magnetic field, this delivers stronger attractive forces between the magnetic filler particles implying a higher stiffness of the sample. In addition, this explains why G' relaxes not back to its initial value when the field is turned off, but remains at about $0.56\,\text{MPa}$. This indicates that the magnetic filler particles still have a small residual magnetisation. This stiffens the sample due to the remaining attraction between the particles in the strings provided a good contact is realized. Contrary, for the silanized particles the close contact is prevented by the silane layer acting as a space-holder [170]. This layer may be increased by bounded polymer chains due to unavoidable reactions of the sulphur

groups during the mixing process at $130\,°C$. Furthermore, the alkyl-groups of the silane improve the compatibility of the particles with the polymer chains leading to a lower mobility. This demonstrates that the use of silane reduces the MRE significantly. Nevertheless, the coupling agent is necessary for a good mechanical performance since it delivers a chemical bonding of the magnetic filler particles to the polymer matrix during curing at $150\,°C$ [106, 107].

8.3 Influence of application temperature on the relative magnetorheological effect

The distribution of the magnetic filler particles during the vulcanisation process is temperature dependent and can be analysed by magnetorheological measurements of the MSE melts. MSE composites were prepared on the basis of NBR and the magnetic filler CIP. The silanisation was taken into account. The silane content has been adjusted to magnetic filler volume fraction. The magnetorheological measurements were made at room temperature and a temperature of $50\,°C$. Figure 59 presents the variation of the storage modulus G' at a shear strain amplitude of 0.1 % and a frequency of $1\,Hz$ during switching on and switching off the magnetic field at two different temperatures: $23\,°C$ and $50\,°C$.

When the power supply is turned on, a magnetic field density close to $0.33\,T$ is generated. The storage modulus G' increases with time confirming an interaction between the filler particles and the magnetic field lines. By turning off the control circuit, the external magnetic field disappears and the storage modulus drops to the initial values. This relaxation behaviour indicates that the magnetically induced dipole-dipole interaction between adjacent soft magnetic filler particles disappears almost completely, due to the quite small remance for the MSE. Turning on the power supply for a second time with a higher magnetic field density of $0.49\,T$ increases the magnetically induced flocculation, which delivers larger modulus values. Rising the measurement temperature to $50\,°C$ considerably reduces the viscosity of the polymer matrix and enhances the mobility of the magnetic filler particles. Accordingly, higher storage moduli are observed in comparison to those measured at $23\,°C$ for the same magnetic filler loading and period of time.
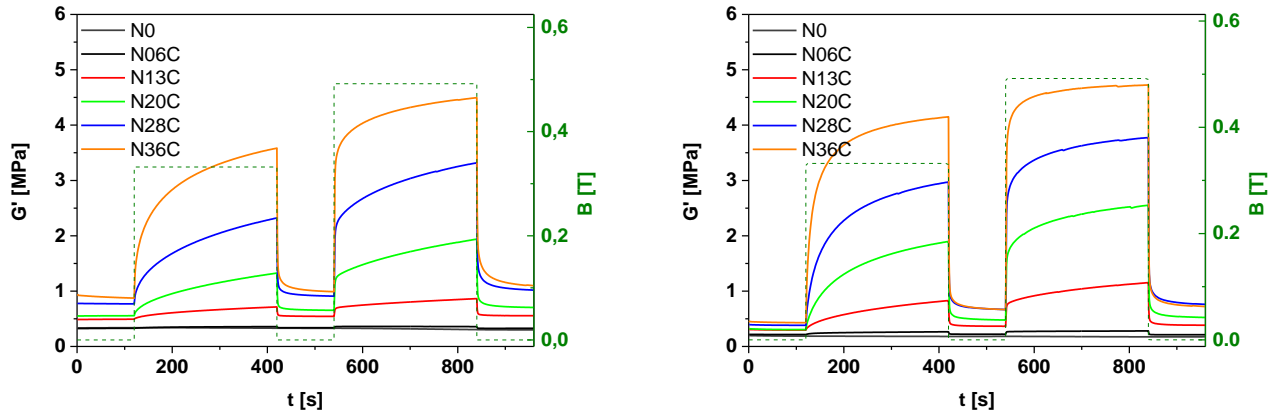
Figure 59: Effect of temperature on the variation of the storage modulus at shear strain of 0.1 % and a frequency of $1\,Hz$ during switching on and switching off the magnetic field for the non-crosslinked melts at $23\,°C$ and $50\,°C$.

The MRE increases with time and with increasing magnetic field strength. It is more pronounced with increasing magnetic filler content and measurement temperature. For the sample N36C with 36 vol.% CIP, G' increases after 800 seconds from 0.875 MPa to 4.495 MPa at $23\,°C$ and from 0.429 MPa to 4.726 MPa at $50\,°C$, which means an absolute increase by more than four or even ten times, respectively [171]. The MRE for MSE samples at both temperatures is listed in Table 11.

Table 11: Maximal MRE for the non-cross-linked melts at $23\,°C$ and $50\,°C$ measured at a shear strain of 0.1 %.

	N06C	N13C	N20C	N28C	N36C
$23\,°C$	0.06	0.59	1.97	2.65	3.54
$50\,°C$	0.27	2.16	4.35	4.69	6.09

9   Magnetorheology of crosslinked systems

Magnetorheological measurements were carried out with the crosslinked MSE composites, which were vulcanised with and without magnetic field to get anisotropic and isotropic MSE respectively. The curing aims to provide a high level of crosslinking between the polymer chains and supports the building of the magnetic filler network. This new structure ensures a larger stiffness for all MSE composites and higher moduli values in comparison to the melts, because the magnetic filler particles are firmly tied to the polymer chains and can no longer be moved along the magnetic field lines. The on-off switching mode was chosen and the magnetic field strength was increased successively up to its maximum of about $0.75\,T$. The direction of the magnetic field was changed after every on-off cycle in order to examine if the polarity of the magnetic field may influence the measured moduli [106, 107].

9.1   Vulcanisation in a magnetic field

In order to determine the influence of the magnetic field strength during the curing process, MSE composites were prepared on the basis of SBR and the magnetic filler CIP. The samples were vulcanised with and without external magnetic field in order to prepare anisotropic and isotropic MSE respectively. For the preparation of anisotropic samples, 3 different magnetic field strengths were applied: $0.08\,T$, $0.11\,T$ and $0.2\,T$. In Figure 60 illustrates the magnetorheological response of the isotropic as well as the anisotropic MSE composites. Measurements were performed at a shear strain amplitude of 0.5 %, a frequency of $10\,Hz$ and an initial temperature of $53°C$.

Obviously, all MSE samples show a more or less pronounced switching effect. The storage modulus abruptly increases when the external magnetic field is turned on and quickly decreases when the external magnetic field is turned off. The switching effect observed for MSE composites confirms the good interaction of the microscaled magnetic filler particles with the external magnetic field.

The degree of change of storage modulus depends on the magnetic filler content, the magnetic field strength during the curing process and the magnetic field strength during the magnetorheological measurements. The anisotropic MSE sample S20C A with 20 vol.% CIP, cured at a magnetic field of $0.2\,T$, shows the largest switching effect compared to all other samples. The storage modulus G' increases by more than 40 % once the magnetic field is turned on. For the isotropic sample S20C I, G' only increases by nearly 5 %.

This is explained by the fact that, the magnetic filler contribute to the mechanical reinforcement of the MSE sample. The more, the better. The magnetic field during the curing enhances the orientation of the magnetic dipoles of the magnetic filler particles and promotes their alignment along the magnetic field lines. Magnetic filler strings are formed within the rubber matrix and an anisotropic inner structure arises . This anisotropic magnetic filler network increases the stiffness of the MSE samples and improves their magnetic sensitivity.

Increasing the magnitude of the magnetic field increases the density of the magnetic filler strings. The magnetic filler particles become closer to each. This increases the anisotropic shape of the filler network, which further promotes the mechanical reinforcement of MSE samples (see Figure 45).
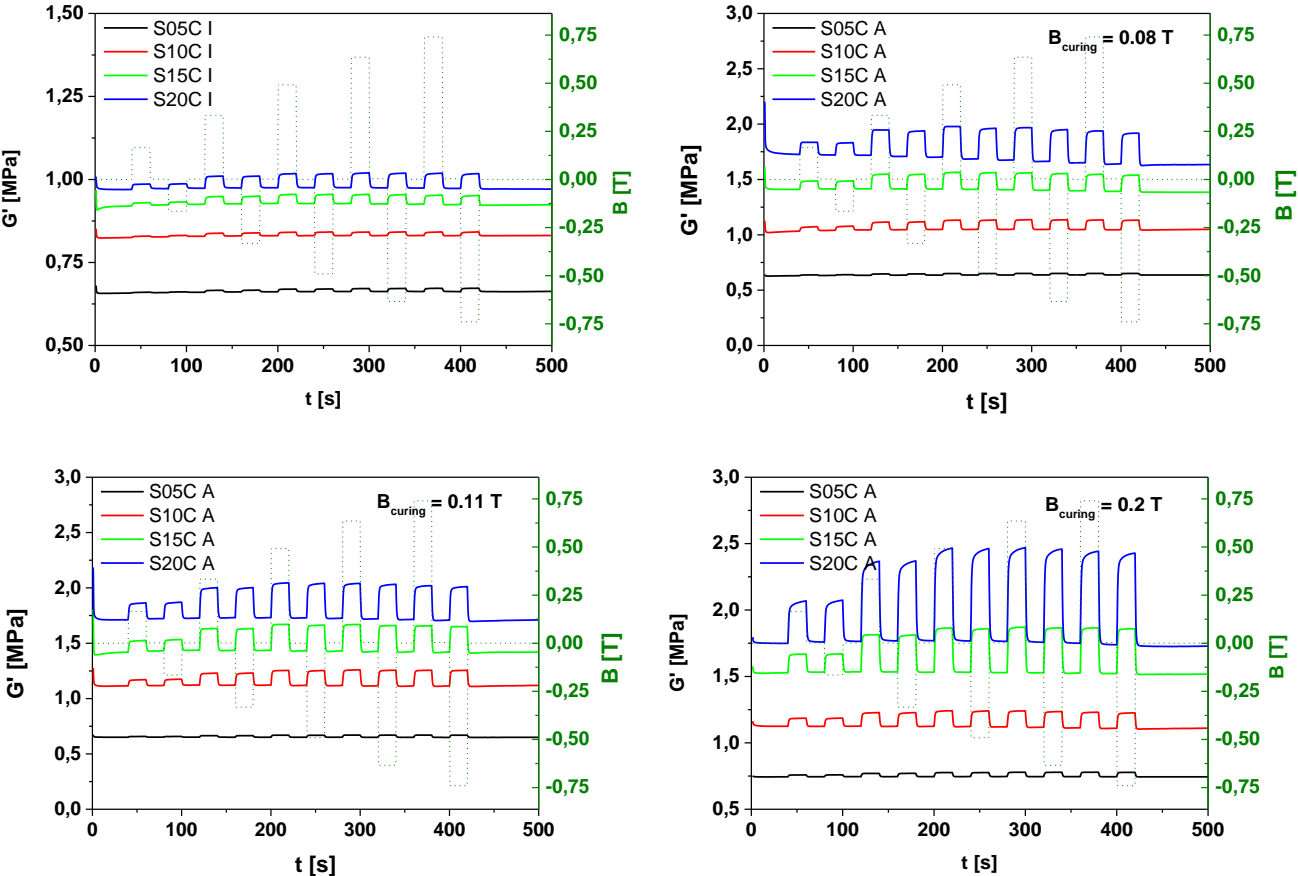
Figure 60: Variation of the storage modulus at shear strain amplitude of $\mathbf{0.5}$ %, frequency of $\mathbf{10\,Hz}$ and initial temperature of $\mathbf{53°C}$ during switching on and switching off the magnetic field. Measurement results for isotropic SBR-samples are shown in the top left corner. Measurement results for anisotropic SBR-samples cured with a magnetic field of $\mathbf{0.08\,T}$, $\mathbf{0.11\,T}$ and $\mathbf{0.2\,T}$ are shown in the top right, bottom left and bottom right corner respectively. The effective magnetic field strengths are probably larger.

Once reached, the switching on and off of the magnetic field does not affect the maximum of the storage modulus G' of the CIP-filled MSE sample. Not even the polarity change of the magnetic field leads to any improvement. It seems that the induced magnetic dipoles are fully saturated at a magnetic field of $0.5\,T$.

The MRE is derived according to equation (92). It depends on the magnetic filler volume fractions, the magnetic field strength during the curing process and the magnetic field strength during the magnetorheological measurements. Figure 61 shows the results for anisotropic SBR samples cured at magnetic field strength of $0.2\,T$. The sample ranking remains the same when the magnitude of the magnetic field changes. Just the MRE become smaller.
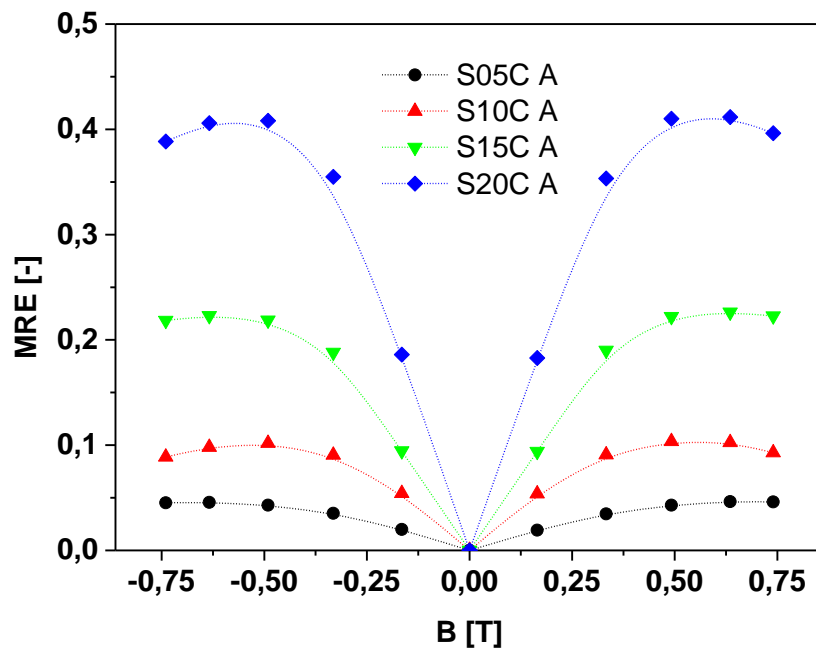
Figure 61: MRE dependency on the magnetic filler content for anisotropic SBR samples cured at a magnetic field strength of **0.2 *T***.

Figure 62 shows the dependency of the MRE of the anisotropic MSE sample S20C A filled with 20 vol.% CIP on the magnetic field during the curing process.
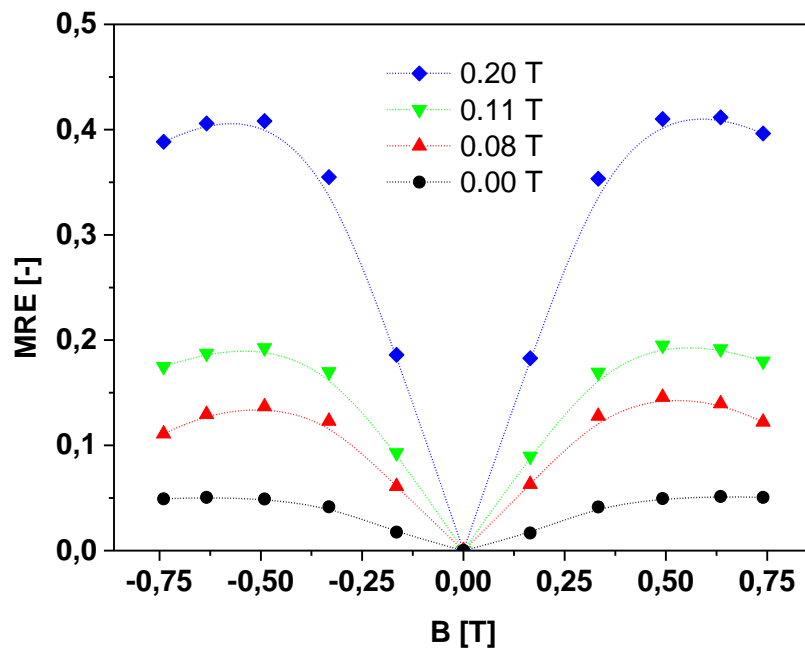
Figure 62: MRE dependency on the magnetic field strength during the curing process for MSE samples filled with **20** vol.% CIP.

During the magnetorheological measurements, higher magnetic field magnitudes than $0.5\,T$ impair the MRE because high magnetic fields are generally generated by high electrical currents. This unnecessarily increases the temperature of the magnetic cell. This inevitably increase in temperature decreases the viscosity of the samples and thus also the storage modulus. Considering the relatives quantities, the MRE is then reduced.

The MRE depends on the magnetic filler content (see Figure 61) and the magnitude of the magnetic field during the curing process (see Figure 62). It tends asymptotic to a threshold value, which can be approximated with one of the following equations:

$$MRE\,(\phi, B) = a(1 - e^{\phi\frac{B}{B_0}}) \tag{93}$$

or

$$MRE\,(\mathrm{B}_c, B) = a(1 - e^{\mathrm{B}_c\frac{B}{B_0}}) \tag{94}$$

where a is a scalar parameter, B_0 is the magnitude of a constant magnetic field of $1\,T$ and B is the magnitude of the magnetic field, by which the samples are tested. The magnetic filler content ϕ in equation (92) and the magnitude of the magnetic field during the curing process B_c in equation (93) represent the preparation criteria of the MSE composites.

9.2 Internal microstructure of MSE

The internal microstructure of MSE composites can be determined by performing microscopic examinations or magnetorheological tests. The scanning electron microscope (SEM) is based on the scanning of the sample surface by means of a very tightly focused electron beam. When the electron beam hits the sample, elastic and inelastic collision processes take place. The resulting deflections of the secondary electrons are recorded to reflect the quality of the sample surface. Magnetorheological measurements point out the preferred direction of magnetisation of the MSE composites. Depending on the direction of the applied magnetic field, different magnetisation behaviour of the MSE composites can be observed. This spatial dependency specifies the magnetic anisotropy of the MSE.

9.2.1 Magnetic anisotropy of MSE using scanning electron microscope

MSE composites were prepared on the basis of NBR and the magnetic filler CIP. The magnetic filler content is 20 vol.%. The vulcanisation was carried out with and without an external magnetic field. SEM images of a cross section of the samples N20C with 20 vol.% CIP are depicted in Figure 63 [171].

The left image in Figure 63 shows that the magnetic filler particles are uniformly dispersed within the rubber matrix. This is achieved when no magnetic field is applied during the vulcanisation. If an external magnetic field is applied during the curing process, the magnetic filler particles are lined up along the magnetic field lines in columnar structure. This illustrates the right image in Figure 63. The orientation of the magnetic moments is caused by a less restricted mobility of the magnetic filler particles within the rubber matrix during the

vulcanisation due to high temperatures. Besides the decrease of the sample viscosity during curing, the mobility of the magnetic filler particles is further improved when plasticizers are used. The MSE sample acquires anisotropic mechanical and magnetic properties.
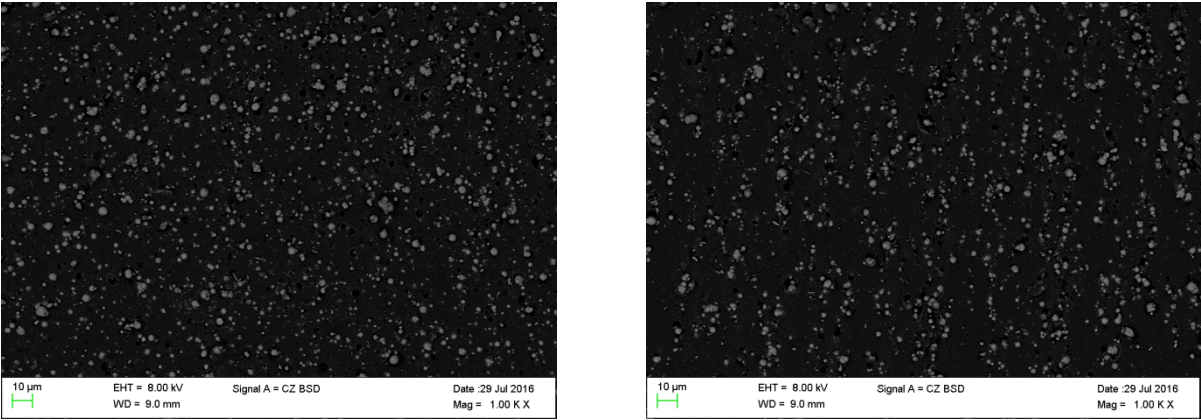
Figure 63: SEM images of a cross section of the N20C samples cured without (left) and with (right) magnetic field.

9.2.2 Magnetic anisotropy of MSE using magnetorheological testing

The magnetic anisotropy of MSE composites can be observed by magnetorheological measurements. The measurement configuration consists of measuring the anisotropic MSE sample at two different sides. With other terms, the orientation direction of the magnetic filler particles can be chosen to be parallel or perpendicular to the external magnetic field, as depicted in Figure 64. Note here that the direction of the applied force and the magnetic field direction in this measurement configuration are the same. The anisotropic N20C was a $6\ mm$ long, $6\ mm$ wide and $6\ mm$ high cube. The electrical current governing the magnetic cell was increased linearly from $0\ V$ to $5\ V$. This corresponds to a magnetic field strength from $0\ T$ to maximal $0.75\ T$.
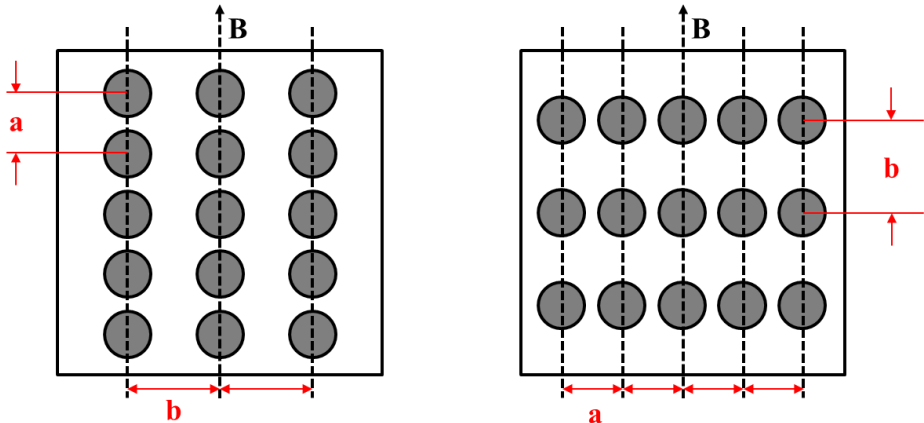
Figure 64: The orientation of the magnetic filler strings within the anisotropic sample N20C during magnetorheological measurements. The magnetic field runs along the vertical z-axis.

The variation of the storage modulus G' at a shear strain amplitude of 0.1 %, a frequency of 10 Hz and initial temperature of 50 °C during switching on and switching off the magnetic field is shown in Figure 65.
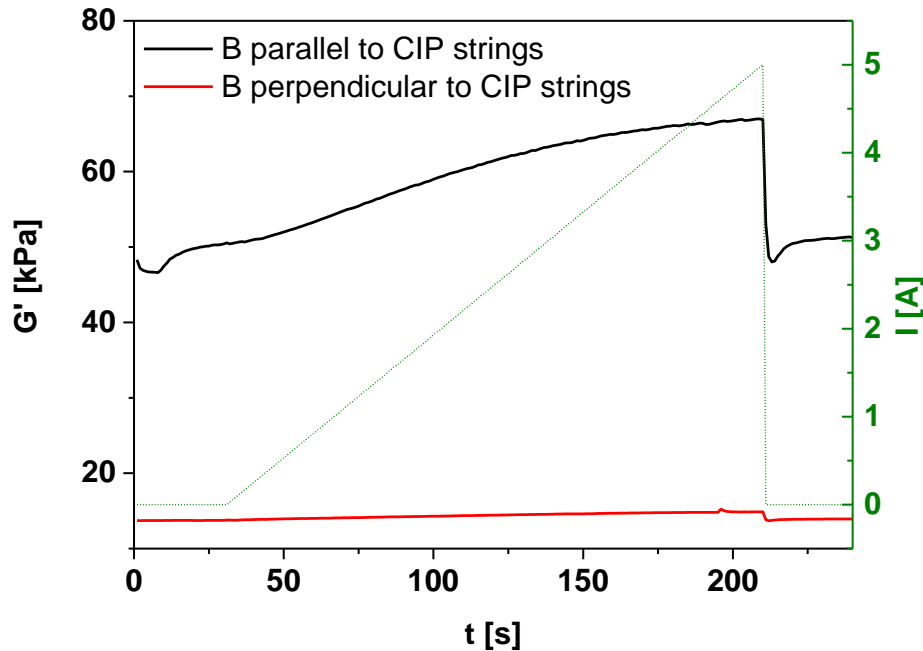
Figure 65: The variation of the storage modulus G' of the anisotropic sample N20C at shear strain amplitude of **0.1** %, frequency of **10 Hz** and initial temperature of **50 °C**. The direction of the magnetic field is parallel or perpendicular to CIP strings.

The magnetic field was first turned off for 30 seconds. The anisotropic sample N20C shows high storage modulus when the CIP strings within the sample are parallel and not perpendicular to the applied force. This direction dependency indicates that the sample stiffness is an anisotropic property. This behaviour is attributed to the columnar structure of the magnetic filler particles within the rubber matrix.

Turning on the electric current and accordingly the magnetic field in the next 180 seconds leads to great changes in the storage modulus G'. While G' slightly increases for the sample where the CIP strings are perpendicular to the direction of the magnetic field, G' shows a strong increase when the CIP strings are parallel to the direction of the magnetic field. A higher magnetic sensitivity is observed when the CIP strings are parallel to the magnetic field direction. When the magnetic field is switched off, G' relaxes to its initial value.

9.3 Influence of particle size

As discussed earlier in sections (7.2.1) and (7.3.2), SBR samples were prepared with two different magnetic fillers at constant volume fraction of 20 vol.%. The magnetic filler used were the microscaled CIP and the nanoscaled MAGSILICA. Figure 66 illustrates the variation of the storage modulus at a shear strain amplitude of 0.5 %, a frequency of 10 Hz and an

initial temperature of 50°C for the isotropic and anisotropic SBR samples. The magnetic field is increased stepwise and the measurement period is reduced to 500 seconds in order to minimise the thermal heating of the magnetic measurement cell.
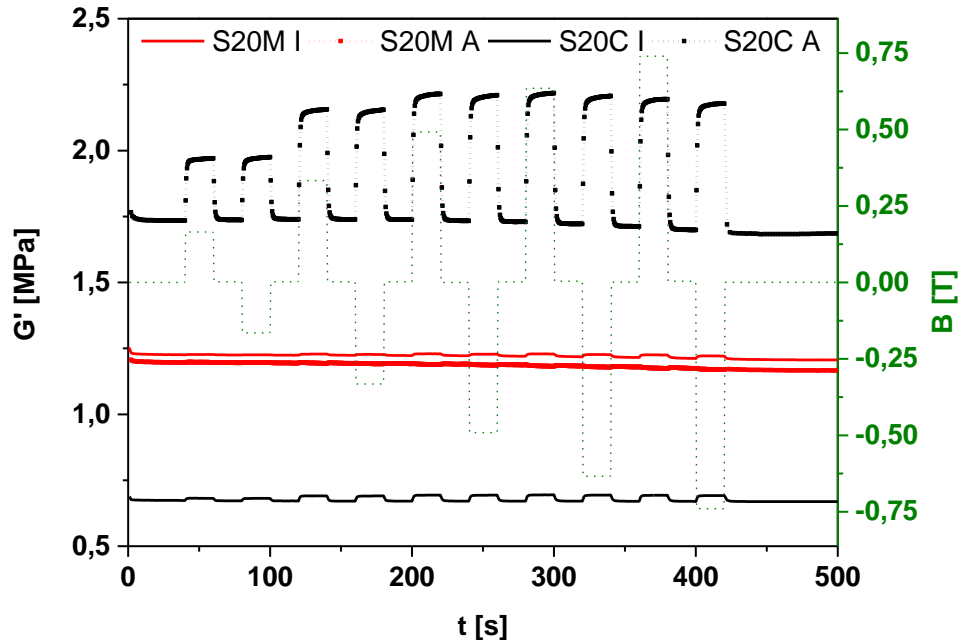
Figure 66: Variation of the storage modulus at shear strain amplitude of **0.5** %, frequency of **10 Hz** and initial temperature of **50°C** during switching on and switching off the magnetic field for isotropic and anisotropic SBR samples with two different magnetic fillers at constant volume fraction of **20** vol.%.

The isotropic samples S20C I with 20 vol.% CIP and S20M I with 20 vol.% MAGSILICA show hardly any switching effect. Similar to the melts (see Figure 56), the sample S20M I shows almost no switching effect but a slight decrease of the moduli values due to thermal heating. The switching effect for the sample S20C I does not exceed 4 %. The MSE samples are not sensitive enough to external magnetic field because the magnetic filler particles are more or less homogeneously distributed within the rubber matrix.

The storage modulus G' of the isotropic sample S20M I is about 1.22 MPa. For the isotropic sample S20C I, it is around 0.68 MPa. This performance has to do with the large reinforcing potential of the nanoscaled magnetic filler particles.

The anisotropic inner structure achieved during the vulcanisation with an external magnetic field makes both samples stiffer because the columnar arrangement of the magnetic filler particles significantly contribute to mechanical reinforcement of the samples. A tiny switching effect is observed for the sample S20M A with 20 vol.% MAGSILICA. The storage modulus G' is hardly affected once the magnetic field is switched on. The change in modulus is more pronounced for the sample S20C A with 20 vol.% CIP. A switching effect of about 30 % is observed.

It is important to note that the magnetic field strength of about $0.75\,T$ is not necessary for reaching the maximum modulus values G'_{max}. This is already observed at about $0.5\,T$ where the induced magnetic dipoles become saturated. Furthermore, the switching effect of vulcanisates is smaller than the switching effect of melts, because the mobility of the magnetic filler particles in the rubber matrix is restricted by the crosslinking achieved during the curing process [106, 107].

9.4   Variation of filler loading

Magnetorheological measurements were carried out with CIP-filled NBR samples with different filler volume fractions. The curing was realized with and without magnetic field to obtain isotropic and anisotropic MSE composites respectively. The variation of the storage modulus at a shear strain amplitude of $0.1\,\%$, a frequency of $10\,Hz$ and an initial temperature of $50°C$ for isotropic and anisotropic MSE are depicted in Figure 67.
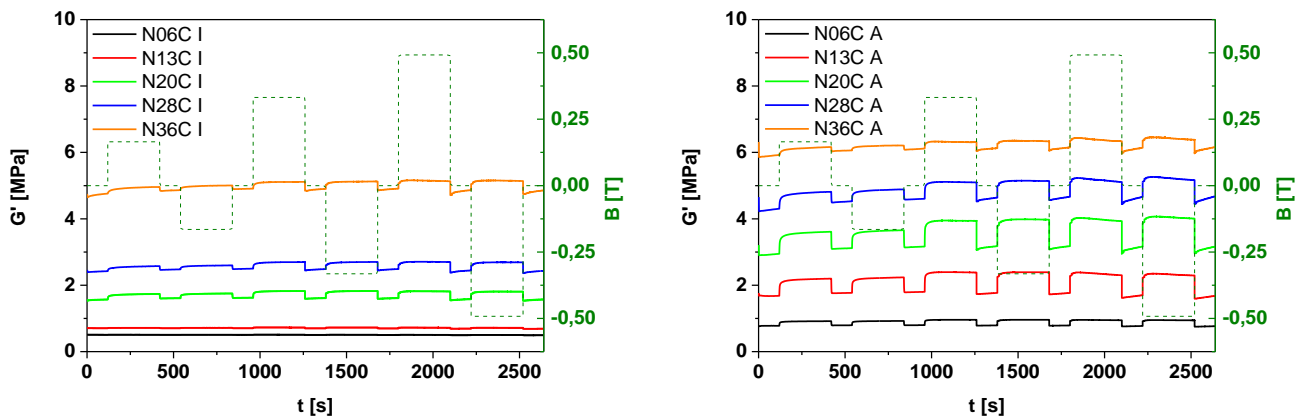
Figure 67: Effect of orientation on the variation of the storage modulus at shear strain amplitude of **0.1** %, frequency of **10 Hz** and initial temperature of **50°C** during switching on and switching off the magnetic field for the crosslinked vulcanisates. On the left the isotropic samples are presented and on the right anisotropic samples are shown.

For isotropic MSE composites, the storage modulus G' increases with increasing the magnetic filler content. Only a slightly small switching effect is observed for all samples because the magnetic filler particles are more or less homogeneously distributed within the rubber matrix. They are not able to form columnar strings through the interaction with the applied magnetic field because they are immobilized by the crosslinking. The maximum switching effect does not exceed **13** % and it is recorded for the sample N20C I with **20** vol.% CIP.

All anisotropic MSE composites become stiffer due to an additional contribution of the magnetic filler network. The arrangement of the magnetic filler particles along the magnetic field lines is achieved during the curing process [**171**]. This inner structure ensures all samples larger stiffness and improves their magnetic sensitivity. A maximum switching effect of **36** % is recorded for the sample N13C A with **13** vol.% CIP.

Obviously increasing the magnetic filler volume fraction is not followed by an increase of the switching effect of both the isotropic and the anisotropic MSE composites. A maximum is reached with a magnetic filler content of 20 vol.% for the isotropic sample and a magnetic filler content of 13 vol.% for anisotropic samples. Above this CIP limit, only an increase in stiffness is observed. It appears that despite the strong magnetic interaction between the magnetic filler particles and the magnetic field, the magnetic ordering of the MSE composites is increasingly disturbed.

Similar to dynamic-mechanical investigations in section 7.3.3, the magnetic filler content seems to play a major role in setting the magnetorheological properties of the finished MSE composites. The volume fraction of the magnetic filler should be optimised and exactly adjusted in order to avoid considerable restriction on the maximum switching effect.

The switching effect for both isotropic and anisotropic MSE is summarized in Table 12.

Table 12: Maximum MRE for isotropic and anisotropic crosslinked MSE samples derived from measurements at shear strain amplitude of 0.1 %, a frequency of $10\ Hz$ and initial temperature of $50°C$.

	N06C	N13C	N20C	N28C	N36C
Anisotropic	0.23	0.36	0.26	0.12	0.03
Isotropic	0.004	0.03	0.13	0.09	0.05

9.5 Influence of coupling agent

Two different SBR samples were prepared at a constant CIP content of 20 vol.% with and without silane on the same way as discussed in section (7.2.1) in order to examine the influence of silane on the switching effect. Figure 68 illustrates the influence of silane on the variation of the storage modulus at a shear strain amplitude of 0.5 %, a frequency of $10\ Hz$ and an initial temperature of $50\ °C$ during the switching on and the switching off of the magnetic field for isotropic and anisotropic samples. The magnetic field is increased stepwise and the measurement period is reduced to 500 seconds in order to minimise the thermal heating of the magnetic measurement cell.
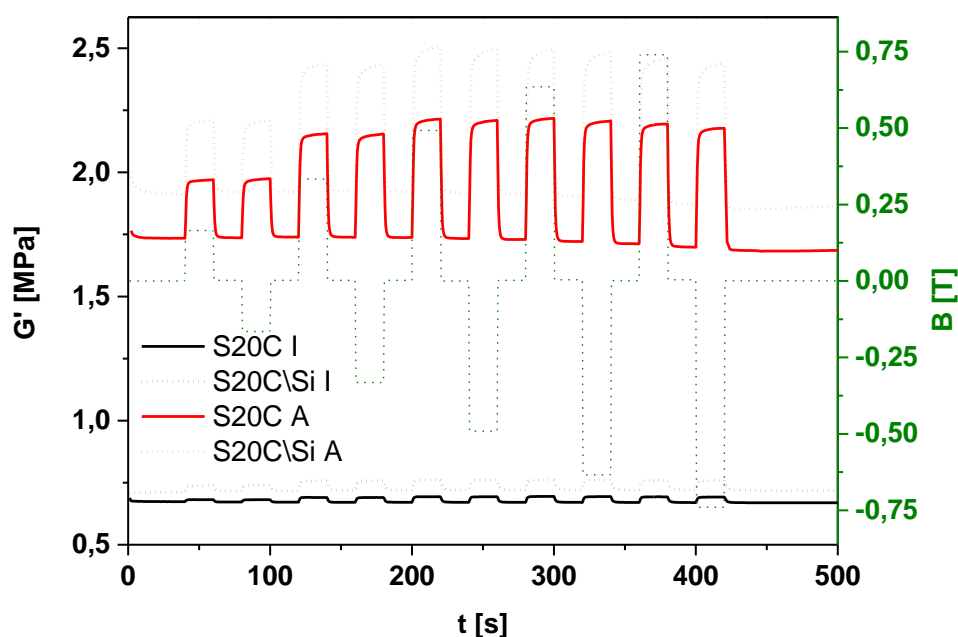
Figure 68: Effect of silane on the variation of the storage modulus at shear strain of **0.5** %, , frequency of **10 Hz** and initial temperature of **50 °C** during switching on and switching off the magnetic field for the SBR samples.

Independently of the particle orientations, smaller switching effect and storage moduli are observed for the silanized SBR samples. This confirms that silane hinders the mobility and prevents a close contact of the magnetic filler particles. Therefore, it reduces the magnetic sensitivity of the silanized samples and, thus, the switching effect. Due to vulcanisation, the rubber matrix becomes crosslinked and the magnetic filler particles are immobilized within the composites. The additional silanisation leads to strong chemical bonding between the polymer chains and the magnetic filler particles, making them less mobile. For the isotropic samples, where the particles are more or less homogeneously distributed, the switching effect has a maximal value of about 4 %. Obviously, the applied external magnetic field is not strong enough to displace the magnetic filler particles sufficiently and make the composites magnetically more sensitive. The magnetic sensitivity of the samples can be enhanced by curing in the presence of an external magnetic field to obtain anisotropic MSE. The magnetic filler particles arrange themselves thereby in oriented particle chains. The most pronounced change of the modulus during switching on and switching off the magnetic field is observed for the anisotropic sample S20C\Si A without silane and it is about 30 % [106, 107].

The same ranking is observed also here as the strain sweep data at 0.5 % strain amplitude obtained with the DMA in Figure 50, despite different experimental setup.

9.6 Magnetic induced relaxation behaviour of MSE

Relaxation experiments provide more insight on the internal dynamics of polymer chains and filler network. They reveal the influence of the different components on the dynamic-mechanical behaviour of elastomer composites and the contribution of each one of them. In the classical sense, test samples are subjected to a constant deformation for a defined period of time. Depending on the load time and the temperature, a time-dependent drop of the mechanical stress σ is observed. This type of decrease is called the relaxation behaviour. However, the aim of studying the magnetic induced relaxation behaviour of MSE composites is to characterise the time span required in order to reach the maximum storage modulus G' once the external magnetic field is switched on. This can be characterised by measuring the time-dependency of the storage modulus G' at constant deformation.

Four different samples were prepared on the basis of EPDM, NR, HNBR and XHNBR with 20 vol.% CIP. The samples were vulcanised in the presence of an external magnetic field. The influence of rubber type on the variation of the storage modulus G' at a shear strain amplitude of $0.5\,\%$, a frequency of $10\,Hz$ and an initial temperature of $10\,°C$ during switching on and switching off the magnetic field for the MSE composites is shown in Figure 69. The maximum magnetic field strength is reduced to $0.5\,T$.
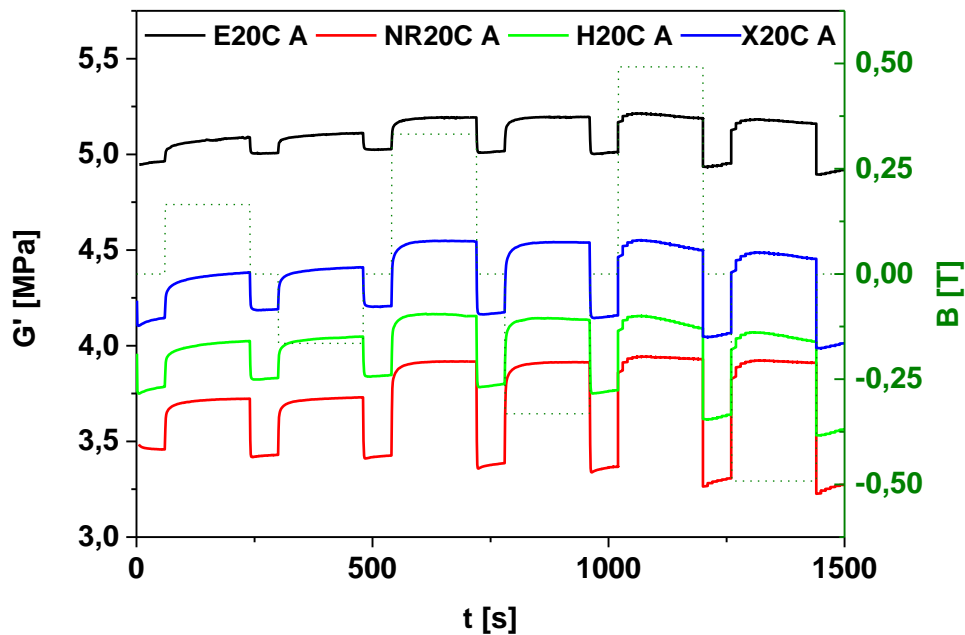
Figure 69: Influence of rubber type on the variation of the storage modulus at shear strain amplitude of $\mathbf{0.5}\,\%$, frequency of $\mathbf{10\,Hz}$ and initial temperature of $\mathbf{10\,°C}$ during switching on and switching off the magnetic field.

Figure 69 shows that the rubber type influences the variation of the storage modulus G' during switching on and switching off the magnetic field. This behaviour is related to the chemical structure and conformation of rubber chains.

The anisotropic EPDM sample E20C A shows the highest storage modulus G' in this sample pool. G' is around 4.92 MPa when the magnetic field is switched off. Apparently, the low viscosity of the EPDM matrix promotes the arrangement of the magnetic filler particles along the magnetic field lines during curing since the magnitude of the magnetic field was kept constant. The magnetic filler particles come closer to each other and a denser columnar structure is created. This configuration increases the anisotropic shape of the filler network and promotes the mechanical reinforcement of the EPDM sample.

The storage modulus G' of the anisotropic NR sample NR20C A is the smallest in this sample pool and it is around 3.45 MPa when the magnetic field is set to zero. The anisotropic HNBR sample H20C A has a storage modulus G' of 3.77 MPa while the anisotropic XHNBR sample X20C A has a storage modulus G' of 4.15 MPa when the magnetic field is switched off.

While the measured storage modulus for the EPDM sample can be explained by the low viscous rubber matrix which enhance the alignment of the magnetic filler particles along the magnetic field lines during curing, the measured storage modulus values for the NR, HNBR and XHNBR samples can be explained by the spatial density of the side chains and the degree of polarity of the rubbers used.

HNBR contains 34 wt.% acrylonitrile CH_2CHCN. This polar group contributes significantly to stiffness of MSE composites by restricting the free moving space of the polymer chains and increasing the entanglements density of the polymer chains. The binding energy of the $C \equiv N$ triple bond is 892 kJ/mol by $298\,K$ and it is larger than 416 kJ/mol for $C - H$ single bond [85]. Furthermore, the number of double bonds in the polymer backbone is limited to 5.5 wt.%. This makes the polymer chains less elastic.

XHNBR has besides an acrylonitrile content of 33 wt.% additional carboxyl groups $R - COOH$. The double bond $C = O$ brings a supplementary binding energy of 708 kJ/mol by $298\,K$ which has to be overcome when the sample is deformed. The polarity of the hydrogen atom in the carboxyl group is opposite to the polarity of the oxygen atom of the double bond. The carboxyl molecules attract each other and form dimers due to hydrogen bonding. Double molecule subsystems are formed. This conformation further increases the entanglements density of the polymer chains and with a residual double bonds content of 3.5 wt.%, the sample becomes less elastic.

The maximum switching effect has a value of about 4 % for the EPDM sample, 8.34 % for the XHNBR sample, 9.21 % for the HNBR sample and 14.24 % for the NR sample. It seems that the higher the storage modulus G', the smaller the MRE is.

The magnetorheological behaviour of the MSE composites can also be studied at different temperatures. Figure 70 shows the influence of temperature on the variation of the storage modulus at a shear strain amplitude of 0.5 % and a frequency of $10\,Hz$ during switching on and switching off the magnetic field for anisotropic sample NR20C A filled with 20 vol.% CIP. The maximum magnetic field strength is $0.5\,T$. The initial measuring temperature increases in $10\,°C$ increments from $10\,°C$ to $50\,°C$.
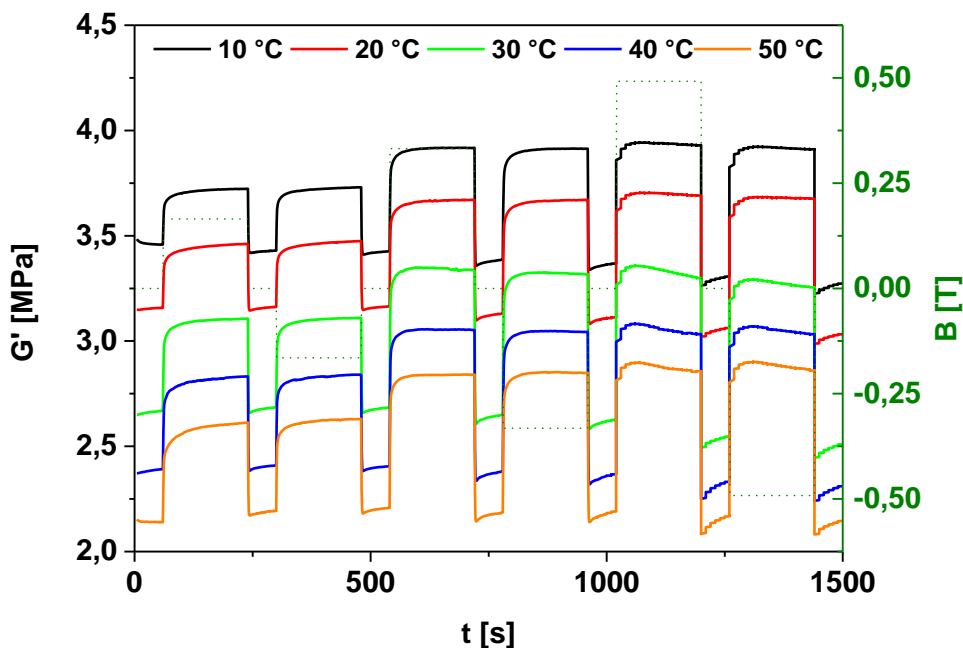
Figure 70: The influence of temperature on the variation of the storage modulus of anisotropic NR sample filled with **20** vol.% CIP at shear strain amplitude of **0.5** % and frequency of **10 Hz** during switching on and switching off the magnetic field. The initial temperature increases in **10 °C** increments from **10 °C** to **50 °C**.

Figure 70 depicts a significant influence of the measuring temperature on the variation of the storage moduli G' of the anisotropic sample NR20C A. Considering first the initial values of storage modulus, they increase with decreasing temperature. At $10 °C$, the NR20C A sample has an initial storage modulus G' of 3.45 MPa compared with 2.13 MPa at $50 °C$. This behaviour is mainly related to the change in the sample viscosity. Rising the measurement temperature considerably promotes the mobility of the polymer chains and thus reduces the viscosity of the polymer matrix. This enhances the orientation of the magnetic dipoles of the magnetic filler particles along the magnetic field lines and leads to a better switching ability.

When the magnetic field is switched off, then a spontaneous relaxation of the storage modulus G' follows. However, G' do not relax to its initial value because the magnetic filler particles do not completely lose their magnetisation. A rest magnetisation of the magnetic filler still remains. This contribute to a further stiffening of the sample still remains.

The magnetic relaxation time describes the occurrence of the magnetisation process of the MSE composites. It corresponds to the time took to align the magnetic dipole moments along the magnetic field lines and to reach in an ideal case the saturation magnetisation. The magnetic induced relaxation behaviour of MSE composites can be derived from the time evolution of the storage modulus G' as shown in Figure 69. The curve range with the highest switching effect is considered for further calculation and it is depicted in Figure 71.
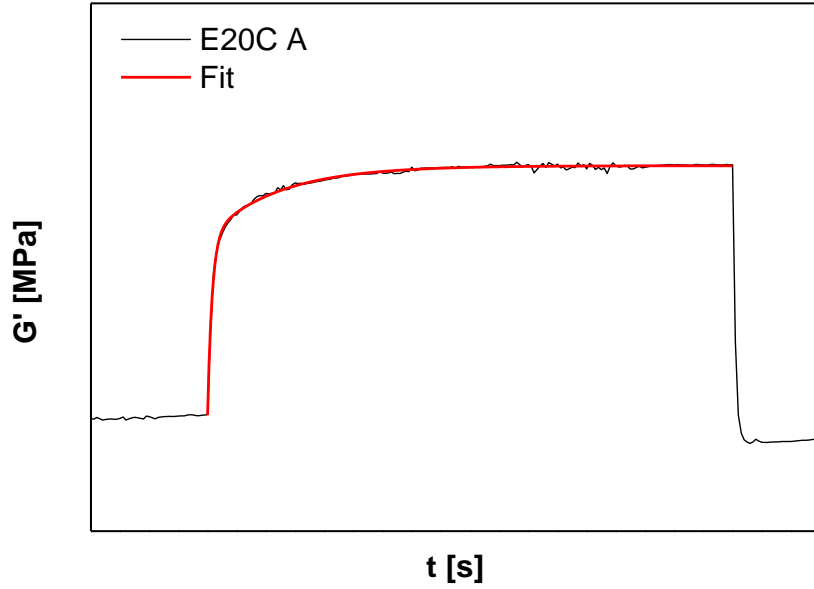
Figure 71: Curve range with the highest switching effect recorded for anisotropic EPDM sample filled with **20** vol.% CIP at shear strain amplitude of **0.5** %, frequency of **10 Hz** and initial temperature of **10 °C** during switching on and switching off the magnetic field.

Once turned on, the magnetic field brings the magnetic dipole moments of the magnetic filler particles to align themselves along the magnetic field lines. The magnetic dipole moments distribution is no longer the same. As a result, the MSE composites become stiffer and show high storage moduli. It can be seen in Figure 71 that the magnetisation process takes place at two different time scales. The storage modulus G' increases abruptly in the first few seconds after switching on the external magnetic field. The quick response of the MSE composite is followed by a gradual more slowly increase of G'. The first relaxation behaviour is attributed to the magnetic filler dynamic due to the high magnetic affinity of the magnetic filler particles. The second relaxation behaviour is attributed to the dynamic of polymer chains.

The storage modulus G' can be expressed by the sum of two exponential functions as follows:

$$G'(t) = G'_0 + \Delta G'_1 \exp\left(-\frac{t-t_0}{\tau_1}\right) + \Delta G'_2 \exp\left(-\frac{t-t_0}{\tau_2}\right) \tag{94}$$

where G'_0 is the initial storage modulus before the magnetic excitation, t_0 is a shift factor on the time axis, $\Delta G'_i$ represents the ith relaxation strength and τ_i is the magnetic induced relaxation time.

Using equation (94), the magnetic induced relaxation times τ_1 and τ_2 can be derived. The results for anisotropic EPDM samples with 20 vol.% CIP are presented in Figure 72.
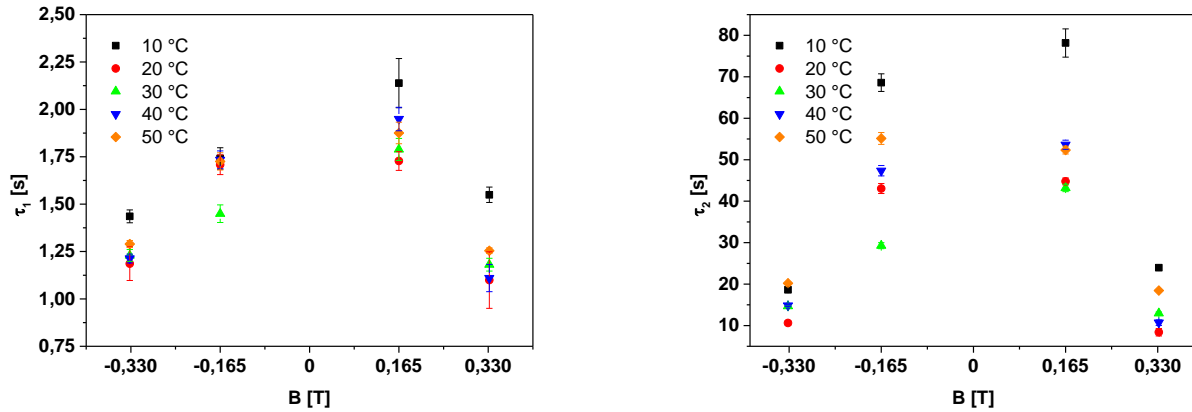
Figure 72: Magnetic induced relaxation times of anisotropic EPDM samples filled with **20** vol.% CIP at different measurement temperatures as a function of the magnetic field. On the right is plotted the short relaxation time τ_1 related to magnetic filler dynamic. On the left is plotted the long relaxation time τ_2 related to polymer dynamic.

Regarding the magnetic filler dynamic, the relaxation time τ_1 varies between 1 to 2 seconds. τ_1 depends on both the magnetic field and the measuring temperature. Increasing the magnetic field flux improves the magnetic interaction between magnetic filler particles and the external magnetic field. This promotes the orientation of the magnetic dipoles along the magnetic field direction. By switching off the magnetic field, this inner microstructure is no longer supported. The samples relax. By reversing the polarity of the magnetic field and keeping its intensity constant, the relaxation time becomes rather smaller. This is explained by the fact the magnetic filler particles are already magnetised but not to saturation. To be subjected to a magnetic field during an additional time leads more magnetic dipoles to get aligned and to have almost the same relaxation behaviour. Compared to initial distribution, the energetically not equivalent magnetic dipoles within the sample become harmonised once the magnetic field is turned on and point in the same direction. The totality of the magnetic dipoles develops a similar relaxation behaviour, which reduces the relaxation time. The relaxation time at high magnetic field strengths regardless of polarisation is not very large. This indicates that the magnetic filler particles are slowly becoming saturated.

The increase of measurement temperature has as a consequence the decrease of the sample viscosity. This promotes the aligning of the magnetic dipoles along the magnetic field lines. The magnetic induced relaxation behaviour of the MSE composites is mainly due to magnetic field but is also indirectly boosted by polymer chains dynamic. At any given magnetic field strength, the relaxation time τ_2 is very large compared to τ_1. τ_2 ranges between 10 and 80 seconds depending on the dynamic of the polymer chains.

The temperature dependency of the magnetic induced relaxation times τ_1 and τ_2 can be associated to the thermal activity the filler-filler and polymer-filler bonds. In Figure 73, the magnetic induced relaxation times τ_1 (attributed to magnetic filler dynamic) and τ_2 (attributed

to dynamic of polymer chains) for an anisotropic EPDM sample with 20 vol.% CIP is plotted against the inverse of the temperature.
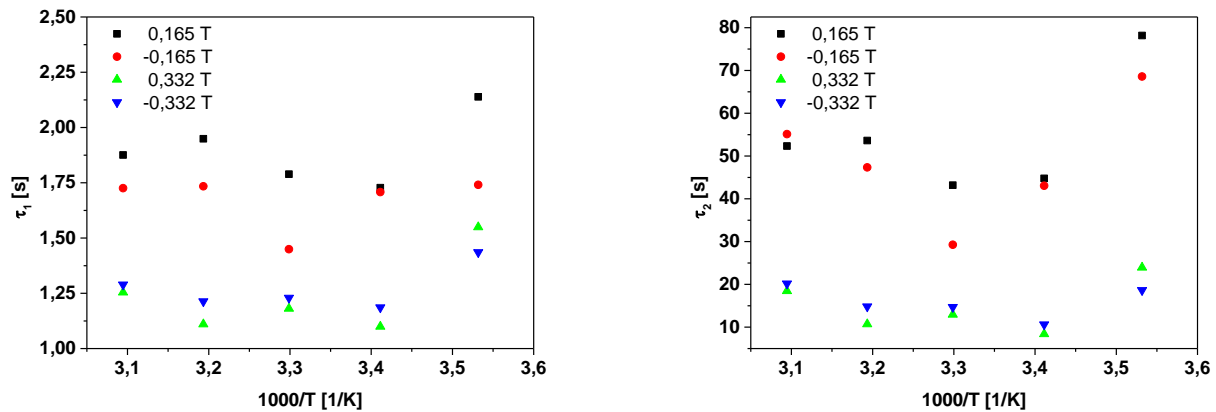
Figure 73: Temperature dependency of the magnetic induced relaxation times τ_1 and τ_2 for anisotropic EPDM sample filled with **20** vol.% CIP.

Obviously, the magnetic induced relaxation times τ_1 and τ_2 show no clear temperature dependency. This relaxation cannot be led back to the thermal activity of the filler-filler and polymer-filler bonds. This is explained by the fact that the relaxation behaviour studied here is magnetically induced and it is not the result of thermomechanical processes even if the measuring temperature changes. The strength of the applied magnetic field is the key factor to determine the time period of the magnetic induced relaxation. It appears clearly from Figure 73 that the magnetic induced relaxation time τ_1 becomes smaller with increasing the magnetic field. The polarity change of the magnetic field can be considered as an additional time to get the magnetic dipole moments of the not yet saturated magnetic filler particles aligned along the magnetic field lines.

The same also applies for similar reasons to second magnetic induced relaxation time τ_2. No similarity with the Arrhenius diagram for rubber materials is provided. The relaxation behaviour of the polymer chains is directly dependent on magnetic processes although the polymer chains are not magnetic. The decrease of the sample viscosity due to increasing the measuring temperature induces new conformations of the polymer chains. The entanglements density of the polymer chains decreases and the internal friction is reduced. This new structural arrangements additionally promote the orientation of the magnetic dipoles of the magnetic filler particles along the magnetic field lines. This results in a minimal increase of the storage modulus G' with increasing measuring time until the magnetic filler particles are completely saturated.

The experimental findings shown in Figure 72 confirms that the magnetic induced relaxation behaviour of the MSE composites is independent from temperature. Both magnetic induced relaxation times τ_1 and τ_2 are the shortest at temperature between $20\,°C$ and $30\,°C$ and not at $50\,°C$.

9.7 Modelling of the magneto-mechanical response of the MSE

MSE composites combine high elasticity and a fast switching ability in the presence of an external magnetic field. Both characteristics make them an attractive alternative to established standard technical elastomers. MSE composites exhibit an additionally magnetic field-induced reinforcement caused by the oriented magnetic filler particles within the rubber matrix. The magneto-mechanical properties of the MSE composites are the result of the coupling between the mechanical load and the external magnetic field. This section is devoted to describe the magneto-mechanical behaviour of MSE composites and to model it using the micromechanical dynamical flocculation model (DFM) for the description of isotherm state change of MSE at a given deformation. Varying the magnetic properties of the surroundings changes the mechanical properties of the samples and makes the fit parameters magnetic field dependent.

The DFM is used for modelling the magneto-mechanical response of the MSE composites. Compared with the Jolly [180], Ivaneyko [181, 182] or finite elements based models [183-188], the DFM is based on physical principles of high viscous polymer chains and contains a physical description of rubber characteristics like the Mullins effect. Therefore, the DFM fit parameters map a more realistic picture of the inner dynamic of the elastomer composites.

With increasing the number of load cycles, rubber materials experience a stress softening. This effect is referred to as Mullins effect [189, 190]. This is explained by the irreversible break of local filler clusters and mechanically unstable crosslinks. Additionally, the stress softening can be caused by the diffusion of adsorbed polymer chains on the surface of the magnetic filler particles, the total desorption from the magnetic filler surface or the entanglements sliding along the chain ends or between crosslinking sites after reaching a load limit. The Mullins effect is considered in the DFM and it is described with the concept of hydrodynamic amplification (see equation (63)).

The measurement were carried out with the dynamic-mechanical analyser MTS in simple shear mode as shown in Figure 31. The influence of a constant magnetic field on mechanical properties is investigated by multihysteresis experiments at room temperature. The material behaviour under four load amplitudes was tested. Each step was repeated five times. The magnetic field was switched off during the first three cycles and then switched on for the last two cycles as illustrated in Figure 74. The third and fifth cycles of loading and unloading curves form the respective reference curves and are displayed by lines. Here is assumed that a quasistatic material state was established. Highly sensitive fluxgate sensor is set in close proximity to the MSE composites to detect the magnetic field density.
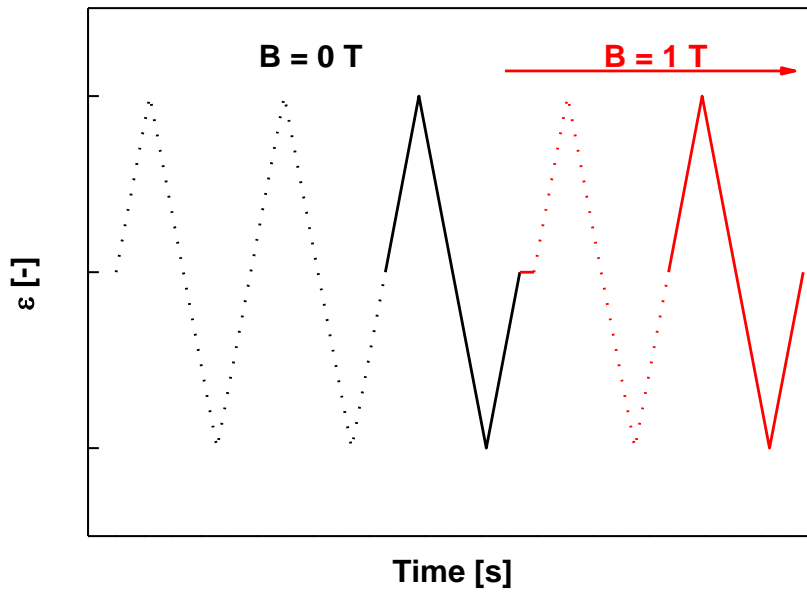
Figure 74: Multihysteresis measurement of MSE composites. In each deformation step, the deformation cycle was repeated five times. The first **3** cycles were performed without magnetic field, while the last **2** cycles with magnetic field. The third and fifth cycles of loading and unloading curves represent the reference curves and are displayed by full lines.

During the measurement tests, several preload cycles are made in order to establish a quasi-static material state. It is an important step to attain an equilibrium mechanical state for the different samples. This pre-conditioning permits to compare the different MSE composites at constant deformation history.

The raw data and the reference cycles from multihysteresis measurements for the anisotropic EPDM samples with 20 vol.% CIP are presented in Figure 75 and Figure 76 respectively.
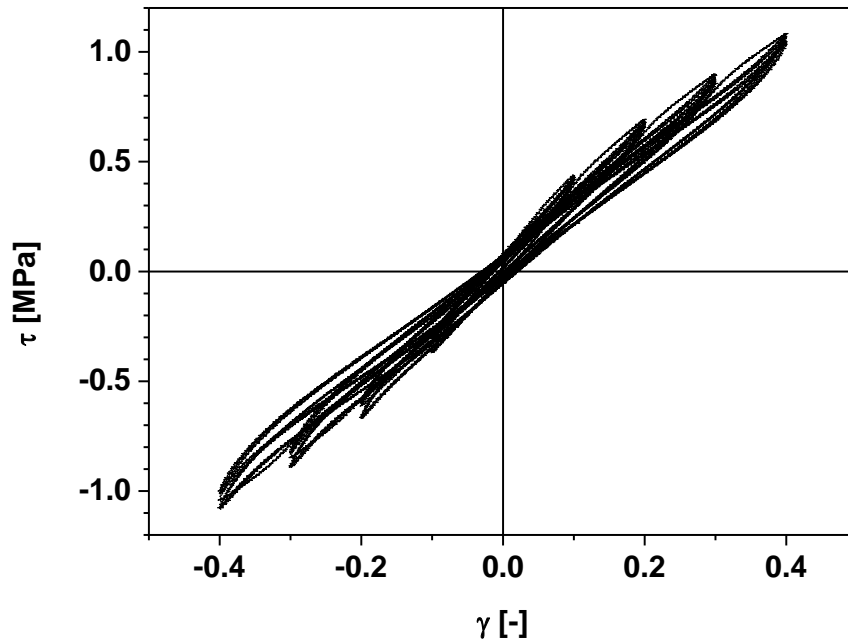
Figure 75: Raw data of multihysteresis measurements for anisotropic EPDM samples with **20** vol.% CIP plots.
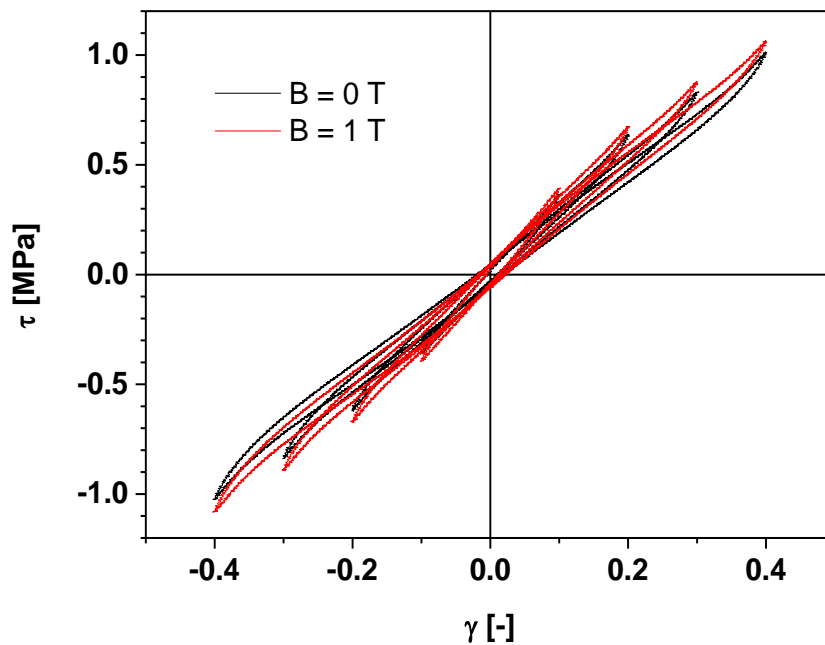
Figure 76: Reference cycles from multihysteresis measurements for anisotropic EPDM samples with **20** vol.% CIP plots.

Both isotropic and anisotropic samples show under cyclic load a hysteresis loop as seen in Figure 76. The hysteresis loop is steeper and larger for the anisotropic MSE composite. This

indicates changing elastic material properties where elastic energy is dissipated. The stress softening is mainly attributed to the destroy of magnetic filler clusters because the rupture of the physical bonds between polymer chains and crosslinking points occurs very slowly and only at high critical loads. However, The filler clusters can reaggregate during the rest phases when the sample is unloaded.

More profound insight about the dynamic-mechanical behaviour of the MSE composites in the presence of an external magnetic field can be achieved by fitting the experimental results using the DFM. Two different MSE composites were prepared on the basis of two different rubbers. EPDM was chosen for its soft matrix and HNBR for its ageing behaviour as well as its weathering resistance. The magnetic filler is CIP with a content of 20 vol.% and all other additives remain the same.

For the multihysteresis measurements shown below, first the third cycle describing the mechanical behaviour of the MSE composites without magnet field is fitted with the DFM. All fitting parameters were random numbers except the effective filler volume fraction. It was set to the magnetic filler content 0.2. This is justified by the spherical shape of the magnetic filler particles. In contrast to standard fillers in rubber technology like carbon black, there is no need to consider any topological effects for CIP particles. When the fitting procedure of the third cycle is finished, the fifth cycle describing the mechanical behaviour of the MSE composites with magnet field is fitted taking into account the following. Since the magnetic affinity of the magnetic filler particles is by far much larger than all components of the MSE composite, only the magnetic filler particles are severely affected by the external magnetic field. Therefore, the fit parameters related to mechanical behaviour of rubber are not influenced by the applied magnetic field and remain unchanged. A significant result of this assumption is that the stiffening observed in the experiments is assigned to the magnetic filler. Further, the cured samples have a very large viscosity restricting the free mobility of the magnetic filler particles even in the presence of an external magnetic field. The latter affects only the orientation of the magnetic moments and do not induce any movement of the magnetic filler particles within the rubber matrix. For this reason, the mean filler cluster size x_0 remains also constant. To fit the fifth cycle describing the mechanical behaviour of the MSE composite in the presence of a magnetic field, all fitting parameters are hold except the tensile strength of virgin bonds s_v and the tensile strength of damaged bonds s_d because only these parameters govern the shape of the hysteresis loop.

The reference cycles of multihysteresis measurements for both isotropic and anisotropic EPDM samples are presented in Figure 77 and Figure 78 respectively. In addition, the DFM fittings are displayed in red.
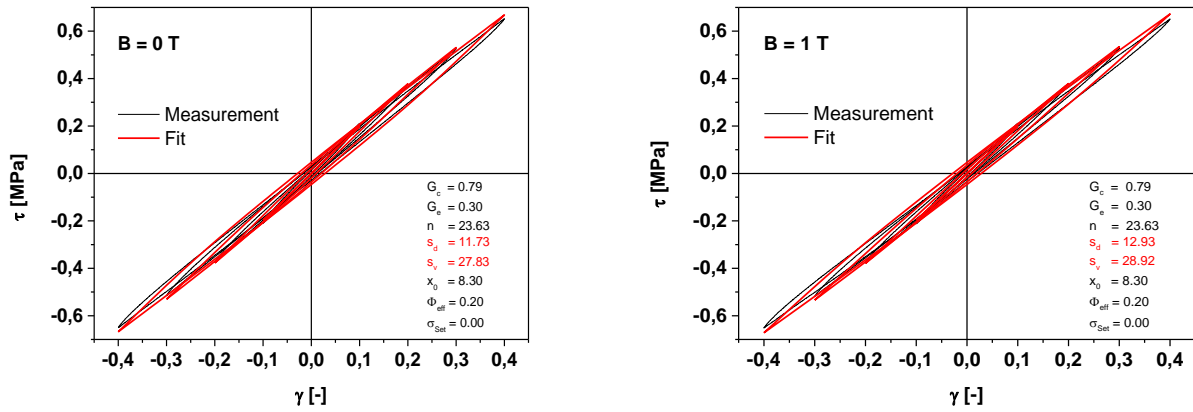
Figure 77: Reference cycles of the multihysteresis measurements for isotropic EPDM samples filled with **20** vol.% CIP and the associated fit curves with DFM. The measurement data were performed without (left) and with (right) magnetic field.

The shear stress τ of the isotropic EPDM sample reaches a peak value of about 0.65 MPa independently of the magnitude of the applied magnetic field. The crosslink modulus G_c is 0.79 MPa and the entanglement modulus G_e is 0.30 MPa. The finite extensibility parameter n amounts to 23.63, which indicate that almost 24 chain segments are between two adjacent entanglements. The mean filler cluster size x_0 is equal to 8.30. It is defined as the quotient of the filler cluster ξ to the primary particle size d. The magnetic filler cluster can be estimated between 25 μm to 37.4 μm because the diameter of CIP particles ranges between 3 μm and 4.5 μm. Without magnetic field, the tensile strength of virgin bonds s_v is 27.83 MPa and the tensile strength of damaged bonds s_d is 11.73 MPa. That s_d is smaller than s_v is self-evident, because the damage bonds cannot be stiffer than virgin bonds.

As mentioned above, turning on the magnetic field concerns only s_d and s_v. The tensile strength of virgin bonds s_v goes from 27.83 MPa to 28.92 MPa and the tensile strength of damaged bonds s_d goes from 11.73 MPa to 12.93 MPa. This increase is attributed to alignment of the magnetic moments of the magnetic filler particles. The orientation of the magnetic moments increases the magnetic interaction between the magnetic filler particles. These different contributions are rapidly summed up and cause a higher mechanical stress in the core of the sample. This increase is accompanied with a small enlargement of the hysteresis loop.

Figure 78 shows the reference cycles of the multihysteresis measurements for anisotropic EPDM samples with 20 vol.% CIP and the associated fitting curves with the DFM. Due to the anisotropic microstructure of the sample realised during the curing process in the presence of an external magnetic field, absolute higher values for all fit parameters are achieved except the finite extensibility parameter n. n drops from 23.63 to 3.01 and points out that the number of chain segments is reduced to an eighth. Only 3 chain segments are between two adjacent entanglements for anisotropic EPDM samples. This can be explained by the new distribution of the magnetic filler particles within the rubber matrix. Indeed, the magnetic

filler particles come easier together between the polymer chains during trying to line up themselves along the magnetic field lines. The mobility of the magnetic filler particles is promoted by the low viscosity of the melt due to a high curing temperature of 150 °C.
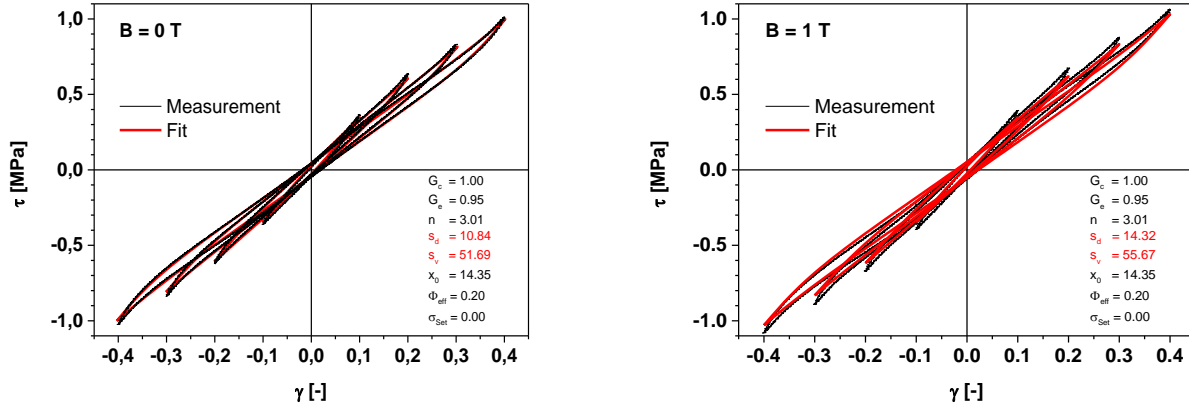
Figure 78: Reference cycles of the multihysteresis measurements for anisotropic EPDM samples filled with **20** vol.% CIP and the associated fit curves with DFM. The measurement data were performed without (left) and with (right) magnetic field.

Regarding the internal microstructure of the EPDM samples, the increase of the crosslink modulus G_c from 0.79 MPa for the isotropic sample to 1.00 MPa for the anisotropic sample and the increase of the entanglement modulus G_e from 0.30 MPa for the isotropic sample to 0.95 MPa for the anisotropic sample can be explained in the same way like the finite extensibility parameter n. It is attributed to the differences in topological space. This trend remains unaffected and all fitting parameters related to magnetic filler increase. The tensile strength of virgin bonds s_v almost doubles from 27.83 MPa and 28.92 MPa to 51.69 MPa and 55.67 MPa, depending on which magnetic field state is available. The stiffness of the virgin filler bonds is supported by the arrangement of the magnetic filler particles in strings during the curing in the presence of an external magnetic field. When the magnetic field is switched on during the measurements, it acts as an additional boost to move the magnetic moments of the filler particles. The already existing inner microstructure becomes clearly more heterogeneous. That magnetic filler particles are still sensitive to the applied external magnetic field shows that the magnetic moments are not completely aligned along the magnetic field lines as discussed in the subsection (3.2). This implies that the magnetic filler particles are not fully saturated during the curing with an external magnetic field and an enhancement of the magnetic filler particles orientation still remains feasible. This can be achieved by higher magnetic fields than $0.2\,T$ during the vulcanisation process of the samples, even if some limitations must be accepted due to topological constraints of the rubber matrix.

The tensile strength of damaged bonds s_d is always smaller than the tensile strength of virgin bonds s_v. During the loading cycle, the largest filler clusters are first destroyed. These are followed by the smaller ones until filler clusters with a minimal size remain (see Figure 28).

When the strain amplitude is reduced after reaching its maximum, an almost complete reaggregation of the magnetic filler clusters may take place. But these filler-filler bonds, which were once destroyed, are significantly weaker than the filler-filler bonds in the virgin sample. Comparison of the tensile strengths of damaged bonds s_d for all EPDM samples shows that they are a bit higher for anisotropic samples. However, they remain on the same scale.

The mean filler cluster size x_0 increases from 8.30 to 14.35. This validates the scanning electron microscope images shown in Figure 63. The magnetic filler clusters are larger for the anisotropic sample compared with the isotropic sample.

The maximum shear stress rises from 0.65 MPa for isotropic EPDM sample to 1 MPa for anisotropic sample. This is explained by the fact that the hysteresis of filled elastomer composites is mainly induced by the filler. This mechanism is based on the internal friction within the rubber matrix and the local high stress values around the magnetic filler clusters. The magnetic filler clusters stores mostly the mechanical energy when they are stretched in the tension field of the elastomer matrix. But when the clusters get destroyed, the stored mechanical energy is dissipated as heat.

The fit parameters of the DFM for the mechanical behaviour of the EPDM samples E20C A with and without magnetic field are summarized in Table 13. The effective filler volume fraction Φ_{eff} is set to 0.2.

Table 13: Fit parameters of the DFM for the EPDM samples with **20** vol.% CIP.

Orientation	B [T]	G_c [MPa]	G_e [MPa]	n [-]	s_d [MPa]	s_v [MPa]	x_0 [-]
Isotropic	0	0.79	0.30	23.63	**11.73**	**27.83**	8.30
	1	0.79	0.30	23.63	**12.93**	**28.92**	8.30
Anisotropic	0	1.00	0.95	3.01	**10.84**	**51.69**	14.35
	1	1.00	0.95	3.01	**14.32**	**55.67**	14.35

The multihysteresis measurements and the associated fit curves using the DFM of HNBR samples under the same measuring conditions as for EPDM samples are shown in Figure 79 and Figure 80. Regarding the curves shape, it is to note that the hysteresis as well as the upturn is much more pronounced for the HNBR samples compared with the EPDM samples. This behaviour is more evident for anisotropic samples. This indicates that the interaction of the polymer chains with the surface area of the magnetic filler particles is much better. However, the maximum value of the shear stress τ becomes smaller. An absolute maximum value of 1 MPa is measured for anisotropic EPDM sample. τ is roughly 0.87 MPa for anisotropic HNBR. A remarkable finding for the HNBR samples is that the maximum value of the shear stress τ is almost the same for the isotropic and the anisotropic samples. For EPDM samples, τ was 0.65 MPa for the isotropic sample and 1 MPa for the anisotropic sample.
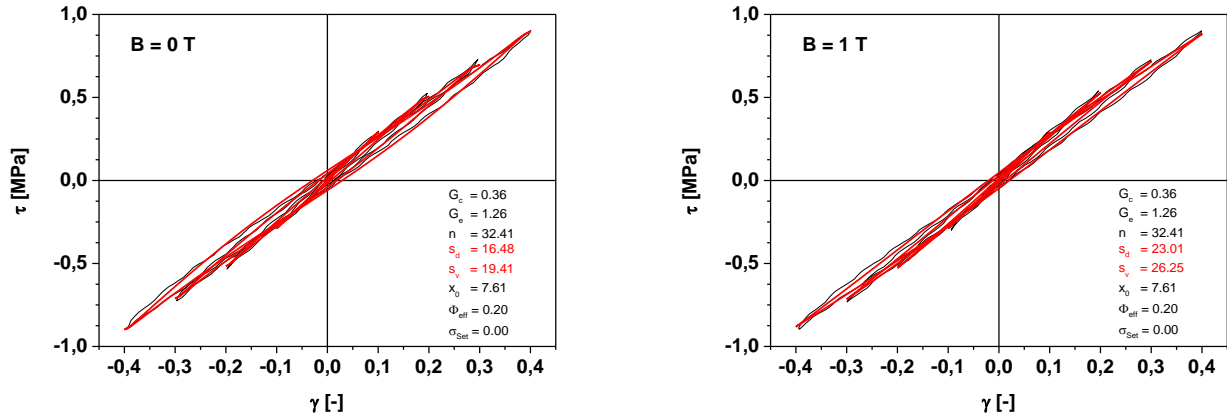
Figure 79: Reference cycles of the multihysteresis measurements for isotropic HNBR samples filled with **20** vol.% CIP and the associated fit curves with DFM. The measurement data were performed without (left) and with (right) magnetic field.
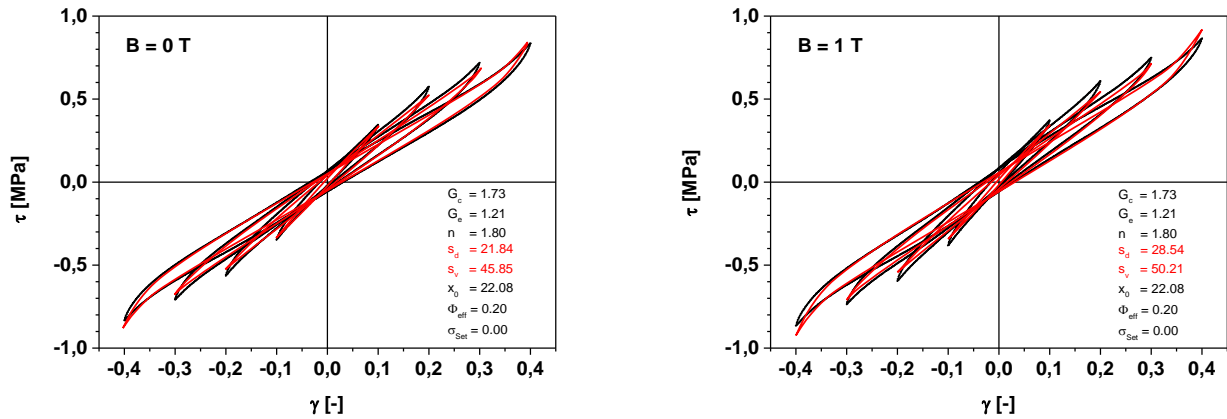
Figure 80: Reference cycles of the multihysteresis measurements for anisotropic HNBR samples filled with **20** vol.% CIP and the associated fit curves with DFM. The measurement data were performed without (left) and with (right) magnetic field.

The fit parameters of the DFM for the mechanical behaviour of the HNBR samples H20C A with and without magnetic field are summarized in Table 14. The effective filler volume fraction Φ_{eff} is set to 0.2.

Table 14: Fit parameters of the DFM for the HNBR samples with **20** vol.% CIP

Orientation	B [T]	G_c [MPa]	G_e [MPa]	n [-]	s_d [MPa]	s_v [MPa]	x_0 [-]
Isotropic	**0**	0.36	1.26	32.41	**16.48**	**19.41**	7.61
	1	0.36	1.26	32.41	**23.01**	**26.25**	7.61
Anisotropic	**0**	1.73	1.21	1.80	**21.84**	**45.85**	22.08
	1	1.73	1.21	1.80	**28.54**	**50.21**	22.08

The DFM fitting shows that the reinforcement mechanism of the MSE composites is similar although the rubber types are different. The fit parameters related to mechanical behaviour of

118

rubber were only affected by the molecular structure of the polymer chains as well as the distribution of the magnetic filler particles within the rubber matrix and not by the applied magnetic field during the measurement. However, the polymer-filler interaction is much better for HNBR samples. This can be explained by the polarity of the rubber. HNBR is much polar than EPDM.

10 Optimization of viscoelastic properties of MSE by hybrid filler systems

The investigations accomplished on MSE composites with single magnetic filler have shown that the magnetic filler used plays the major role for determining the magneto-mechanical behaviour of the sample, when the mechanical performance is coupled to an external magnetic field. Using the magnetic filler CIP or MAGSILICA revealed different mechanical and magnetorheological characteristics, which are opposite to each other. Samples filled with the magnetic filler CIP are associated with bad mechanical but good magnetorheological properties. Exactly the inverse is observed for samples filled with the magnetic filler MAGSILICA: good mechanical and bad magnetorheological properties.

The main reason of the different mechanical performances of the MSE composites is the mechanical reinforcing potential of the magnetic filler used. From static volumetric gas adsorption measurements, a specific surface area of $54\ m^2/g$ for MAGSILICA and $0.4\ m^2/g$ for CIP was determined. The specific surface area criterion suggests that MAGSILICA possesses more high-energy sites on the surface area than CIP. This leads more polymer chains to bond to the surface of the magnetic filler particles and hence to increase the reinforcing potential of the magnetic filler. Besides the filler concentration, the pronounced filler networking of the nanosized MAGSILICA particles is promoted by the particle size. The smaller the size of filler particles is the larger becomes the specific surface area and therefore the mechanical reinforcement of the filler.

The magnetorheological behaviour is explained by different magnetic interaction ranges between the magnetic filler particles and the magnetic field applied. Due to different particle sizes, the nanoscaled magnetic filler MAGSILICA becomes much earlier magnetically saturated than the microscaled CIP. The saturation magnetisation is the maximum possible magnetisation of a material, even if the external magnetic field increases. The saturation magnetisation of magnetic particles is size dependent and can be estimated by the so-called core-shell model [191]. It assumes that magnetic particles of diameter d are surrounded by a non-magnetic shell of thickness h. The saturation magnetisation of the bulk material is related to volume of the individual magnetic particle and it can be described by the following equation:

$$\frac{M_S^p}{M_S^\infty} = \frac{M_S(particle)}{M_S(bulk)} = \frac{V_{core}}{V_p} = 1 - 6\frac{h}{d} + 12\frac{h^2}{d^2} - 8\frac{h^3}{d^3} \approx 1 - 6\frac{h}{d} + O\left(\frac{h^2}{d^2}\right) \qquad (95)$$

where M_S^∞ is the saturation magnetisation of the bulk material, M_S^p is the saturation magnetisation of the particle and V_p is the volume of the magnetic particle.

To overcome these material dependent limitations and in order to enhance the dynamic-mechanical as well as the magnetorheological properties of the finished samples, MSE composites with hybrid filler systems were prepared. Hybrid filler systems permit to find a compromise between the two extreme behaviours. Each filler type, for his part, will contribute to the improvement of just one feature of the MSE composite.

10.1 Hybrid magnetic filler systems

SBR sample with hybrid magnetic filler systems at a constant magnetic filler volume fraction of 20 vol.% were prepared in the same way as the MSE composites with one magnetic filler. The microscaled magnetic filler CIP was replaced in intervals of 5 vol.% by the nanoscaled magnetic MAGSILICA.

10.1.1 Stress-strain behaviour

The stress-strain curves for the SBR samples with 20 vol.% hybrid magnetic fillers system at room temperature are shown in Figure 81.
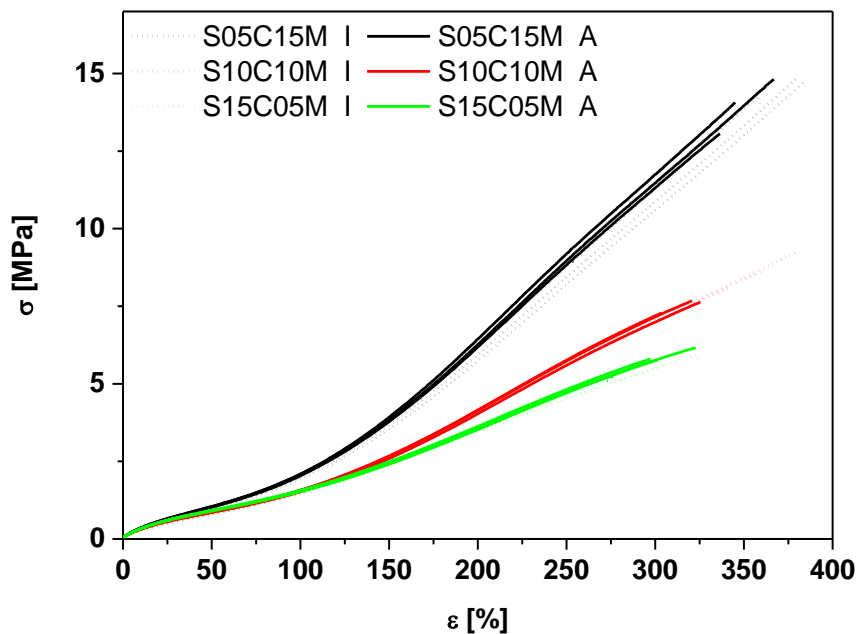
Figure 81: Stress-strain curves for SBR samples with **20** vol.% hybrid magnetic fillers with gradual replacement in intervals of **5** vol.% of CIP by MAGSILICA at room temperature. Isotropic samples are represented by dashed lines. Anisotropic samples are displayed with full lines.

The isotropic sample S05C15M I with 05 vol.% CIP and 15 vol.% MAGSILICA shows stress-strain behaviour similar to conventional reinforcing fillers like silica or carbon black. The stress-strain curves start with a low slope and a typical upturn to higher stress values. As the CIP content increases, the stress-strain curves become more flat and the stress values become smaller at the same deformation. As discussed earlier, the reason of such behaviour is explained by the reinforcement potential of the respective magnetic filler. Regarding the SBR samples with one magnetic filler system, S20C I with 20 vol.% CIP and S20M I with 20 vol.% MAGSILICA, the stress values of SBR samples with hybrid magnetic filler systems at 300 % ranges between a minimum of 5 MPa measured for S20C I and a maximum of 17 MPa measured for S20M I. The current examination shows that the stress and strain values of the

MSE composites filled with hybrid magnetic filler systems can be precisely adjusted and a compromise can be found.

The orientation of the magnetic filler particles within the samples does not play any significant role for these measurements as seen before because it is perpendicular to tensile direction [106, 107].

10.1.2 Dynamic-mechanical analysis

DMTA measurements were performed for the filled SBR samples with 20 vol.% hybrid magnetic fillers system at room temperature and a frequency of 1 Hz. The orientation of the magnetic filler particles was perpendicular to the shearing direction. The experimental results are shown in Figure 82.
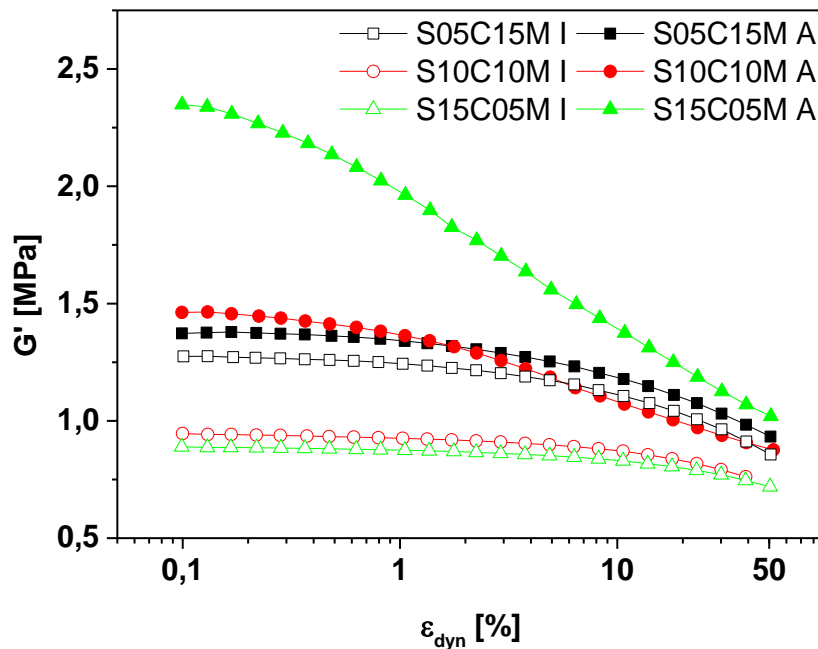
Figure 82: Amplitude dependence of the storage modulus for SBR samples with **20** vol.% hybrid magnetic fillers with gradual replacement in intervals of **5** vol.% of CIP by MAGSILICA at room temperature and a frequency of **1 Hz**. Isotropic samples are represented by open symbols. Anisotropic samples are displayed with closed symbols.

Figure 82 shows that the increasing of the MAGSILICA content in the isotropic MSE composites is followed by a corresponding increase of the storage modulus G'. Additionally, a similar trend as the stress-strain curves in Figure 81 is observed. The storage modulus of the isotropic SBR samples with one magnetic filler system S20C I with 20 vol.% CIP and S20M I with 20 vol.% MAGSILICA represent the external limits of the storage moduli of the isotropic SBR samples with hybrid magnetic filler system (see Figure 46).

G' of the isotropic sample S15C05C I with 15 vol.% CIP and 05 vol.% MAGSILICA is 0.87 MPa at 0.1 %. This is larger than 0.4 MPa; the storage modulus G' of the sample S20C I. In

addition, the isotropic sample S05C15M I with 05 vol.% CIP and 15 vol.% MAGSILICA has a storage modulus G' of about 1.27 MPa at 0.1 %. This is smaller than a storage modulus G' of 1.8 MPa for the sample S20M I at the same strain amplitude. This behaviour is related to the more pronounced filler networking of the nanosized MAGSILICA. The higher the MAGSILICA volume fraction in the isotropic MSE composite, the higher is the storage modulus.

Regarding the orientation of the magnetic filler particles, the strain storage modulus G' increases significantly for the anisotropic samples. A magnetic filler content of 5 vol.% of the microscaled CIP is enough to have a storage modulus G' closer to 1.8 MPa at 0.1 %, the maximal measured value of G' for the anisotropic sample S20M A with 20 vol.% MAGSILICA. The orientation of the microsized CIP particles in a magnetic field during curing appears to contribute more significantly to storage moduli of the samples than the filler networking potential of MAGSILICA. The higher the CIP content in the anisotropic MSE composite, the higher is the storage modulus. The nanoscaled MAGSILICA particles cannot form a pronounced anisotropic filler network due to its poor interaction with the external magnetic field during the vulcanisation. No additional contribution of the anisotropic structure to mechanical stiffening of the MSE composites filled with MAGSILICA can be delivered [106, 107].

10.1.3 Magnetorheology of non-crosslinked melts

Magnetorheological measurements of filled SBR samples with 20 vol.% hybrid magnetic fillers system were carried out. Variation of the storage modulus at a shear strain amplitude of 0.5 %, a frequency of 10 Hz and an initial temperature of 50 $°C$ during switching on and switching off of the magnetic field for the SBR melts with hybrid magnetic fillers system is shown in Figure 83.
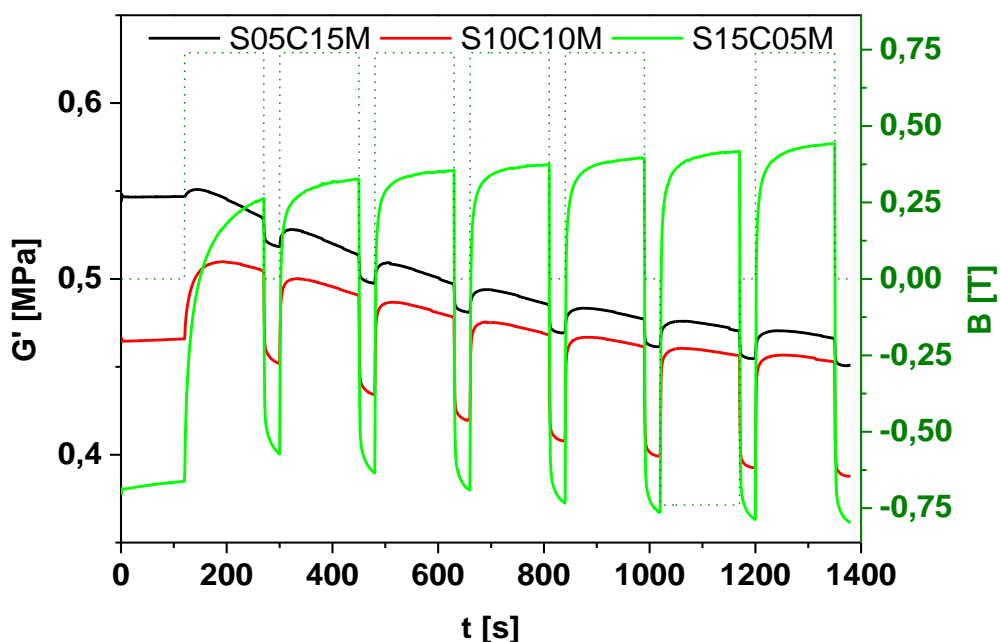
Figure 83: Variation of the storage modulus at shear strain amplitude of **0.5** %, frequency of **10 Hz** and initial temperature of **50 °C** during switching on and switching off the magnetic field for the SBR-melts with hybrid magnetic fillers system at constant **20** vol.%.

In the first 120 seconds, the magnetic field was turned off. The melt with higher amount of MAGSILICA than CIP shows the highest storage modulus G'. This matches with the capacity of nanosized MAGSILICA to build a stronger filler network than the microsized CIP.

The microsized magnetic filler CIP delivers a sufficient attraction in an external magnetic field and promotes the switching effect of the SBR melts. A non-zero MRE can be derived for all samples.

The samples S05C15M with 05 vol.% CIP and 15 vol.% MAGSILICA as well as the sample S10C10M with 10 vol.% CIP and 10 vol.% MAGSILICA are affected by the magnetic field. They additionally show a continuous decrease of the storage modulus G' with increasing flocculation time. This results from of the undesired heating of the magnetic cell during the measurement by about 10 °C after 1400 seconds. At these filler volume fractions, the MAGSILICA is still dominating the magnetorheological response of the SBR melts [106, 107]. The storage modulus G' of the SBR sample S15C05M with 15 vol.% CIP and 05 vol.% MAGSILICA seems to further increase once the magnetic field is switched on even after the measuring time of 1400 seconds. This indicates that the magnetic filler particles are not completely saturated. Naturally, only the CIP particles are concerned.

10.1.4 Magnetorheology of crosslinked samples

Figure 84 shows the variation of the storage modulus at a shear strain amplitude of 0.5 %, a frequency of 10 Hz and initial temperature of 50 °C during switching on and switching off

the magnetic field for isotropic and anisotropic SBR samples with hybrid magnetic fillers system at constant 20 vol.%. To minimize the thermal heating, the magnetic field is increased stepwise and the overall time is reduced to 500 seconds.
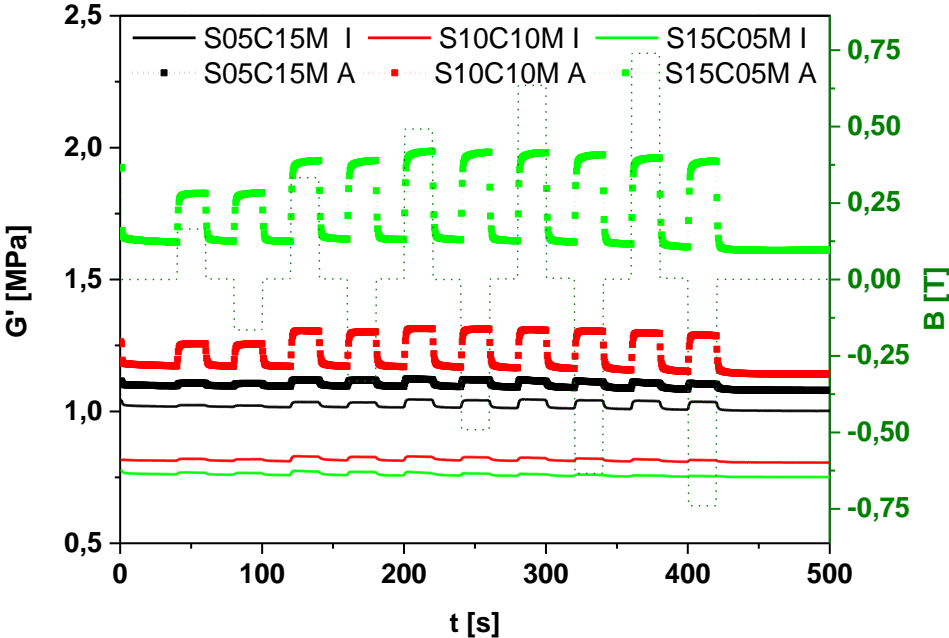
Figure 84: Variation of the storage modulus at shear strain amplitude of **0.5** %, frequency of **10 Hz** and initial temperature of **50 °C** during switching on and switching off the magnetic field for isotropic and anisotropic SBR samples with hybrid magnetic fillers system at constant 20 vol.%.

For isotropic samples, the SBR vulcanisates with higher amount of MAGSILICA than CIP show the highest storage moduli G' confirming the high mechanical reinforcing potential of the nanosized MAGSILICA compared to the microsized CIP. The switching effect of all isotropic MSE composites is very small independently of the CIP volume fraction because the magnetic filler particles are not aligned but more or less homogeneously distributed within the rubber matrix.

The columnar structure of the magnetic filler particles achieved during the curing in external magnetic field to prepare anisotropic samples promotes the magnetorheological response of MSE composites. All anisotropic SBR samples become stiffer and show a higher switching effect. As discussed earlier, this behaviour is directly proportional to magnetic filler amount of CIP.

To note is that the switching effect of vulcanisates is smaller than the switching effect of melts, because the mobility of magnetic filler particles in the rubber matrix is constrained by the crosslinking achieved during the curing process [106, 107].

10.2 Hybrid filler systems

Like all technical elastomeric materials, the MSE composites must have an application-related property profile. In order to satisfy the requirements regarding the dynamic-mechanical as well as the magnetorheological properties and to ensure optimum outcome, hybrid fillers systems were used to overcome the deficiencies of MSE composites filled with one-filler systems. While the microsized magnetic filler CIP contributes to switching ability, the nanosized MAGSILICA promotes the filler networking of the MSE composites.

As shown in the last section, it was found appropriate to use hybrid magnetic filler systems to achieve different dynamic-mechanical and magnetorheological results for several MSE composites. Nevertheless, the mechanical reinforcing potential of such filler systems remains not satisfactory. The MSE composites can be brought to application maturity by a new approach for hybrid filler systems. The microscaled magnetic filler CIP should be maintained as a carrier material for the switching ability of the MSE composites. However, a new nanoscaled filler should be used to obtain a better filler networking than MAGSILICA.

The conventional rubber filler silica (U 7000) was chosen due to its structural and chemical similarity to MAGSILICA to form with the microsized CIP the new hybrid filler system. Silica is a nanosized filler with a specific surface area of $162.5\ m^2/g$. A larger flocculation and thus a better mechanical reinforcement potential is expected compared with MAGSILICA. MAGSILICA has a specific surface area of $54\ m^2/g$. Silica also represents the coating layer of the MAGSILICA particles. The same chemical nature of the surface area ensures the same binding between the polymer chains and the filler particles. The renunciation of MAGSILICA and its iron oxides mixture hardly leads to a disadvantage because the contribution of MAGSILICA to magnetorheological properties of the MSE composites is negligible compared with CIP.

SBR samples with hybrid filler systems at a constant filler volume fraction of 20 vol.% were prepared in the same way as the MSE composites with hybrid magnetic filler systems. The microscaled magnetic filler CIP was replaced in intervals of 5 vol.% by the nanoscaled non-magnetic silica.

10.2.1 Stress-strain behaviour

The stress-strain curves for the SBR samples with 20 vol.% hybrid filler system with gradual replacement in intervals of 5 vol.% of CIP by silica at room temperature are shown in Figure 85. For comparing the results of the silica-filled samples, the measured data obtained for MSE composites with hybrid magnetic filler systems are additionally plotted in the same graph.
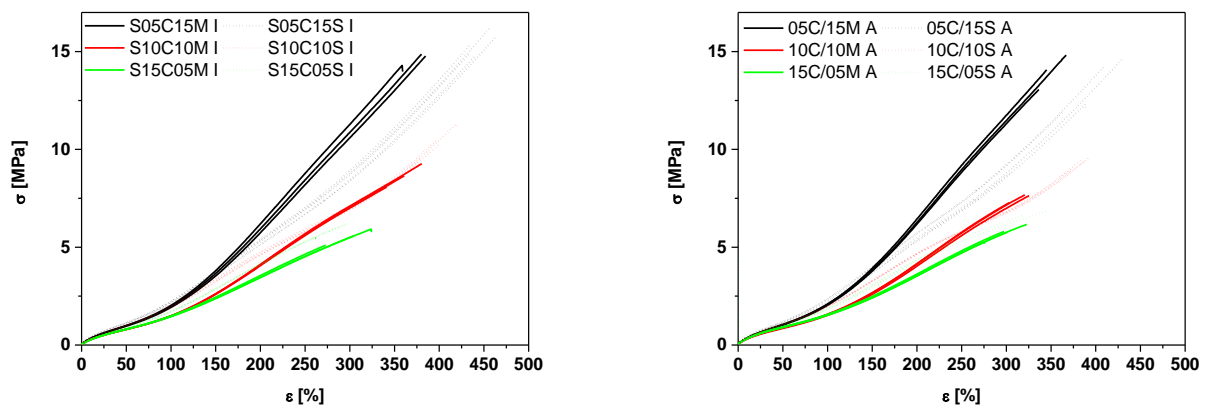
Figure 85: Stress-strain curves for SBR samples with **20** vol.% hybrid filler systems at room temperature. Measured data obtained for MSE composites with hybrid magnetic filler system are additionally plotted. Silica filled samples are represented by dashed lines. MAGSILICA filled samples are displayed with full lines. Isotropic samples are depicted on the left. Anisotropic samples are illustrated on the right.

The MSE composites with the different filler systems show an almost similar stress-strain behaviour for the samples with a larger CIP content.

For the samples with equal shares S10C10S I and S10C10S A with 10 vol.% CIP and 10 vol.% silica as well as S10C10M I and S10C10M A with 10 vol.% CIP and 10 vol.% MAGSILICA, the stress-strain curves have an almost identical curve progression. However, changes were observed. They concern the tensile strength at break and the elongation at break. The tensile strength at break is almost 2 MPa larger for the silica-filled sample. The same behaviour is observed for the elongation at break. It is nearly 50 % higher.

The stress-strain curves of the samples S05C15S I and S05C15S A with 05 vol.% CIP and 15 vol.% silica show from a strain value of 180 % a significant deviation from the stress-strain curves of the MAGSILICA-filled samples at the same filling ratio. This may be related to different synergy effects achieved during the curing process between CIP particles from one side and silica or MAGSILICA particles from the other side. The elongation at break is approximately 100 % larger for the silica-filled sample. The tensile strength at break is 1 MPa larger for the isotropic silica-filled sample.

The observed increase in tensile strength at break and elongation at break of the silica filled samples compared with the MAGSILICA filled samples is related to the high mechanical reinforcement of silica. This evidence was anticipated from the static volumetric gas adsorption measurements. A larger specific surface area of 162.5 m^2/g was derived for silica instead of 54 m^2/g for MAGSILICA.

The orientation of the magnetic filler particles has hardly any effect because the tensile direction is perpendicular to the magnetic filler strings.

10.2.2 Dynamic-mechanical analysis

DMTA measurements were performed for the filled SBR samples with 20 vol.% hybrid fillers system with gradual replacement in intervals of 5 vol.% of CIP by silica at room temperature and a frequency of 1 Hz. The experimental results are shown in Figure 86. The orientation of the magnetic filler particles was perpendicular to the shearing direction. For comparing the results of the silica-filled samples, the measured data obtained for MSE composites with hybrid magnetic filler system are additionally plotted in the same graph.
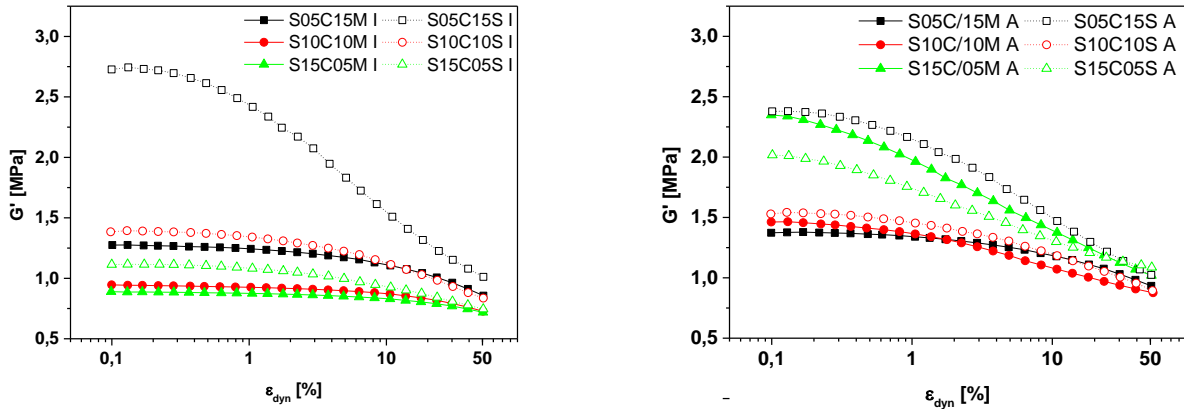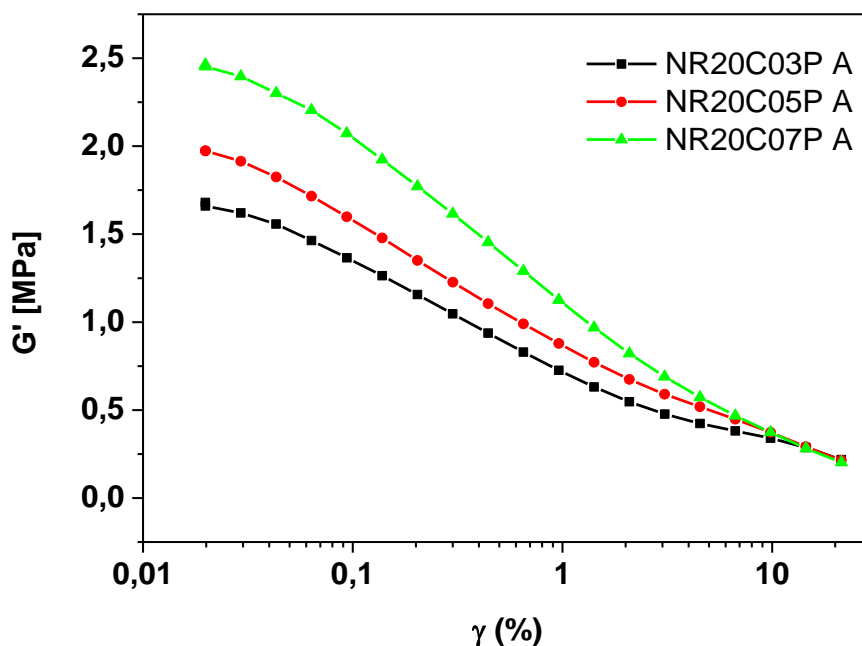

Figure 86: Amplitude dependence of the storage modulus for SBR samples with **20** vol.% hybrid fillers at room temperature and frequency of $1\ Hz$. Measured data obtained for MSE composites with hybrid magnetic filler system are additionally plotted. Silica filled samples are represented by dashed lines and open symbols. MAGSILICA-filled samples are displayed with full lines and closed symbols. Isotropic samples are depicted on the left. Anisotropic samples are illustrated on the right.

All MSE samples show a Payne effect. The strain storage modulus G' continuously decreases with increasing the strain amplitude. This indicates a continuous breakdown of the magnetic filler network.

For isotropic samples, the measured storage moduli G' systematically increase when the volume fraction of the nanoscaled filler increases. G' are larger for silica-filled SBR samples compared with the MAGSILICA-filled samples at the same filling ratio. G' is 2.7 MPa for the sample S05C15S I with 05 vol.% CIP and 15 vol.% silica at a strain amplitude of 0.1 %. It is only 1.3 MPa for the sample S05C15M I with 05 vol.% CIP and 15 vol.% MAGSILICA. This a clear indication of the – already confirmed - better networking behaviour of silica particles in comparison with MAGSILICA particles.

For the anisotropic samples filled with MAGSILICA, a systematic increase of G' is observed with increasing the CIP content. As already discussed, the storage modulus is mainly supported by the columnar microstructure of the CIP particles achieved during curing with an external magnetic field.

For the anisotropic samples filled with silica, G' is 2.4 MPa for the sample S05C15S A with 5 vol.% of CIP and 15 vol.% silica, 1.5 MPa for the sample S10C10S A with 10 vol.% of CIP

and 10 vol.% silica and 2.0 MPa for the sample S15C05S A with 15 vol.% of CIP and 5 vol.% silica at a strain amplitude of 0.1 %. This ranking remains unchanged until the end of the measurement. The fact that the anisotropic sample S05C15S A with only 5 vol.% of CIP has the largest storage modulus G' among the anisotropic silica filled MSE composites shows that G' is not only supported by the columnar microstructure of the CIP particles achieved during curing with an external magnetic field. The contribution of the network of the second filler in the hybrid filler system to G' can no longer be neglected. This behaviour confirms the presence of different synergy effects between CIP particles from one side and silica or MAGSILICA particles from the other side.

The existence of different synergy effects can also be verified when the two samples filled with 5 vol.% of CIP and 15 vol.% silica are considered. The isotropic sample S05C15S I has a storage modulus G' of 2.75 MPa at a strain amplitude 0.1 %. However, G' is only 2.4 MPa for the anisotropic sample S05C15S A. It appears that the silica network is more dominant than the CIP strings when the silica content is at least 15 vol.%. The CIP strings certainly disturb the emergence of a stiff silica network within the rubber matrix but they cannot prevent it.

10.2.3 Magnetorheology of crosslinked samples

Magnetorheological measurements were carried out for the filled SBR samples with 20 vol.% hybrid fillers system with gradual replacement in intervals of 5 vol.% of CIP by silica at a temperature of $50\,°C$, a shear strain amplitude of 0.5 % and a frequency of $10\,Hz$. The experimental results are shown in Figure 87. The magnetic field, shown on the right axis, is increased stepwise and the overall time is 500 seconds. For comparing the results of silica filled samples, the measured data obtained for MSE composites with hybrid magnetic filler system are additionally plotted in the same graph.
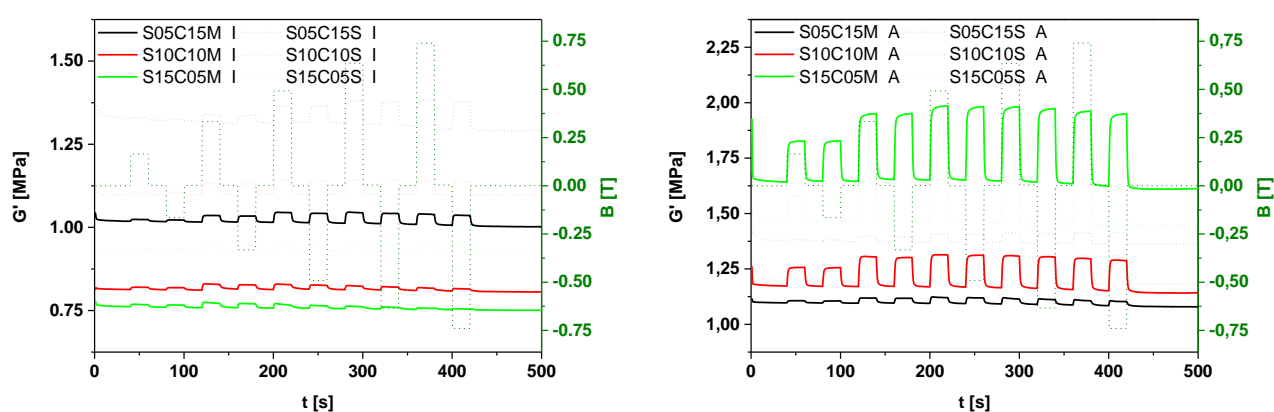
Figure 87: Variation of the storage modulus for SBR samples with **20** vol.% hybrid at strain amplitude of **0.5** %, frequency of **10 Hz** and initial temperature of **50°C** during switching on and switching off the magnetic field. Measured data obtained for MSE composites with hybrid magnetic filler system are additionally plotted. Silica filled samples are represented by

dashed lines. MAGSILICA-filled samples are displayed with full lines. Isotropic samples are depicted on the left. Anisotropic samples are illustrated on the right.

For isotropic samples, the achieved results confirm the earlier findings shown in Figure 86 despite the differences in test geometries and measurement conditions. The storage modulus G' increases with increasing the volume fraction of the nanoscaled filler in the hybrid filler system. Moreover, G' is larger for the vulcanisates filled with silica than with MAGSILICA. The silica filled samples additionally show a larger switching effect than the MAGSILICA filled samples. The largest magnetorheological effect (MRE) of 7 % is calculated for the sample S05C15S I with 5 vol.% of CIP and 15 vol.% silica and not for the MAGSILICA filled samples.

For anisotropic samples, higher storage moduli G' for all the samples are registered due to the additional contribution of the CIP strings to mechanical reinforcement. However, the ranking does not match with the previous DMTA results shown in Figure 86. This behaviour manifests the presence of more complex synergy effects between CIP particles from one side and silica or MAGSILICA particles from the other side

The MAGSILICA filled samples show a higher switching effect than the silica filled samples. Despite the small saturation magnetisation of MAGSILICA, the MAGSILICA particles are still affected by the applied magnetic field and support the improvement of the magnetic sensitivity of the MSE composites. This results in a maximum MRE of 23 % for the sample S15C05M A with 15 vol.% of CIP and 05 vol.% MAGSILICA and a maximum MRE of 18 % for the sample S15C05S A with 15 vol.% of CIP and 05 vol.% silica.

It can be recognised that the CIP - silica - systems can in general adjust the property profile of the finished MSE composites. Technical silica can indeed better enhance the dynamic-mechanical behaviour of the MSE composites than MAGSILICA. However, it should be taken into account that the switching effect can be significantly reduced due to the diamagnetic ordering of silica on the one side and due to the different synergy effects between the filler particles during curing on the other side.

It additionally appears that independently of the hybrid filler system used, the largest switching effect is realised by the one filler system CIP. A MRE of 30 % is observed for the anisotropic sample S20C A with 20 vol.% CIP. A CIP content of 20 vol.% represents an indispensable threshold value for optimising the magnetorheological response of the MSE composites.

10.3   Adaptive systems for active bearing platform

MSE composites can be used in diverse industrial and technical application areas. They consume less energy compared to other smart materials whilst ensuring safe operation processes and thus reducing the environmental impacts. Besides, they prolong the lifetime of elastomeric materials by optimizing the instantaneous usage to required property profile. They are successfully implemented in the field of sensor technology. For dynamic applications, the magneto-mechanical properties and ageing behaviour under mechanical load of MSE composites is under development. An application-related property profile is not yet completed.

Based on the results obtained so far, a simple draft for adaptive systems for an active bearing platform is designed. An adaptive system can adjust its behaviour and adapt it to changing surroundings through integrated sensors according to fixed control algorithms [192-194]. This new bearing platform should be able to detect the mechanical vibrations during operation in one side. In the other side, it should be able to self-handle and to actively react to these external circumstances. Within the framework of this thesis, an appropriate adaptive elastomer composite is realised. Figure 88 shows the operational principle of the active bearing platform.
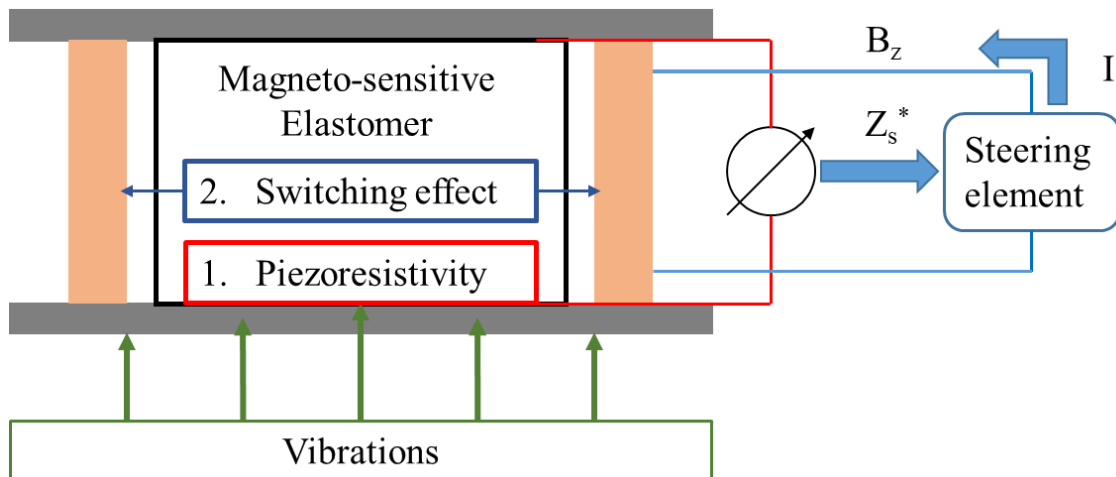
Figure 88: Operational principle of the active bearing platform

To catch the mechanical vibrations, the operational principle of the active bearing platform is based on the piezoresistive effect. A piezoresistive sensor is a pressure gauge. It is a composite material comprising a pressure transducer and a signal converter. The elastic strain gauge consists of a silicon membrane to which ohmic resistors are attached. The ohmic resistors are arranged as Wheatstone bridge so that the electrical resistance linearly changes with the elongation. The piezoresistive sensor measures the change in the electrical resistance of the strain gauge caused by a mechanical deformation [195, 196].

The piezoresistive effect can also be observed in high viscous elastomer composites. A necessary prerequisite is the existence of an electrically conductive filler network within the rubber matrix. If the sample is deformed, the elasticity modulus decreases with increasing the

strain amplitude according to Payne effect. This behaviour is caused by the breaking of the filler network. At high strain amplitudes, the desorption of adsorbed polymer chains at the filler surface areas could also take place.

The upper graph in Figure 89 shows the structure of a virgin filler network with a mean filler cluster size of ξ_0. The red lines display the available paths for the charge carriers to move freely. Placing the sample between two electrodes forms a sample capacitor according to the measuring principle of the capacitive electric field. This arrangement forms an electrically closed circuit and permits to measure the dielectric quantities of the test sample.

If the sample is deformed, the filler network gets broken. The corresponding structure is illustrated in the lower graph in Figure 89. The available paths for the charge carriers become longer because the path concentration is reduced. This results in a decrease of the elasticity modulus and the dielectric conductivity. Accordingly, the resistance of the sample increases.
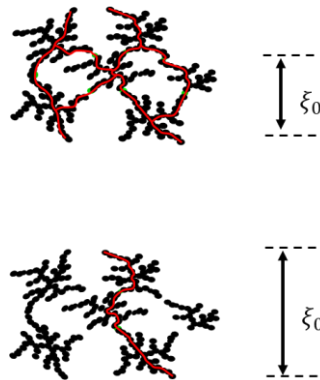
Figure 89: Breaking of the filler network during cyclic mechanical loading [**197**]

To prepare adaptive systems for the active bearing platform, MSE composites with hybrid fillers systems are used. As previously discussed, the nanoscaled fillers MAGSILICA and silica are characterised by a high networking potential compared to the microscaled CIP. They contribute as a part of hybrid filler system to improve the mechanical response of the MSE composites despite the negative impact on the switching ability. Nevertheless, MAGSILICA and silica are not appropriate for the development of adaptive systems for the active bearing platform because they are electrically non conducting. Silica is a well-known electrical insulator [88]. MAGSILICA particles are indeed produced on the basis of iron oxides but they are coated by an insulating layer in order to prevent eddy currents [116].

Instead, the nanosized Printex XE2-B is used. It is an electrically super conductive carbon black. Furthermore, it has a BET specific surface area of $1000 \; m^2/g$, which indicates a high mechanical reinforcing potential (see Table 1). Both characteristics make Printex XE2-B suitable for the development of adaptive systems for the active bearing platform.

In order to ensure the active bearing platform high adaptability, the microscaled magnetic filler CIP is used for its large magnetic sensitivity. As described in the section 9.4, a wide operational efficiency is realised by a CIP content of 20 vol.%. The anisotropic structure

achieved during curing with an external magnetic field further contributes to a higher mechanical reinforcement of the MSE composites.

In this approach, the MSE composites take advantage of the microsized magnetic filler CIP to increase the switching ability and benefit from the nanosized Printex XE2-B to create a stiff and conductive filler network. The MSE composites were prepared on the basis of NR. The Printex XE2-B filler content were varied between 0.8 vol.% and 1.8 vol.% in order to determine the dielectric threshold at which an electrically conductive filler network is built. An unnecessary increase of the sample viscosity can also be avoided. The increase in viscosity can hinder the mobility of CIP particles during the vulcanisation and consequently their orientation along the magnetic field lines. This would enormously affect the switching effect of the MSE composites.

10.3.1 Stress-strain behaviour

The stress-strain curves for the NR samples with hybrid filler systems at room temperature are shown in Figure 90.
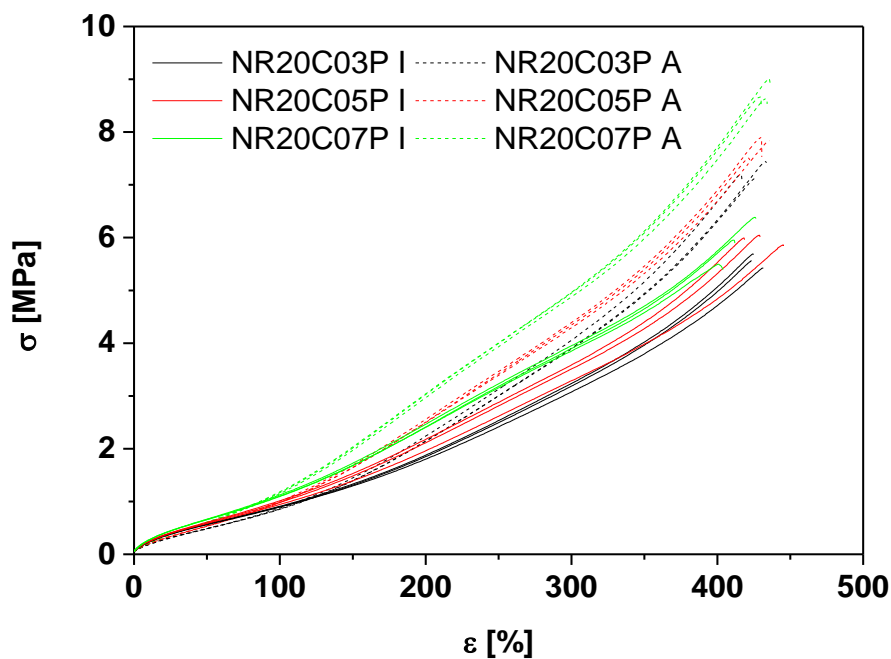
Figure 90: Stress-strain curves for NR samples with hybrid filler systems at room temperature. Isotropic samples are represented by full lines. Anisotropic samples are displayed with dashed lines.

The MSE composites with the different filler systems show an almost similar stress-strain behaviour. The stress values of the samples increase with increasing the Printex XE2-B content. The strain values remain almost unchanged at 430 %.

Larger stiffness values are measured for the MSE composites filled with the current hybrid filler systems compared to the NR samples NR20C I and NR20C A with only 20 vol.% CIP

shown in Figure 42. Obviously, the nanosized Printex XE2-B enhances the stiffening of all samples because a stable and reinforcing filler network is created. A Printex XE2-B content of 0.8 vol.% for the MSE composites NR20C03P I and NR20C03P A seems sufficient to attain the mechanical threshold.

In contrast to earlier stress-strain measurements for weakly polar rubbers (see Figure 40 and Figure 43), the anisotropic samples have significantly larger stress values than the isotropic samples. The difference between the stress values due to different inner microstructures is almost 2 MPa at a strain value of 400 %. This behaviour can also be attributed to the filler network of the nanosized Printex XE2-B. The reason is the perpendicular orientation of the columnar CIP strings within the samples to tensile direction.

10.3.2 Dynamic-mechanical thermal analysis

In order to determine the influence of the filler particle distribution on the dynamic mechanical response of the MSE composites, DMTA measurements were performed for the anisotropic NR samples with hybrid filler systems at room temperature and a frequency of $10\ Hz$. The amplitude dependence of the storage modulus G' is shown in Figure 91.

Figure 91: Amplitude dependence of the storage modulus for anisotropic NR samples with hybrid filler systems at room temperature and frequency of **$10\ Hz$**.

Obviously, all MSE composites show an amplitude dependent storage modulus. The storage modulus G' continuously decreases with increasing the strain amplitude. This confirms the findings of the last section. A stable filler network already exists. The decrease in G' is the result of the breaking of the hybrid filler network.

The storage modulus G' increases with increasing the Printex XE2-B volume fraction. This indicates that a reinforcing filler network is created from the nanosized Printex XE2-B particles. This additional structure improves the sample stiffness, beside the contribution of the oriented CIP strings. The mechanical threshold is reached by a Printex XE2-B content of 0.8 vol.%.

10.3.3 Magnetorheology of crosslinked samples

In order to determine the switching effect of the MSE composites, magnetorheological measurements were carried out on anisotropic NR samples with hybrid filler systems at room temperature, a frequency of 10 Hz and a shear strain amplitude of 0.5 %. The magnetic field is increased stepwise until a maximum of 0.49 T without changing the polarity. The measurement period is 1100 seconds. The experimental results are shown in Figure 92.
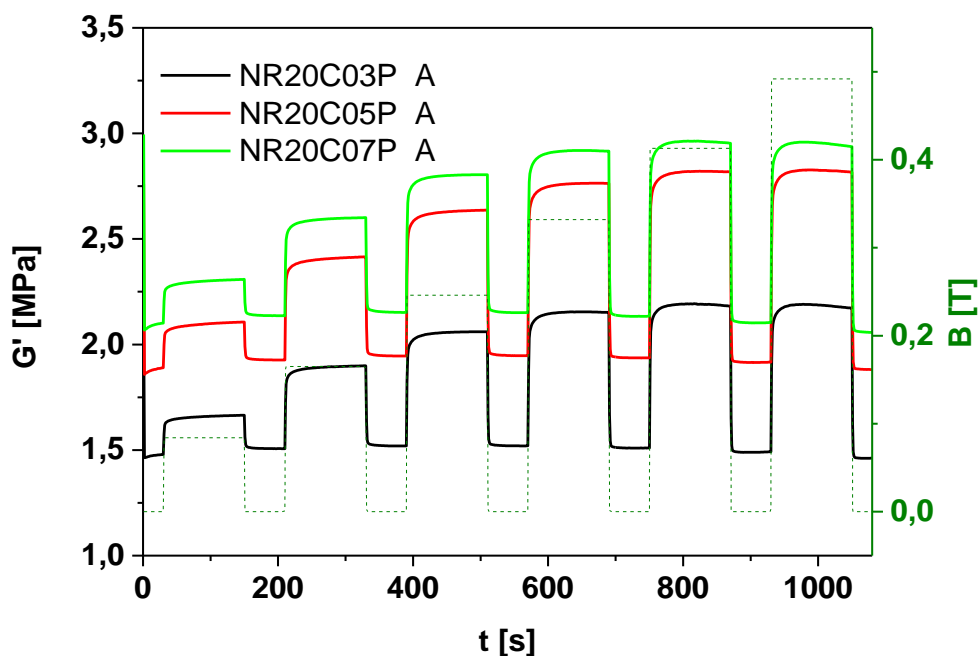
Figure 92: Variation of the storage modulus at room temperature, frequency of **10 Hz** and shear strain amplitude of **0.5** % during switching on and switching off the magnetic field for anisotropic NR samples with hybrid filler systems.

Anisotropic NR samples were prepared during the vulcanisation in external magnetic field. As mentioned earlier, the achieved columnar structure of the magnetic filler particles improves the magnetic sensitivity of the MSE composites. A magnetorheological effect (MRE) of 35 % is observed for the anisotropic sample NR20C07P A with 20 vol.% CIP and 1.8 vol.% Printex XE2-B. The MRE of the anisotropic sample NR20C05P A with 20 vol.% CIP and 1.3 vol.% Printex XE2-B is 44 %. The MRE of the anisotropic sample NR20C03P A with 20 vol.% CIP and 0.8 vol.% Printex XE2-B is 43 %.

The increase in the Printex XE2-B content has contributed to the increase of the sample viscosity. All NR samples become stiffer due to the enhanced filler networking. But this led to the decrease of the switching effect because the orientation of the microscaled CIP particles during curing along the magnetic field lines as well as the orientation of the magnetic dipoles during the magnetorheological measurements become more difficult. The optimal Printex XE2-B content for the best magnetorheological response seems to be at 1.3 vol.%. However, it remains to examine if the dielectric threshold of the MSE composite is therefore reached.

10.3.4 Combined rheological and dielectric measurements

Combined dielectric and rheological investigations at room temperature and a frequency of 10 Hz were carried out. The strain history is depicted in Figure 93.
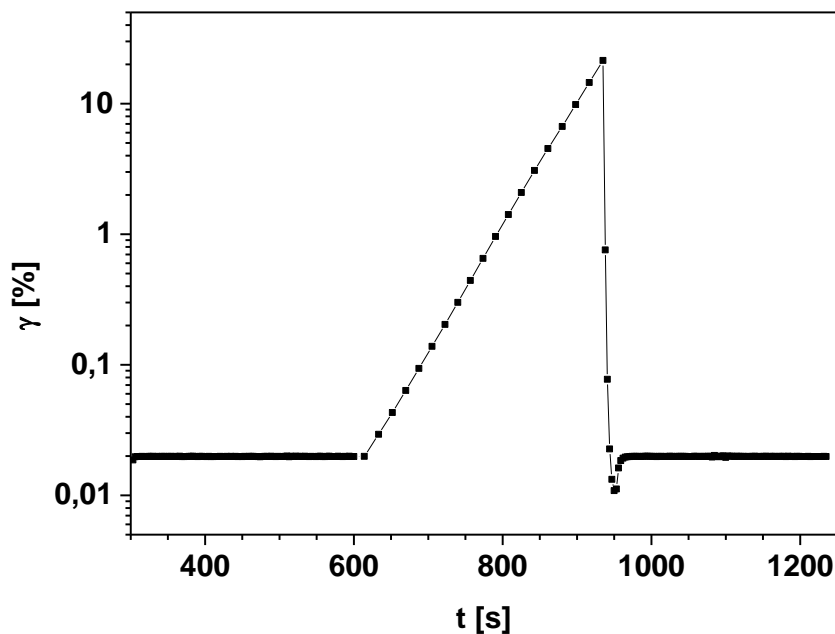
Figure 93: Strain history for combined rheological and dielectric measurements.

The MSE composites were first subjected to small shear amplitude γ of 0.02 % for 600 seconds. Afterward, γ was gradually increased from 0.02 % to 21 % to examine the amplitude dependence of the storage modulus G' and the real part of the impedance Z'_s. In the last step, γ is abruptly reduced to 0.01 % for a short time and is then kept at 0.02 % for 300 seconds to determine the relaxation behaviour of the samples.

In order to determine the dielectric threshold of the adaptive systems for active bearing platform, dielectric investigations have revealed that the samples are dielectric conductors when the content of the nanosized Printex XE2-B is above 1.8 vol.%.

Figure 94 shows the amplitude-dependent variation of the storage modulus G' and the real part of the impedance Z'_s for the anisotropic sample NR20C07P A with 20 vol.% CIP and 1.8 vol.% Printex XE2-B.
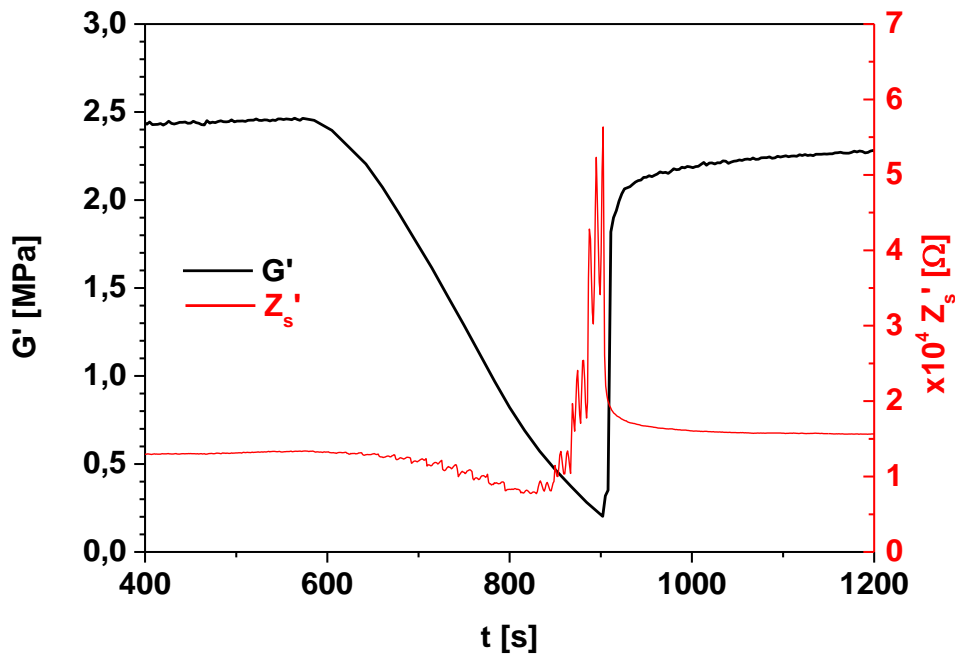
Figure 94: Combined rheological and dielectric measurements on the anisotropic NR sample NR20C07P A with **20** vol.% CIP and **1.8** vol.% Printex XE2-B at room temperature and frequency of **10 Hz**. As a function of time, the storage modulus is plotted on the left y-axis and the real part of the impedance is plotted on the right y-axis.

Figure 94 displays a correlation between the dynamic-mechanical and dielectric measurements. At constant shear amplitude, the anisotropic sample NR20C07P A is in a state of equilibrium. The storage modulus G' is almost 2.45 MPa after 600 seconds while the real part of the impedance Z_s' is nearly 1.3 10^4 Ω.

In the second step, the storage modulus G' decreases continuously with increasing the shear amplitude. This behaviour is related to a constant breaking of the filler network. G' decreases from 2.45 MPa at 0.02 % to 0.17 MPa at 21 % after 300 seconds. The drop of storage modulus G' is associated with a long-term increase of the real part of the impedance Z_s'. At first Z_s' behaves like G' for 230 seconds and decreases from 1.3 10^4 Ω at 0.02 % to 0.77 10^4 Ω at 4.5 %. The decrease of Z_s' means that the dielectric conductivity of the sample has increased. This can be mainly attributed to a further flocculation of the Printex XE2-B particles while the deformation increases. Consequently, a compact and conductive filler network within the sample is maintained. This can be explained by the fact that large filler clusters are first broken compared with small filler clusters because they carry more local stress. In this case, increasing the deformation breaks first the large CIP clusters. The Printex XE2-B clusters are preserved and come even closer to one another. This process is retained until the most CIP clusters are broken.

After the slight decline, a disproportionate increase of Z'_s from $0.77 \, 10^4 \, \Omega$ at $4.5 \, \%$ to $5.6 \, 10^4 \, \Omega$ at $21 \, \%$ is observed within 70 seconds. This indicates that the Printex XE2-B network already started to break apart.

In the last step of this measurement, the relaxation behaviour of the sample is examined. The deformation is abruptly reduced to $0.01 \, \%$ and is then kept at $0.02 \, \%$ for 300 seconds. Plateau values are observed. The storage modulus G' is $2.28 \, \text{MPa}$ while the real part of the impedance Z'_s is $1.52 \, 10^4 \, \Omega$. The relaxation behaviour is related to reflocculation processes, which are always associated with stress softening. This explains why the initial values of both the storage modulus G' and the real part of the impedance Z'_s are not reached.

10.3.5 Influence of the mechanical fatigue on MRE

The mechanical fatigue represents a main pillar of the property profile of the MSE composites. For active bearing platform, it is useful to perform the mechanical tests in compression mode in contrast to what was done in section 7.4.1.

The measurement sequence was as follows. The relative magnetorheological effect (MRE) was first determined for all virgin MSE composites. Afterwards, the samples were subjected to mechanical fatigue tests in compression mode using the dynamic-mechanical analyser Eplexor. The MRE of the damaged samples is measured for the second time under the same condition. The magnetorheological measurements were carried out at room temperature, a shear strain amplitude of $0.5 \, \%$ and a frequency of $10 \, Hz$.

The anisotropic sample NR20C07P A with 20 vol.% CIP and 1.8 vol.% Printex XE2-B was subjected to a constant static load of $300 \, N$ and a variable dynamic load over 10.000 cycles. The dynamic force was $50 \, N$, $100 \, N$, $150 \, N$ or $200 \, N$. A virgin sample was used for each dynamic-mechanical measurement. The measurements were performed at room temperature and a frequency of $10 \, Hz$.

Figure 95 shows the dynamic-mechanical behaviours of MSE composites after 10.000 loading. As a function of dynamic force, the storage modulus E' is displayed on the left y-axis and the dynamic strain ε_{dyn} is displayed on the right y-axis.
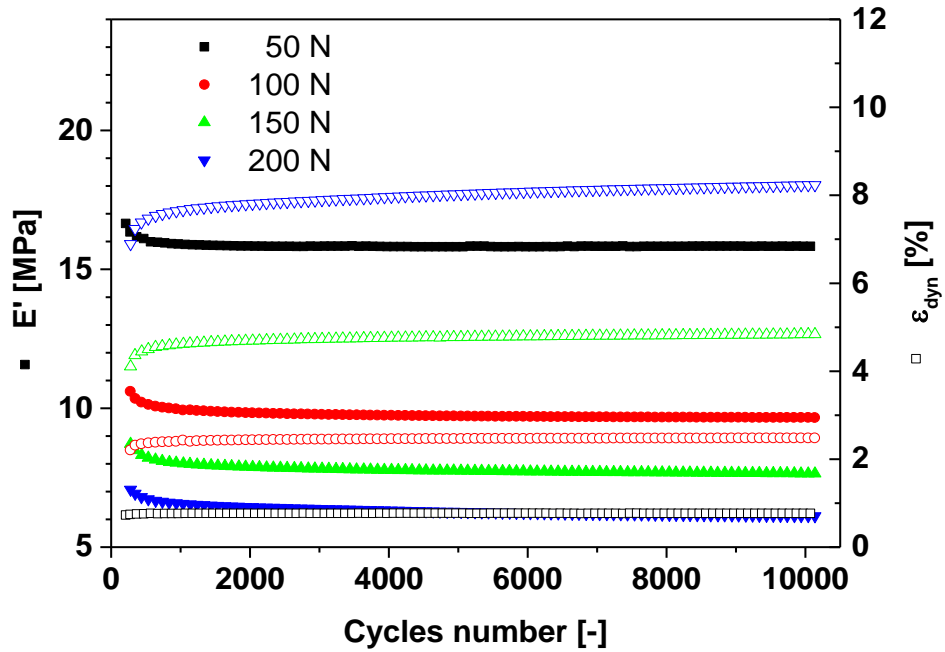
Figure 95: Dynamic-mechanical behaviour of the anisotropic sample NR20C07P A with 20 vol.% CIP and 1.8 vol.% Printex XE2-B after $\mathbf{10.000}$ loading cycles at room temperature and frequency of $\mathbf{10\,Hz}$. As a function of dynamic force, the storage modulus is represented with full symbols and is plotted on the left y-axis. The dynamic strain is represented with empty symbols and is plotted on the right y-axis.

The anisotropic samples NR20C07P A were deformed by a constant static force of 300 N and an additional dynamic force. With increasing the amplitude of the dynamic force, the dynamic strain ε_{dyn} increases.

At a constant dynamic force, the increase in the number of loading cycles results in a time-dependent deformation process. The dynamic strain ε_{dyn} further increases while the storage modulus E' shows a steady decrease. The time t can be estimated according to the following equation:

$$t = \frac{N}{f} \tag{96}$$

where N is the number of loading cycles and f is the frequency.

This behaviour corresponds to a creep behaviour of the MSE composites. The sample is instantaneously deformed after load application. This is followed by an approximately exponential increase of the dynamic strain ε_{dyn} with increasing the number of loading cycles. The creep behaviour can be characterised by relaxation time spectra. In extreme cases, ε_{dyn} increases linearly with time [198].

Figure 96 shows the magnetorheological responses of the MSE composites after 10.000 loading cycles during switching on and switching off the magnetic field. An on-off switching

mode of the magnetic field without alternating polarity is considered. The magnitude of the magnetic field is plotted on the right y-axis
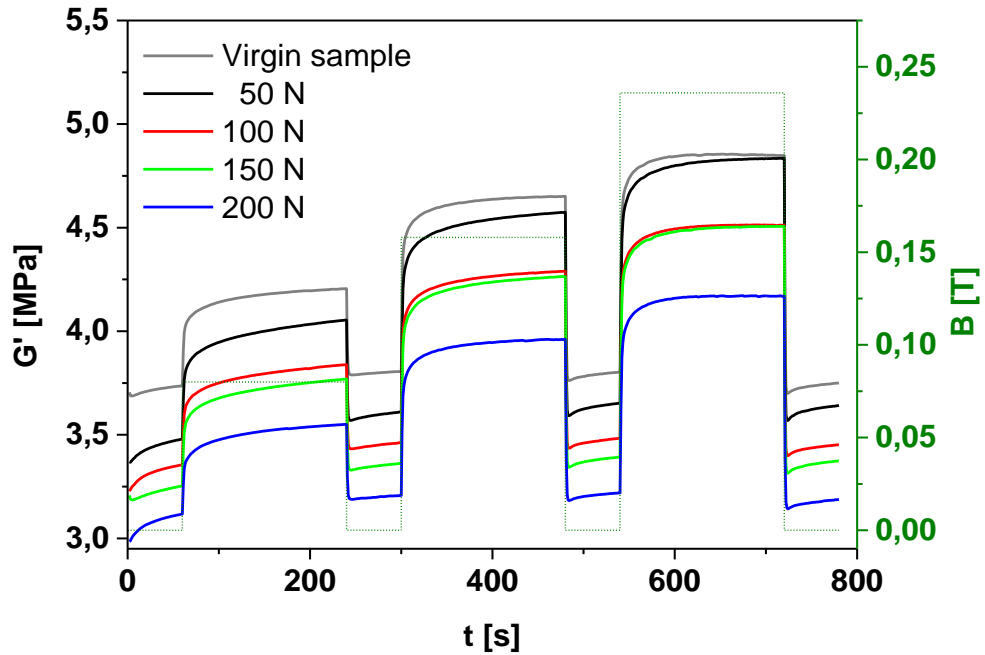
Figure 96: Variation of the storage modulus at room temperature, shear strain amplitude of **0.5** % and frequency of **10 Hz** during switching on and switching off the magnetic field for the anisotropic sample NR20C07P A with 20 vol.% CIP and 1.8 vol.% Printex XE2-B after **10.000** loading cycles. As a function of time, the storage modulus is plotted on the left y-axis and the magnitude of the magnetic field is plotted on the right y-axis.

Figure 96 shows that the relative magnetorheological effect (MRE) of the NR samples is slightly affected by the different mechanical loads. The switching effect for the anisotropic samples is summarized in Table 15.

Table 15: MRE for the anisotropic samples NR20C07P A derived from magnetorheological measurements at room temperature, shear strain amplitude of 0.1 % and frequency of 10 Hz.

B \\ F	0 N	50 N	100 N	150 N	200 N
0.08 T	0.12	0.17	0.13	0.15	0.14
0.16 T	0.22	0.26	0.25	0.27	0.23
0.24 T	0.28	0.32	0.30	0.35	0.30

Obviously, all loaded samples have a higher MRE than the virgin sample. It seems that the CIP clusters were remained intact even at a high force amplitude of 200 N. This corresponds to a dynamic strain ε_{dyn} of 8 %. At this limit, the examined samples show a Payne effect (see Figure 44, Figure 46, Figure 47 and Figure 50). The reason behind this is the parallel arrangement of the columnar structure of the CIP particles relative to the compression direction. The CIP particles are pressed together and are not sheared. In addition, this loading

mode reduces the mean distance between the CIP clusters. Therefore, the magnetic sensitivity of the samples increases.

The difference in the MRE values for the loaded samples cannot only be attributed to the value of the force amplitude. No classification scheme can be created. Apparently, a close magnetic interaction remains between the magnetic dipoles of the CIP particles. This does not only concern the first CIP clusters, but also the newly formed soft CIP clusters.

Furthermore, the storage modulus G' decreases with increasing the dynamic force. This matches with the DMTA results shown in Figure 91 and corresponds to the Mullins effect. A stress softening is observed due to mechanical damage induced.

Figure 97 summarizes both the dynamic-mechanical and the magnetorheological response of the anisotropic sample NR20C07P A with 20 vol.% CIP and 1.8 vol.% Printex XE2-B. The amplitudes of the dynamic force are displayed on the x-axis. The limit values of the storage modulus G'_{inf} after 10.000 cycles are shown on the left y-axis. The relative magnetorheological effect (MRE) is presented on the right y-axis.
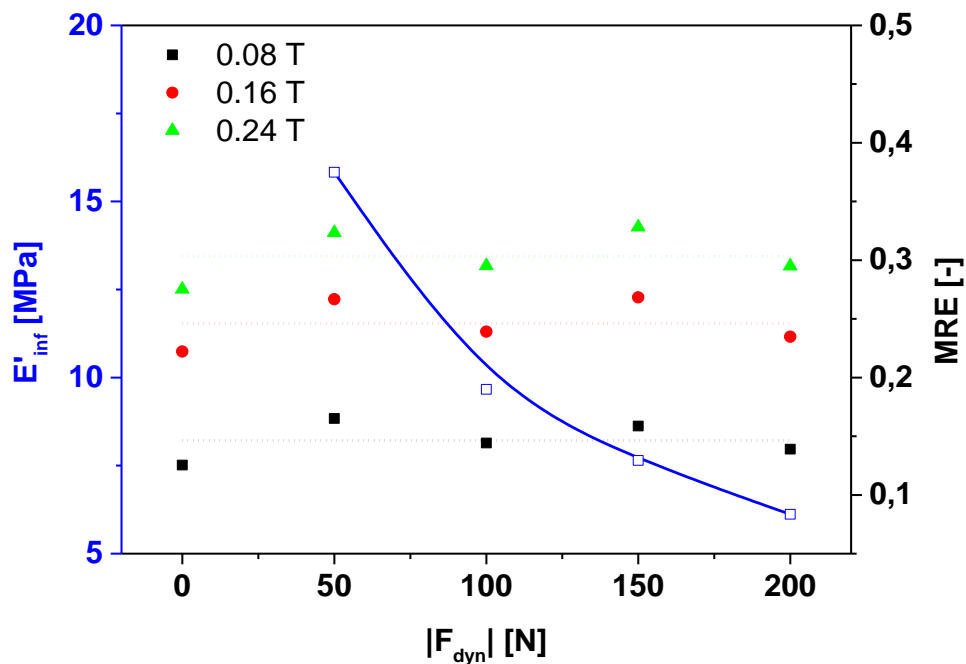
Figure 97: Influence of mechanical fatigue tests on the storage modulus E' and the magnetorheological effect for the anisotropic sample NR20C07P A with 20 vol.% CIP and 1.8 vol.% Printex XE2-B.

10.4   Outlook: New hybrid filler systems for MSE composites

It was shown in the previous sections that the dynamic-mechanical as well as the magnetorheological properties of the MSE composites can be set with hybrid filler systems. A compromise was found between the stiffness and the switching effect of the samples by combining the microscaled CIP with a nanoscaled filler. The microscaled iron-based CIP was responsible for the magnetic sensitivity of the samples. The nanoscaled reinforcing filler was responsible for the sample stiffness.

Despite the results achieved, it should be taken into account that a decrease in stiffness. is always associated with the hybrid filler systems. The reduction of the particle size can enhance the mechanical reinforcement of the sample [170]. But, this downsizing is almost always correlated with an increase in the sample viscosity provided that the surface structure of the particles is considered. This in turn implies an inevitable deterioration of the switching effect [106, 107].

Composite materials made of elastomers and reinforcing supports are widely used in technical application. Novel approaches have improved the functionality of the elastomeric materials in terms of lifetime, durability, and comfort by using new carbon based fillers. New innovative elastomer composites on the basis of carbon nanotubes (CNT), graphene and textile fibres are already being examined and discussed. In the rubber technology, the carbon based fillers were used in combination with conventional rubber fillers [199-204]. These new elastomer composites fulfil a variety of functional requirements such as high tensile strength, high dynamic load resistance, crack resistance, abrasion resistance or sufficient electrical conductivity. The major factor responsible for this is the anisotropic structure of CNT, graphene and textile fibres.

To provide the two-dimensional carbon based fillers magnetic properties, CNT, graphene as well as textile fibres can be coated with iron or iron oxides. These novel concepts can then be used to improve the property profile of the MSE composites. The following subsections are proposed for consideration in new studies only.

10.4.1 Magnetic graphene

Magnetic graphene nanosheets are used for applications in lithium storage units [205, 206], biosensing [207] and biomedicine [208-210].

Reduced graphene oxide (rGO) are prepared by arranging the iron and/or iron oxide particles on the graphene surface at high temperature in a hydrogen/argon atmosphere. An iron-iron oxide matrix emerges on graphene. The iron was a zero valent iron (ZVI). ZVI has a filled valence shell and is electrically neutral. It is denoted by Fe^0. The iron oxide used was magnetite (Fe_3O_4). At a temperature of $400\,°C$, a high porous matrix of reduced graphene oxide with iron and iron oxide rGO-Fe^0-Fe_3O_4 is formed. At $600\,°C$, Fe_3O_4 is entirely transformed into ZVI. A reduced graphene oxide with iron rGO-Fe^0 is formed. Figure 98 illustrate the reduced graphene oxide with iron and iron oxide rGO-Fe^0-Fe_3O_4 on the left and the reduced graphene oxide with iron rGO-Fe^0 on the right.
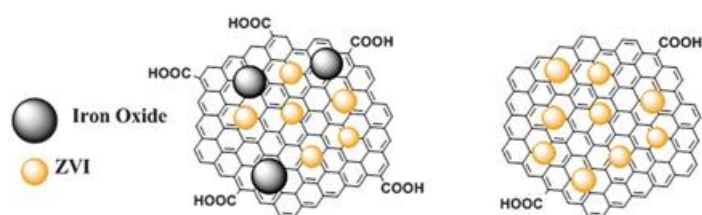
Figure 98: The reduced graphene oxide with iron and iron oxide rGO-Fe^0-Fe$_3$O$_4$ is illustrated on the left. The reduced graphene oxide with iron rGO-Fe^0 is depicted on the right [**212**]

Besides the superparamagnetic character, the reduced graphene oxides rGO-Fe^0-Fe$_3$O$_4$ and rGO-Fe^0 have a highly heterogeneous structure. The gas adsorption measurements were performed with nitrogen N_2. The specific surface area is obtained using the BET model (see chapter 6). The specific surface area of rGO-Fe^0-Fe$_3$O$_4$ is 384.6 m^2/g. It is 124.3 m^2/g for rGO-Fe^0 and 140.7 m^2/g for the reduced graphene oxide with magnetite rGO- Fe$_3$O$_4$ [212].

10.4.2 Magnetic Carbon Nanotubes

The carbon nanotubes (CNT) consist of closed cylindrical graphite layer. They have a diameter of a few nanometres and a length in the micrometre range [213]. Depending on the manufacturing processes, CNT can be single-walled (SWCNT), double-walled (DWCNT) or multi-walled (MWCNT). CNT are divided according to the spatial arrangement of the atoms. Achiral CNT are highly symmetric and chiral CNT are spirally symmetric. Achiral CNT can have a zig-zag structure or an armchair structure [214-216]. These different CNT structures are depicted in Figure 99.
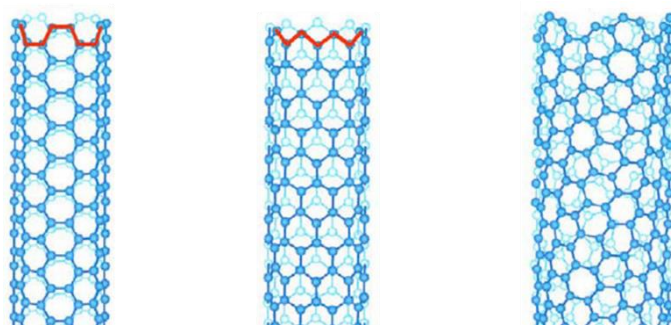
Figure 99: Carbon nanotube structures. The graph on the left represents achiral CNT with armchair structure. In the centre graph, achiral CNT with zig-zag structure are displayed. On the right, chiral CNT are illustrated [**214**].

This distinction is relevant because it determines the mechanical and the electrical properties of CNT. CNT exhibit extreme high mechanical strengths and stiffness values. Arm chair CNT conduct the electricity like metals. The other CNT behave like semiconductors [212-214]. The CNT are used among others in the semiconductor technology [215-217], sensors [218-

220] and biomedical applications [221-223]. CNT are also used in the rubber technology to improve the mechanical and dielectric properties of elastomer composites [224, 225].

In order to realise versatile systems, CNT can be further optimised through functionalisation with magnetic or superparamagnetic particles to obtain magnetic CNT (Mag-CNT). In the following, a short list of already prepared Mag-CNT is presented, which can be considered for use as hybrid filler systems in MSE composites.

To impart magnetic properties, CNT can be filled with metals or ferrofluids as shown in Figure 100. Prepared with "nanostraws" technique, the ferrofluid – a suspension of magnetite (Fe_3O_4) in hexane – is poured into CNT. An external magnetic field is used to promote the penetration of Fe_3O_4 particles in the tubes. The solvent is later removed by evaporation [225].
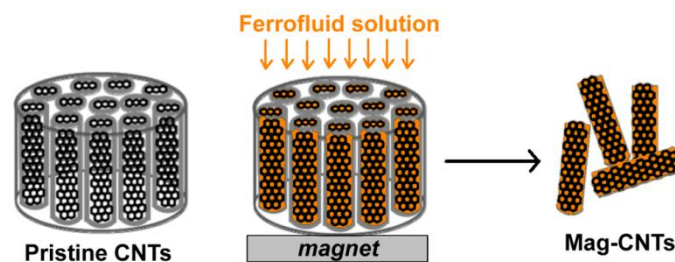
Figure 100: Preparation of Mag-CNT by filling CNT with a ferrofluid – a suspension of Fe_3O_4 in hexane [**225**].

Mag-CNT can also be realised by coating the surface of CNT with single-molecule magnets $(Mn_{12}O_{12}(O_2CCH_3)_{16}(H_2O)_4)$, spinel ferrites $(Me-Fe_2O_4)$, cobalt-containing magnetic polyoxometalate $((As_2W_{20}O_{68}Co(H_2O))^{8-})$ or iron nanoparticles.

The coating with iron nanoparticles can be achieved according to the Fenton´s reagent synthetic scheme as shown in Figure 101. A Fe_2O_3-CNT composite is realised [225].
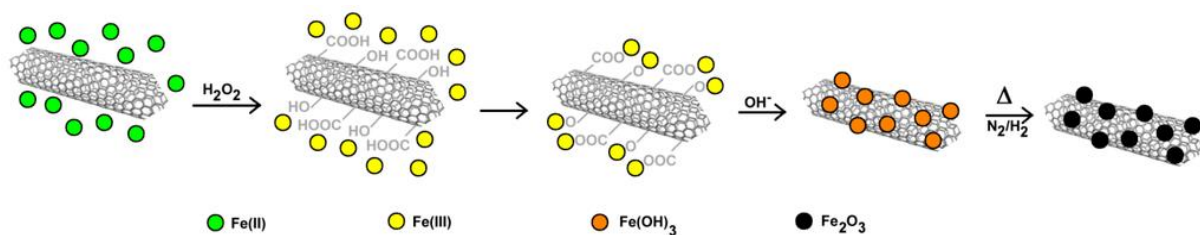
Figure 101: Preparation of Mag-CNT by coating the CNT with iron nanoparticles [**225**].

Mag-CNT can be a very interesting alternative to hybrid filler systems discussed earlier because they can additionally be coated with silica layer as shown in Figure 102 [226].
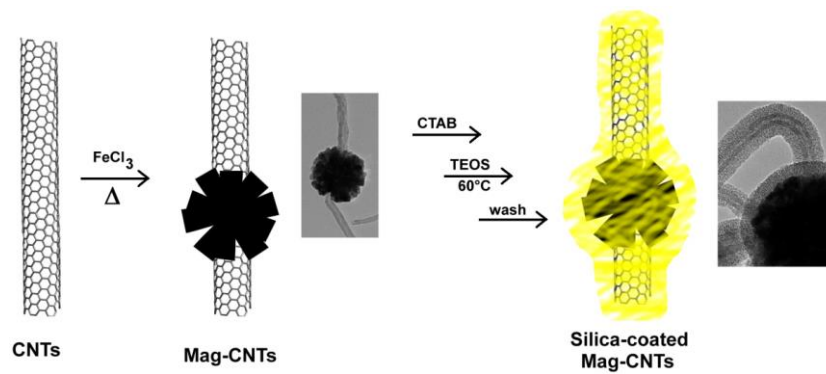
Figure 102: Preparation method of silica coated Mag-CNT [**226**].

11 Summary and Conclusions

Magneto-sensitive elastomers (MSE) consist of an insulating rubber matrix in which magnetic filler particles are embedded. They are able to vary in real time their rheological properties in order to ensure adaptability to changing environmental conditions. This behaviour is achieved by means of magnetic fields, which yield to a coupling between the dynamic-mechanical and the magneto-rheological properties of MSE. In contrast to conventional elastomer composites, the MSE responses can then be actively controlled according to the magnetic field settings.

Two different magnetic fillers were used. The carbonyl iron particles SW-S (CIP) is a microscaled iron-based magnetic filler. MAGSILICA is a nanoscaled magnetic filler. It consists of iron oxide mixture embedded in a silica matrix. Static volumetric gas adsorption measurements were performed in order to determine the specific surface area of the magnetic fillers according to the BET model. This constitutes an important tool for predicting the filler networking. A specific surface area of $0.4\ m^2/g$ was derived for CIP. MAGSILICA has a specific surface area of $54\ m^2/g$.

The vulcanisation was achieved in the presence of a magnetic coil system in order to influence the setting up of the filler network within the rubber matrix. As soon as no magnetic field was applied, the magnetic filler particles were homogenously dispersed and isotropic MSE composites were obtained. But if the magnetic field was applied, the magnetic filler particles aligned themselves along the magnetic field lines due to magnetic dipole-dipole interactions. A columnar structure arose and the MSE composites became anisotropic. SEM images confirmed the inner structure of the magnetic filler network.

From design and choice of the different components, through vulcanisation process until applied magnetic field during application, different factors influence the properties of the final MSE composites to different degrees.

Mechanical measurements showed that the mechanical reinforcement is mainly supported by the nanoscaled magnetic filler. The mechanical reinforcement potential is attributed to the networking capacity of the filler used, which can be evaluated through the formation of a physically bonded filler network and a strong polymer-filler coupling. With a higher specific surface area, MAGSILICA offers a larger surface area for the polymer chains to adhere compared to CIP.

Stress-strain measurements provide the first evidence for the better networking potential of MAGSILICA. The samples S20M A and S20M I with 20 vol.% MAGSILICA showed larger stress values than the samples S20C A and S20C I with 20 vol.% CIP at the same strain amplitude. Similar to conventional reinforcing fillers like silica or carbon black, the stress values of the MSE composites increase with increasing the filler loading. Furthermore, it was found that the polarity of rubber may play a non-negligible role in determining the stress-strain behaviour of the samples.

The orientation of the magnetic filler particles did not really affect the stress-strain values of the MSE composites. The reason for this lies in the fact that the loading direction was perpendicular to the magnetic filler strings.

Dynamic-mechanical measurements showed that all MSE composites were subject to the Payne effect. The storage modulus decreased with an increase in the strain amplitude. Moreover, the distribution of the magnetic filler particles within the rubber matrix during vulcanisation seems to play a key role. High storage moduli were obtained when the magnitude of the magnetic field applied during curing were increased. This is the result of a better magnetic dipole-dipole interaction between the magnetic filler particles and the applied magnetic field during curing, which governs the distribution of the magnetic filler particles within the rubber matrix and thus the degree of anisotropy of the MSE composites. This leads to the creation of a distinctive columnar structure promoting the mechanical reinforcement of MSE composites. However, the storage moduli of the filled samples N36C A and N36C I with 36 vol.% CIP show no discernible difference due to anisotropy. Obviously, there is a clear limitation to the filler volume fraction. This behaviour indicates that no magnetic filler strings were formed during the curing process, even in a magnetic field. This can be related to a strong reciprocal mobility restriction of the polymer chains and the magnetic filler particles, which inhibits the orientation of the magnetic filler particles along the magnetic field lines.

The coupling agent silane was used to enhance the interaction between polymer chains and the magnetic filler CIP as well as MAGSILICA. A strong chemical bonding at the polymer-filler interface was established through the coupling reaction of the silane with the magnetic filler during mixing and the rubber matrix during the vulcanisation. This led to a better distribution of the magnetic filler particles in the sample and to a high mechanical reinforcement.

Both mechanical and thermal ageing experiments showed a similar ageing behaviour of the MSE composites to conventional rubber samples. There were no indications that the magnetic filler particles lost their covering coating and react directly or indirectly with the polymer chains even under high dynamic loading.

Magnetorheological measurements were performed on the non-crosslinked melts in order to visualise the effect of particle orientation during the curing process. The MSE composites filled with the microscaled CIP showed a pronounced switching effect once the magnetic field is turned on. The relative magnetorheological effect (MRE) was more than 40 % for the sample S20C filled with 20 vol.% CIP. However, the sample filled with the nanoscaled MAGSILICA was hardly affected by the magnetic field. This indicates different interaction strengths between the magnetic filler particles and the applied magnetic field. It was found that the magnetic dipole-dipole was direct proportional to the particle size. Obviously, the magnetic moments of the nanoscaled MAGSILICA were too small to deliver a satisfactory attraction in an external magnetic field. The particles were relatively quickly saturated in contrast to the microscaled CIP particles, which interacted well with the magnetic field by aligning themselves along the magnetic field lines. Beside the particle size, the filler

composition played also a decisive role. Pure iron has a comparably large saturation magnetisation than iron oxides.

Moreover, the switching effect has increased with increasing the magnitude of the magnetic field. This trend was maintained until the magnetic filler particles became completely saturated. The reason for this was a larger magnetic interaction between the magnetic filler particles and the magnetic field. The additional increase in measurement temperature also led to a larger switching effect. The MRE of the sample N36C with 36 vol.% CIP was 354 % at room temperature and 609 % at a temperature of 50 °C. This is explained by the fact that the temperature increase has actively supported the mobility of the magnetic filler particles within the rubber matrix and thus facilitated their orientation along the magnetic field lines.

It was seen, that the silanisation has a big influence on the MRE of the samples. A MRE of more than 140 % was derived for the sample without silane S20C\Si while a significantly weaker MRE of nearly 40 % was obtained for the silanized sample S20C. This behaviour was related to the combined effect of a higher mobility of the magnetic filler particles without a shielding silane layer and the ability of the magnetic filler particles to come in close contact when they arrange in strings along the magnetic field lines.

Magnetorheological measurements were also carried out with the crosslinked MSE composites. The curing was done with and without magnetic field to get anisotropic and isotropic MSE respectively. This new structure ensures a larger stiffness for all MSE composites and higher moduli values in comparison to the melts, because a high level of crosslinking between the polymer chains was achieved and a magnetic filler network was built. The switching effect remains proportional to the microscaled magnetic filler content and the magnetic field strength during curing. However, the MRE of the vulcanised samples has become smaller than the MRE of the non-crosslinked melts because the magnetic filler particles are firmly tied to the polymer chains and can no longer be moved along the magnetic field lines. The maximum MRE was recorded for the anisotropic sample N13C A with 13 vol.% CIP. It was 36 %.

Furthermore, it was shown that the size of the magnetic filler particle as well as the magnitude of the magnetic field during curing determine the value of the MRE. The filler content cannot also be infinitely increased. A CIP volume fraction of 20 vol.% seemed appropriate to have an optimal property profile for almost all MSE composites. Similar to melts, the silane was needed to establish a good polymer-filler interface and cannot be sacrificed due to its negative impact on the switching effect.

It was shown that the magnetorheological response of the MSE composites can be described by the magnetic induced relaxation behaviours of the magnetic filler and the polymer chains. Short relaxation times of 1 to 2 seconds were observed for the magnetic filler while the relaxation of the polymer chains took between 10 and 80 seconds.

Quasi-static measurements in the presence of external magnetic field showed a strong coupling between the mechanical properties of MSE composites and the magnetic properties of the surroundings. The dynamic flocculation model (DFM) gave a deep insight into the inner structure of the samples and the ongoing measuring processes. Since the mechanical stiffening of the MSE composites was assigned to the magnetic filler, the fit parameters related to mechanical behaviour of rubber were only affected by the molecular structure of the polymer chains as well as the distribution of the magnetic filler particles within the rubber matrix and not by the applied magnetic field during the measurement. However, the tensile strength of virgin bonds s_v and the tensile strength of damaged bonds s_d have been affected by the applied magnetic field during the measurement. s_v has increased from 27.83 MPa to 28.92 MPa for the isotropic EPDM sample once the magnetic field was applied. The same happened for the anisotropic sample. The difference is significantly higher. s_v has increased from 51.69 MPa to 55.67 MPa when the magnetic field was turned on. The same behaviour was observed for s_d. The difference between turned on or off magnetic field is less pronounced.

The use of hybrid filler systems showed that the property profile of the finished MSE composites can be accordingly adjusted. The dynamic-mechanical behaviour of the samples can be indeed improved by using nanoscaled filler like MAGSILICA, technical silica or carbon black. However, the 20 vol.% limit of magnetic filler CIP seems indispensable to realise the highest switching effect. It was shown that the MSE composites with hybrid filler systems could be in the near future a serious option for mature application fields. These hybrid filler systems could be further extended to other types of nanoscaled fillers like graphene or carbon nanotubes, which have also had a favourable impact on improving the dynamic-mechanical properties of the finished elastomeric materials.

Bibliography

1. B. F. Spencer Jr., M. K. Sain, "Controlling buildings: a new frontier in feedback", IEEE Control Systems, pp. 19-35, December 1997.

2. B. F. Spencer Jr., S. Nagarajaiah, "State of the Art of Structural Control", J. Struct. Eng., pp. 845-856, July 2003

3. W. Demtröder, Experimentalphysik 1, Springer-Verlag Berlin Heidelberg, pp. 353-363, March 2008, ISBN 978-3-540-79294-9.

4. T. Kobori, "Future direction on research and development of seismic-response-controlled structure," Proc. 1st World Conf. on Struct. Control, Los Angeles, CA, Panel: 19-31, August 1994.

5. M. Sakamoto, T. Kobori, T. Yamada, and M. Takahashi, "Practical applications of active and hybrid response control systems and their verifications by earthquake and strong wind observations," Proc. 1st World Conf. on Struct. Control, Los Angeles, CA, pp. WP2:90-99, August 1994.

6. K. Tanida, Y. Koike, K. Mutaguchi, and N. Uno, "Development of hybrid active-passive damper," Active and Passive Damping, ASME, PVP-vol. 211, pp. 21-26, 1991.

7. Y. Koike, T. Murata, K. Tanida, T. Kobori, K. Ishii, and Y. Takenaka, "Development of V-shaped hybrid mass damper and its application to high-rise buildings," Proc. 1st World Conf. on Struct. Control, Los Angeles, CA, pp. FA2:3-12, August 1994.

8. J. Hirai, A. Hisanori, and E. Tsuji, "Study on tuned active damper for control tower of Kansai International Airport," Proc. Int. Workshop on Struct. Control, Honolulu, HI, pp. 206-13, 1993.

9. T. Suzuki, M. Kageyama, A. Nobata, S. Inaba, and O. Yoshida, "Active vibration control system installed in a high-rise building," Proc. 1st World Conf. on Struct. Control, Los Angeles, CA, pp. FP3:3-11, August 1994.

10. Y. Fujino and H. Yamaguchi, "Implemented examples of structural response control for civil structures with emphasis on active control," Japan Soc. Steel Const., vol. 12, pp. 16-22, 1994.

11. H. Iemura, A. Igarashi, Y. Inoue, and M. Sakamoto, "Nonlinear active control experiment of a real size frame structure," Proc. 2nd Int. Workshop on Struct. Control, Hong Kong, pp. 241-252, December 1996.

12. J. Cai, G. Bu, C. Yang, Q. Chen and Z. Zuo, "Calculation methods for inter-story drifts of building structures," Advances in Structural Engineering, Vol 17, Issue 5, 2014

13. J. Zhou, G. B. Bu and K. N. Li, "Calculation methods for inter-story drifts of building structures," 15th World Conf. on Earthquake Engrg WCEE, Lisbon, September 2012

14. J. M. Kelly, "Aseismic base isolation: its history and prospects," Proc. 1st World Cong. on Joints and Bearings, ACI-SP-70, vol. 1, pp. 549-586, 1981.

15. J. M. Kelly, "Aseismic base isolation: review and bibliography," Soil Dyn. and Earthquake Engrg., vol. 5, no. 3, pp. 202-216, 1986.

16. I. G. Buckle and R. L. Mayes, "Seismic isolation history, application and performance-a world view," Earthquake Spectra, vol. 6, no. 2, pp.161-201, 1990.

17. T. T. Soong and M. C. Constantinou, Eds., Passive and active Structural Vibration Control in Civil Engineering, Springer-Verlag, Wien and New York, 1994, ISBN 978-3-211-82615-7.

18. A. M. Reinhorn, T. T. Soong, and C. Y. Wen, "Base isolated structures with active control," Proc. ASME PVP Conf, San Diego, CA, PVP-127, pp. 413-420, 1987.

19. J. M. Kelly, G. Leitmann and A. G. Soldatos, "Robust control of base isolated structures under earthquake excitation," J. Opt. Theory and App., vol. 53, no. 2, pp. 159-180, 1987.

20. W. E. Schmitendorf, F. Jabbari, J. N. Yang, "Robust control techniques for buildings under earthquake excitation," Earthquake Engrg. and Struct. Dyn., 23, pp. 539-552, 1994.

21. J. N. Yang, J. C. Wu, A. M. Reinhorn, M. Riley, "Control of sliding isolated buildings using sliding mode control," J. Struct. Engrg., ASCE, vol. 122, no. 2, pp. 179-186, 1996.

22. P. Causemann, "Moderne Schwingungsdämpfung," ATZ 11/2003 Jahrgang 105

23. J. N. Yang, J. C. Wu, Z. Li, "Control of seismic-excited buildings using active variable stiffness systems," Engrg Struct , vol 18, no 8, pp.589-596, 1996

24. T. Kobori, M. Takahashi, T. Nasu, N. Niwa, K. Ogasawara, "Seismic response controlled structure with active variable stiffness system," Earthquake Engrg. and Struct. Dyn., vol 22, pp. 925-941, 1993

25. W. M. Winslow, "Method and means for translating electrical impulses into mechanical forces", U.S. Patent No US2417850 A, 1947

26. W. M. Winslow, "Induced fibration of suspensions" J. Appl. Phys., vol 20, pp. 1137-1140, 1949

27. J. Rabinow, "The magnetic fluid clutch", AIEE Transactions, 67, pp 1308-1315, 1948

28. T. Nishi,"Elastomeric-Seismic Protection Isolators at the East Japan Giant Earthquake", Plenary speech, 10th Fall Rubber Colloqium, Hannover, 2012

29. H. Deng, X. Gong, L. Wang, "Development of an adaptive tuned vibration absorber with magnetorheological elastomer", Smart Mater. Structure 15, 2006, 111

30. J. D. Carlson, M. R. Jolly, "MR Fluid, Foam and Elastomer Devices", Mechatronics 10, 2000, pp 555-569

31. J. Ginder, M. Nichols, L. Elie, J. Tardiff, "Magnetorheological elastomers: properties and applications, Smart structures and materials" Proc. SPIE, 3675, 1999, pp 131-138

32. K. Popp, M. Kröger, W. Li, X. Zhang, P. Kosasih, "MRE Properties under Shear and Squeeze Modes and Applications", J. Int. Mat. Sys. and Structure 21, 2010, 1471

33. Y. Li, J. Li, W. Li, B. Samali, "Development and characterisation of a magnetorheological elastomer based adaptive seismic isolator", Smart Materials and Structure 22, 2013, 035005

34. M. K. Sethi, P. Kumar and A. Kumar, "Transient vibration reduction of a powertrain using MRE based adaptive tuned vibration absorber", Proc. Eng. 144, 2016, pp. 689–696

35. Z. Xu, X. Gong, G. Liao and X. Chen, "An active damping-compensated magnetorheological elastomer adaptive tuned vibration absorber", J. Intell. Mater. Syst. Struct. 21, 2010, pp. 1039–1047

36. G. J. Liao, X. L. Gong, C. J. Kang and S. H. Xuan, "The design of an active–adaptive tuned vibration absorber based on magnetorheological elastomer and its vibration attenuation performance", Smart Mater. Struct. 20, 2011, 075015

37. R. Sinko, M. Karnes, J. H. Koo, Y. K. Kim and K. S. Kim, "Design and test of an adaptive tuned vibration absorber for reducing cryogenic cooler vibrations" ASME 2011 Conf. on Smart Materials, Adaptive Structures and Intelligent Systems, 2011, pp. 325–331

38. S. Sun, J. Yang, W. Li, H. Deng, H. Du and G. Alici, "Development of an MRE adaptive tuned vibration absorber with self-sensing capability" Smart Mater. Struct. 24, 2015, 095012

39. S. Sun, H. Deng, J. Yang, W. Li, H. Du, G. Alici and M. Nakano, "An adaptive tuned vibration absorber based on multilayered MR elastomers", Smart Mater. Struct. 24, 2015, 045045

40. H. Deng, X. Gong and L. Wang, "Development of an adaptive tuned vibration absorber with magnetorheological elastomer", Smart Mater. Struct. 15, 2006, pp. N111–116

41. N. Hoang, N. Zhang and H. Du, "A dynamic absorber with a soft magnetorheological elastomer for powertrain vibration suppression" Smart Mater. Struct. 18, 2009, 074009

42. T. Komatsuzaki, T. Inoue and Y. Iwata, "Experimental investigation of an adaptively tuned dynamic absorber incorporating magnetorheological elastomer with selfsensing property", Exp. Mech. 56, 2016, pp.871–880

43. M. Behrooz, X. Wang and F. Gordaninejad, "Performance of a new magnetorheological elastomer isolation system", Smart Mater. Struct. 23, 2014, 045014

44. C. Yang, J. Fu, M. Yu, X. Zheng and B. Ju, "A new magnetorheological elastomer isolator in shear compression mixed mode", J. Intell. Mater. Syst. Struct. 26, 2015, pp. 1290–1300

45. M. Behrooz, S. Yarra, D. Mar, N. Pinuelas, B. Muzinich, N. G. Publicover, G. Pekcan, A. Itani and F. Gordaninejad, "A self-sensing magnetorheological elastomer-based adaptive bridge bearing with a wireless data monitoring system", Proc. SPIE 9803 98030D, 2016

46. G. Park, S. Chen, R. Li, Z. Zhang and X. Wang, "Multi-scale analysis and optimized design of laminated-MRE bearings", Proc. SPIE 9799 97993M, 2016

47. R. Li, X. Li, Y. Wu, S. Chen and X. Wang, "Analysis of longitudinal seismic response of bridge with magnetorheological elastomeric bearings" Proc. SPIE 9803 98034I, 2016

48. Z. W. Xing, M. Yu, J. Fu, Y. Wang and L. J. Zhao, "A laminated magnetorheological elastomer bearing prototype for seismic mitigation of bridge superstructures", J. Intell. Mater. Syst. Struct. 26, 2015, pp. 1818–1825

49. H. Du, W. Li and N. Zhang, "Semi-active variable stiffness vibration control of vehicle seat suspension using an MR elastomer isolator", Smart Mater. Struct. 20, 2011, 105003

50. S. Sun, J. Yang, H. Deng, H. Du, W. Li, G. Alici and M. Nakano, "Horizontal vibration reduction of a seat suspension using negative changing stiffness magnetorheological elastomer isolators", Int. J. Veh. Des. 68, 2015, pp. 104–118

51. X. X. Bai and N. M. Wereley, "Magnetorheological impact seat suspensions for ground vehicle crash mitigation" SPIE Smart Structures and Materials + Nondestructive Evaluation and Health Monitoring (International Society for Optics and Photonics), 2014, p 90570R

52. I. L. Ladipo, J. D. Fadly and W. F. Faris, "Characterisation of magnetorheological elastomer (MRE) engine mounts", Mater.Today Proc. 3, 2016, pp. 411–418

53. B. Kavlicoglu, B. Wallis, H. Sahin and Y. Liu, "Magnetorheological elastomer mount for shock and vibration isolations", Proc. SPIE 7977 79770Y, 2011

54. V. Bogdanov, D. Borin, G. Stepanov and A. Andruszkiewicz, "Usage of magneto-active elastomers in a bumper of a vehicle for front impact protection", J. Phys. 149, 2009, pp. 1–4

55. Adaptive linear Crash-Systems, ThyssenKrupp techforum 1, 2006, pp. 41-47

56. T. Huber, B. Bergmair, C. Vogler, F. Bruckner, G. Hrkac, D. Suess, "Magnetoelastic resonance sensor for remote strain measurements", App. Phys. Lett. 101, 2012, 042402

57. B. Bergmair, J. Liu, T. Huber, O. Gutfleisch, D. Suess, „Wireless and passive temperature indicator utilizing the large hysteresis of magnetic shape memory alloys", App. Phys. Lett. 101, 2012, 042412

58. B. Bergmair, "Sichere Kühlkette", Physik Journal 12, Juni 2013, p. 14

59. T. I. Volkova, V. Böhm, T. Kaufhold, J. Popp, F. Becker, D. Yu. Borin, G. V. Stepanov, K. Zimmermann, "Motion behaviour of magneto-sensitive elastomers controlled by an external magnetic field for sensor applications", J. Magn. Mater. 431, 2017 , pp. 262-265.

60. L. Ge, X. Gong, Y. Wang, S. Xuan, "The conductive three dimensional topological structure enhanced magnetorheological elastomer towards a strain sensor", Compos. Sci. Technol. 135, 2016, pp. 92-99

61. N. Ghafoorianfar and F. Gordaninejad, "A magnetorheological elastomer compressive and shear sensor", Proc. SPIE 9435 94351E, 2015

62. I. Bica, "Magnetoresistor sensor with magnetorheological elastomers", J. Indus. Eng. Chem. 17, 2011, pp. 83–89

63. W. Li, K. Kostidis, X. Zhang and Y. Zhou, "Development of a force sensor working with MR elastomers", IEEE/ASME Int. Conf. on Advanced Intelligent Mechatronics, 2009, AIM (Piscataway, NJ: IEEE) pp. 233–238

64. X. Wang, F. Gordaninejad, M. Calgar, Y. Liu, J. Sutrisno and A. Fuchs, "Sensing behavior of magnetorheological elastomers", J. Mech. Des. 131, 2009, 091004

65. R. Sykora, V. Babayan, M. Usakova, J. Kruzelak, I. Hudec, "Rubber Composite Materials With the Effects of Electromagnetic Shielding", Polym Compos. 2015, doi:10.1002/pc.23490

66. R. Sykora, V. Babayan, M. Usakova, J. Kruzelak, I. Hudec, "Elastomer Composites With the Effects of Electromagnetic Shielding", 11th Fall Rubber Colloqium, Hannover, 26. – 28. Nov. 2014

67. H. Bose, R. Rabindranath and J. Ehrlich, "Soft magnetorheological elastomers as new actuators for valves", J. Intell. Mater. Syst. Struct. 23, 2012, pp. 989–94

68. M. Farshad and M. Le Roux, "A new active noise abatement barrier system", Polym. Test. 23, 2004, pp. 855–860

69. G. Du and X. Chen, "MEMS magnetometer based on magnetorheological elastomer Measurement" 45, 2012, pp. 54–58

70. D. Lee, M. Lee, N. Jung, M. Yun, J. Lee, T. Thundat and S. Jeon, "Modulus-tunable magnetorheological elastomer microcantilevers", Smart Mater. Struct. 23, 2014, 055017

71. Y. Q. Ni, Z. G. Ying and Z. H. Chen, "Magneto-rheological elastomer (MRE) based composite structures for microvibration control", Earthq. Eng. Eng. Vib. 9, 2010, pp. 345–356

72. M. Behrooz and F. Gordaninejad, "Behavior of a flexible controllable micropump" Proc. SPIE 9431 943109, 2015

73. M. Behrooz and F. Gordaninejad, "A flexible micro fluid transport system featuring magnetorheological elastomer", Smart Mater. Struct. 25, 2016, 025011

74. F. Jonsdottir, F. B. Gudmundsson, K. H. Gudmundsson and C. Lecomte, "Preparation and characterisation of a prototype magnetorheological elastomer for application in prosthetic devices", 7th ECCOMAS Thematic Conf. on Smart Structures and Materials, 2015

75. M. Behrooz, "A controllable flexible micropump and a semi-active vibration absorber using magnetorheological elastomers", PhD Thesis University of Nevada, Reno, 2015

76. F. Röthmeyer; F. Sommer, "Kautschuktechnologie",München; Wien: Hanser, 2001 ISBN 3-446-16169-4

77. R. H. Schuster, "Kautschuke", Internal lecture for training seminars in DIK, 2007

78. GAK 12/1998, Jahrgang 51, p. 985

79. "Uhlmann's Encyclopedia of Industrial Chemistry", VCH Verlagsgesellschaft mbH, 1993

80. Therban.com, XHNBR

81. Arlanxeo, Product data sheet, XHNBR

82. Lanxess Green Mobilität

83. Lanxess Grüne Reifen

84. R. Steudel, "Eigenschaften von Schwefel-Schwefel Bindungen", Angewandte Chemie, 87. Jahrgang 1975, Heft 19, pp 683-720

85. E. Riedel, C. Janiak, "Anorganische Chemie", Walter de Gruyter GmbH & Co.KG, 2007 ISBN 978-3-11-018903-2

86. Orion Engineered Carbons, Product data sheet, N550

87. Orion Engineered Carbons, Product data sheet, Printex XE2-B

88. Evonik, Product data sheet, Ultrasil 7000 GR, short U7000

89. Magnetic materials, http://ruby.chemie.uni-freiburg.de/Vorlesung/angewandte.html, Materials for the lecture "Applied solid state chemistry"

90. W. Demtröder, "Experimentlphysik 3", Springer Verlag, 2005 ISBN 3-540-21473-9

91. D. Meschede, "Gerthsen Physik", Springer Verlag, 2002, ISBN 678-3-662-07461-9

92. P. A. Tipler, G. Mosca, "Physik für Wissenschaftler und Ingenieure", Spektrum Akademischer Verlag, Auflage 6, 2009, ISBN 978-3827419453

93. M. Getzlaff, "Fundamentals of Magnetism", Springer Berlin, 2007, ISBN 978-3-540-31150-8

94. W. F. Brown Jr., "Micromagnetics", John Wiley & Sons, Inc., 1963, Library of Congress Catalog Card Number 63-18566

95. R. L. Carlin, "Magnetochemistry", Springer Verlag, 1986, ISBN 3-540-15816-2

96. R. M. Cornell, U. Schwetmann, "The Iron Oxides: Structure, Properties, Reactions, Occurrences and Uses", WILEY-VCH Verlag GmbH & Co. KGaA, Weinheim, 2nd Edition 2003, ISBN 3-527-30274-3

97. U. Schwetmann, R. M. Cornell, "Iron Oxides in the Laboratory", WILEY-VCH Verlag GmbH & Co. KGaA, Weinheim, 2nd Edition 2000, ISBN 3-527329669-7

98. E. Ürögiova, I. Hudec, D. Bellusova, "Magnetic and mechanical properties of strontium ferrite rubber composites", KGK Mai 2006, pp. 224-228

99. D. Bellusova, T. Alshuth, R. H. Schuster, M. Myndyk, V. Sepelak, I. Hudec, "Influence of barium Ferrites on the performance of BR-elastomers", KGK März 2008, pp. 118-123

100. J. Kruzelak, R. Szabova, D. Bellusova, G. Kysela, I. Hudec, "Elastomeric materials with magnetic fillers for intelligent tyres construction", KGK Januar/Februar 2010, pp. 20-24

101. D. Bellusova, T. Alshuth, R. Schuster, M. Myndyk, V. Sepelak, "The effect of mechanical milling of co-precipitated barium hexaferrite on the properties of BR-composites", KGK November/Dezember 2011, pp. 22-28

102. Th. Alshuth, M. Ramspeck, R. H. Schuster, B. Halbedel, F. Zschunke, "Magnetorheologische Elastomere", KGK September 2007, pp. 448-455

103. C. W. Karl, J. McIntyre, T. Alshuth, M. Klüppel, "Magneto-rheological elastomers with switchable mechanical properties", KGK 1-2 2013, pp. 46-53

104. J. McIntyre, T. Alshuth, "Crack propagation in magnetorheological elastomers", KGK 11-12 2013, pp. 29-35

105. P. Wagner, S. Robin, J. McIntyre, T. Alshuth, R. H. Schuster, U. Giese, P. Gaczynski, K. D. Becker, D. Menzel, "Synthesis and characterisation of soft magnetic $MnFe_2O_4$ particles as a basis for magneto-active elastomers", KGK 5 2014, pp. 40-46

106. S. Aloui, M. Klüppel, "Magneto-rheological response of elastomer composites with hybrid-magnetic fillers", Smart mater. Struct., 24, 2015, 025016

107. M. Klüppel, S. Aloui, "Optimization of mechanical properties of magneto-sensitive elastomers by applying hybrid-magnetic fillers", Constitutive Models for Rubber IX, Marvalova & Petrikova (Eds), Taylor & Francis Group London, 2015, pp. 633-638, ISBN 978-1-138-02873-9

108. L. Mond, C. Langer and F. Quincke, "Action of carbon monoxide on nickel", J. Chem. Soc., Trans., 57, 1890, pp. 749-753

109. L. Mond, C. Langer, "On iron carbonyls", J. Chem. Soc., Trans., 59, 1891, pp. 1090-1093

110. J. Dewar, H. O. Jones, "The physical and chemical properties of iron carbonyl", Proceedings of the royal society A,76, 513, 1905, pp. 558- 577

111. A. Mittasch, "Über Eisencarbonyl und Carbonyleisen", Zeitschrift für angewandte Chemie, 41, 1928, pp- 827-850

112. J. E. Huheey, E. A. Keiter, R. L. Keiter, "Anorganische Chemie prinzipien von Strukturen und Reaktivität", Walter de Gruyter Berlin New York, 1995, ISBN 978-3-110-13557-2

113. D. S. Terekhov, N. V. Emmanuel, "Direct extraction of nickel and iron from laterite ores using the carbonyl process", Minerals Engineering, 54, 2013, pp. 124-130

114. BASF SE, Carbonyl Iron Powder

115. BASF SE, CIP technical data sheet

116. Evonik Industries, MAGSILICA Technical data sheet

117. S.-J. Lee, J.-R. Jeong, S.-C. Shin, J.-C. Kim und J.-D. Kim, "Synthesis and characterization of superparamagnetic maghemite nanoparticles prepared by coprecipitation technique", J. Magn. Magn. Mat., 282, 2004, pp. 147-150

118. S. Mornet, J. Portier und E. Duguet, "A method for synthesis and functionalization of ultrasmall superparamagnetic covalent carriers based on maghemite and dextran", J. Magn. Magn. Mater., 293, 1, 2005, pp. 127-134

119. I. Dzyaloshinsky, "A thermodynamic theory of "weak" ferromagnetism of antiferromagnetics", J. Phys. Chem. Solids, 4, 4, 1958, pp. 241-255

120. T. Moriya, "Anisotropic superexchange interaction and weak ferromagnetism", Phys. Rev., 120, 1, 1960, pp. 91- 98

121. M. -Z. Dang, D. G. Rancourt, J. E. Dutrizac, G. Lamarche, R. Provencher, "Interplay of surface conditions, particle size, stoichiometry, cell parameters, and magnetism in synthetic hematite-like materials", Hyperfine Interactions 117, 1-4, 1998, pp. 271–319

122. W. Grellmann, S. Seidler (Hrsg.), „Kunststoffprüfung", Carl Hanser Verlag München, 3. Auflage, 2015, ISBN 978-3-446-44350-1.

123. K. P. Menard, "Dynamic mechanical analysis: a practical introduction", CRC Press, 2nd. edition, 2008, ISBN 978-1-4200-5312-8

124. J. D. Ferry, "Viscoelastic Properties of Polymers", 3rd ed., Wiley, New York, 1980, ISBN 978-0-471-04894-7

125. M. L. Williams, R. F. Landel, J. D. Ferry, J. Am. Chem. Soc. 77, 1955, 3701

126. M. L. Williams, J. D. Ferry, "Second approximation calculations of mechanical and electrical relaxation and retardation distributions", J. Polym. Sci 11, 2, 1953, pp. 169-175

127. M. Klüppel, "Evaluation of viscoelastic master curves of filled elastomers and applications to fracture mechanics", J. Phys.: Condesn. Matter, 21, 2009, 035104

128. M. Saphiannikova, V. Toshchevikov, I. Gazuz, F. Petry, S. Westermann, G. Heinrich, "Multiscale Approach to Dynamic-Mechanical Analysis of Unfilled Rubbers", Macromolecules 47, 2014, pp. 4813-4823

129. I. Ivaneiko, V. Toshchevikov, M. Saphiannikova, K. W. Stöckelhuber, F. Petry, S. Westermann, G. Heinrich, "Modeling of dynamic-mechanical behavior of reinforced elastomers using a multiscale approach", Polymer, 82, 2016, pp. 356-365

130. I. Ivaneiko, V. Toshchevikov, K. W. Stöckelhuber, M. Saphiannikova, G. Heinrich, "Superposition approach to the dynamic-mechanical behaviour of reinforced rubbers", Polymer, 127, 2017, pp. 129-140

131. M. Klüppel, "Characterisation of nonideal networks by stress-strain measurements at large extensions", J. Appl. Polym. Sci. vol. 48, issue 7, 1993, pp 137-150

132. M. Klüppel, J. Schramm, "A generalized tube model of rubber elasticity and stress softening of filler reinforced elastomer systems", Macromol. Theory Simul. 9, 2000, pp. 742-754

133. M. Klüppel, J. Schramm, Proceedings: Kautschuk-Herbst-Kolloquium 98, Hannover 1998, p. 341

134. G. Heinrich, E. Straube, G. Helmis, "Rubber elasticity of polymer networks:theories", Springer Berlin/Heidelberg, Adv. Polym. Sci. 85, 1988, pp. 33-87

135. G. Heinrich, M. Kaliske, "Theoretical and numerical formulation of a molecular based constitutive tube-model of rubber elasticity", Comput. Theor. Polym. Sci. 7 (3/4), 1997, pp. 227-241

136. M. Klüppel, J. Schramm, "A generalized tube model of rubber elasticity and stress softening of filler reinforced elastomer systems", Macromol. Theory Simul. 9, 2000, pp. 742-754

137. M. Klüppel, H. Menge, H. Schmidt, H. Schneider, R. H. Schuster, "Influence of Preparation Conditions on Network Parameters of Sulfur-Cured Natural Rubber", Macromolecules, 34 (23), 2001, pp. 8107-8116

138. M. Klüppel, "The role of disorder in filler reinforcement of elastomers on various length scales", Adv. Polym. Sci. 164, 2003, pp. 1–86

139. M. Klüppel, "Hyperelasticity and stress softening of filler reinforced polymer networks", Macromol. Symp., vol. 200, 2003, pp. 31–43

140. M. Klüppel, J. Meier, G. Heinrich, "Impact of pre-strain on dynamic-mechanical properties of carbon black and silica filled rubbers". Busfield, Muhr (Eds.) Constitutive Models for Rubber III, Swets & Zeitlinger, Lisse, 2003, p. 333

141. M. Klüppel, J. Meier, M. Dämgen, "Modelling of stress softening and filler induced hysteresis of elastomer materials". Austrell, Kari (Eds.) Constitutive Models for Rubber IV, Taylor & Francis, London 2005, p. 171.

142. H. Lorenz, J. Meier, M. Klüppel, "Micromechanics of internal friction of filler reinforced elastomers", Besdo D., Heimann B., Klüppel M., Kröger M., Wriggers P., Nackenhorst U. (Eds.), Elastomere Friction: Theory, Experiment and Simulation, Lecture Notes in Applied and Computational Mechanics, vol. 51. Springer, Berlin, Heidelberg, New York, 2010, pp. 27–52, ISBN: 978-3-642-10656-9

143. H. Lorenz, M. Freund, D. Juhre, J. Ihlemann, M. Klüppel, "Constitutive generalisation of a microstructure-based model for filled elastomers", Macromol. Theory Simul. 20, 2011, pp 110–123

144. H. Lorenz, M. Klüppel, G. Heinrich, "Micro-structure based modelling and FE-implementation of filler-induced stress softening and hysteresis of reinforced rubbers", Z. Angew. Math. Mech., 92, 8, 2012

145. H. Lorenz, M. Klüppel, "Microstructure-based modelling of arbitrary deformation histories of filler-reinforced elastomers", J. Mech. Phys. Solids 60, 2012, pp 1842-1861

146. H. Lorenz, "Mikrostruktur-basierte Modellierung des mechanischen Verhaltens gefüllter Elastomere", Dissertation at Technical University Dresden, 2012

147. A. Einstein, "Berichtigung zu meiner Arbeit :Eine neue Bestimmung der Moleküldimensionen", Ann. Phys. 34, 1911, pp 591-592

148. P. Meakin, "Fractal aggregates", Adv. Colloid Interface Sci. 28, 1987, pp 249-331

149. H. Blumenauer, G. Pusch, "Technische Bruchmechanik", VEB Deutscher Verlag für Grundstoffindustrie Leipzig, 2. Auflage, 1987, ISBN: VLN 152-915/68/86

150. A. A. Griffith, "The phenomena of rupture and flow in solids", Philosophical Transactions of the Royal Society of London, Series A, vol. 221, 1921, pp 163–198

151. M. Kuna, „Numerische Beanspruchungsanalyse von Rissen", Vieweg+Teubner, 2008, ISBN 978-3-8351-0097-8

152. H. Blumenauer, G. Pusch, "Bruchmechanik. Grundlagen Prüfmethoden, Anwendungsgebiete", VEB Deutscher Verlag für Grundstoffindustrie Leipzig, 1. Auflage, 1973, ISBN: VLN 152-915/62/73

153. S. Sähn, H. Göldner, "Bruch- und Beurteilungskriterien in der Festigkeitslehre", Fachbuchverlag Leipzig-Köln, 2. Auflage, 1993, ISBN: 3-343-00854-0

154. U. Eisele, S. Kelbch, H.-W. Engels, "The Tear Analyzer – A New Tool for Quantitative Measurements of the Dynamic Crack Growth of Elastomers", Kautsch. Gummi Kunstst. 45, 1992, pp. 1064–1069

155. P. Paris, F. Erdogan, "A critical analysis of crack propagation laws", J. Basic Eng. 85, 1963, pp 528-534

156. H. Blumenauer, "Werkstoffprüfung", 6. Auflage, Deutscher Verlag für Grundstoffindustrie, Leipzig, 1994, ISBN 3-342-00547-5

157. U. Eisele, "Introduction to Polymer Physics", Springer Berlin Heidelberg, 1990

158. Arlanxeo, Product data sheet, Keltan 4450

159. Arlanxeo, Product data sheet, NBR 3945

160. Arlanxeo, Product data sheet, HNBR 3467

161. Arlanxeo, Product data sheet, XHNBR

162. Lanxess, Product data sheet, Buna VSL 2525-0

163. Operating instruction for MTS

164. ARES User´s Manual

165. Operating instruction for Eplexor®

166. Operating instruction for TFA

167. Operating instruction for Anton Paar: magnetic cell

168. Operating instruction for Anton Paar: dielectric cell

169. Novocontrol Owner´s Manual, Novocontrol User´s Manual

170. T. A. Vilgis, G. Heinrich, M. Klüppel, "Reinforcement of Polymer Nano-Composites", Cambridge University Press, Cambridge 2009

171. S. Aloui, M. Klüppel, Effect of Particles Orientation on Dynamic-Mechanical Response and Switching-Ability of Magneto-Sensitive Elastomers, 2017 submitted

172. A. R. Payne, "The dynamic properties of carbon black loaded natural rubber vulcanizates", J. Appl. Polym Sci , 21, 1962, pp. 368-372

173. DIN 50035 (2012-09): Begriffe auf dem Gebiet der Alterung von Materialien – Polymere Werkstoffe

174. G. W. Ehrenstein, S. Pongratz, "Beständigkeit von Kunststoffen", Carl Hanser Verlag, München Wien, 2007, ISBN 978-3-446-21851-2

175. A. R. Azura, S. Ghazali, M. Mariatti, "Effects of the Filler Loading and Ageing Time on the Mechanical and Electrical Conductivity Properties of Carbon Black Filled Natural Rubber", J. Appl. Polym. Sci. 110, 2008, pp. 747–752

176. O. Claessen, T. Mang, H. G. Dikland, M. van Duin, "Helle Fensterprofilmaterialien: Alterungsverhalten auf Basis von peroxidisch vernetztem EPDM". Kautsch. Gummi Kunstst. 63, 2010, pp. 350–360

177. K. Oßwald, K. Reincke, S. Döhler, U. Heuert, B. Langer, W. Grellmann, "Aspekte der Alterung elastomerer Werkstoffe", KGK Kautschuk Gummi Kunststoffe 70, 2017, 8, pp. 498–506

178. B. N. J. Persson, E. A. Brener, "Crack propagation in viscoelastic solids", Phys. Rev. E, 71, 2005, 036123

179. M. Klüppel, "Evaluation of viscoelastic master curves of filled elastomers and applications to fracture mechanics", J. Phys.: Condens. Matter, 21, 2009, 035104

180. M. R. Jolly, J. D. Carlson and B. C. Munoz, "A model of the behaviour of magnetorheological materials", Smart Mater. Struct., 5, 1996, pp. 607–614

181. D. Ivaneyko, V. P. Toshchevikov, M. Saphiannikova and G. Heinrich, "Magneto-sensitive elastomers in a homogeneous magnetic field: A regular rectangular lattice model", Macromol. Theory Simul., 20, 2011, pp. 411–424

182. D. Ivaneyko, V. Toshchevikov, M. Saphiannikova and G. Heinrich, "Effects of particle distribution on mechanical properties of magneto-sensitive elastomers in a homogeneous magnetic field", Condens. Matter Phys., 15, 3, 2012, pp. 33601: 1-12

183. L. Borcea, and O. Bruno, "On the magneto-elastic properties of elastomer-ferromagnet composites", J. Mech. Phys. Solids, 49, 2001, pp. 2877–2919

184. J. Ginder, S. Clark, W. Schlotter and M. Nichols, "Magnetostrictive phenomena in magnetorheological elastomers", Int. J. Mod. Phys. B, 16, 2002, pp. 2412–2418

185. X. Guan, X. Dong and J. Ou, "Magnetostrictive effect of magnetorheological elastomer", J. Magn. Magn. Mater, 320, 2008, pp. 158–163

186. P. Ponte Castaneda and E. Galipeau, "Homogenization-based constitutive models for magnetorheological elastomers at finites train", J. Mech. Phys. Solids, 59, 2011, pp. 194–215

187. K. Danas, S. V. Kankanala and N. Triantafyllidis, "Experiments and modelling of iron-particle-filled magnetorheological elastomers", J. Mech. Phys. Solids, 60, 2012, pp. 120–138

188. E. Galipeau and P. Ponte Castaneda, "The effect of particle shape and distribution on the macroscopic behavior of magnetoelastic composites", Int. J. Solids Struct., 49, 2012, pp. 1-17

189. L. Mullins and N. R. Tobin, "Stress softening in rubber vulcanizates. Use of a strain amplification factor to describe the elastic behavior of filler-reinforced vulcanized rubber", J. Appl. Polym Sci , 9, 1965, pp. 2993-3009

190. J. A. C. Harwood, L. Mullins, and A. R. Payne, "Stress Softening in Natural Rubber Vulcanizates", J. Appl. Polym Sci , 9, 1965, pp. 3011-3021

191. A. E. Berkowitz, W. J. Schuele , P. F. Flanders, "Permanent magnets and fine particles", J. Appl. Phys. 39, 1968, 1261

192. H. Blumenauer, "Werkstoffe und Diagnosemethoden für adaptive mechanische Systeme", In: G. Leps, H. Kausche (Eds) 40 Jahre Werkstofftechnik in Merseburg, Selbstverlag, 1999, ISBN 3-86010-578-7

193. A. Ritter, "Smart materials – in Architektur, Innenarchitektur und Design", Birkhäuser Basel, 2007, ISBN 978-3-7643-7326-1

194. D. M. Addington, D. L. Schodek, "Smart Materials and Technologies – For the Architecture and Design Professions", Elsevier Science Publishers B. V. Amsterdam, 2007, ISBN 978-0-7506-6225-3

195. P. W. Bridgman, The Effect of Tension on the Electrical Resistance of Certain Abnormal Metals, Proc. Amer. Acad. Arts Sci., 57, 3, 1922, pp. 41-66

196. H. R. Tränkler, "Taschenbuch der Meßtechnik: mit Schwerpunkt Sensortechnik", Oldenburg, 1996, ISBN 3-486-23670-9

197. D. Steinhauser, M. Möwes, M. Klüppel, "Carbon black networking in elastomers monitored by simultaneous rheological and dielectric investigations", J. Phys.: Condens. Matter, 28, 2016, 495103

198. C. Wrana, "Polymerphysik", Springer Spektrum, 2014, ISBN 978-3-642-45075-4

199. M. M. Möwes, F. Fleck, M. Klüppel, Effect of filler surface activity and morphology on mechanical and dielectric properties of NBR/Graphene nanocomposites", Rubber Chem. Technol., 87, 1, 2014, pp. 70–85

200. A. Das, K.W. Stöckelhuber, R. Jurk, M. Saphiannikova, J. Fritzsche, H. Lorenz, M. Klüppel and G. Heinrich, "Modified and unmodified multiwalled carbon nanotubes in high performance solution-styrene–butadiene and butadiene rubber blends", Polymer, 49, 2008, pp. 5276–5283

201. J. Fritzsche, H. Lorenz and Manfred Klüppel, "CNT based elastomer-hybrid-nanocomposites with promising mechanical and electrical properties", Macromol. Mater. Eng., 294, 2009, pp. 551–560

202. D. Steinhauser, K. Subramaniam, A. Das, G. Heinrich and M. Klüppel, "Influence of ionic liquids on the dielectric relaxation behavior of CNT based elastomer nanocomposites", eXPRESS Polym. Lett., 6, 11, 2012, pp. 927–936

203. J. Fritzsche, H. Lorenz and M. Klüppel, "Elastomer carbon nanotube composites", Polymer carbon nanotube composites: preparation, properties and applications, T. McNally und P. Pötschke, Eds., Woodhead Publishing Limited, 2011, pp. 193-229, ISBN 978-1-84569-761-7

204. A. Das, K. W. Stöckelhuber, J. Fritzsche, R. Jurk, M. Klüppel and G. Heinrich, "Coupling activity of ionic liquids between diene elastomers and multi-walled carbon nanotubes", Carbon, 47, 14, 2009, pp. 3313-3321

205. D. Yu and L. Dai, "Self-Assembled Graphene/Carbon Nanotube hybrid films for supercapacitors", J. Phys. Chem. Lett., 1, 2, 2010, pp. 467-470

206. S. Yang, Y. Sun, L. Chen, Y. Hernandez, X. Feng and K. Mullen, "Porous iron oxide ribbons grown on graphene for high-performance lithium storage", Sci. Rep., 2, 427, 2012, pp. 1-7

207. Y. He, Q. Sheng, J. Zheng, M. Wang and B. Liu, "Magnetite–graphene for the direct electrochemistry of hemoglobin and its biosensing application", Electrochim. Acta, 56, 5, 2011, pp. 2471-2476

208. Y. Gao, D. Ma, G. Hu, P. Zhai, X. Bao, B. Zhu, B. Zhang and D. S. Su, "Layered-carbon-stabilized iron oxide nanostructures as oxidation catalysts", Angew. Chem. Int. Ed. Engl., 50, 43, 2011, pp. 10236-10240

209. V. Chandra, J. Park, Y. J. Chun, W. Lee, I. C. Hwang and K. S. Kim, "Water-dispersible magnetite-reduced graphene oxide composites for arsenic removal", ACS Nano, 4, 7, 2010, pp. 3979-3986

210. H. Jabeen, V. Chandra, S. J. Jung, W. Lee, K. S. Kim and S. B. Kim, "Enhanced Cr(VI) removal using iron nanoparticle decorated graphene", Nanoscale, 3, 2011, pp. 3583-3585

211. X. Yang, X. Zhang, Y. Ma, Y. Huang, Y. Wang and Y. Chen, "Superparamagnetic graphene oxide–Fe_3O_4 nanoparticles hybrid for controlled targeted drug carriers", J. Mater. Chem., 19, 2009, pp. 2710-2714

212. P. Bhunia, G. Kim, C. Baik and H. Lee, "A strategically designed porous iron–iron oxide matrix on graphene for heavy metal adsorption", Chem. Commun., 48, 2012, pp. 9888–9890

213. S. Iijima, "Helical microtubules of graphitic carbon", Nature, 354, 1991, pp. 56-58

214. H. P. Monner, S. Mühle, P. Wierach and J. Riemenschneider, "Carbon nanotubes- ein multifunktionaler Leichtbauwerkstoff für die Adaptronik", Adaptronic Congress 2003

215. J.F. Harris Peter, "Carbon Nanotubes and Related Structures – New Materials for the Twenty-first Century", Cambridge University Press, Cambridge, 1999, ISBN 978-0-511-60581-9

216. B. I. Yakobson, C. J. Brabec, J. Bernholc, "Nanomechanics of carbon tubes: instabilities beyond linear range", Phys. Rev. Lett., 76, 14, 1996, pp. 2511-2514

217. M. S. Fuhrer, B. M. Kim, T. Dürkop and T. Brintlinger, "High-mobility nanotube transistor memory," Nano Lett., 2, 2002, pp. 755–759

218. M. Freitag, Y. Martin, J. A. Misewich, R. Martel and P. Avouris, "Photoconductivity of single carbon nanotubes," Nano Lett., 3, 2003, pp. 1067–1072

219. J. A. Misewich, R. Martel, P. Avouris, J. C. Tsang, S. Heinze, and J. Tersoff, "Electrically induced optical emission from a carbon nanotube FET", Science, 300, 5620, 2003, pp. 783–786

220. J. Kong, N. R. Franklin, C. Zhou, M. G. Chapline, S. Peng, K. Cho, and H. Dai, "Nanotube molecular wires as chemical sensors," Science, 287, 5453, 2000, pp. 622–625

221. A. Modi, N. Koratkar, E. Lass, B. Wei, and P. M. Ajayan, "Miniaturized gas ionization sensors using carbon nanotubes," Nature, 424, 2003, pp. 171–173

222. C. Staii, A. T. Johnson, M. Chen, and A. Gelperin, "Dna-decorated carbon nanotubes for chemical sensing," Nano Lett., 5, 2005, pp. 1774–1778

223. K. Kostarelos, A. Bianco and M. Prato, "Promises, facts and challenges for carbon nanotubes in imaging and therapeutics", Nat. Nanotechnol., 4, 2009, pp. 627–633

224. H. Wu, X. Chang, L. Liu, F. Zhao and Y. Zhao, "Chemistry of carbon nanotubes in biomedical applications", J. Mater. Chem., 20, 2010, pp. 1036–1052

225. A. Masotti and A. Caporali, "Preparation of magnetic carbon nanotubes (Mag-CNTs) for biomedical and biotechnological applications", Int. J. Mol. Sci., 14, 2013, pp. 24619-24642

226. X. Lu, H. Liu, C. Deng and X. Yan, "Facile synthesis and application of mesoporous silica coated magnetic carbon nanotubes", Chem. Commun., 47, 2011, pp. 1210–1212

List of figure

List of tables

Annexe

Annexe A: List of abbreviations

TMD	Tuned mass damper
HMD	Hybrid mass damper
HBI	Hybrid base isolation
MRF	Magnetorheological fluids
ERF	Electrorheological fluids
MSE	Magneto-sensitive Elastomers
NR	Natural rubber
EPDM	Ethylene propylene diene terpolymers
SBR	Styrene butadiene rubber
NBR	Acrylonitrile butadiene rubber
HNBR	Hydrogenated acrylonitrile butadiene rubber
XHNBR	Carboxylate hydrogenated acrylonitrile butadiene Rubber
DMTA	Dynamic-mechanical thermal analysis
MRE	Magnetorheological effect
Fe	Iron
FeO	Wüstite
α-Fe_2O_3	Hematite
δ -Fe_2O_3	Maghemite
Fe_3O_4	Magnetite
A	Anisotropic
I	Isotropic

Annexe B: Symbol directory

m	Mass		[kg]
D	Spring constant		[N/m]
F	Restoring force according to Hooke´s law		[N]
F_d	Frictional force, Stokes' drag		[N]
γ	Shear amplitude		[-]
T	Temperature		[°C]
T_0	Initial temperature		[°C]
T_C	Currie temperature		[°C]
T_k	Compensation temperature		[°C]
T_N	Néel temperature		[°C]
G*	Complex shear modulus		[MPa]
G'	Storage modulus		[MPa]
G''	Loss modulus		[MPa]
η*	Viscosity		[Pa.s]
η'	Real part of η*		[Pa.s]
η''	Loss modulus		[Pa.s]
tan δ	Loss angle		[-]
G_c	Crosslink modulus		[MPa]
G_e	Entanglement modulus		[MPa]
n	Finite extensibility parameter		[-]
s_d	Damaged/Soft bonds strength		[MPa]
s_v	Virgin bonds strength		[MPa]
x_0	Average cluster size		[-]
S_{set}	Set stress		[MPa]
ε_0	Vacuum permittivity	$8.85 \ 10^{-12}$	[As/(Vm)]
μ	Magnetic moment		[A².m]
μ_B	Bohr magneton		[J/T]

g_s	g-factor		[-]
q	Charge of the particle		[C]
S	Spin angular momentum		[kg.m²/s]
μ_0	Vaccum permeability	$4\pi.10^{-7}$	[Vs/(Am)]
χ_m	Magnetic susceptibility		[-]
Φ_B	Magntic flux		[Wb]
H	Magnetic flux		[A/m]
B	Magnetic flux density		[T]
M	Magnetisation		[T]
J	Magnetic polarization		[T]
k_B	Boltzmann constant	$1.38 \ 10^{-23}$	[J/K]
R	Gas constant	8.314	[J/(mol.K)]

Mathematical convention

A	Vectorial quantity in bold
A	Scalar quantity

Annexe C: List of materials and additives

Rubbers

Pale Crepe	Weber & Scher
Perbunan 3945	Lanxess
Keltan 4450	Lanxess
Therban 3467	Lanxess
Therban XT	Lanxess
VSL 2525-0	Lanxess

Fillers

CIP SW-S	BASF
MAGSILICA	Evonik
N550	Orion
Printex XE-2B	Orion
Ultrasil 7000 GR	Evonik

Additives

Dioctyl Phthalate	Aldrich
Treated distillate aromatic extract	Aldrich
Zinc oxide	Grillo Zinkoxid GmbH
Stearic acid	Henkel KGaA
Sulphur	Solvay Barium Strontium GmbH
CBS	Bayer (Vulkacit CZ)
DPG	Lanxess
6PPD	Aldrich
IPPD	Lanxess
Si 69	Evonik

Annexe D: Curriculum vitae

Name: Sahbi Aloui

Born on   24 Juni 1980 in Menzel Bourguiba, Tunisia

Professional experience

11.2017 -   Netzsch Gabo Instruments GmbH

                   Application engineer

07.2012 – 06.2017 German Institute of Rubber Technology e. V. (DIK)

                   Research associate

Education

10.2014-   Gottfried Wilhelm Leibniz University Hannover

                   Institute of Physical Chemistry and Electrochemistry

                   Target degree: Doctor of Natural Sciences (Dr. rer. nat.)

                   Dissertation: Preparation, Characterisation and Micromechanical

                   　　　　　　Modelling of Magneto-Sensitive Elastomers

10.2006 – 04.2011 Gottfried Wilhelm Leibniz University Hannover

                   Institute of Theoretical Physics

                   Degree: Diploma in Physics (Dipl.-Phys.)

                   Diploma thesis: Creation of Non-Abelian Gauge Potential in Ultracold

                   　　　　　　Quantum Gases

09.1998 – 06.2002 Ecole supérieure des sciences économiques et commerciales in Tunisia

                   Degree: „Maîtrise" in Economics

                   Thesis: Functioning of a Trading Room

Annexe E: List of publications and conference contributions

Publications

1. S. Aloui, M. Klüppel, Magneto-rheological response of elastomer composites with hybrid-magnetic fillers, Smart mater. Struct., 24, 2015, 025016

2. M. Klüppel, S. Aloui, Optimization of mechanical properties of magneto-sensitive elastomers by applying hybrid-magnetic fillers, Constitutive Models for Rubber IX, Marvalova & Petrikova (Eds), Taylor & Francis Group London, 2015, ISBN 978-1-138-02873-9, pp. 633-638

3. S. Aloui, M. Klüppel, Effect of Particles Orientation on Dynamic-Mechanical Response and Switching-Ability of Magneto-Sensitive Elastomers, Current smart mater., 3, 2018, pp. 1-10

Conference contributions: Presentations

1. Sahbi Aloui, Manfred Klüppel, Introduction to magnetorheological response of elastomers, Materiakonzepte und Modellierung Seminar Hannover (2013)

2. Sahbi Aloui, Manfred Klüppel, Magnetorheological response of elastomers: technical basis, DIK Kolloquim Hannover (2013)

3. Sahbi Aloui, Manfred Klüppel, Introduction to magneto-sensitive elastomers, Internationales ECEMP Kolloquium Dresden (2014)

4. Sahbi Aloui, Manfred Klüppel, Magneto-sensitive elastomers based on magnetic filler hybrid systems, 11. Kautschuk Herbst Kolloquium (KHK) Hannover (2014)

5. Sahbi Aloui, Manfred Klüppel, Magneto-sensitive elastomers, Deutsche Physikalische Gesellschaft (DPG) Frühjahrestagung Berlin (2015)

6. Sahbi Aloui, Manfred Klüppel, Magnetorheological elastomers for sensor applications, 35. Mitgliederversammlung Deutsche Kautschuk Gesellschaft (DKG) Hannover (2016)

7. Sahbi Aloui, Manfred Klüppel, Preparation and properties of magneto-sensitive elastomers, European PhD Rubber Seminar Hannover (2016)

Conference contributions: Posters

1. Sahbi Aloui, Manfred Klüppel, Smart elastomers based on magneto-sensitive filler systems, Zentrum für Festkörperchemie und neue Materialien, Summer school Hannover „Energy Materials" (2014)

2. Sahbi Aloui, Manfred Klüppel, Magneto-Sensitive Elastomers for Adaptive Vibration Control Systems, DKT Nürnberg (2015)

3. Sahbi Aloui, Manfred Klüppel, Magnetorheological Elastomers for Adaptive Vibration Control Systems, "Iron in functional materials" Symposium Hannover (2016)